# Formation of stars and star clusters in colliding galaxies

Pierre-Emmanuel Belles

UNIVERSITÉ PARIS SUD

Comprendre le monde, construire l'avenir®

University of Hertfordshire

UNIVERSITE PARIS-SUD et UNIVERSITY OF HERTFORDSHIRE

ÉCOLE DOCTORALE : ED127
Laboratoire Astrophysique, Interactions, Multi-échelles (AIM)
(Service d'Astrophysique du CEA-Saclay)

***DISCIPLINE** : Astrophysique*

**THÈSE DE DOCTORAT**

soutenue le 28/11/2012

par

**Pierre-Emmanuel BELLES**

# Formation d'étoiles et d'amas stellaires dans les collisions de galaxies

~

# Formation of stars and star clusters in colliding galaxies

| | | |
|---|---|---|
| **Directeur de thèse :** | Pierre-Alain DUC | Docteur (Laboratoire AIM) |
| **Co-directeur de thèse :** | Elias BRINKS | Professeur (University of Hertfordshire) |
| **Composition du jury :** | | |
| *Président du jury :* | Guillaume PINEAU-DES-FORETS | Professeur (Université Paris-Sud XI) |
| *Rapporteurs :* | Martin HARDCASTLE | Docteur (University of Hertfordshire) |
| | Pascale JABLONKA | Docteur (École Polyt. Fédérale de Lausanne) |
| *Examinateurs :* | Frank BIGIEL | Docteur (University of Heidelberg) |
| | Carole MUNDELL | Professeur (Liverpool John Moores Univ.) |

A mon grand père Aimé,
qui a des étoiles plein les yeux quand je lui parle d'astronomie;
Et à ma grand mère Marie,
qui a rejoint les étoiles récemment.

# Abstracts

## English abstract

Mergers are known to be essential in the formation of large scale structures and to have a significant role in the history of galaxy formation and evolution. Besides a morphological transformation, mergers induce important bursts of star formation. These starburst are characterised by high Star Formation Efficiencies (SFEs) and Specific Star Formation Rates, i.e., high Star Formation Rates (SFR) per unit of gas mass and high SFR per unit of stellar mass, respectively, compared to spiral galaxies. At all redshifts, starburst galaxies are outliers of the sequence of star-forming galaxies defined by spiral galaxies.

We have investigated the origin of the starburst-mode of star formation, in three local interacting systems: Arp 245, Arp 105 and NGC 7252. We combined high-resolution JVLA observations of the 21-cm line, tracing the H I diffuse gas, with UV *GALEX* observations, tracing the young star-forming regions. We probe the local physical conditions of the Inter-Stellar Medium (ISM) for independent star-forming regions and explore the atomic-to-dense gas transformation in different environments. The SFR/H I ratio is found to be much higher in central regions, compared to outer regions, showing a higher dense gas fraction (or lower H I gas fraction) in these regions. In the outer regions of the systems, i.e., the tidal tails, where the gas phase is mostly atomic, we find SFR/H I ratios higher than in standard H I-dominated environments, i.e., outer discs of spiral galaxies and dwarf galaxies. Thus, our analysis reveals that the outer regions of mergers are characterised by high SFEs, compared to the standard mode of star formation.

The observation of high dense gas fractions in interacting systems is consistent with the predictions of numerical simulations; it results from the increase of the gas turbulence during a merger. The merger is likely to affect the star-forming properties of the system at all spatial scales, from large scales, with a globally enhanced turbulence, to small scales, with possible modifications of the initial mass function. From a high-resolution numerical simulation of the major merger of two spiral galaxies, we analyse the effects of the galaxy interaction on the star forming properties of the ISM at the scale of star clusters. The increase of the gas turbulence is likely able to explain the formation of Super Star Clusters in the system.

Our investigation of the SFR–H I relation in galaxy mergers will be complemented by high-resolution H I data for additional systems, and pushed to yet smaller spatial scales.

## Résumé en Français

Les fusions sont un évènement essentiel dans la formation des grandes structures de l'Univers; elles jouent un rôle important dans l'histoire de formation et l'évolution des galaxies. Outre une transformation morphologique, les fusions induisent d'importants sursauts de formation d'étoiles. Ces sursauts sont caractérisés par des Efficacités de Formation Stellaire (EFS) et des Taux de Formation Stellaire Spécifiques (TFSS), i.e., respectivement, des Taux de Formation Stellaire (TFS) par unité de masse gazeuse et des TFS par unité de masse stellaire, plus élevés que ceux des galaxies spirales. A toutes les époques cosmiques, les galaxies à sursaut de formation d'étoiles sont des systèmes particuliers, en dehors de la séquence définie par les galaxies spirales.

Nous explorons l'origine du mode de formation stellaire par sursaut, à travers trois systèmes in interaction: Arp 245, Arp 105 et NGC 7252. Nous avons combiné des observations JVLA haute résolution de la raie à 21-cm, traçant le gaz H I diffus, avec des observations *GALEX* dans l'UV, traçant les jeunes régions de formation d'étoiles. Nous sommes ainsi en mesure de sonder les conditions physiques locales du Milieu InterStellaire (MIS) pour des régions de formation d'étoiles indépendantes, et d'étudier la transformation du gaz atomique en gaz dense dans différents environnements. Le rapport SFR/H I apparaît bien plus élevé dans les régions centrales que dans les régions externes, indiquant une fraction de gaz dense plus élevée (ou une fraction de gaz H I moins élevée) dans les régions centrales. Dans les régions externes des systèmes, i.e., les queues de marées, où le gaz est dans une phase principalement atomique, nous observons des rapports SFR/H I plus élevés que dans les environnements standards dominés par le H I, i.e., les régions externes des disques de spirales et les galaxies naines. Ainsi, notre analyse révèle que les régions externes de fusions sont caractérisées par des EFS élevées, par comparaison au mode de formation stellaire standard.

Observer des fractions de gaz dense élevées dans les systèmes en interaction est en accord avec les prédictions des simulations numériques; ceci résulte d'une augmentation de la turbulence du gaz durant une fusion. La fusion affecte les propriétés de formation stellaire du système probablement à toutes les échelles, depuis les grandes échelles, avec une turbulence augmentant globalement, jusqu'aux petites échelles, avec des modifications possibles de la fonction de masse initiale. A partir d'une simulation numérique haute résolution d'une fusion majeure entre deux galaxies spirales, nous analysons les effets de l'interaction des galaxies sur les propriétés du MIS à l'échelle des amas stellaires. L'accroissement de la turbulence du gaz explique probablement la formation de Super Amas Stellaire dans le système.

Notre étude de la relation SFR–H I dans les fusions de galaxies sera complétée par des données H I haute résolution pour d'autres systèmes, et poussée vers des échelles spatiales encore plus petites.

# Acknowledgements

First of all, I'd like to thank my supervisors: Elias & Pierre-Alain. If I have the first part in this story, they have undoubtedly the second parts. They have always been present when I needed them, they advised me, they supported me and, of course, they taught me what being a scientist is. Because knowledge is freedom of mind, I'll be grateful to them for the rest of my life. Their kindness and human qualities make me proud of having studying / working with them. Besides, I'd like to thank Frédéric Bournaud, who kept a mindful eye on my work and with whom I had very useful discussions, as well as Martin Hardcastle and Pascale Jablonka, the "rapporteurs" of this dissertation, the members of the jury (made of the two rapporteurs, Carole Mundell, Frank Bigiel, Guillaume Pineau-des-Forêts and my supervisors), Pierre-Olivier Lagage and Michel Talvard, the heads of the department, Marc Sauvage, the head of the scientific team. I also thank Pascale Chavegrand and Christine Toutain not only for their help with administrative paperwork, but also for their kindness.

Then, there would be no thesis if Florent Renaud, Roger Leiton, Stéphanie Juneau, Katarina Kraljic, Kevin DeGiorgio, Mark Sargent, Joana Gomez, Harriet Parson, Luke Hindson were not here day-after-day. Because having support from young postdocs, other PhD students or office-mates is essential, I'd like to thank all of them. I also acknowledge Antonio Portas, the first one to trust my work and promote it. I wish them all a great success for their promising career and all the best in their life.

Finally, I must confess that, over the past three years, there have been hard times. If I managed to go through them, it's undoubtedly because my relatives and close friends never left me. I'd first like to thank Mary Poppins, who used several times her magic umbrella to cheer me up and to support me. I kiss my parents Françoise and Gilbert, as well as my dear beloved cousins, Maryn and Peter, and my girlfriends' parents, Véronika and Noël. I'm very grateful to some special friends, like Mélanie Guittet, Elodie Bicilli, Teddy Majourel and Hugo Martinez because they all gave me support, at some point, when I needed it.

# Contents

# List of Figures

# List of Tables

# Part I

# Introduction

# Chapter 1

# The role of mergers in the cosmological evolution of galaxies

Our understanding of the cosmological evolution of galaxies started with the famous Hubble sequence (Hubble, 1926). From the classification of galaxies based on their morphologies, a first evolutionary scheme was established to propose possible transformations of galaxies from one morphological type to another. Once the idea that two spiral galaxies can merge and form an elliptical galaxy appeared (in particular thanks to the pioneering modelling work by Toomre 1977 ), a whole field of investigation on the process of galaxy mergers was opened (see Schweizer 1996 and Duc & Renaud 2012 for reviews).

The advent of numerical simulations in modern Astronomy triggered a great step forward. Cosmological simulations have shown how the Cold Dark Matter (CDM) component (the most abundant form of matter in the Universe) structured the Universe, from the formation of small structures by gravitational collapse, to the largest and biggest ones by mergers (Melott et al., 1983; White et al., 1987; Gramann, 1988; Springel et al., 2005; Gao et al., 2005; Springel et al., 2006). This scenario of structure growth is referred to as the hierarchical scenario (Peebles, 1971). The merging of structures is a key event in this current paradigm; it explains the origin of galaxy pairs, groups, clusters, super-clusters, filaments and voids, which are observed at all redshifts in the Universe.

Although the merger of CDM halos is essential in the formation of large scale structures, it does not mean that the merger of the galaxies that populate them is the dominant event in the cosmological evolution of galaxies; this for at least two simple reasons: (1) not all the CDM halos are necessarily populated by galaxies; (2) the merger of two halos is not *immediately* followed by the merger of the galaxies that assembled in each of their potential wells. In other words, the galaxy merger rate depends (at least) on (1) the halo occupation distribution (see Yang et al. 2005 and references therein), (2) a key timescale reflecting the cosmologically-averaged "observability" of mergers (see Lotz et al. 2011 and references therein); both varying with the halo mass (or galaxy mass). Unfortunately, several uncertainties enter in the treatment of the baryonic physics in galaxies (Hopkins et al., 2010b), especially in the stellar feedback, which might be responsible for the overestimation of the number of dwarf galaxies occupying low-mass halos in numerical simulations (Moore et al., 1999; Klypin et al., 1999). If stronger in small structures, feedback could exceed a "simple" effect of star formation regulation (Scannapieco et al., 2008) and suppress bulge formation in small CDM halos. In addition to this, issues arise in the determination of the key timescale, mainly due to the way galaxy mergers are identified in observations.

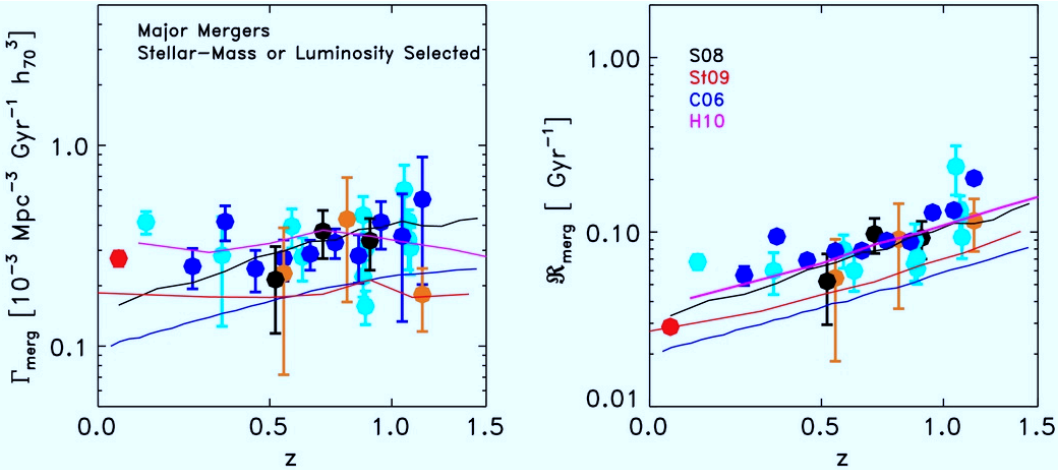


Figure 1.1: [From Lotz et al. (2011)] Observed galaxy merger rates (dots) and theoretical predictions (lines). Volume-averaged major merger rate (left panel), i.e., the co-moving number density of ongoing galaxy merger events per unit time, and fractional major merger rate (right panel), i.e., the number of galaxy merger events per unit time per selected galaxy. The theoretical predictions are in good agreement with the observed major merger rates.

Observationally, merger candidates are either identified as galaxies in close pairs (sometimes in 3-D space) or as morphologically disturbed galaxies (by visual inspection or through the use of a parameter assessing the asymmetry of the system). Ignoring simple sensitivity effects, the close pair method is biased toward early-stage mergers, whereas the morphology based method (with the identification of tidal features) suffers from observational biases (as collisional debris are of low surface brightness). This results in a great deal of confusion when trying to assess the merger rate and comparing observational studies with each other. In the end, an assumption on the the merger time must be made and the merger rate is poorly constrained. In Fig. 1.1, we show one of the most up-to-date determinations of the merger rate as a function of redshift (Lotz et al., 2011). The volume-averaged major merger rate appears relatively constant over cosmic times, whereas the fractional major merger rate decreases with time. Most recent results suggest that minor mergers are a possible scenario for galaxy growth; they succeed in reproducing the characteristics (like size, concentration, colours) of present-day early-type galaxies (Naab et al., 2009; Kaviraj et al., 2009) and could dominate the total merger rate and contribute significantly to the stellar mass assembly of galaxies (López-Sanjuan et al., 2010; Hopkins et al., 2010a; Kaviraj et al., 2010; López-Sanjuan et al., 2011; Lotz et al., 2011; McLure et al., 2012; Newman et al., 2012).

Besides a morphological transformation, mergers induce enhanced star formation (Kennicutt et al., 1987) and enhanced Far Infra-Red emission (Xu & Sulentic, 1991). The enhancement can be extreme and produce a burst of star formation, the so-called "starbursts" (Sanders & Mirabel, 1996; Dasyra et al., 2006), sometimes reaching values of $\sim 1000\,\mathrm{M}_\odot\,\mathrm{yr}^{-1}$. It turns out that, at $z \sim 0$, the strong Infra-Red (IR) emission of Luminous Infra-Red Galaxies (LIRGs, with $10^{11}\,\mathrm{L}_\odot \leq L_{IR} = L[8-1000\mu\mathrm{m}] \leq 10^{12}\,\mathrm{L}_\odot$)[1] and Ultra Luminous Infra-Red Galaxies (ULIRGs, with $L_{IR} \geq 10^{12}\,\mathrm{L}_\odot$)[2] is associated with the burst of star formation that is caused

[1] equivalent to a SFR of $20\,\mathrm{M}_\odot\,\mathrm{yr}^{-1} \leq \mathrm{SFR} \leq 200\,\mathrm{M}_\odot\,\mathrm{yr}^{-1}$
[2] equivalent to a SFR $\geq 200\,\mathrm{M}_\odot\,\mathrm{yr}^{-1}$

by the interaction of two galaxies (see review by Sanders & Mirabel 1996). At low redshift, all ULIRGs are merging systems (while the inverse is not true). Since LIRGs are found to dominate the IR-emitting galaxy population at $0.5 < z < 1$ (Chary & Elbaz, 2001; Le Floc'h et al., 2005; Magnelli et al., 2009) and ULIRGs at $z > 1$ (Chapman et al., 2005; Caputi et al., 2007; Daddi et al., 2007), the conclusion that galaxy mergers would be the dominant mode of star formation in the Universe would be tentative. Yet, the (U)LIRG(z) − merger(z) connection is far from being established at all z. Recent *Herschel* observations of ULIRGS at $z = 2$, combined with high-resolution HST observations, have revealed, through the study of their morphological and kinematic features, that a significant fraction (between 25 and 50%) of ULIRGs are in fact gas rich spirals and not the result of a merger (Kartaltepe et al., 2012). Using deep FIR observations obtained with the *Herschel* Space Observatory, Elbaz et al. (2011) showed that the fraction of starburst galaxies represents less than 20% of the IR-emitting population, including high-z ULIRGs. The contribution of merger induced starbursts to the SFR density tends to be weak at all redshifts (Sargent et al., 2012). Then, considering that galaxies form half of their stellar content at redshifts above 1 (Marchesini et al., 2009), where the population of ULIRGs dominates, these results would suggest that the building of the stellar content of galaxies would be dominated by a "secular" mode of star-formation. Mergers would only play a minor role in the global history of star formation.

Then, if mergers do not account for the bulk of stellar mass in galaxies, why should we be interested in studying them? As we show in the next Chapter, mergers offer an environment for probing the process of star-formation and the scaling relations that result from it, like the Star Formation Rate - Gas content or Schmidt-Kennicutt relation.

# Chapter 2

# What can mergers tell us about the fundamental scaling relations of star formation?

## 2.1 The scaling relations of Star Formation

In recent years a number of scaling relations involving the SFR have been found:

- the SFR – Stellar Mass relation (Noeske et al., 2007; Elbaz et al., 2007; Daddi et al., 2007; Pannella et al., 2009; González et al., 2011), which shows a tight relation between SFR and stellar mass. At all redshift, the Specific Star Formation Rate (sSFR = SFR/$M_{star}$) decreases with mass. This anti-correlation between sSFR and stellar mass is stronger at high–$z$ and suggests a "downsizing" scenario (Cowie et al., 1996), in which most massive galaxies form first (at high $z$). The sSFR - stellar mass relation is redshift-dependent, with average sSFRs increasing with redshift.

- An IR "main-sequence" (Elbaz et al., 2011), for LIRGs and ULIRGs, which corresponds to a constant $L_{IR}/L_{8\,\mu m}$, far–to mid–IR ratio.

- the SFR – Gas content relation, also called Schmidt-Kennicutt (SK) law (Schmidt, 1959; Kennicutt, 1998b), which relates SFR and gas density through a power law. While the pioneering work of Schmidt (1959) introduced a relation between SFR and gas *volume* density, Kennicutt (1998b) applied this prescription to observable *surface* densities[1]:

$$\Sigma_{SFR} = A\ \Sigma_{Gas}^{N} \tag{2.1}$$

  with $\Sigma_{SFR}$ the SFR surface density in $M_\odot\,y^{-1}\,kpc^{-2}$, $\Sigma_{Gas}$ the gas surface density in $M_\odot\,pc^{-2}$. The "Gas" refers to both the atomic and molecular components. For a sample of 61 "normal" local spiral galaxies, Kennicutt (1998b) measures $N = 1.4 \pm 0.15$ and $A = (2.5 \pm 0.7) \times 10^{-4}$. All the measurements are averaged over the entire spatial extent of the galactic discs. Often, the ratio $\Sigma_{SFR}/\Sigma_{Gas}$ is referred to as the Star Formation Efficiency (SFE), its inverse is referred to as the depletion time $\tau_{dep}$. The median gas depletion time for the sample of spiral galaxies of Kennicutt (1998b) is found to be $\sim 2.1\,Gyr$[2].

[1] In the case of a galactic disc seen face-on, the surface densities corresponds to the average gas volume density multiplied by the thickness of the disc.

[2] For normal spiral discs only

All these relations should be considered when studying the process of Star Formation. They reveal a population of "standard" systems, the spiral galaxies which experience a normal mode of Star Formation, and a population of "deviant" systems, the starbursts which, at a given Stellar Mass / 8 $\mu$m-Luminosity / Gas mass, exhibit higher SFRs than the normal galaxies. In this thesis, we will focus only on the SFR – Gas relation and will specifically treat the case of galaxy mergers.

## 2.2 Exploring of the SFR – Gas relation

The SK-law has been the starting point of more than to decades of intense research, testing its validity form high to low gas density environments, and across a range of linear scales, from measurements obtained by integrating the SFR and gas content over entire galaxies to detailed spatially resolved studies down to typically a few hundred parsec scales.

The comparison between starbursts and normal galaxies at low and high redshifts, revealed two sequences of star-forming systems (or "modes" of star formation):

- a sequence of normal galaxies (or long-lasting mode), traced by spiral galaxies at low (Kennicutt, 1998b) and high $z$ (Tacconi et al., 2010), and additionally by BzK galaxies at high $z$ (Daddi et al., 2010a);
- a sequence of starburst galaxies (or rapid mode), with SFEs $\sim$ 10 times higher than normal galaxies, traced by ULIRGs at low $z$ and "Hyper-LIRGs" at high $z$ (see previous chapter), and, additionally by Sub-Millimetre galaxies at high $z$ (Bouché et al., 2007).

The interpretation given to the sequences of star formation, which are shown in Fig. 2.1 is still debated. A universal tight SFR – Dense Gas[3] relation is observed in all environments (Gao & Solomon, 2004a,b; Juneau et al., 2009). The origin of the double sequence might be more linked to the way low density gas is transformed into intermediate density gas (as traced by CO), before the onset of star formation — this process is dealt with in Chapter 7 (in Part II) based on predictions of numerical simulations —, or simply the way the molecular mass is estimated from CO line observations through the $X_{CO}$ conversion factor, with different values taken for normal galaxies and starbursts (see Narayanan et al. (2011), which explore the effects of gas thermodynamics on the intensity of the CO emission line, resulting in an underestimation of the inferred $H_2$ mass in a starburst environment). It was also claimed that introducing the dynamical time-scale of the systems — rotation time-scale (Daddi et al., 2010b) or free-fall time-scale (Krumholz et al., 2009) — the two sequences of star formation can be made to follow a single $\Sigma_{SFR} - \Sigma_{gas}/\tau_{dyn}$ sequence; this would suggest that global galactic mechanisms (setting $\tau_{dyn}$) regulates the star formation process of the system.

Parallel to the exploration of the high gas density case, a major breakthrough in our understanding of the star formation process was made with the advent of interferometers. The high angular resolution achieved by these instruments allows us to resolve individual regions of galaxies and especially to isolate star forming regions from each other. Thus, one of the main goals of "The H I Nearby Galaxy Survey" (THINGS, Walter et al. 2008) is to investigate the relation between Inter-Stellar Medium (ISM) properties and Star Formation, from a sample of 34 nearby galaxies, at a spatial resolution of $100 - 500$ pc and a velocity resolution of 5.2 km s$^{-1}$. Combining H I data from the THINGS project and CO data from the HERACLES survey (Leroy

[3]The dense gas can be traced by molecules with high dipole moments like HCN (which emits a line at 3 mm), CS and $HCO^+$. The density of the gas traced by HCN molecules is typically 2 orders of magnitude higher than that traced by CO (see Gao & Solomon 2004a and references therein)

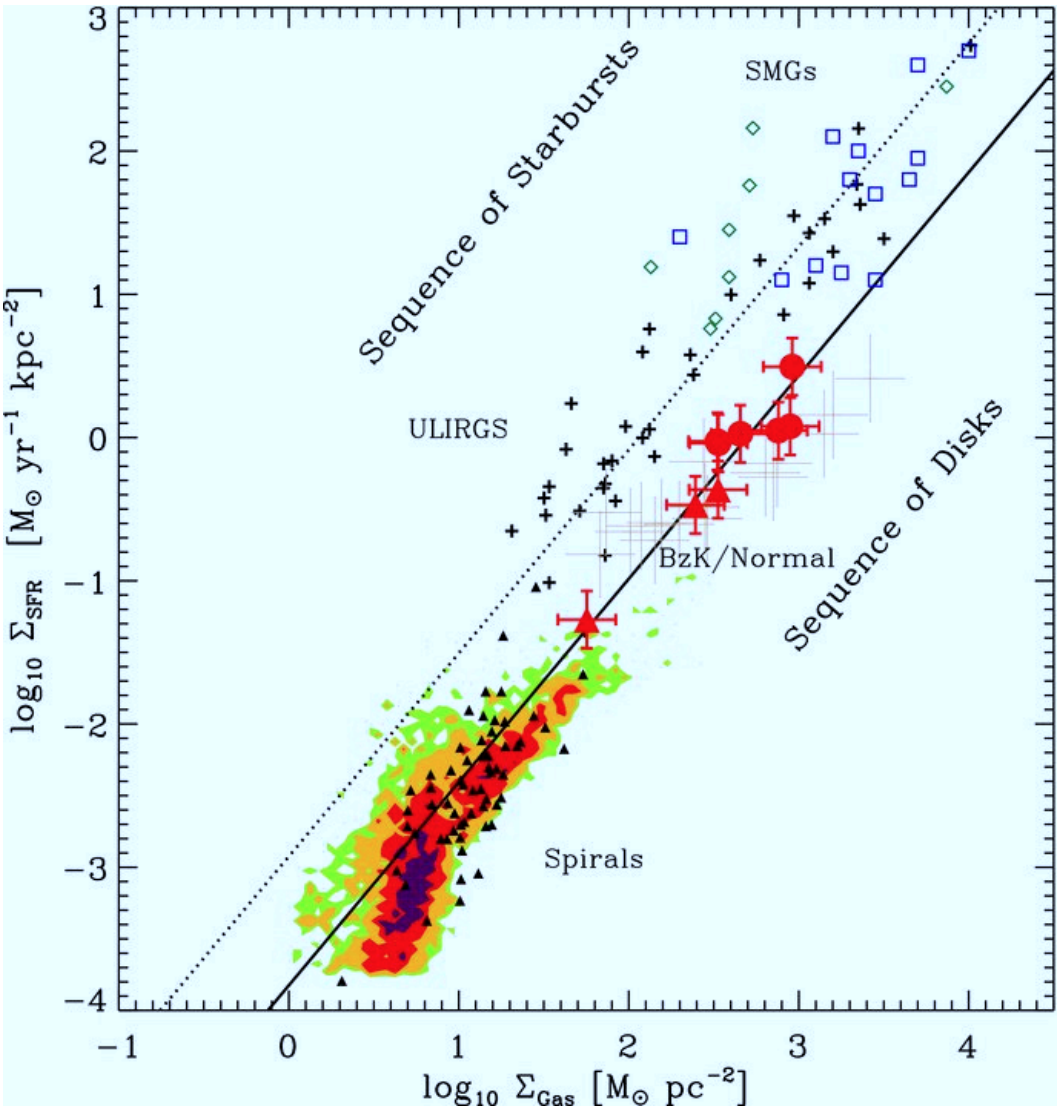


Figure 2.1: [From Daddi et al. (2010b)] SFR density as a function of the gas (atomic and molecular) surface density. The lower solid line is a fit to local spirals and $z = 1.5$ BzK galaxies (slope of 1.42), and the upper dotted line is the same relation shifted up by 0.9 dex to fit local (U)LIRGs and Sub-Millimetre Galaxies.

et al., 2009) with the usual tracers of star formation, Bigiel et al. (2008) reveal the existence of two gas surface density "regimes":

- an H I–dominated regime, generally in the outskirts of late-type galaxies or in dwarf galaxies, with the possible presence of diffuse H I gas, where the correlation between $\Sigma_{SFR}$ and $\Sigma_{Gas}$ is weak ;
- an $H_2$–dominated regime, in the inner regions of spiral galaxies, where the correlation between $\Sigma_{SFR}$ and $\Sigma_{H2}$ is strong, with a constant molecular gas depletion time of $\sim 2$ Gyr, independent of galaxy characteristics.

The existence of such gas phase regimes for star formation, with a strong relation between $\Sigma_{SFR}$ and $\Sigma_{H2}$ (Wong & Blitz, 2002; Bigiel et al., 2008), reveals that, on a local scale, the SFR is controlled by the fraction of molecular gas within each clump. Once the molecular gas is formed, its transformation into stars appears to be a uniform process, at least in standard systems (spirals / dwarfs). This relation appears as the local-scale analog of the disc-averaged relation between SFR and Gas density, presented earlier, for low and high redshift spiral galaxies. In fact, Lada et al. (2012) argue that there is a fundamental scaling relation that directly connects the local star formation process with that operating globally within a galaxy. The star formation would simply be controlled by the the amount of *dense* molecular gas that can be assembled within a star formation complex (irrespective of if this is in a single molecular cloud or an entire galaxy).

The extreme case, on the low gas density side, of the SFR–gas relation is explored by the "LITTLE THINGS" (Local Irregulars That Trace Luminosity Extremes, The HI Nearby Galaxy Survey) project (Hunter et al., 2012), with a sample of 41 gas-rich dwarf irregular galaxies observed at a resolution similar to, or higher than the galaxies of the THINGS project.

In this context, we present the first investigation of the SFR – Gas relation in another "extreme" case: interacting systems (mergers). Indeed, mergers are often characterised by strong starbursts (see Chapter 1) and, as a consequence, are outliers of the standard SK-law. We aim at understanding the origin of this deviation. Similarly to the recent projects that benefit from the high-resolution achieved by interferometry, we have access to the physical conditions of the ISM for star-forming regions independently, so that we can explore the H I-to-dense gas relation at all scales.

We start our investigation of the SFR–gas relation on a local scale with a sample of three mergers: Arp 245, Arp 105, and NGC 7252. We present our high-resolution JVLA data, their reduction and their analysis in Part III. Our results are discussed in Part IV in the light of the various gas phase regimes defined by Bigiel et al. (2008). Our initial sample will soon be complemented by additional high-resolution H I data (Chaotic THINGs project) and additional tracers of star formation (Chapter 10 presents our outlook).

As the merger is expected to have effects at all scales, from a large-scale increase of the turbulence of the system (the collision of two galaxies injects an important quantity of kinetic energy in the system and stirs the gaseous component), down to the scale of single star formation[4], we also explore the consequences of the merger on the properties of the ISM via the formation of star clusters during the interaction. We present the analysis we made of the population of (Super) Star Cluster that forms in a simulation of a wet major merger in Chapter 6.

[4]See Elmegreen (2005) for a review on the investigation of variations of the Initial Mass Function (IMF) in starbursts. Variations towards a top-heavy IMF in starbursts are an alternative interpretation to the sequence of starbursts, since one has to assume an IMF when deriving SFR from luminosities.

# Chapter 3

# Outline of the thesis and summary of my personal contribution

The body of the manuscript is divided in three big parts, besides the general introduction (Part I) and conclusions (Part V).

**Part II**

Part II presents the predictions from numerical simulations made by the Saclay group on the properties of the ISM, Star-Formation and Star Cluster Formation in mergers. This part provides the theoretical framework to the topic.

My personal technical and scientific contribution in this part is the following:

- I made the detailed analysis of the output of a numerical simulation of a wet merger, exploring the data cube at different snapshots.
- I wrote the codes that identify, track and extract the properties of the star clusters (except the routine that determine the kinematic properties of the clusters, which was implemented later-on by D. Miralles-Caballero),
- I wrote a paper, entitled "Formation and evolution of massive stellar clusters in a simulated galaxy merger: on the track of the origin of GCs, TDGs and UCDs", presenting the pipeline of the code and the analysis of the star cluster populations that form in the simulation. This paper has been submitted to MNRAS and is presented in Chapter 6),
- I contributed to the comparative study between simulations and observations, presented in Miralles-Caballero et al. (see Appendix A). This paper has also been submitted to MNRAS.

**Part III**

From theories and predictions we switch to observations, with Part III being devoted to the SFR-H I relation. Our H I data-set and data reduction is presented in Chapter 8; the analysis is presented in Chapter 9.

Virtually all material presented here is the result of my work, including:

- the calibration of the H I data and combination with archival data and mapping of the three systems studied in this report (Arp 245, Arp 105 and NGC 7252),
- the correlation of the H I maps with the UV *GALEX* maps, the latter obtained from the archives,
- the analysis of the spatial evolution of the SFR-H I relation in these systems.

**Part IV**

In Part IV, we discuss the results, observational biases, and present our perspectives: an extension of the H I survey (Chapter 10 and inclusion of other phase of the gas, in particular the $H_2$ traced by CO (Chapter 11), and the so-called dark gas (Chapter 12).

My personal technical and scientific contribution in this part is the following:

- I performed the entire calibration and data reduction of the H I observations of the merger NGC 7252 (the Giraffe H$\alpha$ observations were processed by P. Weilbacher),
- I did the complete analysis of the gas kinematics of its tidal dwarf galaxy NGC 7252NW. AS part of this, I wrote code that extracts the emission lines from the spectral data cubes and creates PV-diagrams,
- I wrote a paper, entitled "Missing baryons in Tidal Dwarf Galaxies: the case of NGC 7252", presenting the analysis of the baryonic content of NGC 7252NW and the search for dark gas (paper to be submitted and presented in Sect. 12.2),
- I prepared the observations of the follow–up project, Chaotic THINGS, i.e., defined the time repartition between the different array configurations, and entered the dynamical scheduling of the new JVLA observations with the on-line Observation Preparation Tool (OPT).

# Part II

# Predictions from numerical simulations of mergers

# Chapter 4

# Theory of star and star cluster formation in mergers

## 4.1 From star to star cluster formation

One of the main effects of mergers is to increase the gas turbulence. This cascades to all scales, having an impact on the structure of the Inter-Stellar Medium (ISM), and thus possibly on the stellar Initial Mass Function (IMF), on the maximum mass of the Giant Molecular Clouds (GMCs), thus on its ability to form massive clusters and consequently on the shape of the Cluster Mass Function (CMF). The connection between all these scales of interest for our study is detailed below.

Molecular gas, is generally found to have a clumpy structure and to be organised in clouds. Giant Molecular Clouds (GMCs) have dense cores but that only represents $\sim 10\%$ of the total mass and total surface of the cloud. The most massive and densest cores ($10 - 1000\,\mathrm{M}_\odot$, $n(H_2) \sim 10^{3-4}\,\mathrm{M}_\odot\,\mathrm{pc}^{-2}$) encompass proto-clusters, that are still embedded in dust cocoons. A breakthrough in the understanding of how star clusters form in GMCs was achieved by Lada & Lada (2003) who compiled a catalogue of nearby Galactic Giant Molecular Clouds and studied their embedded clusters. They concluded that less than 4% of the proto-clusters survive more than 100 Myr, revealing a high "infant mortality" rate. Thus most of the stars initially formed in clusters quickly disperse in the ISM. Given the high rate of cluster formation ($\geq 2$ clusters $\mathrm{Myr}^{-1}\,\mathrm{kpc}^{-2}$) and destruction, stars that form in clusters represent the vast majority of the stars populating the disc of galaxies (Allen et al., 2007). Studying the formation of clusters, as done in Chapter 4 of this thesis, is therefore insightful for understanding star-formation in general.

The important role played by star clusters in star formation led Kroupa and collaborators (Kroupa & Weidner, 2003; Weidner & Kroupa, 2005) to propose the concept of an Integrated Galactic Mass Function (IGMF)[1], i.e. the sum of all the IMFs of all the dissolved star clusters. A priori, the IGMF depends on the IMF of each cluster[2], on the CMF and its evolution with

[1] the IGMF is simply the IMF one would determine by simply observing a field of stars. The IMF is generally measured in star clusters, ensuring that a single age stellar population is considered.

[2] The IMF has for long been considered universal, with a shape $\xi(m) = m^{-\alpha}$, with a slope of 1.3 for stars with $M \leq 0.5\mathrm{M}_\odot$ and the Salpeter/Massey-slope of 2.35 for $M > 0.5\mathrm{M}_\odot$ stars. However, different IMFs have been proposed in the literature, like the Kroupa IMF (Kroupa, 2001), often motivated by a possible effect of

time (starting with an Initial CMF, ICMF[3]).

## 4.2 Building the shape of the Cluster Mass Function

Whereas the universality of the IMF has not yet firmly proven to be wrong, the CMF shows a high variety of shapes, depending on the host of the clusters, spiral or elliptical galaxies, or their age. In particular, the young Star Clusters born in nearby mergers follow a power law mass function, of index $\sim -2$ (Zhang & Fall, 1999; Mullan et al., 2011). The mass function of older Star Clusters, like the Globular Clusters (GCs) that are found orbiting elliptical galaxies, follows a log-normal distribution (Jordán et al., 2007). Since the most massive elliptical galaxies are believed to originate from galaxy mergers, it is tempting to establish a temporal link between the two CMFs, stating that the Globular Cluster Mass Function is an evolved form of the Young Cluster Mass Function[4].

In practise, *the determination of the shape of the CMF* might be affected by:

- the existence of a relation between the SFR and the maximum mass of clusters (Larsen, 2002; Weidner et al., 2004; Bastian, 2008). Mergers that often exhibit a high SFR[5] form more massive clusters in absolute terms and thus offer a better sampling of the high mass end of the CMF than quiescent galaxies;
- the dependence of the CMF parameters, like the low-mass turnover and the dispersion, on host galaxy luminosity (Villegas et al., 2010).

The *precise shape of the CMF and its evolution* might be driven by the following effects:

- the infant mortality. Whether it is mass dependent or not is still debated (Lamers et al., 2005; Whitmore et al., 2007; Fall et al., 2009; Bastian et al., 2012);
- internal processes, such as two-body relaxation and stellar evaporation, which can cause heavy mass loss;
- environmental effects, in particular during mergers through gravitational shocks, dynamical friction and tidal fields. The tidal field is found to have a complex effect on the clusters, either disrupting them in a few billion years (Fleck & Kuhn, 2003), or making them tighter bound in the case of tidal compressive modes (Renaud et al., 2008, 2009).

Furthermore observations and models suggest that the *global* shape of the CMF might change with the large scale environment. In particular, in mergers the CMF could be top heavy, as speculated for the IMF of their stars. Arguments in favor of an excess of massive clusters in mergers, or the presence of a bi-modality in the CMF, are the following:

the environment on the IMF. Whether it could be top-heavy in the starburst regions of mergers has often been proposed but never directly confirmed.

[3]At a time t, the Initial Cluster Mass Function is defined as the Cluster Mass Function of only the clusters born at t. Given that the time scale of a single cluster formation is $\sim 10$ Myr, the uncertainty on t is at least 10 Myr.

[4]Note however that a fraction of the GCs around massive galaxies might be of primordial origin, while another one might correspond to old GCs accreted together with low-mass satellites.

[5]a significant fraction of them are Luminous Infrared Galaxies while all Ultra-luminous Infrared galaxies are mergers.

- the observation in colliding systems of stellar structures with masses reaching that of dwarf galaxies that are not observed in other environments: either compact ones, such as the ultra-massive Super Star Cluster (SSC) W3 in the prototypical merger NGC 7252 (Maraston et al., 2004; Fellhauer & Kroupa, 2005), or more extended and gas-rich ones, located along prominent tidal tails: the Tidal Dwarf Galaxies (TDGs; Duc & Mirabel, 1994; Duc et al., 1997; Duc & Mirabel, 1998; Duc et al., 2000; Hibbard et al., 2001a; Mendes de Oliveira et al., 2001; Iglesias-Páramo & Vílchez, 2001; Temporin et al., 2003; Knierman et al., 2003; Hancock et al., 2009; Sheen et al., 2009). In Sect. 12.2 we present a detailed study of one TDG: NGC 7252NW.

- models accounting for the high levels of gas turbulence in mergers, that predict the formation of clouds with a high velocity dispersion that later collapse to form massive star clusters or dwarf galaxies, in particular in tidal tails (Elmegreen et al., 1993; Kaufman et al., 1994; Duc et al., 2004).

- models reproducing the successive mergers of clusters, leading to build-up of a central massive cluster within a few $10^7$ years , the gradual increase of its half–mass radius and finally the formation of objects similar to dwarf-Spheroidals (dSph) or dwarf-Ellipticals (dE; Kroupa, 1998). The merger of sub-clusters in turbulent molecular clouds is supported by the numerical models of Bonnell et al. (2011), Saitoh et al. (2011), and Fujii et al. (2012).

# Chapter 5

# Insight from numerical simulations of mergers

How do mergers affect star-formation in galaxies? In order to understand this, one should study how each galactic component involved in the process is affected: from the low density ISM, the dense molecular clouds in which stars are born to the more evolved star-clusters. This requires multi-wavelength, multi-scale observations which are in practise difficult to acquire. Indeed, the closest major merger – the Antennae – is located at more than 20 Mpc, preventing detailed studies. Furthermore, such observational data do not provide hints on the temporal evolution, unless a statistical approach is used and large samples of systems observed. Then again, one faces the lack of merging systems in the nearby Universe.

Instead, numerical simulations of mergers provide time scales, and for the most current state-of-the-art models, maps with high dynamical spatial and density ranges, allowing us to determine simultaneously the evolution of the diffuse gaseous material during the collision and that of the most compact stellar systems born during the merger. Furthermore, such models provide a 3D view, unlike observational data. This is especially a limitation in observations of mergers for which projection effects may be tricky to deal with.

Provided that the physics implemented in the numerical codes is realistic enough, simulations may provide predictions that can be checked in real systems, once adapted/converted to their limited resolution. Conversely observations may reveal the physics or initial conditions in the simulations need improvement.

## 5.1 Historical perspective on simulations

From the pioneering work of Toomre & Toomre (1972), in the early 1970s, numerical simulations have been continuously improving, reaching ever higher levels of realism (see Duc & Renaud 2012 for an exhaustive review on numerical simulations of interacting systems). Toomre & Toomre (1972) showed that the formation of filaments ("tidal tails" and "bridges") during the encounter of two spirals was caused by intense gravitational tides. This allowed one to at last understand if not reproduce the morphology of the "peculiar" galaxies that had been identified a decade earlier when a complete deep atlas of the sky became available. An evolutionary sequence sorting the interacting systems by dynamical stage, from the encounter of the galaxy discs (and the apparition of the tails) until their final coalescence and their merger, was proposed (Toomre, 1977). A

Figure 5.1: Formation of tidal tails during the interaction of two galaxies, illustrated with a sample of observed systems, from left to right: NGC 5427 & NGC 5426, Arp 274, NGC 1512 & IC 4970, NGC 5566 & NGC 5569, NGC 6872 & IC 4970, NGC 4038 & NGC 4039 and NGC 2623

modern view of this sequence is shown on Fig. 5.1, illustrating the different stages of the merger, from the formation of tidal tails early-on during the interaction until their propagation into the intergalactic medium.

Although the simulations of Toomre & Toomre (1972) could reproduce well the disturbed morphology of observed systems, the numerical recipe did not include dynamical friction, a key parameter governing the time scale of the merger. Then, self-consistent simulations, in which all the particles interact with each other, appeared (e.g. White 1978; Gerhard 1981, quickly followed by time-saving computational methods, like tree-codes (Barnes & Hut, 1986; Hernquist, 1987). The era of simulations of multi-components galaxies started with Barnes (1988), who showed the influence of the dark-matter halo on the system dynamics. The gas component was incorporated in the codes, to couple gravitation and hydrodynamics (Hernquist & Katz, 1989). Until recently, two main techniques were used to represent gas particles properties:

- Smooth Particle Hydrodynamics (SPH Lucy, 1977; Gingold & Monaghan, 1977), in which gas particle properties (density, temperature) are smoothed over a kernel of finite size;
- Sticky-particle (SP), in which gas particles are collision-less and organised in clouds. Clouds can undergo inelastic collision; during a collision a fraction of the energy is dissipated in the medium (Negroponte & White, 1983).

Following these attempts to include multi-components, the process of star formation in mergers started to be studied (Noguchi & Ishibashi, 1986; Mihos et al., 1991, 1992, 1993). They allowed a better understanding how a gravitational interaction with a massive companion can induce at the same time the concentration of large quantities of dense gas in the central regions and the expulsion of the more diffuse gaseous component along the tidal tails. The torque exerted by the companion on the disc is illustrated on Fig. 5.2.

Most numerical studied were focused on the gas inflows, consequences on the central starburst and dilution of the metallicity of the central regions (Mihos & Hernquist, 1996; Barnes & Hernquist, 1996). The SFR enhancement due to the merger were estimated, ranging from factors of 10 (Mihos & Hernquist, 1996; Cox et al., 2006) to just a few (Di Matteo et al., 2007) compared to isolated galaxies.

The most recent improvements in the simulations deal with the treatment of the ISM, with enormous gains in the resolution allowed by adaptive mesh refinement (AMR) techniques (Kim

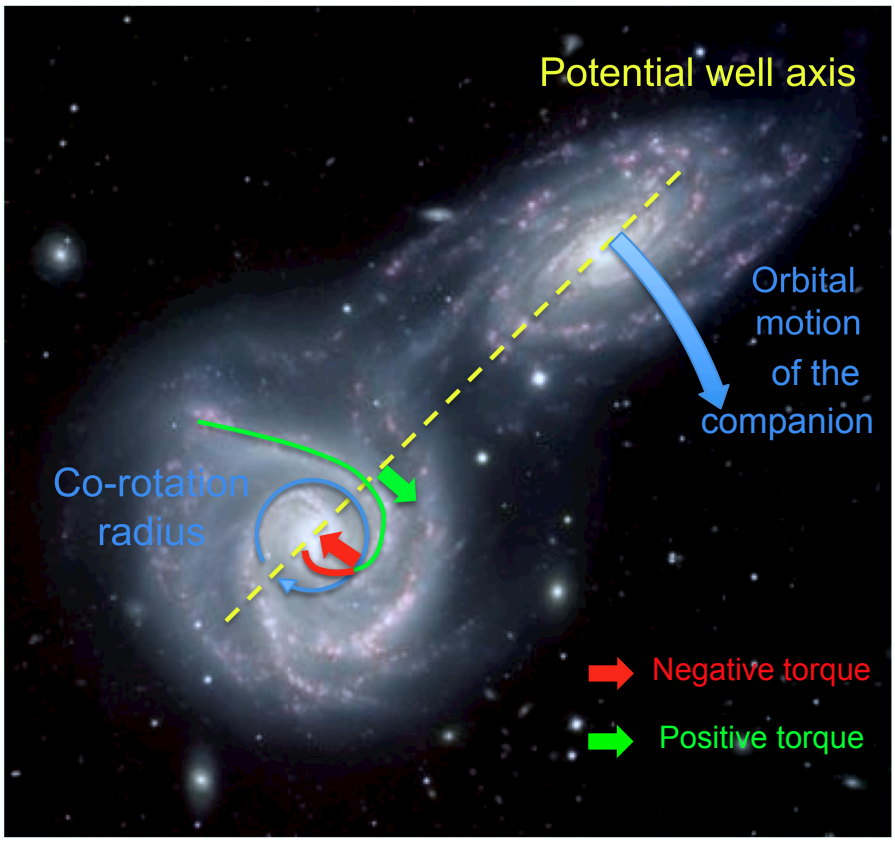


Figure 5.2: Effect of the torque due to gravity on a galactic disc, during a prograde encounter. The torque is negative within the radius at which the angular rotation speed of the disc equals the orbital angular velocity of the companion, usually at a few kpc. The gas loses angular momentum, causing a gas inflow onto the central part of the system. Beyond this radius, the torque is positive: the gas gains angular momentum, causing a part of the galactic disc to be expelled into the intergalactic medium. In the case of a retrograde encounter, the co-rotation radius is not defined and the torque is always negative. However, due to the high relative velocity of the companion, the net effect of the torque on the disc is less efficient than in the prograde case. The tidal field exerted by the companion galaxy may be strong enough to strip off a part of the disc.

et al., 2009; Teyssier et al., 2010). The resolution of the mesh on which the gravitational potential is computed is refined as a function of the particle density; the regions with the highest densities (those of interest for a study of star formation) are then better resolved. For instance, the AMR hydrodynamical simulation by Teyssier et al. (2010) can reproduce not only the global morphology of the system but also the details of the ISM distribution.

The tremendous progress made during the last 40 years in the numerical simulations of mergers is illustrated in Fig. 5.3 showing the various attempts to reproduce of "The Antennae" galaxy.

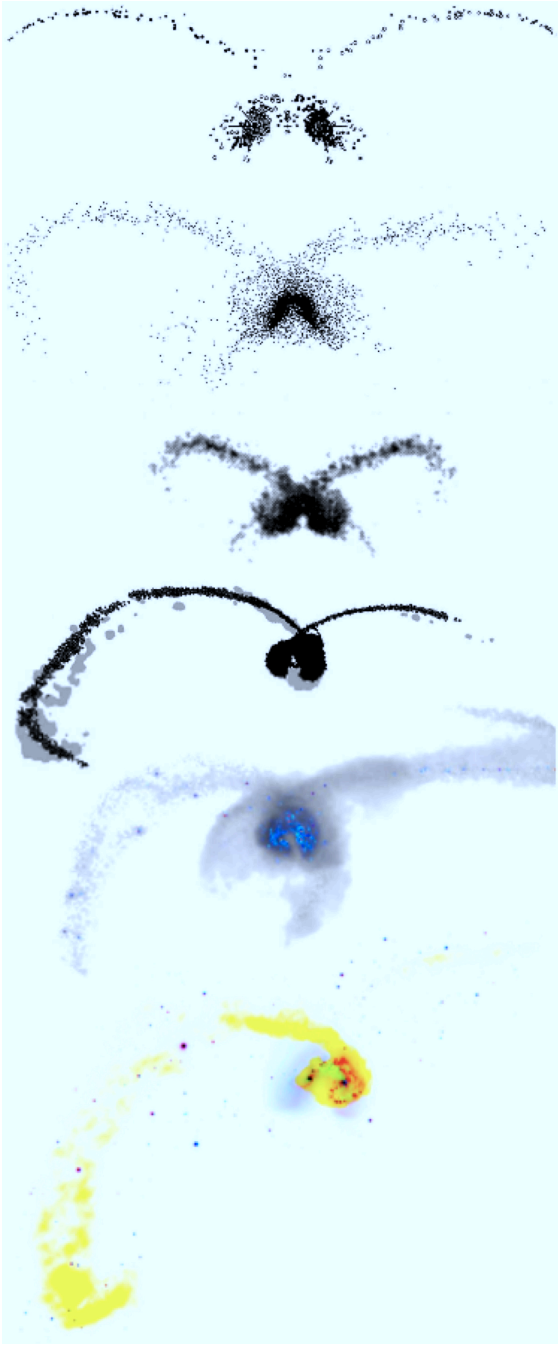

Figure 5.3: [Based on Fig. 4 from Duc & Renaud (2012)] Four decades of history in numerical simulations of interacting systems: the case of the prototypical merger "The Antennae" galaxies. From top to bottom: Toomre & Toomre (1972); Barnes (1988); Mihos et al. (1993); Karl et al. (2010); Teyssier et al. (2010) and composite image of "The Antennae" (H I neutral hydrogen gas is in yellow, mapped with the NRAO VLA, superimposed on an optical image from the CTIO 0.9 m in blue and red - Credits: NRAO/AUI/NSF/SCIENCE PHOTO LIBRARY).

## 5.2 Insight from the Saclay simulations

I present in the following results obtained with two types of simulations that have been developed by the Saclay group (Bournaud et al., 2008, 2011; Teyssier et al., 2010):

- a simulation with sticky particles with a resolution high enough to get to the scale of star clusters and spatially resolve the most massive of them. I made a detailed analysis of the output of the simulation as a function of time, and in particular wrote algorithms aimed at identifying and tracking the clusters during the merger sequence. We determined where/when they were born and how their mass function changed with time. We could thus investigate the signature of environmental processes on the building-up of the CMF. We found that the clusters are good probes of the location of the star-forming regions and their evolution during the merger sequence. Our results were confronted with observations of a sample of interacting systems with high rates of star and star cluster production, studied by collaborators in Spain. The results from these simulations were presented in two papers. They are detailed in section 6, the paper on the comparison with observations is given in Appendix A;
- purely hydrodynamical simulations which provide precise predictions on the temporal evolution of the distribution of the ISM. I checked the predictions about the Probability Density Function (PDF) of the gas density[1] on a sample of nearby interacting systems for which high resolution VLA B-array H I maps, tracing the low dense gas, and UV/mid and far infrared maps, indirectly tracing the dense gas, have been obtained. The data reduction and analysis are presented in Chapter III the thesis.

[1]The Gas density PDF of a gaseous region of which the total mass is M, represents the mass fractions m/M of gas per bin of gas density.

# Chapter 6

# Formation of Super Star Clusters in an idealised merger simulation

## 6.1 Properties of the simulation

Only few simulations of mergers have so far had the resolution (and thus the required number of particles) to identify and track star clusters. Among those, the numerical simulation of a merger of two gas-rich equal-mass spirals, published by Bournaud et al. (2008, hereafter BDE08) was able to reproduce the formation of gravitationally bound structures, with stellar masses of $10^{5-7}M_{\odot}$. Given their typical sizes and half-mass radius, i.e., their compactness, BDE08 argued that they were robust GC progenitor candidates. This study revealed a possible bimodality in the CMF at the end of the simulation, with a secondary peak corresponding to a population of objects with masses of $10^{8-9}M_{\odot}$, radii of order 1kpc and with velocity fields indicating rotational support. Such objects resemble observed TDGs. BDE08 propose that the formation history of such TDG-like objects may be different from that of the compact GC progenitors. We revisit this hypothesis in the present study by performing a systematic analysis of the same simulation at different epochs and tracking the massive stellar objects born in mergers in the time domain.

### 6.1.1 Resolution of the sticky-particles code

The dynamics and the dissipation mode of the energy of the gas component used in BDE08 are those of a SP with a parameter of elasticity of 0.6. In this model, the particles are organised in clouds which will undergo non-elastic collisions or mergers. Only the turbulent pressure, which represents about 90% of the total pressure on gas clouds (Elmegreen & Scalo, 2004; Mac Low & Klessen, 2004; Ballesteros-Paredes et al., 2007), helps to dissipate the energy in SP codes (since the system is supposed to be isothermal, the temperature is not computed).

In a simulation that aims at producing realistic models of galaxies down to the level of compact GCs, the spatial and mass resolutions are key. In SP codes, this means using a number of particles as large as possible. The components of each galaxy – stars, gas and dark matter – were simulated with 6 millions particles, for a total of $36 \times 10^6$ particles. The grid cell size is fixed to 32 pc in the densest regions (near the galaxy centres) and 128 pc in the regions with the lowest density. A fixed cell size in low density regions implies a high enough number of particles so that the formation and dynamics of objects larger in size than a few $\sim 100$ pc in low surface brightness structures (such as TDGs in tidal tails) can be measured. The present simulation resolves the formation of clusters with masses above $10^5M_{\odot}$ and sizes of at least 150 pc.

### 6.1.2 Initial conditions

The details of the simulation were given in BDE08. We summarise here the most relevant parameters for this study. The numerical simulation follows the merger of two equal-mass gas-rich spiral galaxies during $\sim 1\,\mathrm{Gyr}$, in steps of 13 Myr. The initial conditions were not chosen to be necessarily representative of most frequently encountered types of interacting systems but instead were geared to maximise the number and variety of sub-structures born in the merger remnant. The motivation was to populate the high-mass end of the CMF, which suffers from poor statistics (Larsen, 2009). In particular, a relatively high gas fraction (17 %) and the presence of an extended gaseous disc in the progenitor galaxies ensured the formation of gaseous gravitationally bound structures in the collisional debris. An extended dark matter halo prevented these sub-structures to be tidally stirred (see Bournaud & Duc 2006 – hereafter BD06 – for an analysis of the connection between dark matter halo properties and TDG formation). A moderate velocity encounter ($150\,\mathrm{km\,s^{-1}}$), a small pericentre distance (25 kpc) and a prograde orbit for one of the two galaxies favour the development of long tidal tails where tidal objects are more likely to survive. The second galaxy was chosen to move on a retrograde orbit to probe other physical conditions. The inclination angle of the encounter is 30° for the prograde galaxy and 70° for the retrograde one. With $t = 0$ corresponding to the start of the run, the star formation process is activated at $t = 39\,\mathrm{Myr}$, the first pericentre passage occurs at $t = 190\,\mathrm{Myr}$, the second at $t = 370\,\mathrm{Myr}$ and the merger of the two cores (final coalescence) occurs at $t = 525\,\mathrm{Myr}$.

## 6.2 Analysis pipeline: tracking the stellar structures

Fig. 6.1 shows an example of a projected map of the young particle distribution at $t = 156\,\mathrm{Myr}$. A large variety of sub-structures, i.e. compact or elongated condensations, can be seen. Their identification and tracking as a function of time is at the heart of this study.

The extraction of the sub-structures was made on a series of two dimensional projected images, in the same way as an observer would do on images of real systems. With respect to methods using the 3D data cube (for instance friend-of-friend algorithms), this technique has several advantages: (1) adding up the data along a line-of-sight increases the ability to detect weak objects, (2) the computation time is considerably reduced, (3) a straightforward comparison with observations can be made.

Once the objects were extracted, the determination of the various properties of the clusters (mass, size, velocities) was directly made in 3D. There is therefore no bias due to projection effects in our measurements.

### 6.2.1 Extraction algorithm: detection and identification

Extraction refers here to the process of selecting pixels in 2D–maps and gathering them into common objects. As a first step, the algorithm looks for pixels (of value V) that show up against the local background. The local background (B) is estimated by using median values in different circular apertures around the object. The noise level $\sigma$ is determined from the standard deviation of B. Every pixel which matches the condition $\mathrm{SNR} = \frac{V-B}{\sigma} \geq 5$ is selected as a candidate. If the candidate is surrounded by at least two other pixels with $\mathrm{SNR} \geq 3$, it is a detection.

Then, we use a percolation algorithm to define the boundaries of a projected object spread over adjacent pixels. We derive a first estimate of the 2D–position of the centre, the projected radius and their associated errors. If two objects are aligned along the same line–of–sight, they can overlap and then are defined as only one object. The loss of one object in a projection does

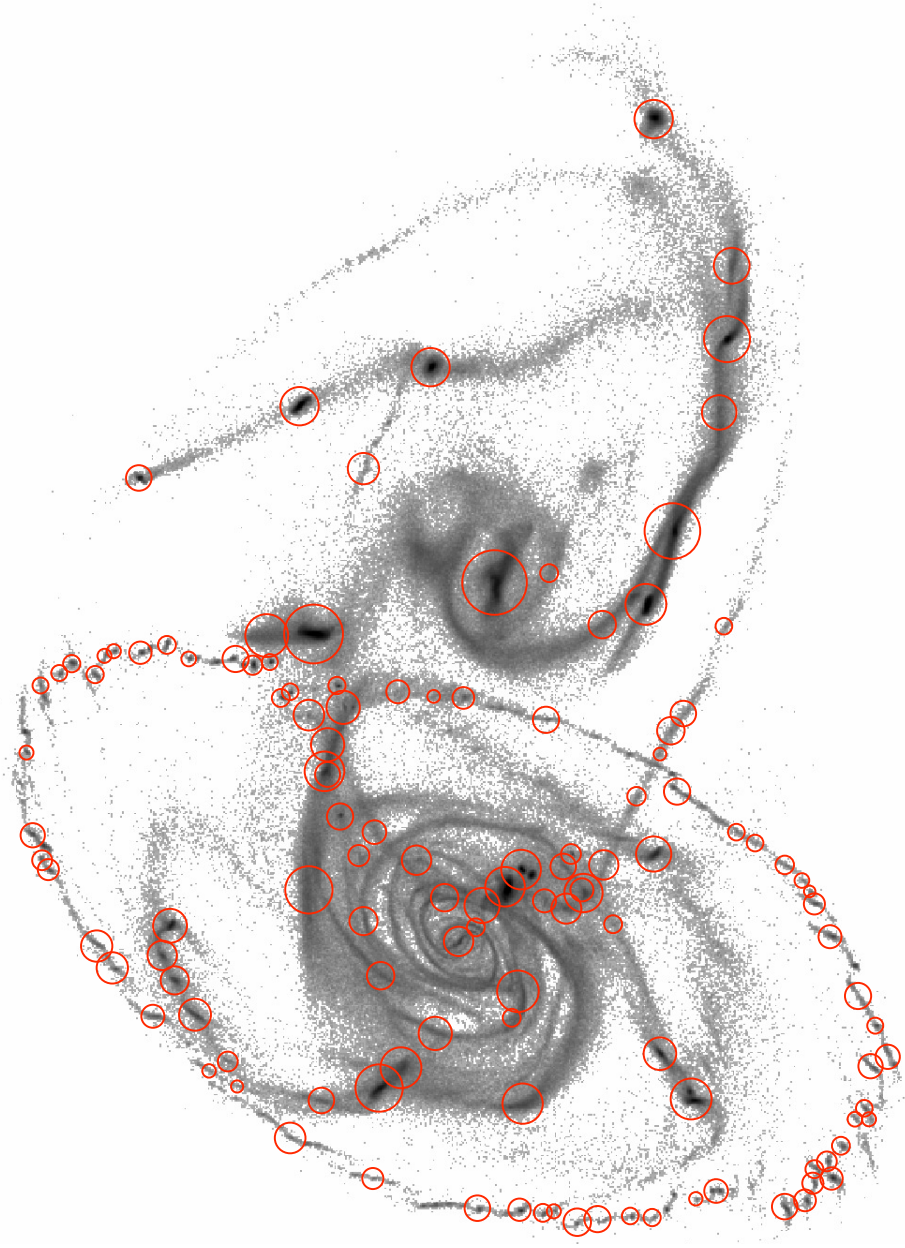

Figure 6.1: Sub-structures detected at $t = 156\,\mathrm{Myr}$. The diameter of the circles corresponds to the estimated size of the stellar groups. Stellar groups encompass stable clusters (or long-lived clusters, see Sect. 6.2.3) and non-persistent clusters, which will be excluded from the analysis. Note that a logarithmic scale is used for this map.

not necessary mean that the corresponding star cluster will not be detected: thanks to the other projections, the missing information can be retrieved.

Objects that are dense enough are identified as "groups". The identification of the groups is done in 3D by cross-correlating the 2D coordinates pairwise[1] and taking into account the associated errors. In general, the 3D coordinates of the object can be retrieved without ambiguity. If at least one coordinate is uncertain, sets of coordinates in other planes are created to make sure that no cluster will be left out. If necessary, these additional objects will be rejected by the next step of the process: the 3D photometry.

The precise *location* of an object is given by the barycentre of the particles belonging to it. The *radius* of an object is defined where the derivative of its surface density profile drops to zero. We checked visually that the full spatial extent of the clusters is recovered. The half-mass radius is noted $r_{\rm h}$. The cluster *mass* is simply computed from the number of particles included in the cluster boundaries and is corrected for the local stellar background, i.e. contamination by the diffuse stellar streams in which clusters lie.

Bastian et al. (2012) emphasised the importance of an accurate definition of a "cluster". The definition relies essentially on the distinction between bound and unbound dynamical structures: gravitationally bound stellar groups are clusters while unbound groups are associations. Massive star clusters, younger than 10 Myr, are especially difficult to define since they are not dynamically relaxed. In our case, the time step of the simulation (13 Myr) ensures that a stellar group that is detected at two different times is *a priori* evolved and bound. We applied a density threshold to remove the loose associations and checked this hypothesis using the dynamical information of the groups.

### 6.2.2 Determination of the kinematic parameters

In order to study the kinematic evolution of the clusters detected in the simulation we have computed the rotation velocity and the velocity dispersion.

For each isolated cluster, we compute the particle velocities with respect to the cluster centre. The background particles that have velocities significantly higher than the median value are discarded. These particles belong to stellar streams in which some clusters may find themselves during their evolution. Even if they represent a small fraction of the total number of particles in a given cluster (less than 20 %), they can bias significantly the measurements.

We assume that each cluster is rotating around only one axis, at the angular velocity $\omega$, and is symmetric around this axis. We note $I$ the inertial momentum of the cluster along the rotation axis. The rotation velocity of a particle located at a distance $r$ with respect to the rotation axis is related to $\omega$, $I$ and the total angular momentum $\boldsymbol{L}(r)$ of the particle by the relation:

$$v_{\rm rot}(r) = \omega r = \frac{||\boldsymbol{L}(r)||}{I} r \tag{6.1}$$

Depending on the mass of a cluster, we adopt two different techniques to measure the rotation velocity. Clusters that are less massive than $5 \times 10^7 {\rm M}_\odot$ have radii smaller than 500 pc, just a few times the grid cell size in the outer regions of the system. In this case, the rotation velocity of the cluster, $v_{\rm rot}^{\rm cluster}$, is defined as $v_{\rm rot}(r_{\rm h})$, i.e. the rotation velocity at the half mass radius of the cluster. For clusters more massive than $5 \times 10^7 {\rm M}_\odot$, with radii greater than at least four times the grid cell size, $v_{\rm rot}^{\rm cluster}$ is assessed using only particles within the shell: $(1.0 \pm 0.3) \times r_{\rm h} < r < (2.5 \pm 0.5) \times r_{\rm h}$, where the velocity field normally becomes flat. After subtraction of the cluster

[1] In other words, the (X,Y,Z) triplet is obtained from the cross-correlation of the three couples of coordinates (X,Y), (X,Z) and (Y,Z)

rotation velocity, we obtain a residual velocity $v_{\rm res}(r) = v_{\rm rot}(r) - v_{\rm rot}^{\rm cluster}$ for each particle. This residual velocity is used to compute the velocity dispersion of the cluster:

$$\sigma = \sqrt{\frac{\sum_{i=1}^{N} v_{\rm res}(r_i)^2}{N}} \tag{6.2}$$

where $N$ is the number of particles in the cluster and $r_i$ is the distance of the $i$-th particle to the axis of rotation.

Depending on the mass of the clusters, the selection of the $N$ particles varies. The clusters more massive than $5 \times 10^7$ $M_\odot$ are formed by several thousands of particles and can extend up to several hundreds of pc. The velocity dispersion is computed in four different regions within the cluster (excluding the barycentre), and the lowest value is taken. The clusters less massive than $5 \times 10^7$ $M_\odot$ have less than a thousand particles and are much less extended: their outer radius is a few times the linear resolution of the simulation. In this case, the velocity dispersion, the angular and the inertial momenta are determined using all the particles.

### 6.2.3 Cluster tracking and sample definition

The cluster tracking process is based on the use of "tracers", i.e. particles which can be re-identified at each time-step. A set of tracer–particles is chosen within each cluster at each time step $t$. In practise, we choose the particles closest to the centre of the cluster, i.e. those who have the best chance to be strongly bound.

For each cluster, we compare the location of the tracer–particles chosen at $t$ with the location of the same tracer-particles at $t + 1$. If a significant fraction of tracer–particles is found to be within a cluster identified at $t+1$, we considered the two clusters were the same. In practise, we use a fraction of 30 per cent tracer–particles. As some clusters can be missed at some time-steps, we allow the algorithm to skip a limited number of time-steps (up to 8) to retrieve them later.

Using that method, we could track a total of approximately 800 clusters. Among them, we define a population of 163 *stable clusters* matching one of the following conditions:

- if formed during the first 500 Myr of the simulation, a stable cluster lives for at least 500 Myr;
- if formed after the first 500 Myr of the simulation, a stable cluster lives for at least 200 Myr.

As shown in Fig. 6.2, 500 Myr appears as a characteristic time scale, splitting the population of clusters into two groups of cluster lifetimes. The stable clusters selected according to the second criterion represent less than 7% of the overall stable population. The second condition ensures that clusters that may form late are included in the sample of stable clusters and no bias towards a scenario that predicts early-on formation of SSCs is introduced. The softening of the condition on the lifetime duration is justified by the evolution of the physical conditions in the merger: after 500 Myr of evolution, the final coalescence occurs and the system of clusters is likely to enter a steadier phase of evolution.

Finally, we highlight that this pipeline does not take into account the mergers of clusters. If a merger event occurs between two clusters, one of them undergoes a mass gain whereas the other one is stated as "destroyed".

Globally, the reliability of the tracking algorithm can be evaluated looking at the mass curves of the clusters. In Fig. 6.3, we plotted the time variation of the mass of two massive clusters tracked all along the simulation. The continuity of the mass curves proves that we are able to track efficiently the clusters over long time intervals and that the measures are accurate enough to give close and consistent values for the mass from one time step to another.

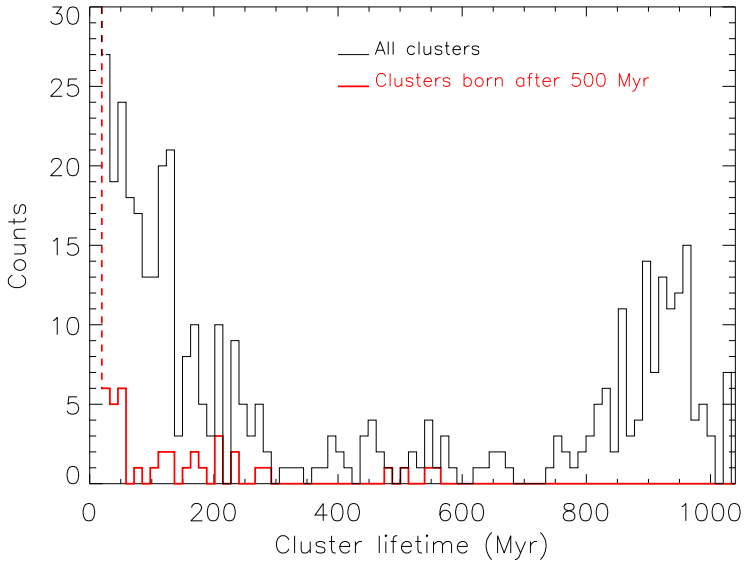


Figure 6.2: Distribution of cluster lifetimes, represented for two populations: all clusters (black thin line) and the population restricted to the clusters that form after 500 Myr (red thick line). The first bin (dashed line) goes up to 331 and 51 clusters respectively.

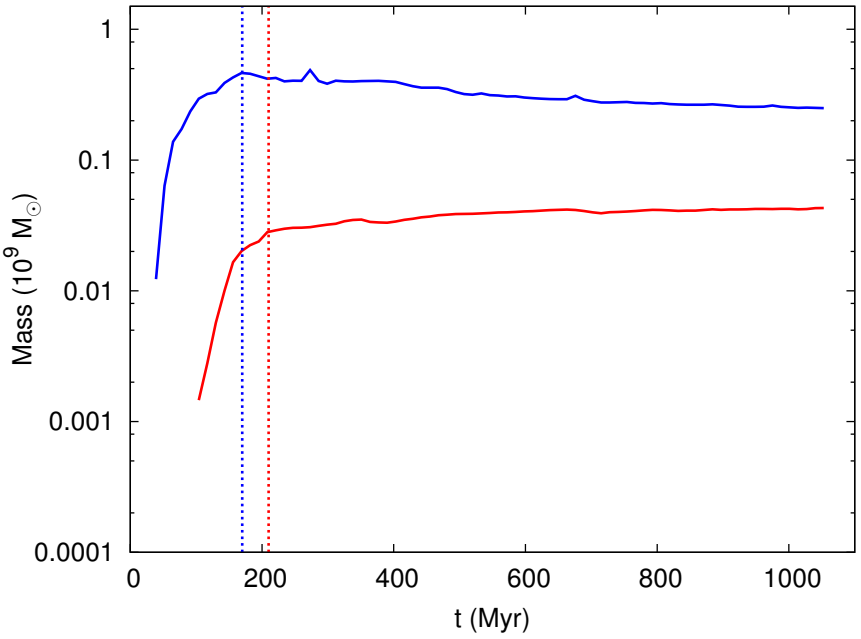


Figure 6.3: Mass curves of two massive clusters. The "initial mass" of the cluster is defined as the mass reached at the end of the growth phase, before the cluster enters the phase of steady mass evolution (see dotted line). This period generally corresponds to the first 100 Myr of cluster evolution.

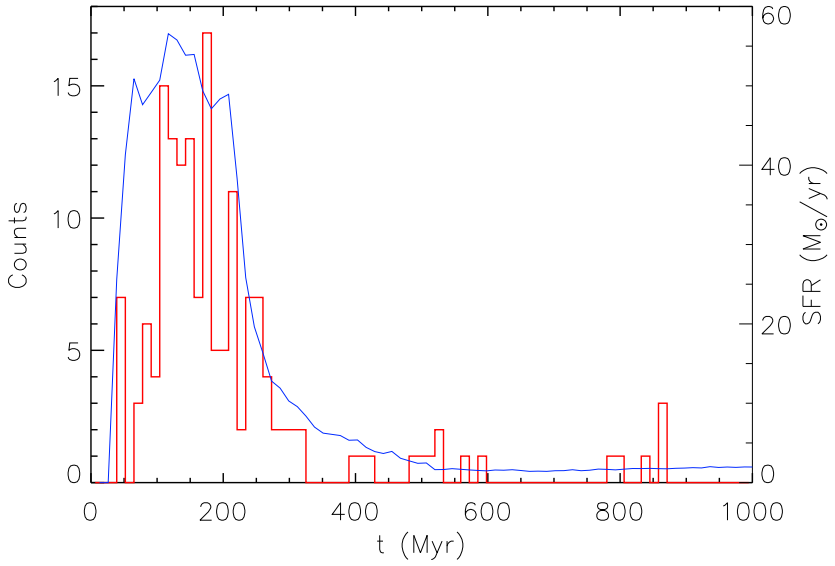


Figure 6.4: Number of clusters (red) and SFR (blue) as a function of time. The absence of new clusters after 850 Myr results from the criteria defined to select stable clusters.

Clusters with masses below $10^{6.5}M_{\odot}$ are not particularly well identified and tracked by the algorithm. Therefore, we adopt this value as the global mass reliability threshold. Because of the border effects of the simulation mentioned above, the mass curves of the few objects that approach the boundary of the simulation box show a sudden decline. The physical properties of these clusters are fixed at their last value before they reach the simulation boundary.

Fig. 6.1 illustrates the results of the detection algorithm at $t = 156$ Myr (i.e. 40 Myr before the first passage). Note the abundance of small dense stellar groups forming along a ring-like structure in the retrograde galaxy (galaxy at the bottom of the figure), as opposed to the large size of the structures forming in the prograde galaxy (galaxy at the top of the figure).

## 6.3 Cluster Formation and Evolution

### 6.3.1 History of Cluster and SSC Formation

Fig. 6.4 shows the Cluster Formation History, as traced by the detection time of the stable clusters. Most stable clusters form during the first 300 Myr. This period corresponds to the star formation peak. We observe a good correlation between the Cluster Formation Rate (CFR) and the SFR, i.e., the cluster formation history traces the star formation history of the whole system. This is a nice illustration that cluster formation and star formation are intimately related. The long-lived clusters appear as an especially good tracer of the star formation activity and history of the system.

Now, one might wonder whether this relation SFR–CFR depends on the mass of the cluster or not.

Fig. 6.5 represents the initial mass of the stable clusters that form during the simulation as

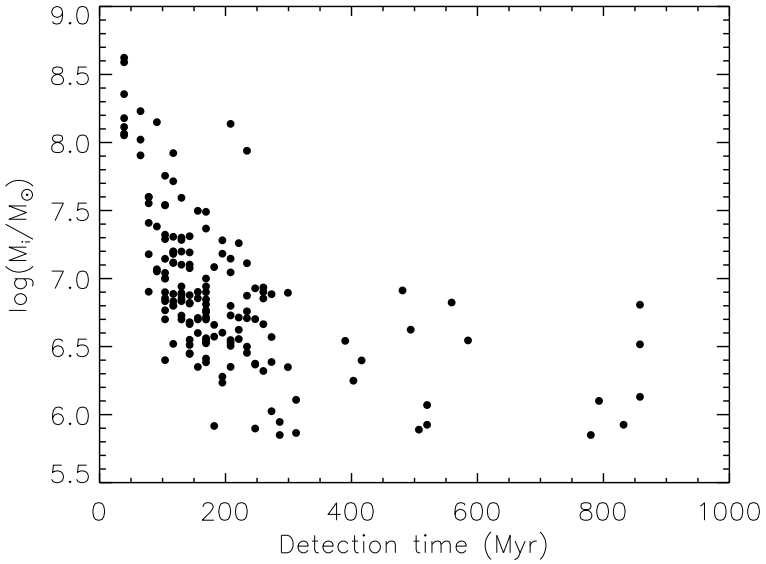


Figure 6.5: Distribution of the stable cluster population, in the initial mass versus detection time plane.

a function of their detection time. Integrating over the masses gives the distribution plotted in Fig. 6.4. Fig. 6.5 shows that, on average, the initial mass is a decreasing function of the detection time (i.e. the epoch of formation). In other words, as the merger proceeds, the clusters that form are less and less massive. In fact, the most massive clusters of the simulation were formed early-on, at an epoch characterised by a high SFR. After $t = 300\,\mathrm{Myr}$, while the SFR is at a low level, only low mass clusters form. If SFR and mass of the most massive cluster follow a similar evolution after $t = 100\,\mathrm{Myr}$, at early times (i.e. before $t = 100\,\mathrm{Myr}$) they seem to be anti-correlated. Cluster statistics is particularly low at early times though.

Two different regimes of cluster formation can be observed in our simulation:

- a regime of high-mass cluster formation, early-on during the encounter and until the second pericentre passage (at $t = 370\,\mathrm{Myr}$), associated with a high SFR;
- a regime of intermediate and low mass cluster formation, after pericentre passage, associated with a moderate SFR.

Interestingly, these two regimes are related to their birth places. The birth place of a cluster is simply parametrised by the distance to the centre of its progenitor galaxy, at the birth time. Tracking back in time each cluster individually, we can determine the progenitor galaxy and compute the distance to the centre for each cluster. For clusters born after the coalescence of the two galactic cores, the radial distance is computed relatively to the barycentre of the system. Fig. 6.6 shows the radial distance distributions of the stable cluster population and the whole cluster population, at their birth time. The global size of the system strongly varies along with the merger stage, mainly because of the large radial excursions of the tidal tails, especially after the second pericentre passage, at $t = 370\,\mathrm{Myr}$. At this later stage of the interaction, clusters may form all along the tidal tails, thus up to large distances. This is confirmed by the evolution

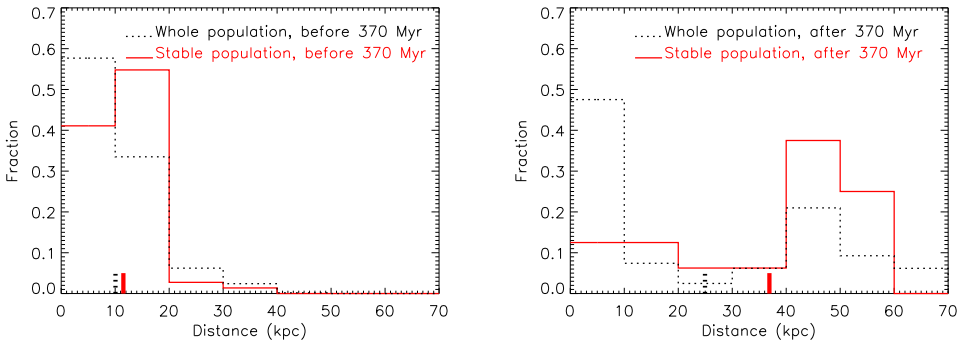


Figure 6.6: Radial distribution of the clusters at their birth time (distances are taken at birth time), for clusters born before $t = 370\,\mathrm{Myr}$ (left) and after $t = 370\,\mathrm{Myr}$ (right). The stable clusters (red histograms) and whole population (dotted black histograms) are included. Average distances are marked on the distance axis.

of the average birth distances with time: the clusters tend to form further and further as the interaction goes on.

The high star formation regime is associated with a centrally concentrated cluster formation, with an average characteristic distance of about 9.3 kpc (11.5 kpc if restricted to stable clusters only) while the low star formation regime is associated with a sparser cluster formation (with some enhancement in the outer regions), with an average characteristic distance of 24.8 kpc (36.9 kpc if restricted to stable clusters only). On average, the stable clusters form further away from the galactic centres than the general population. In other words, the outermost regions (external disc, then tidal tails) are the preferential sites of stable cluster formation. The case of the 15 most massive clusters of the simulation[2] is illustrated in Fig. 6.7, where their birth places have been located at two different times: $t = 39\,\mathrm{Myr}$ and $t = 104\,\mathrm{Myr}$. The two figures reveal that these massive clusters form in the outer regions of the discs of the parent galaxies, preferentially in the prograde galaxy, and then are dragged out in the tidal tail.

These results are consistent with the models of Elmegreen et al. (1993) who proposed that the enhanced turbulence of the ISM caused by galaxy interactions triggers the formation of self–gravitating gas clumps with masses above $10^8$ $\mathrm{M}_\odot$. At the beginning of the simulation, all the conditions are met to enhance (massive) cluster formation in the outer discs: as the tidal interaction between the two galactic discs begins, non-circular motions develop and cause an increase of the gas velocity dispersion $\sigma$. Consequently, the Jeans mass increases ($M_{\mathrm{Jeans}} \propto \sigma^4$), gravitational instabilities can develop on large scales ($L_{\mathrm{Jeans}} \propto \sigma^2$) and lead to the formation of massive self–gravitating clumps. In addition to this, compressive tidal modes add an extra pressure on the gaseous component which helps gravity to bind the structures (Renaud et al., 2008): the mass fraction in the compressive mode always peaks at pericentre configurations, independently of the merger parameters (Renaud et al., 2009).

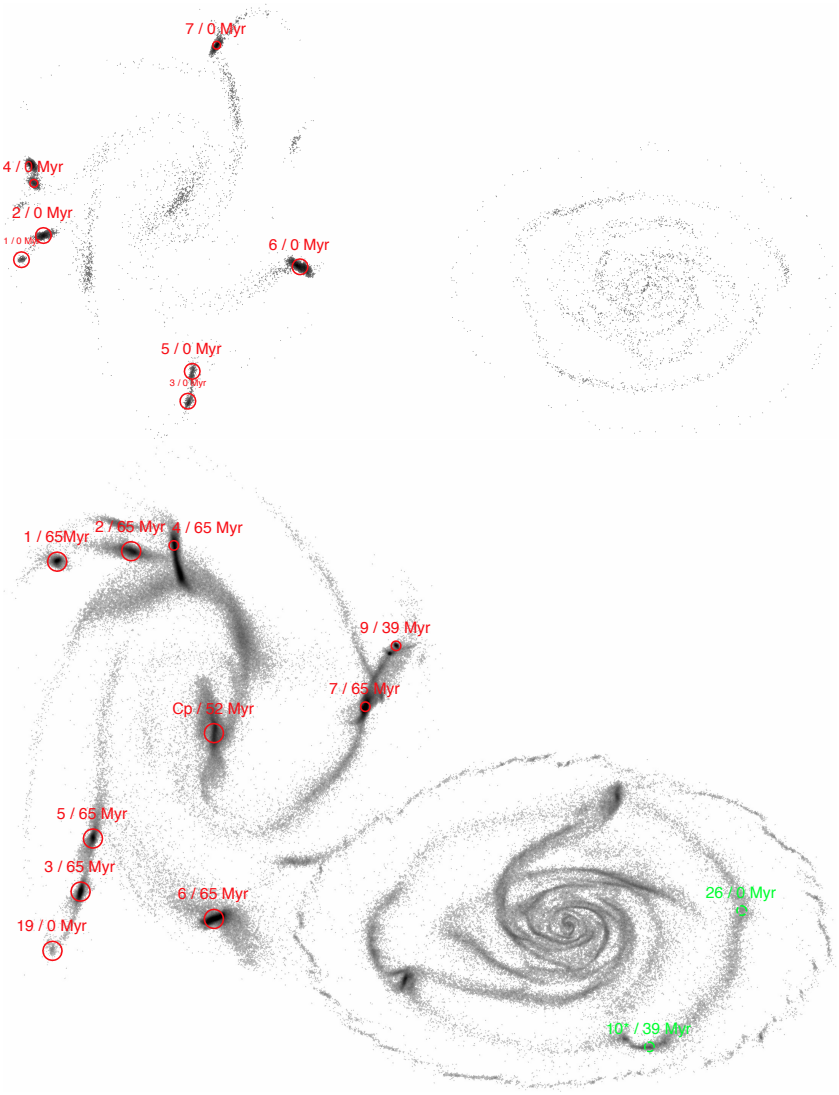


Figure 6.7: XY projections of the spatial distribution of the young stellar component at $t = 39\,\mathrm{Myr}$ (top) and $t = 104\,\mathrm{Myr}$ (bottom). Massive clusters formed in the prograde galaxy (left) and in the retrograde galaxy (right) are identified with the red circles and green dashed circles, respectively. The size of each circle is proportional to the future mass gain of the cluster, with larger circles indicating a positive gain. Each cluster is labelled as follows: cluster number / age of the cluster. $C_p$ corresponds to the nucleus of the prograde galaxy.

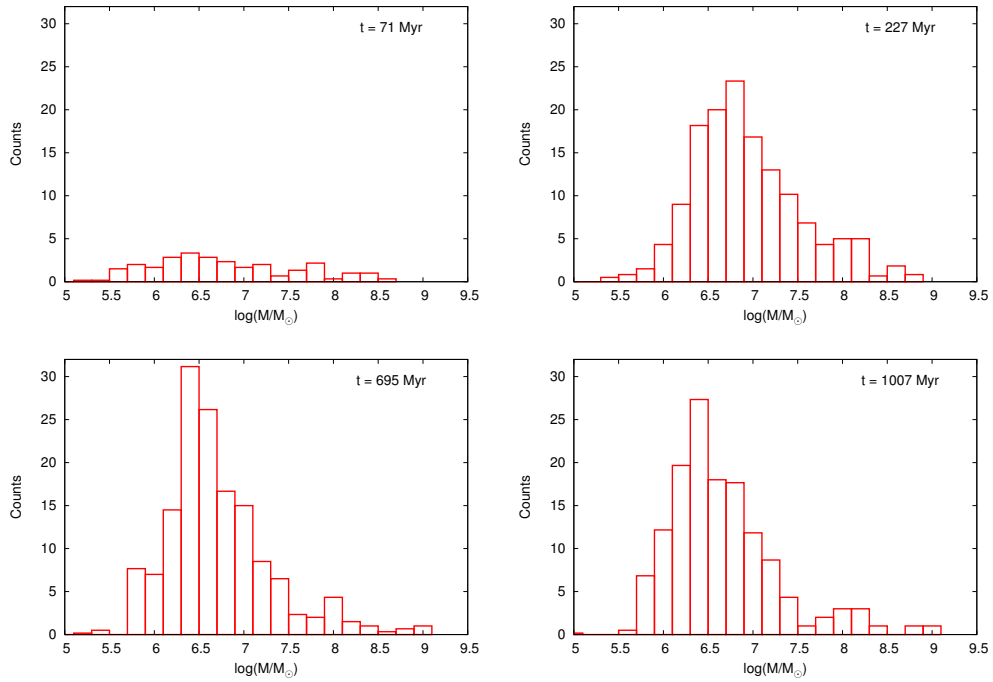


Figure 6.8: Cluster Mass Function at different epochs of the simulation. Each histogram represents the average distribution over 78 Myr (6 time-steps).

### 6.3.2 (Initial) Cluster Mass Function

Applied to each time-step of the simulation, the detection algorithm allows one to determine the CMF as a function of time. Fig. 6.8 presents a chronological sequence of the mass function at four epochs. At first sight, the mass distribution seems to present a turnover shortly after the onset of the interaction (with a peak at $10^{6.5}M_{\odot}$). The presence of a turnover mass is observed in quiescent galaxies (e.g., Harris, 1996; Waters et al., 2006; Jordán et al., 2007; Villegas et al., 2010), with values depending on the galaxy mass. For ellipticals, this value is typically $\sim 2 \times 10^5 M_{\odot}$ (Jordán et al., 2006). In star-forming colliding systems, a large number of young and massive clusters is observed; the mass distribution does not exhibit any turnover and is well approximated by a power law of index $\sim -2$ (Whitmore et al., 1999; Zhang & Fall, 1999; de Grijs et al., 2003; McCrady & Graham, 2007). Here, in the numerical model, the apparent turnover mass is likely to be the result of the lack of resolution at low masses. The high-mass end follows a power-law, consistent with observations (Miralles et al., 2012, and references therein).

A second characteristic feature, observed in several snapshots, is a gap at $\sim 10^{7.5}M_{\odot}$, and a bump at $\sim 10^8 M_{\odot}$, as illustrated in Fig. 6.8. BDE08 argued that this feature could correspond to a bimodal distribution of the young clusters. Recent high angular resolution observations of the CO molecular gas in the overlap region of the Antennae galaxies (NGC 4038/39) have revealed a bimodal mass distribution. The distinct break appears at $M_{mol} \sim 10^{6.5}M_{\odot}$ and confirms the presence of two populations of Giant Molecular Clouds (Wei et al., 2012). Nevertheless, the poor sampling of the high mass end of the simulated CMF makes the statistical significance of this bimodality rather weak.

Fig. 6.9, which represents the mass–size scaling relation for the stable clusters, in fact rather suggests a continuity in the mass and size distributions of the stable clusters, a result which is somewhat surprising with respect to the observations by Wei et al. (2012) of a bimodality both in the mass and size distributions. Note the huge range of masses – a factor of 1000 – and sizes – a factor of 10 – exhibited by clusters formed during a single collision. This figure also shows that, as expected, the most massive clusters have the largest apparent size. However, due to simulation limitations, the sizes measured for each cluster must be considered as upper limits. More specifically, the use of a softening length in the gravitational potential description stops the cluster dynamical evolution at a pseudo-equilibrium, as shown by BDE08, and prevents them from contracting until reaching effective sizes of a few tens of pc. Virialised clusters would be located lower in the mass–size plane, as shown by the arrow on Fig. 6.9; their sizes would be smaller by typically a factor 2/3 (according to BDE08).

In addition to a mass criterion, the distinction by BDE08 of two cluster populations was also supported by a kinematic analysis. The clusters with masses above $10^{7.5}M_{\odot}$ appeared to be extended, supported by rotation, thus showing several similarities to observed TDGs. The clusters with masses below $10^{7.5}M_{\odot}$ looked more compact, supported by pressure, and were thus considered as progenitors of GCs. Motivated by the claim of BDE08, as well as observational features of real systems[3], we decided to further distinguish among the population of stable clusters those clusters with initial masses above $10^{7.5}M_{\odot}$. There are 15 of them in our simulation. For this sub-population, the resolution was good enough to allow a study of their mass and dynamical evolution. Table 6.1 summarises their characteristics: formation time, initial and final masses and sizes, fraction of young to old stars.

The in-depth investigation of the cluster kinematics (see Fig. 6.11) did not reveal any obvious

[2]These clusters have masses above $10^{7.5}M_{\odot}$ during the phase of steady mass evolution. $10^{7.5}M_{\odot}$ appears as a characteristic mass in the CMF.

[3]Observed TDGs and low-mass GCs born in mergers have apparently different structural and kinematic properties.

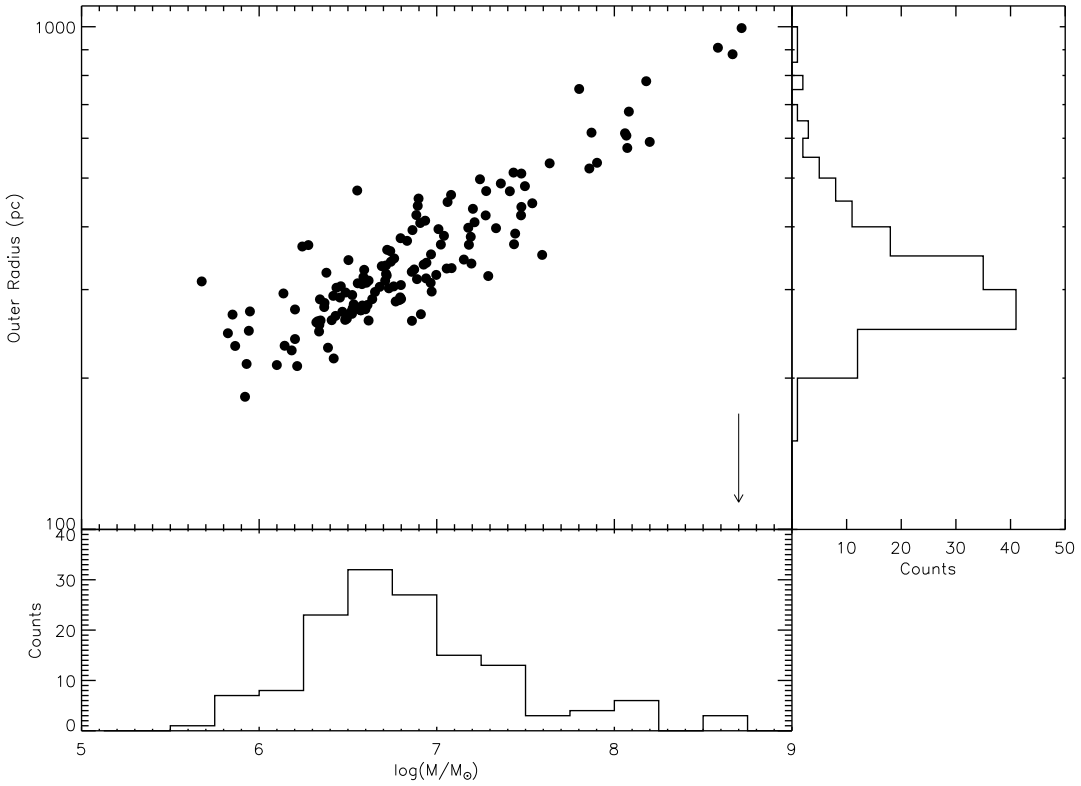


Figure 6.9: Mass–Size relation for a sample of 163 stable clusters. Masses and sizes are taken 125 Myr after the first detection of the structures. The corresponding histograms of the masses and radii are also shown. The choice of 125 Myr is justified by the interval of variation of the growth phase duration. Using time shifts within the $100 - 150$ Myr range does not change significantly the mass–size distribution.

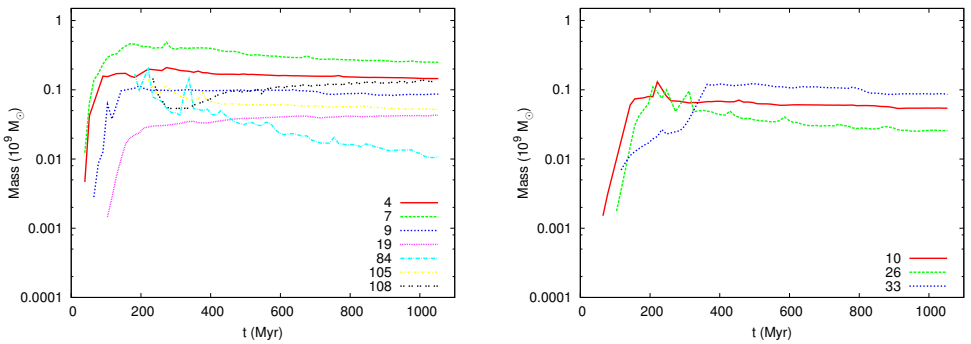


Figure 6.10: Mass curves of the massive clusters belonging to the prograde galaxy (top) and the retrograde galaxy (bottom). Only the clusters not affected by boundary effects are represented. The individual clusters are labelled with an ID number.

Table 6.1: Properties of our sample of 15 massive clusters and of the nucleus of the prograde galaxy.

| Cluster ID | Birth Time (Myr) | Mass ($10^9 M_\odot$) Initial ($M_i$) | $t = 234$ Myr | Final ($M_f$) | $M_f$ / $M_i$ | Radius (pc) Initial | $t = 234$ Myr | (# old stars) / (# young stars) Birth time | Final time |
|---|---|---|---|---|---|---|---|---|---|
| 1 | 39 | 0.113 | 0.128 | 0.171 | 1.52 | 300 | 580 | 0.07 | 0.002 |
| 2 | 39 | 0.130 | 0.143 | 0.158 | 1.22 | 470 | 650 | 0.22 | 0.027 |
| 3 | 39 | 0.151 | 0.164 | 0.243 | 1.61 | 400 | 600 | 0.11 | 0.023 |
| 4 | 39 | 0.171 | 0.168 | 0.145 | 0.85 | 410 | 1270 | 0.58 | 0.025 |
| 5 | 39 | 0.116 | 0.132 | 0.150 | 1.30 | 330 | 610 | 0.47 | 0.005 |
| 6 | 39 | 0.420 | 0.441 | 0.583 | 1.39 | 540 | 960 | 0.33 | 0.024 |
| 7 | 39 | 0.389 | 0.400 | 0.250 | 0.64 | 580 | 890 | 0.29 | 0.013 |
| 9 | 65 | 0.105 | 0.098 | 0.087 | 0.83 | 390 | 570 | 0.09 | 0.005 |
| 10 | 65 | 0.074 | 0.131 | 0.054 | 0.74 | 160 | 640 | 0.84 | 0.010 |
| 19 | 104 | 0.032 | 0.030 | 0.043 | 1.33 | 290 | 420 | 0.03 | 0.003 |
| 26 | 104 | 0.057 | 0.075 | 0.026 | 0.46 | 260 | 650 | 0.32 | 0.065 |
| 33 | 117 | 0.021 | 0.027 | 0.086 | 4.17 | 450 | 470 | 0.12 | 0.095 |
| 84 | 182 | 0.170 | 0.079 | 0.010 | 0.06 | 890 | 630 | 0.43 | 0.067 |
| 105 | 221 | 0.141 | 0.099 | 0.052 | 0.34 | 810 | 680 | 0.14 | 0.018 |
| 108 | 234 | 0.087 | 0.146 | 0.131 | 1.52 | 950 | 950 | 0.80 | 0.147 |
| $C_p$ † | 52 | 0.550 | 0.538 | 0.895 | 1.64 | 380 | 1010 | 51.19 | 3.595 |

† : nucleus of the prograde galaxy. Note the abundance in old stars.

The birth time is when the cluster is detected for the first time; the initial time is the time of transition between the growth phase and the steady phase; the final time corresponds to the last snapshot of the simulation. The initial mass was measured from the mass curves shown in Fig. 6.10 (see main text).

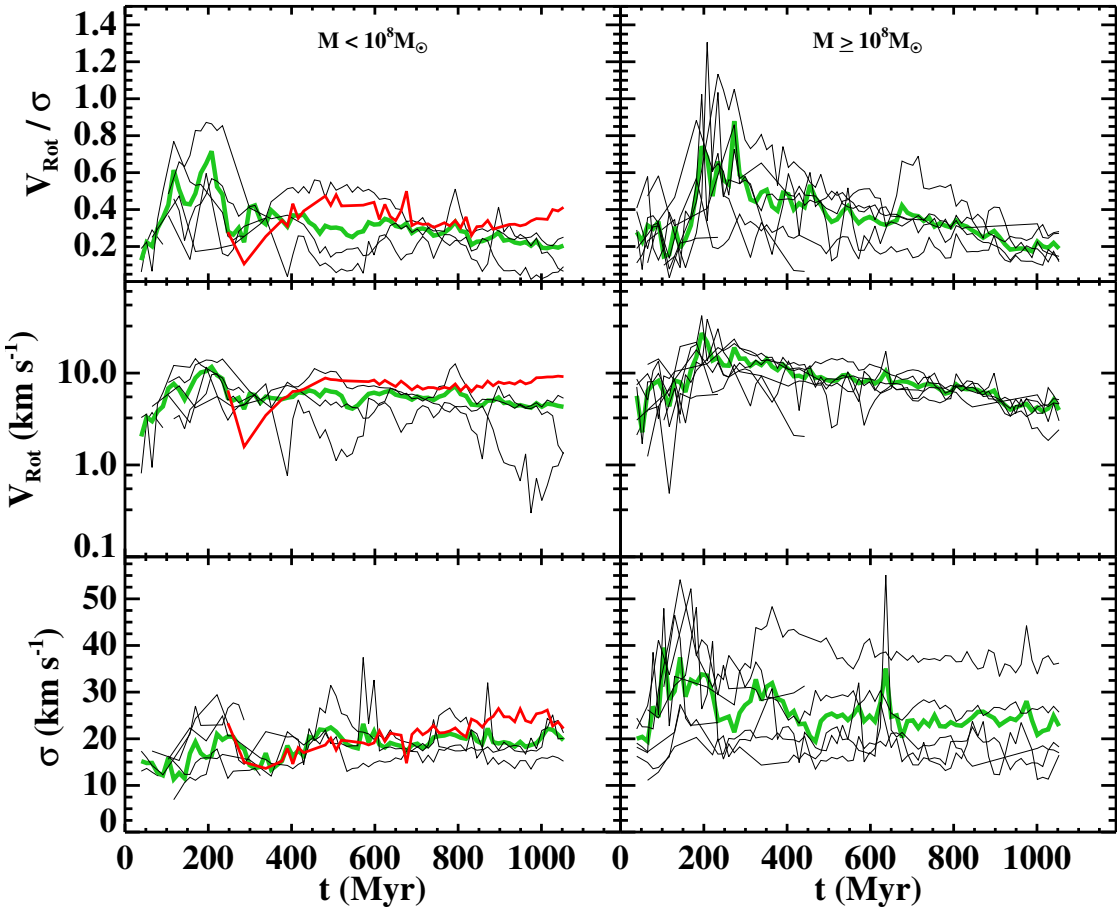


Figure 6.11: Evolution of the kinematic parameters of the 15 most massive clusters. They are divided in two initial mass intervals. Note that $v_{\rm rot}$ is plotted with a logarithm scale. The green curves represent the average trend while the red ones represent Cluster 108, the only massive sub-structure formed in-situ in tidal tails, and which may qualify as a TDG.

dichotomy of the $v_{\rm rot}/\sigma$ parameter. The kinematic analysis only confirms that high mass clusters have on average higher $v_{\rm rot}$ and $\sigma$ than less massive ones. Observations of GMCs in the Antennae by (Wei et al., 2012) did not reveal either a clean separation between the high-mass and low-mass groups, although about half of the clouds exhibit a velocity gradient indicating shear or rotation. The mean and median values of the velocity dispersion of the molecular component were lower than $10\,{\rm km\,s^{-1}}$, while the cluster kinematics, as probed by the young stars, is higher than this value in the simulated clusters.

Here again, resolution effects of the simulations are likely to explain these rather surprising findings. In theory, the grid cell size limits the measure of $v_{\rm rot}$ to objects larger than $\sim 500\,{\rm pc}$, i.e. more massive than $10^{7.5}\,{\rm M}_\odot$. In practise, measuring $v_{\rm rot}$ is difficult for objects less massive than $10^8\,{\rm M}_\odot$, and the low resolution of the cluster dynamics may be responsible for a lowering of the actual rotation velocity the stellar objects should acquire.

However, one may highlight the large range of $v_{\rm rot}/\sigma$ values (a factor of 6) and their somehow unexpected variations with time: we observe a global trend towards a reduction of the rotation

velocity, such that at the end of the simulation, all clusters, even the most massive ones have a velocity dispersion which is much higher than the rotation velocity. This intriguing observation suggests that resolution effects might not be the only factor driving the kinematic properties. A plausible hypothesis would point to a systematic bias introduced by the use of the young particles[4] as tracer of the formation, evolution and properties of sub-structures in interacting systems. The few studies made on the kinematics of fast-rotating TDGs indicate that, while the velocity curves determined using the atomic and molecular gas (H I, CO) and the ionised gas (as traced by the H$\alpha$ line) globally match, the values of the maximum velocities differ (Bournaud et al., 2007). The rotation velocity is underestimated when derived from the gas ionised by the young massive stars that only probe the innermost regions. The stellar component considered in our simulation corresponds, in observations, to the young stars traced by the ionised gas *plus* the relatively older stars with ages up to a few tens of Myr that have formed since the birth of the cluster. The latter stellar component that might have acquired a higher velocity dispersion during the cluster evolution is usually not taken into account in the study of real system kinematics. This might explain why the rotation velocities determined in the simulated clusters are not as high as those measured in TDGs, and why they tend to decrease with time.

Finally, one might note that the systematic bias introduced by using exclusively young stars affects mainly the kinematic analysis. Old stars contribute little to the mass budget of the young clusters: the fractions of the old to new stars indicate that the abundance in old stars is low after $\sim 1$ Gyr of evolution: it varies between 1 per thousand (for the oldest clusters) and 10 per cent (for less evolved clusters). The old star fraction is surely negligible in real SSCs born in mergers, that rapidly expel their gas because of strong internal feedback. The old component might represent a significant fraction of the stellar budget in only the most massive TDGs (Kaviraj et al., 2012), but its value is particularly difficult to estimate (Boquien et al., 2010).

### 6.3.3 Cluster evolution, fate and environmental effects

Fig. 6.12 presents the mass evolution of the various cluster populations as a function of their final location (i.e. the distance to the remnant at the end of the simulation). The mass evolution is given by the ratio $M_f/M_i$ and the distance is used as a proxy of the environment. Large distances correspond to the tidal tail (distance $> 30$ kpc). For the massive clusters in the outer regions of the system, we considered boundary effects and corrected for them when necessary. We also took into account mergers of clusters, identified by mass kicks in the mass curves.

We observe that most clusters lose mass and end up in the inner regions of the system. The dynamical friction can slow down the clusters on their orbits and cause a global fall onto the centre. In the central regions, the tidal forces can be intense, causing a heavy mass loss and, sometimes destroy the cluster.

More generally, there seems to be a correlation between mass variation and cluster location: in proportion, there are fewer clusters losing mass in the tidal tails than in the inner regions and more cluster gaining mass in the tidal tails than in the inner regions (excluding mergers). Clusters located in the tidal tails are surrounded by large gaseous reservoirs; gas can be accreted and they suffer a weaker tidal effect (Renaud & Gieles, in prep.).

The fate of the clusters is largely governed by the initial position of the clusters and their subsequent trajectories during the merger. Fig. 6.13 shows that the clusters in the prograde and

[4] "Young" particles result from the transformation of gas particles during the merger; they trace the regions of high gas densities. A young particle has a mass of 8333 $M_\odot$. "Old" particles, those which pre-exist the merger, have masses approximately 10 times higher.

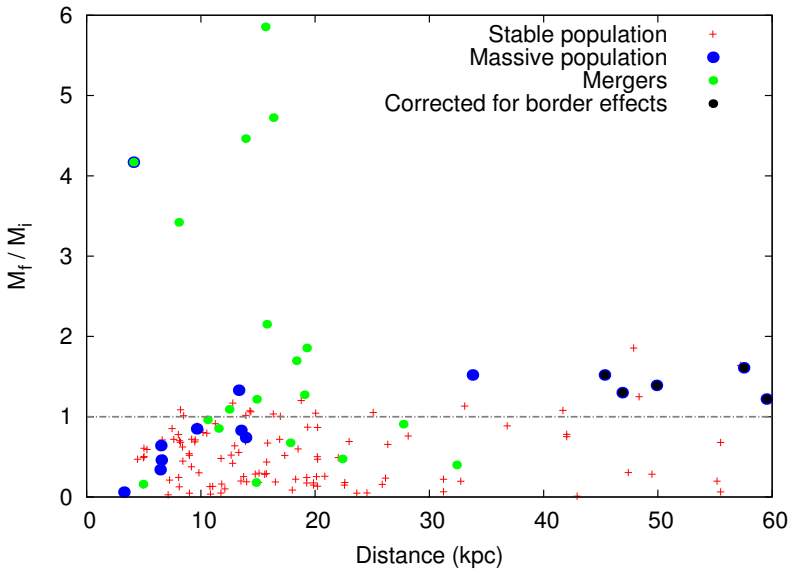


Figure 6.12: Cluster mass evolution as a function of the distance to the remnant. $M_i$ ($M_f$, respectively) is the cluster mass at the beginning (end, respectively) of the simulation.

retrograde galaxies follow different types of trajectories. Those formed in the retrograde galaxy stay closer to their progenitor galaxy and end orbiting around the remnant. Those formed in the prograde galaxy tend to be expelled along with the gas and star particles and end up in the long tidal tails, especially at their tip. The location of the massive clusters at the end of the simulation is shown in Fig. 1 of BDE08. Placed on "safe orbits", with small eccentricity and at large distance from their parents, clusters can survive during 2 Gyr, as shown by simulations of BD06. The weakness of the disrupting tidal field on such orbits is likely to help them to survive over a long period of time (Renaud & Gieles, in prep.).

Finally, we highlight the importance of the geometry of the collision, especially of the galaxy orbit, on the efficiency of the cluster formation. The prograde galaxy forms less than half the number of clusters as the retrograde galaxy, but its clusters are more massive on average. This difference of response is likely to be a direct consequence of the spin-orbit coupling. As explained in Duc & Renaud (2012, and references therein) the net effect of the tidal field is seen for a longer time by the structures of the prograde galaxy than by those in the retrograde one, which results in the formation of denser substructures in the prograde galaxy.

## 6.4 Comparison with observations

### 6.4.1 The formation of Globular Clusters, UCDs, cE and TDGs in mergers

SSCs, GCs, Ultra-Compact Dwarf Galaxies (UCDs) and TDGs are four classes of stellar objects that have been observed in the vicinity of interacting systems and at some point claimed to have been possibly formed in mergers (among other alternative scenarios). The physical connection between each sub-class is however actively discussed in the literature (starting with their

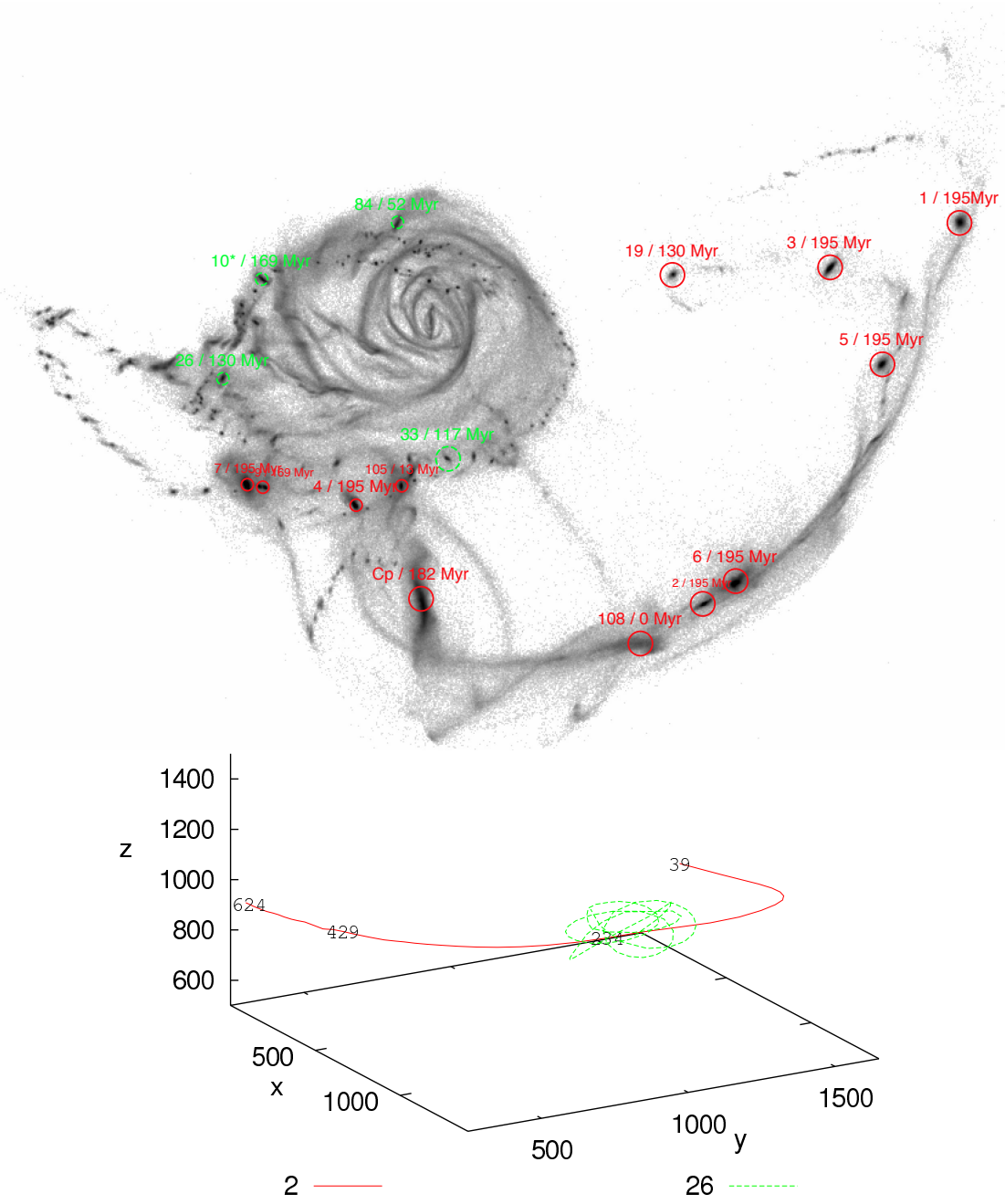


Figure 6.13: [Top] Same as Fig. 6.7, but at $t = 234$ Myr. An asterisk next to the cluster ID, means that the cluster was missed at this time step and was identified by eye. [Bottom] Projections of two typical cluster orbits: Cluster 2 belongs to the retrograde galaxy (green dashed line), Cluster 26 belongs to the prograde galaxy (red solid line). The numbers along the prograde orbit denote times in Myr.

definition and characteristics). They have in common a low dark matter content.

Are the surviving SSCs the progenitors of GCs? Are UCDs the high-mass end of GCs — implying that they were formed under the same physical conditions — (Mieske et al., 2012) or tidally stripped dwarf galaxies (Goerdt et al., 2008)? Do TDGs belong to the high-mass end of the stellar systems born in mergers? Some of these questions might receive a partial answer from the analysis of our simulation. The large variety of masses, sizes, kinematic properties of objects that formed all along our simulated merger might indeed correspond to the variety of observed systems described above. We discuss here whether physically distinct classes of objects formed during the simulation, and whether they might correspond to different classes of real observed stellar systems. Conversely, this analysis will allow us to determine how objects apparently as different as GCs, UCDs or TDGs may be formed during a single merger.

GCs, UCDs and TDGs occupy distinct positions in fundamental planes, such as the stellar mass versus half-mass radius. Misgeld & Hilker (2011) gathered on such a diagram a comprehensive collection of stellar objects. Fig. 6.14 displays its analogue for our simulation: the total stellar mass of the clusters are plotted against their half-mass radius at the end of their growth phase[5].

When considering only clusters with $r_{\rm h}$ above 100 pc (i.e., about 3 times the softening length), it is striking to note that:

- a few low-to-intermediate mass clusters (with mass range $10^6 - 10^7 {\rm M}_\odot$) have half-mass radii larger than the most massive clusters ($10^8 {\rm M}_\odot$), up to 200 pc. They occupy the locus of Local Group dwarf Spheroidal galaxies (LG dSph).

- the spatially resolved massive clusters have effective sizes just above 100 pc, placing them between the locus of compact ellipticals (cE) and UCDs. Unfortunately, the progenitors of GCs, with half-mass radii smaller than 10 pc, are below the resolution limit.

Looking at the upper-end of the cluster size distribution, one may conclude that our simulation was able to produce at least a few objects ($\sim 10$) with structural properties similar to dwarf ellipticals (dE) and LG dSph. Like observed dSph, they are slowly rotating objects, with moderate to low $v_{\rm rot}/\sigma$. Whether some LG dSph surrounding the Milky Way and the Andromeda galaxies may be of tidal origin has been discussed in the literature (see Metz & Kroupa 2007 and references therein). Recently, old ($1 - 2$ Gyr) TDG candidates, with light profiles similar to dEs were found near a massive elliptical galaxy (Duc et al., 2011).

Among the clusters formed in the merger, only one actually resembles the typical gas-rich, star-forming and (fast-) rotating TDGs observed in young merging systems, such as Arp 245, NGC 7252 or Arp 105 (Duc et al. 2000; Belles et al., in prep.; Duc & Mirabel 1994): cluster ID 108 (see Fig. 6.13). This is a cluster born later than all the other massive clusters and which was able to sustain a rotation pattern until the end of the simulation (with a rotation velocity of about 10 km s$^{-1}$, see Fig. 6.11). Cluster 108 was formed in a tidal tail and accreted about 50 per cent of its initial mass during the 600 Myr following the growth phase, reaching a mass of about $1.3 \times 10^8$ M$_\odot$ at the end of the simulation.

Many of our simulated SSCs occupy the region of the fundamental plane between the two branches delineated by the cEs / UCDs / GCs and the dEs / LG dSph, respectively. This region

[5]Due to the limitation of the simulation, especially with respect to the determination of the cluster size evolution, a similar analysis at the end of the simulation would not be meaningful. Indeed (1) the cluster dynamical evolution is stopped at a pseudo-equilibrium, as shown by BDE08 – half-mass radii have been corrected by the typical 2/3 factor (see Fig. 6.9); (2) The gravitational potential being computed in 128 pc-wide cells (in the most unfavourable case), internal dynamics (including rotation motions, or tidally induced effects) of clusters smaller than $\sim 500$ pc, and their secular evolution, is potentially unrealistic.

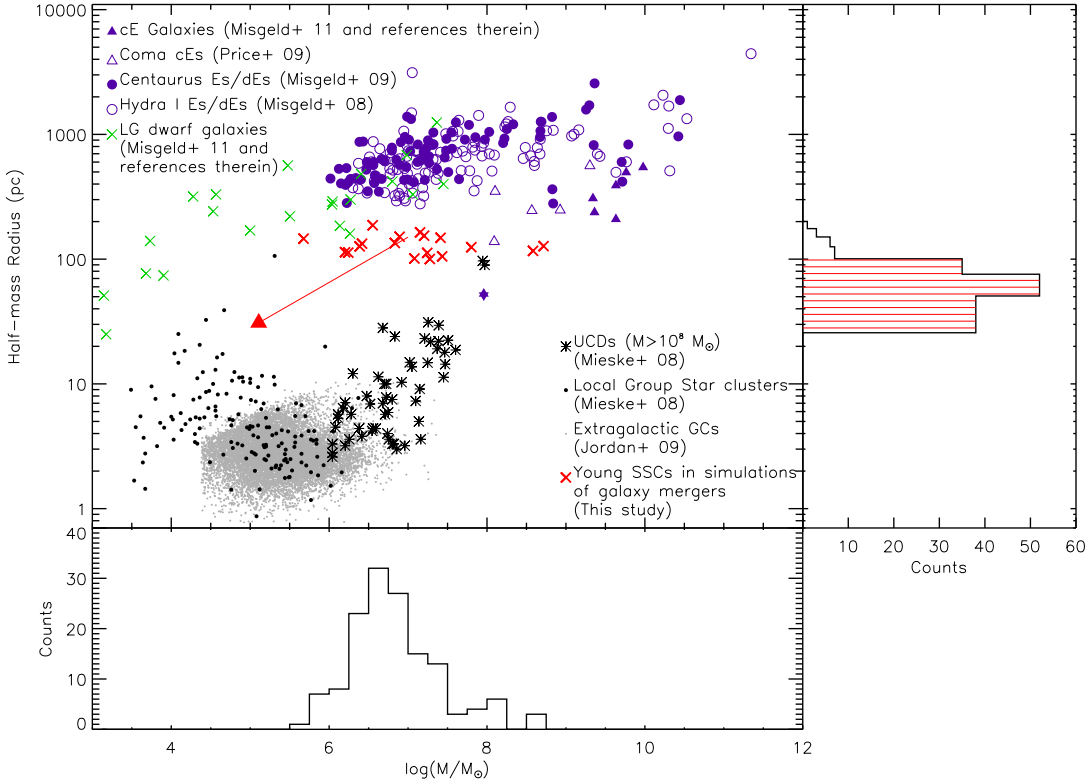


Figure 6.14: Half-mass radius, $r_{\rm h}$, versus stellar mass of our sample of simulated stable clusters 125Myr after their detection. The corresponding histograms are plotted along each axis. Observed dynamically hot stellar objects from the compilation made by Misgeld & Hilker (2011) have been added on the diagram. Clusters that are potentially affected by resolution effects have not been shown. They are however represented in the histogram of $r_{\rm h}$ encompassing the area highlighted in red. The red arrow represents a possible direction for the evolution of the clusters affected by tidal disruption and experiencing a mass loss of 99 per cent.

of the plane is poorly populated by real evolved stellar objects. This could either mean that our simulation is not realistic – the resolution is not good enough to get a reliable measure of the mass and effective radius – or that the present location of the simulated clusters on this fundamental plane is only temporary: they will later on either be totally destroyed or have their mass and radius evolve in such a way that they reach one of the two observed branches. We further speculate here on the existence of a segregating process leading to a mass gain (or at least which can keep the mass constant) for some clusters and a mass loss for others, resulting in two separated groups of objects.

In our simulation, the two evolutionary tracks appear as a natural consequence of the spatial segregation. On the one hand, the most massive clusters formed very early, in the prograde galaxy. At the epoch probed by the simulation, they already share similar structural properties with cE or UCDs. Once ejected in the tidal tails they will keep their mass or slightly increase it, and stay on the same branch of the $M - r_{\rm h}$ diagram. At large distances from the remnant, they are likely to survive for at last several Gyr. On the other hand, the SSCs that will stay in the central regions will face severe tidal interactions, leading to (1) a mass loss of about 2 order of magnitudes — 99 per cent of the initial mass according to Kroupa (1997); (2) an homologous contraction: during the mass-loss dominated regime the clusters are expected to contract such that $r_{\rm h} \propto M^{\alpha} R_G^{2/3}$ (Gieles et al., 2011), where $R_G$ is the galacto-centric radius and[6] $\alpha = 1/3$. The resulting evolution of the clusters under this process is indicated by the red arrow in Fig. 6.14.

### 6.4.2 Mass and Luminosity Functions of the clusters

We have seen above that the excess of high mass clusters in the simulated CMF corresponds to real structures, such as massive SSCs or TDGs. Is however the *global* shape of the CMF, and in particular the power-law index, realistic?

Fig. 6.15 (top) presents the power-law index of the CMF as a function of the merger stage. It was computed fitting the CMF for each snapshot. Globally the power-law index varies only weakly during the interaction, having a mean value $\alpha \sim -1.8$, in agreement with the values found for young star cluster populations in the few galaxy mergers in which it could be determined: between $-1.5$ and $-2.0$ (See Miralles et al., in Appendix A). Unfortunately the determination of the mass of stellar clusters is not straight-forward and requires expensive multi-band photometry. On the other hand, data for the Cluster Luminosity Function are available for many more systems. In particular, as mentioned earlier, several studies have been trying to connect the CLF of young SSCs in interacting systems (a power law of index -2) with the CLF of the GC population associated with elliptical galaxies (a log-normal distribution).

This was the motivation for estimating the Cluster Luminosity Function (CLF) from our simulated CMF. Converting masses into light (or vice versa) requires the use of stellar population synthesis models. We refer to Section 3.2.2 of the paper given in Appendix A for a detailed description of the methodology used to convert the cluster masses into luminosities. We took into account the clusters' Star Formation History (SFH), considering two different phases: the growth phase and the steady phase (as given by Fig. 6.3) and the different stellar populations (i.e. different stellar ages) that result from it. We assumed a solar metallicity, consistent with observations of tidal tails (Duc & Renaud, 2012). The luminosities were derived for the *HST* F435W ($B$) and F814W ($I$) photometric bands, which are often used for SSC studies.

We compared our simulated CLF with that determined by Miralles-Caballero et al. (2011) –

[6] Given the way our clusters were defined, a value of $\alpha = 1/6$ also hypothesised by Gieles et al. (2011) is less probable.

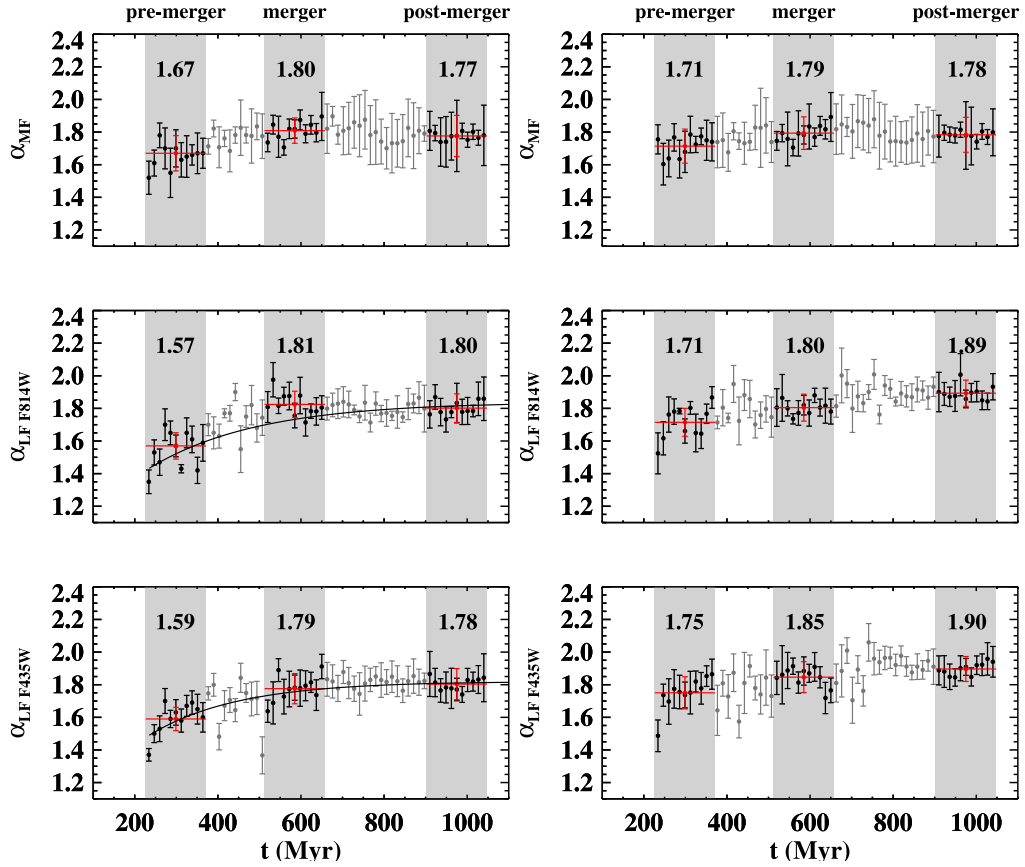


Figure 6.15: Evolution of the power law index of the simulated CMF (top) and the CLF for the F814W (middle) and F435W (bottom) filters. The red crosses, together with the numbers displayed above, represent the median values over interaction phases indicated by the shaded areas. Left panels take into account all the clusters whereas right panels exclude the youngest clusters (i.e., those that appeared over the past 13 Myr) (adapted from Miralles et al., 2012).

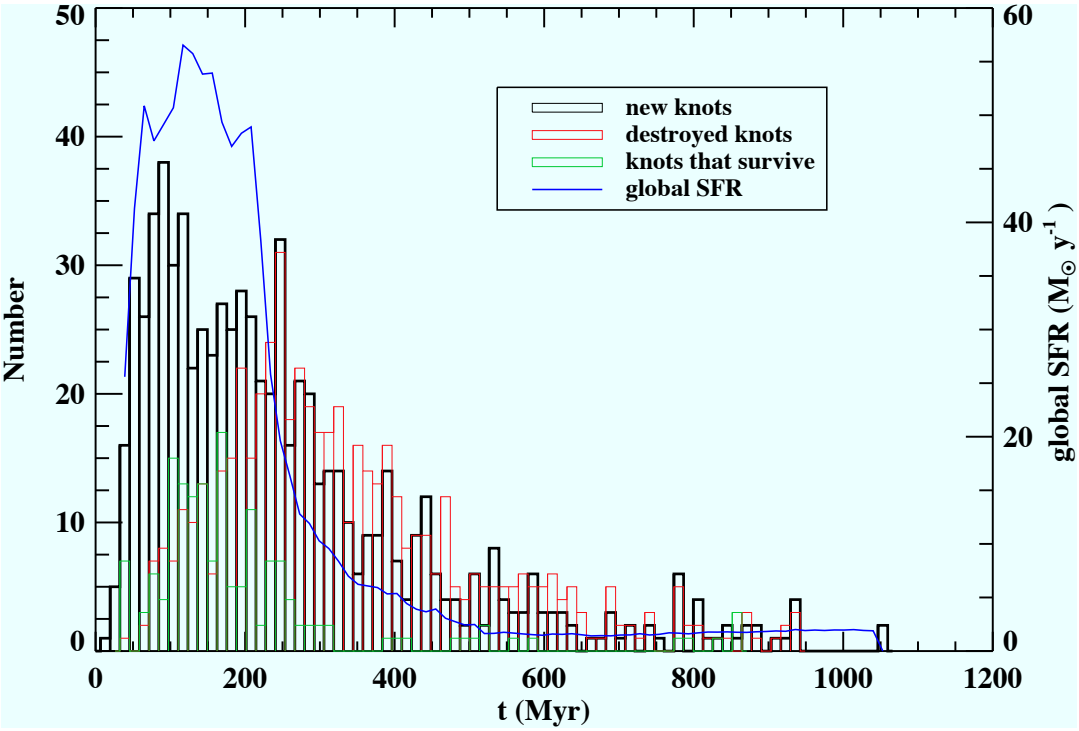


Figure 6.16: Global Cluster Formation Rate (black histogram) and Destruction Rate (red histogram) as a function of time. The Stable CFR is shown in green whereas the blue line shows the Global SFR (adapted from Miralles et al., 2012).

hereafter MC11 – for a sample of 32 nearby (Ultra-)Luminous Infrared Galaxies[7] –(U)LIRGs – all involved in an on-going merger. MC11 identified on F435W and F814W *HST* images a high number of young compact stellar clusters, and computed for each system the Cluster Luminosity Function. Their sample turns out to be particularly suited for a comparison with our simulated SSCs: a similar spatial resolution ($\sim 30$ pc), similar selection of systems with high SFRs hence probably high-mass star clusters, and similar availability of a time sequence: the (U)LIRGs were classified according to their phase of evolution (pre-merger, merger and post-merger) based on their morphology, with enough systems per phase to follow any possible evolution of the CLF.

MC11 noted a slight steepening of the CLF as a function of the merging stage, which, as shown by Fig. 6.15 (middle, bottom) seems to be also reproduced in our model. How to interpret this steepening, in light of the simulations?

The young star cluster population (with typical ages $< 20$ Myr) being more luminous than the old population (with typical ages $> 100$ Myr) by up to a factor 100, they are likely to drive the evolution of the LF. The flattening of the curve $\alpha(t)$ when the young clusters are excluded from the fit (see right panel of Fig. 6.15) supports this explanation.

Stable clusters are massive and luminous clusters, but are not the dominant cluster population. 6.16 shows the evolution of the overall Cluster Formation Rate (CFR) and Cluster Destruction Rate (CDR). The great similarity between the CFR and CDR after $\sim 500$ Myr,

[7] with infrared luminosity $10^{11}$ L$_\odot$ <= $L_{IR}[8-1000\mu\mathrm{m}]$ <= $10^{13}$ L$_\odot$

shown in 6.16, proves that a lot of short-lived clusters form. We counted only 163 stable clusters in the simulation out of a total of more than 800 clusters. This population of short-lived clusters, with only young stellar population, dominates the overall cluster population and drives the evolution of the CLF. During the early phase of the interaction, the CFR is especially high, so is the one of young clusters. The contribution of these young star clusters results in a flatter CLF.

### 6.4.3 Radial mixing

Galaxies exhibit a mass-metallicity relation (Lequeux et al., 1979): low-mass galaxies are metal poor whereas high-mass galaxies are metal-rich. The chemical enrichment of galaxies is directly linked to their star formation activity (via nucleosynthesis), coupled with gas inflows (from outside the galaxy) and outflows that prevent the further infall of gas (Dalcanton, 2007). Interestingly, central regions of interacting galaxies are found to be under-abundant in metals compared to galaxies on the mass-metallicity relation (Ellison et al., 2008; Peeples et al., 2009). Furthermore, strongly interacting galaxies have oxygen abundance depressed in nuclear regions and flattened metallicity gradients(Rupke et al., 2010a).

These intriguing observations are explained by the combination of two properties: (1) the progenitor galaxies exhibit a metallicity gradient, with low metallicities in the outer disc and high metallicities in the inner regions (Zaritsky et al., 1994); (2) during a galaxy merger, gravitational torques drive gas from the outskirts of galactic discs to the central regions (see Sect. 5.1). As a result, the metallicity of inner regions is diluted by the infall of metal-poor gas (Rupke et al., 2010b; Di Matteo et al., 2011) and the metallicity gradient is flattened (Rupke et al., 2010b; Perez et al., 2011).

Our simulation reproduces the important radial mixing of the ISM during the collision. It may be traced by the different trajectories of the clusters, used as test particles (see bottom panel of Fig. 6.13). The expulsion of material from the inner to the outer regions accounts for the high metallicities observed at large radii and thus for the flattening of the metallicity gradient.

The results we have presented thus far are drawn from a single simulation, with a specific star formation recipe and model for the gas particles. In the next sections we discuss the limits of our simulation and compare our results to those found by other (statistical) studies.

## 6.5 The limits of our simulation

### 6.5.1 The star formation recipe

The conversion of the single–phase gas into stars is computed using a Schmidt–Kennicutt law with an exponent 1.5. "Young" particles result from the transformation of gas particles during the merger; they trace the regions of high gas densities. Star formation occurs only in clouds with densities above some density threshold. The efficiency of the gas particles transformation into stars and the value of the density threshold are chosen to reproduce the Schmidt–Kennicutt law in nearby galaxy discs. Supernova feedback is taken into account with a simple description in terms of radial velocity kicks, which can threaten the stability of the structures. The star-formation and feedback recipes determine the Star Formation Efficiency (SFE) and the abundance of gas within the cluster. In observed TDGs, the bulk of the mass comes from the atomic hydrogen (see review by Duc & Renaud, 2012), even after several hundreds Myr of evolution. So, in principle, the gaseous content cannot be ignored in the total mass budget. We demonstrate here that, in our simulation, the SFE is unrealistically high and results in a rapid exhaustion of the gas

supplies associated with the cluster.

The growth phase of the cluster, i.e. the first $100 - 150$ Myr of a cluster life, corresponds to a period of active star formation: the mass can increase by up to 1.5 dex and corresponds to an increase in the number of young stars, as shown by the evolution of the ratio (number of young stars) / (number of old stars) given in Table 6.1. Once the cluster reaches the steady phase, star formation may still occur but at a much lower rate, showing that most gas supplies have been used up[8]. However, the growth phase is much longer than the free fall time[9]. Typically, the free fall time of a $10^8\,M_\odot$ cluster, which has a typical radius of 600 pc (see Fig. 6.9), is $\sim 20$ Myr. Which process accounts for these different time scales? Fragmentation is a first explanation. High resolution hydrodynamical simulations of mergers (e.g. Teyssier et al., 2010) predict gas fragmentation on small spatial scales. The idealised cluster simulations of Kroupa (1998) highlight the presence of individual star clusters within these SSCs. They are not observed in our own model, perhaps due to a lack of resolution and incomplete prescriptions for the feedback.

The highly efficient conversion of gas into stars is likely to be responsible for underestimating the growth phase duration and overestimating the stellar mass. There is evidence that the most massive star clusters observed around mergers, like W3 in NGC 7252, have mixed stellar populations, with age spreading over $300 - 500$ Myr (Schweizer & Seitzer, 1998; Maraston et al., 2001). This further indicates that the formation of clusters might be stretched over long periods. The TDGs themselves have rather long gas depletion time (see Fig. 8 in Braine et al., 2001), and thus a growth of their stellar mass much more sedate than predicted by the simulation.

In Sect. 9.2, our exploration of the SFR-Gas relation at the scale of individual (or a few) star-forming regions in real interacting systems, suggests that this relation may not be unique and may vary across the system. Spatial variations of the SFE are not reproduced by the single SFR-Gas relation used in the simulation to model the star formation process.

### 6.5.2 Model for the gas particles

The gas particles are simulated using an SP code, whereas most simulations use an SPH description of the gas component. As mentioned in Sect. 5.1, in an SPH code, a particle has a spatial extent over which its physical properties (density, temperature) are smoothed by a kernel function. In particular, heating and cooling of the gas can be taken into account in SPH simulations.

Saitoh et al. (2010) performed a SPH simulations of equal-mass, gas rich galaxy mergers. Like for our SP code, their model was able to produce massive star clusters (with masses between $10^6$ and $10^8\,M_\odot$). They derived a CMF consistent with a power-law with a slope of $-2$, close to ours. Extensive comparisons between between a Tree-SPH code and a grid-based N-body SP code, based on simulations of interacting systems have been made by Di Matteo et al. (2008). The star formation enhancement driven by disc fragmentation is reproduced similarly by both types of codes. In the case of SP codes, the efficiency of the gas dissipation process (related to the disc stability) is controlled by the parameter $\beta$. $\beta = 0.6$ ensures that the disc is stable for gas rich spirals, so the formation of massive clumps in BDE08 is not artificial.

More recently, Teyssier et al. (2010) performed a hydrodynamical simulation of a major merger, resembling the Antennae interacting system. Coupled with an Adaptive Mesh Refinement (AMR) technique, they could lower the spatial resolution down to 12 pc and resolve the

[8] when the cluster masses are measured (i.e. the initial mass) the gas mass fraction is negligible.

[9] $t_{ff} = \sqrt{\frac{3\pi}{32G\rho}}$

cooling of the gas in the densest structures, down to a few 100 K (the cooling rate increases with the gas density). The multiphase nature of the ISM could then be reproduced. Similarly to our simulation, the authors observed the formation of massive gas clumps with masses between $10^6$ and $10^8$ $M_\odot$, proving that the formation of massive clusters in the tidal tails of mergers would not be suppressed by working at this higher resolution.

Starbursts usually take place in the central parts of galaxies with retrograde orbits (see the statistical study by Di Matteo et al., 2007, including several hundreds of galaxy collisions, with different orbits, mass ratios, etc.), in agreement with the picture in which gas loses momentum by the effect of differential rotation (see Sect. 5.1). Although one galaxy in our simulation has a retrograde orbit, we do not observe any starburst in it. Instead, the star formation is sparser and more diffuse. Moreover, in our simulation, the SFH does not show the secondary peak often associated with the final coalescence (Di Matteo et al., 2008). Di Matteo et al. (2007) showed however that a great variety of SFH are found during mergers. For instance, the prograde (direct) encounter of 2 spirals, entitled "gSbgSb05dir00", shown in Fig. 8 of Di Matteo et al. (2007), exhibits a SFH similar to our case (star formation enhancement during the phase of approach, no starburst at their merger epoch). The same authors also state that pairs that undergo an intense tidal field at pericentre have low SFR during the merging phase. The orbital parameters of our simulation were specifically chosen to produce a strong disturbance of the galactic discs during the collision, so that they form massive clumps and extended tidal tails. Although meeting these encounter parameters all at once is not very likely in the real Universe, in its final stage, the simulated system shows a striking resemblance with the famous old–stage merger NGC 7252 (Hibbard et al., 1994; Hibbard & Mihos, 1995, Belles et al., in prep.), even though it was not tailored for that. This suggests that the simulation is not that unrealistic.

## 6.6 Summary

Compared to early works on the formation of clusters in mergers, the originality of our approach lies in the time tracking of the individual structures we were able to perform thanks to the high number of particles used in the simulation. We have access to a measure of various physical parameters (mass, size, kinematics and dispersion velocities, fraction of old/young stars) and their variation as a function of time. Especially, we could determine the location and epoch of formation of the clusters. This paper analyses the formation and evolution of the stable clusters, those which survived for at least 500 Myr (or so), and puts a particular focus on the most massive of them.

We draw the following conclusions:

- The method that we used — detection of the clusters on several 2D projected images of the young particles, tracking of the clusters in the 3D data cube based on the labelling of particles and their re-identification from one snapshot to another — proved to be particularly efficient and allowed a study of the temporal evolution of 163 stable clusters. For 15 of them, with the highest masses, the internal kinematics could be measured. The clusters produced by the merger show a large range of masses (a factor of 1000), corresponding to a large range of total sizes (factor of 10), and kinematic properties such as $v_{\rm rot}/\sigma$. The most massive clusters have the highest $v_{\rm rot}$, $\sigma$ and $v_{\rm rot}/\sigma$ ratio.

- The CMF measured at several epochs shows a possible secondary peak at M $\sim 10^8 M_\odot$, and thus the shape of the CMF may be described as "top-heavy". The *global* shape of the CMF is fitted by a power-law with an index of -1.8, which does not change significantly

with time, and is consistent with that measured in real systems. A Cluster Luminosity Function was derived from the CMF and compared to that determined in a sample of mergers with high star-formation rates observed with *HST*. The simulated and observed CMF present similar (weak) evolution as a function of the merger stage, corresponding to the ageing of the clusters.

- In our simulation, the main mass growth of the clusters occurs within $100 - 150\,\mathrm{Myr}$; it is due to the internal transformation of gas into stars, rather than mergers with other clusters. Only a few of these mergers, identified as a sudden mass increase in the mass curve, were found. After the acquisition of their initial, steady mass, the majority of clusters slowly lose mass; those pulled away to large galacto-centric distances along the tidal tails are more able to keep their mass.

- The Cluster Formation Rate follows the global Star Formation Rate (SFR), and peaks at pericentre passage. Thus, the most stable clusters were formed in the discs of the colliding galaxies, rather than in the collisional debris. There is strong evidence that the most massive clusters were born first, early-on during the collision, and preferentially in the prograde galaxy. This corresponds to locations and times when the velocity dispersion of the gas is high. These results support the model of Elmegreen et al. (1993) which predicts the initial formation of gas clouds with high Jeans mass in colliding systems, and their subsequent expulsion due to tidal forces. Observations of massive, young, Stellar Super Clusters (SSCs) in the discs of colliding galaxies like the Antennae are also consistent with this picture.

- By comparison with the observed stellar systems claimed to have been born in mergers, a tentative classification of the clusters based on their structural properties – mass and half-mass radius, was made. About ten clusters, with relatively high half-mass radii ($r_\mathrm{h} > 100$pc) and intermediate stellar masses, lie in the locus occupied by dwarf Elliptical (dEs) and dwarf Spheroidal (dSph) galaxies. Several massive ones ($\mathrm{M} > 10^{7.5}\mathrm{M}_\odot$) turned out to have smaller half-mass radii that bring them into the compact Ellipticals (cEs) and Ultra-Compact Dwarf Galaxies (UCDs) domain. In our simulation, only one stellar object – the only massive cluster born in-situ in the tidal debris – resembles the star-forming, fast-rotating, Tidal Dwarf Galaxies (TDGs) observed in young mergers. For the vast majority of the clusters with apparently small $r_\mathrm{h}$, the spatial resolution is too limited to directly compare their structural properties with those of Globular Clusters (GCs).

# Chapter 7

# The structure of the ISM in hydrodynamical simulations of mergers

Early simulations of the gas component in mergers (see Sect. 5.1) had put forward a possible dual mode of star-formation in mergers: the nuclear starburst is driven by gas infall in the central regions, while the extended mode of star-formation is fuelled by gas expelled along tidal tails. Each mode of star formation might have its own efficiency (see Part IV).

The recent hydrodynamical simulations made by the Saclay group (Teyssier et al., 2010; Bournaud et al., 2011) with the code RAMSES, analysed here, indicate that besides the gas dynamics governed by gravity torques, the gas turbulence might be key in understanding star-formation in mergers.

## 7.1 The role of turbulence

Hydrodynamical simulations based on AMR techniques model in detail the increase of the ISM turbulence in galaxy mergers, down to the pc scale (Teyssier et al., 2010; Bournaud et al., 2011).

The specifics of the simulation by Teyssier et al. (2010) relies on its ability to reproduce gas fragmentation into dense clouds down to masses of $10^6\,M_\odot$ and star formation therein. Star formation is triggered only above a gas density threshold $\rho_0$. The SFE of a dense cloud is a function of the free-fall time and is parametrised by a numerical efficiency factor $\epsilon$. $\rho_0$ and $\epsilon$ are calibrated using observations of nearby galaxies.

In interacting systems, the gas component is often predicted to be more turbulent than in an isolated disc. Fig. 7.1 shows a strong correlation between the SFR and the velocity dispersion of the gas during the merging sequence. This is likely to be, first, a direct consequence of the galaxy collision, which stirs the gaseous component, and second, an effect of the tidal force, which induces non-circular motions on short timescales in the galactic disc.

An increase of the velocity dispersion of the gas necessarily implies an increase in the Jeans length, the spatial scale characterising the size for which the gravitational energy budget and the turbulent energy budget of a cloud are balanced. The Jeans mass scales with $\sigma^4$, that is, a small variation of the gas turbulence can strongly affect the masses of the clouds that form in the ISM, and thus the ability to form massive star clusters.

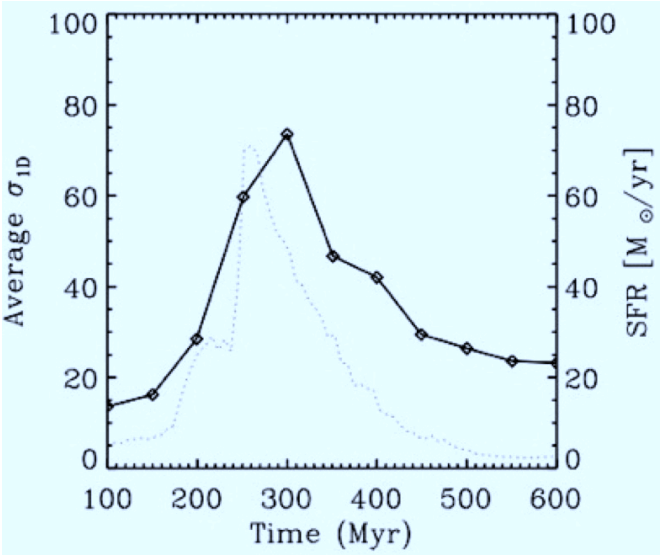


Figure 7.1: Evolution of the SFR and the velocity dispersion of the gas in a simulation of a galaxy merger (Bournaud et al., in prep.).

## 7.2 Impact on the shape of the PDF

The simulation shows that the starburst activity is actually dominated by a gas fragmentation process, with rapid star formation in the dense clouds. Interestingly, the starburst regime, i.e. the regime of enhanced star formation per unit of gas, is found to be mainly caused by the rapid evolution of the gas density PDF during the galaxy interaction. The difference between a starburst regime and a normal regime of star formation appears in integrated quantities (such as the PDF), not on small scale measurements (such as local gas densities).

Although the processes involved in the building of a multiphase ISM are various and complex (gas heating and cooling, supernova feedback, stellar feedback, self-gravity), the PDF of the density of an isothermal gas phase appears to be universal. Hydrodynamical simulations of isolated galaxies show that it has a log-normal shape (Vazquez-Semadeni, 1994), with a power-law tail in some cases (Passot & Vázquez-Semadeni, 1998). The left panel in Fig. 7.2 illustrates the gas density PDF of an isolated disc. The PDF can be decomposed into 3 different domains:

- the upper gas density side, usually traced in extragalactic observations by the HCN molecule (and subsequent forms of dense gas), made of star forming clouds (with short free-fall times);
- the lower gas density side, traced by the diffuse atomic hydrogen H I, where star formation is inefficient (the clumps are supported by thermal pressure);
- the intermediate gas density range, traced by the CO molecule.

In a turbulence dominated medium, such as a galactic disc, the full-width-at-half-maximum of the PDF scales with $\sigma$ (Passot & Vázquez-Semadeni, 1998), the velocity dispersion, which is between 5 and 10 $\mathrm{km\,s^{-1}}$ in the Milky Way. Given the temperatures of the molecular clouds (between 10 and 50 K) and of the cold neutral medium (between 80 and 100 K), the sound

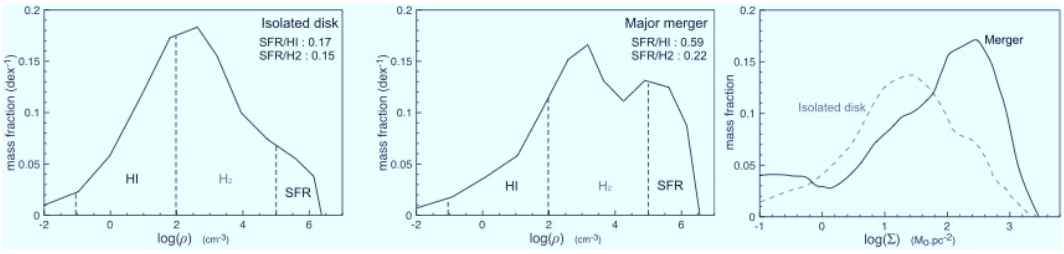


Figure 7.2: Probability Distribution Function (PDF) of the local 3D density in simulations of discs (left) and mergers (middle), measured in 1 kpc regions around star-forming knots. Increased turbulence in mergers leads to an excess of dense gas ($> 10^4\,\mathrm{cm}^{-3}$). Derived variations of the SFR/H I and SFR/$H_2$ ratios are indicated. Interestingly, they show variations higher for SFR/H I than SFR/$H_2$. Right: computed 2D surface density PDF of a merger simulation compared to an isolated disc.

speed in the ISM[1] is lower than $0.9\,\mathrm{km\,s}^{-1}$. As a result, converging flows are faster than the thermal pressure regulation and the molecular and neutral atomic gas phases are highly compressible (hence able to form stars). Often, the turbulence in galactic discs is described as being moderately-to-strongly supersonic.

Since the width of the density PDF and the gas turbulence are intimately related (see previous paragraph), interacting systems are expected to exhibit a different PDF than those found in discs. The increase of the turbulence in colliding galaxies is expected to transform the log-normal shape gas density PDF into a top-heavy distribution, i.e. a distribution with an excess of dense gas clumps. The high resolution hydrodynamical simulations indeed exhibit an excess of dense gas during the merger, as shown in the middle and right–hand panels of Fig. 7.2.

A direct measure of the PDF in real systems is still beyond our observing capabilities and discrete gas tracers, such as H I, CO or HCN, should be used instead. Interestingly, we note that the SFR/H I ratio is expected to increase more significantly during a major merger than the SFR/$H_2$ ratio. Thus, the SFR/H I ratio is a better tracer than SFR/$H_2$ of the *evolution* of the ISM structure as determined by the PDF, and indirectly of the SFE of the system.

This result is consistent with the claims of a universal SFR-$H_2$ relation (see for instance Leroy et al., 2008, who show that the $\Sigma_{SFR} - \Sigma_{H_2}$ relation is not, or at least weakly, dependent on the properties of the environment), implying that any variation of the efficiency of the star formation process does not originate from the molecular gas conversion into stars, but is more linked to the H I-to-$H_2$ transformation. Thus, if the $\Sigma_{SFR}/\ \Sigma_{H_2}$is constant, the variations of the star formation efficiency, a priori measured by $\Sigma_{SFR}/\ (\ \Sigma_{H_2} + \Sigma_{HI})$, can be probed by the key parameter $\Sigma_{SFR}/\ \Sigma_{HI}$.

This prediction from the numerical model turns out to be particularly convenient since H I maps of extended systems like mergers are much easier to obtain than CO maps. Indeed the millimetric antennas that survey the CO molecule have a much smaller field of view than the radio antennas used from H I, 21 cm, observations.

[1] $c_s = \sqrt{\frac{k_B T}{\mu m_p}}$ with the Boltzmann constant $k_B$, the temperature T, the molecular weight $\mu$, and the proton mass $m_p$

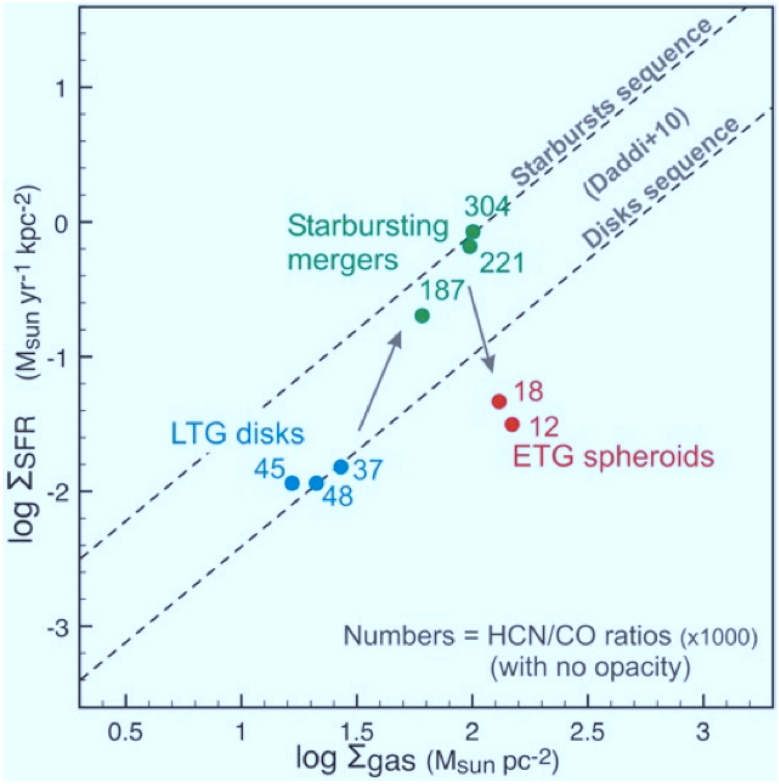


Figure 7.3: The Schmidt-Kennicutt relation as seen by numerical simulations. The evolution of the SFR and gas surface densities of several regions of simulated colliding galaxies are plotted as a function of the merging sequence, from the initial phases (LTG discs) to the post merger phase (ETG spheroids). Adapted from Powell et al., 2012, in prep.

## 7.3 Impact on the star-formation efficiency

In the introduction, we presented the scaling relation that exists between SFR density and gas surface density, the so-called Schmidt-Kennicutt relation. The universality of this relation has been recently questioned with the possible presence of a specific sequence of star formation associated to star-bursting merging galaxies, (Daddi et al., 2010b): mergers are extreme systems exhibiting the highest SFRs per unit of gas mass. They are also extreme because of the rapid change of their environment. Figs. 6.4 and 7.1 illustrate that the full episode of star formation can occur over only 200 Myr. Over this period, strong and rapid variations of the SFR of the system and of the properties of SSCs that form during the merger are observed (see Sect. 6.3). These changes translate in a rapid variation of the SFE or in an evolutionary track in the SK-diagram, which is convincingly reproduced in the numerical hydrodynamical simulation made with RAMSES (See Fig. 7.3). The interacting Late-Type Galaxies (LTG) are initially on the sequence of disc galaxies. Their star formation activity is enhanced during the merger, which place them on the sequence of starburst galaxies. Finally, after the collision, the system relaxes, the gas turbulence goes down and the star formation activity and efficiency of the system drops, reaching the level of Early-Type Galaxy (ETGs).

One prediction of the numerical simulation is an enhancement of the SFE in the whole system, and not only in the central regions where strong gas inflows occur. To check this, the SK-relation should be studied at local scales, i.e., in individual regions, within the merger. What is however the characteristic size one should reach to characterise the "local conditions"? There are physical motivations to consider the Jeans length, corresponding to the typical size of gravitationally unstable clumps – i.e. star forming regions, in the ISM. Observations of interacting systems often reveal structures like "beads on a string", i.e. successive star forming regions separated by a common length, generally $\sim 1\,\mathrm{kpc}$, matching the value of the Jeans length in the ISM of mergers (Elmegreen et al., 1993). 1 kpc also corresponds to the injection scale of turbulence (Elmegreen & Scalo, 2004).

In the following chapter, we check, on a sample of nearby colliding systems, the predictions of the hydrodynamical simulations presented here, in particular: (a) the increase of turbulence, as traced by the increase of the H I velocity dispersion as, (b) the increase of the SFR/H I ratio during the merger phase, and discuss the implication of these variations of the SFE on local scales.

# Part III

# The kpc-scale HI–SFR relation in galaxy mergers

# Chapter 8

# 21-cm line observations of three interacting systems

## 8.1 Sample selection

One of the goals of our project is to determine the origin of the deviations shown by mergers from the standard sequence defined by the SK-relation, in particular determine at which spatial scale any enhanced Star Formation Efficiency (SFE) occurs. The numerical simulations presented in the previous chapter provided us with specific predictions about the star formation conditions in mergers, for instance a global enhancement of the SFR/H I ratio. They further provided hints on what scale they should be checked: the kpc scale seemed physically motivated.

Reaching kpc-scale resolutions can be achieved thanks to radio-interferometers like the Karl G. Jansky Very Large Array (JVLA) with synthesised beam sizes down to 5″ (the B–array configuration of the VLA)[1] for systems at distances up to 40 Mpc. Coincidentally, 5″ turns out to be the typical resolution provided by two of the space telescopes commonly used to derive SFRs: *GALEX* (in the UV) and *Spitzer* (in the mid and far IR).

We selected a sample of interacting systems, in the local Universe, for which tracers of star formation and at least low-resolution radio H I maps were already available. If *GALEX* and *Spitzer* data are rather common, radio-interferometric observations are more rare. The H I rogues gallery[2] (Hibbard et al., 2001b), gathers an important collection of interacting systems observed with the VLA. We preferentially considered (1) interacting "isolated" galaxies located outside compact groups, to probe conditions as simple as those in our idealised simulations (2) major mergers, maximising the tidal disturbances (3) wet mergers, with abundant gas reservoirs, and thus likely enhanced star formation activity. We selected mergers at different stage of interaction, in order to identify any possible trends with merger stage.

Unfortunately, the number of systems matching these criteria being rather limited at distances below 40 Mpc, we were forced to consider systems with distances reaching up to 120 Mpc. In Section 10.1, we present the program that we initiated to expand our sample of interacting systems. 21 cm data obtained with the C (or C plus D) array configurations, which provide a

[1] The A-array configuration has too low sensitivity for H I studies; see Sect. 8.2.1 for further explanation of the VLA configurations

[2] available publicly at `http://www.nrao.edu/astrores/HIrogues/`

maximum angular resolution of $\sim 15''$, are already available in the archive for several systems, they must be complemented by data obtained with the B-array configuration. In addition to this, archival radio-observations often have "low" spectral resolutions ($20\,\mathrm{km\,s^{-1}}$ and above), which do not resolve the velocity dispersion of the ISM (typically of $7-10\,\mathrm{km\,s^{-1}}$ in a spiral galaxy). Our new observations have higher spectral resolution: up to $2.5\,\mathrm{km\,s^{-1}}$.

The work presented here relied on observations made of three systems: the well-known advanced merger NGC 7252 (also called "Atoms for Peace"), and 2 pairs of interacting galaxies, Arp 245 and Arp 105. Arp 105 is the most distant system, at a distance of 120 Mpc; the highest resolution achieved by the interferometer on this system sets the limiting linear scale of our study: $\sim 7.5''$ (equivalent to 4.5 kpc; see Sect. 8.3). A detailed description of each system is presented in Sect. 9.1.1. The on-going project Chaotic THINGS (PI: P.-A. Duc) is currently expanding this sample (see Section 10.1).

As more and more systems are included in our analysis, the most distant systems will eventually be treated as a separate group so as to lower this limiting linear scale down to the kpc-scale for the more nearby galaxy sample. In the mean time, our analysis was carried out at the 4.5 kpc scale, which is sufficient to isolate individual star forming regions or small groups of star forming regions. The data reduction is presented Section 8.3.

## 8.2 Image synthesis in radio-interferometry

This section aims at introducing the principles and the vocabulary necessary to understand Sect. 8.3 about the specific reduction techniques we applied to our H I data.

### 8.2.1 Basic principles of radio-interferometry

Diffraction theory teaches us how light is scattered when going through an aperture. Consider, for instance, the case of a circular aperture (like a radio-telescope), lit by a beam of parallel rays, propagating perpendicularly to the plane of the aperture. A lens is used to form the image of the light diffracted by the aperture. In the image plane of the lens we observe an Airy pattern. The radius of the central spot of this pattern is such that:

$$R = 1.22\frac{f.\lambda}{d} \tag{8.1}$$

where $\lambda$ is the wavelength of the incoming light, d is the diameter of the aperture and f is the focal length of the lens used to produce the image of the scattered light. Often, this radius is expressed as an angular size:

$$\theta \sim \frac{\lambda}{d} \tag{8.2}$$

where d is the diameter of the aperture, or radio dish. Simply considering this formula, one realises that, in order to increase the resolution of the instrument, i.e., to decrease $\theta$, the diameter must be increased. Cost and technical limitations limit the size of fully steerable radio telescopes about 100 m. The power of interferometry lies in the ability to coherently combine signals of independent telescopes, the resolution of the interferometer increasing as a function of the *distance* between telescopes (also known as baseline). The era of large arrays of telescope was born from this simple idea: ALMA, e-MERLIN, JVLA, LOFAR, ASKAP, MeerKAT, SKA and so on.

The building block of modern interferometers is a two-element interferometer. A good analogy is Young's slit experiment. This teaches us how light diffracted by two apertures produces an interference pattern, so-called "fringes". The width of the central fringe of the pattern is related to the wavelength $\lambda$ of the incoming light and the distance D of the two apertures:

$$\theta \sim \frac{\lambda}{D} \tag{8.3}$$

An interferometer is made of antenna pairs, whose input signals are multiplied in a (digital) correlator[3]. A modern interferometer consists of dozens of individual antennae, creating the possibility of creating instantaneously hundreds of interferometer pairs. They sample what is known as the spatial coherence function (also called a spatial auto-correlation function or visibility function) of an electric field $\boldsymbol{E}_\nu$. For an electric field of intensity $I_\nu = \|\boldsymbol{E}_\nu\|^2$, which is the quantity we want to measure, the visibility function is defined as:

$$V(\tau) = \iint_{\Omega_{Source}} \boldsymbol{A}(\boldsymbol{\Omega}) \times I_\nu(\boldsymbol{\Omega}) \times e^{-2i\pi\nu\tau} \, \mathrm{d}\Omega \tag{8.4}$$

where we used:

- $\boldsymbol{\Omega}$ a vector that points in a particular direction of the sky; it will be referred to as the phase tracking centre;
- $\boldsymbol{A}(\boldsymbol{\Omega})$ the antenna response, also called primary beam or normalised reception pattern. The antenna responses are supposed to be the same;
- $\Omega_{Source}$ the astrophysical source solid angle;
- $\tau$ is a geometrical delay introduced to ensure that the signal hits the detectors in both telescopes at exactly the same time.

$\tau$ depends only on the relative positions of the antennae, expressed through the baseline vector (or antenna separation vector) $\boldsymbol{B}$:

$$\tau = \frac{\boldsymbol{B}.\boldsymbol{\Omega}}{c} \tag{8.5}$$

Interferometry consists in measuring $V(\tau)$ and inverting Eq. 8.4 in order to derive $I_\nu(\boldsymbol{\Omega})$. This is known as the Van Cittert-Zernike theorem. In a well-chosen coordinate system, and under some conditions, this relation can be reduced to a simpler form. Traditionally, the source direction[4], $\boldsymbol{\Omega}_0$, which is defined as a unit-vector, is used to define the normalised coordinate frame $(\boldsymbol{u}, \boldsymbol{v}, \boldsymbol{\Omega}_0)$. In this coordinate frame, $(\boldsymbol{u}, \boldsymbol{v})$ is the tangent plane to the source direction, i.e., the plane on to which the celestial sphere projects when looking in the source direction. We express $\boldsymbol{\Omega}$ as $\boldsymbol{\Omega} = (l, m, n)$, and the baseline vector $\boldsymbol{B}$ in units of the wavelength of observation, $\lambda$:

$$\boldsymbol{B} = \lambda(u, v, w) \tag{8.6}$$

Then, the visibility function can be expressed as:

$$V(u, v, w) \propto \iint \boldsymbol{A}(l, m) \times I_\nu(l, m) \times e^{-2i\pi(ul+vm+wn)} \, \mathrm{d}l \, \mathrm{d}m \tag{8.7}$$

[3] A correlator is an electronic device made of a voltage multiplier and an integrator.
[4] Note that, a priori, $\boldsymbol{\Omega}$, the phase tracking centre, can be different from $\Omega_0$, the target direction.

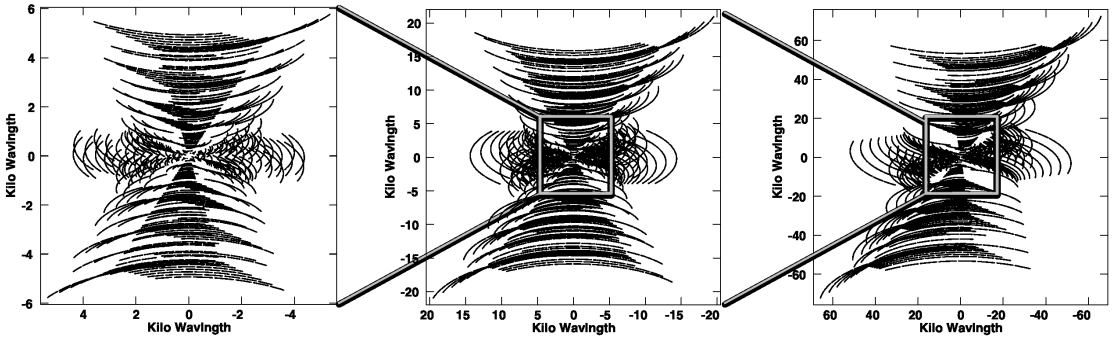


Figure 8.1: Examples of *uv*–coverage by the D-array (left), C-array (middle) and B-array (right) configurations of the JVLA. Each segment of this plane, symmetric with respect to the origin, corresponds to the *uv*–components measured by one baseline. The length of each segment is a function of the duration of the observations.

which has the form of a Fourier Transform, involving the spatial variables (l,m) and their conjugates in the Fourier domain, the (u,v) spatial frequencies. Inverting the relation 8.4 then boils down to taking its Fourier Transform and interferometry consists in creating an image from measuring its Fourier Transform.

The $(\boldsymbol{u}, \boldsymbol{v})$ plane is defined to be perpendicular to the target's direction; it represents the Fourier domain in which the visibility function is measured and is often referred to as the *uv*–domain. The coverage of the *uv*–domain is ensured by (1) there being various baselines involved in the interferometer, characterised by different baseline lengths (2) the Earth rotation, which changes the source direction hence the projected baselines (orientation and distance) between the antennae. An example of *uv*–coverage is given in Fig. 8.1. The JVLA can adopt different configurations, each configuration allows one to probe different regions of the *uv*–domain. The standard configurations of the JVLA and the effective resolution at 21–cm wavelength are:

- the D-array configuration with a maximum arm length of 1.03 km, corresponding to angular scales down to $46''$
- the C-array configuration with a maximum arm length of 3.4 km, corresponding to angular scales down to $15''$;
- the B-array configuration with a maximum arm length of 11.1 km, corresponding to angular scales down to $4.5''$;
- the A-array configuration with a maximum arm length of 36.4 km, corresponding to angular scales down to $1.3''$;

The baseline lengths of the configurations scale approximately by a factor 3.

What is the physical interpretation of a *uv*–component? In the formalism of interferometry, *uv*–domain and image domain are related by a Fourier Transform. The Fourier Transform extracts the periodic information contained in a signal. In the case of a signal periodic in time, the Fourier Transform of the signal corresponds to its temporal frequency spectrum. By analogy, in the case of a signal periodic in space, the Fourier Transform of the signal corresponds to its

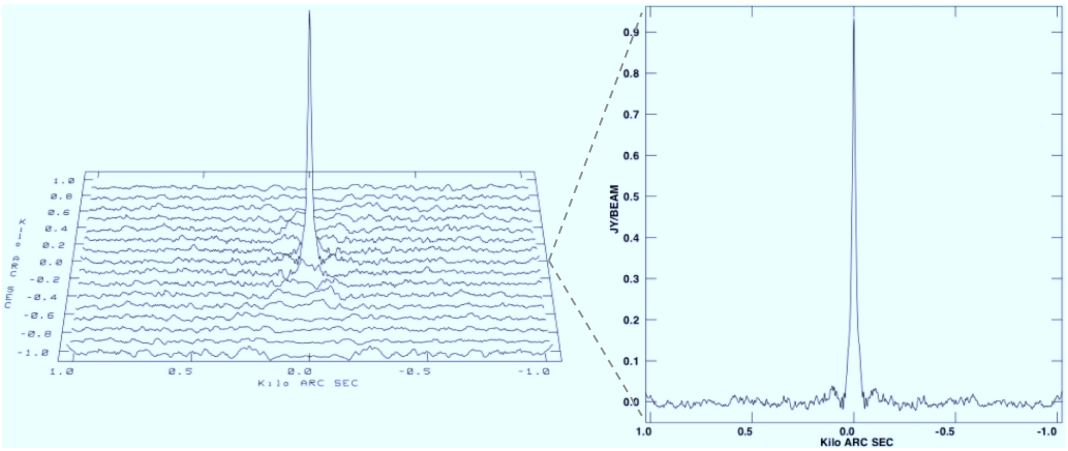


Figure 8.2: Representation of the synthesised beam in 2 dimensions (left) and along a slice including the peak (right). Note the presence of low-level oscillating wings in the response of the interferometer, known as side-lobes.

spatial frequency spectrum[5]. At the wavelength $\lambda$, baseline length and distance in the $uv$–domain are related by:

$$\frac{\|\boldsymbol{B}\|}{\lambda} = \sqrt{\boldsymbol{u}^2 + \boldsymbol{v}^2} \tag{8.8}$$

where we neglected the components of $\boldsymbol{B}$ along the axis pointing in the target direction. From Eqs. 8.3 and 8.8, we derive that angular sizes in the image domain and spatial frequencies in the $uv$–domain are inversely correlated: large spatial scales corresponds to low spatial frequencies.

In Fig. 8.1, we observe that the $uv$–domain is only *partially* covered; this means that the spatial information contained in the source is partially retrieved. That is the cost of interferometry: the full spatial information of the source can not generally be measured. Yet, the strength of interferometry resides in the possibility to reconstruct an image from a finite sample of points in the $uv$–domain.

Finally, some of the benefits of image synthesis in radio interferometry is that the phase centre can be shifted or that the $uv$–data can be arbitrarily weighted *after the correlation of the data*. Two types of weights are common:

- a "natural" weighting, in which the weights depend on the signal to noise ratio of the data. This weighting generally brings out extended structure, since the density of $uv$–data is higher for short baselines (so large scales) than long baselines (see Fig. 8.1);
- a "robust" weighting, in which the weights can be chosen to either enhance the contribution of large baselines (i.e., small scale structures) or the contribution of small ones (i.e., large scale structures). The robust weighting is parametrised by the ROBUST parameter: the smaller the ROBUST parameter, the larger the weights of large baselines.

### 8.2.2 Cleaning algorithm, synthesised beam and primary beam

The image obtained after Fourier Transformation of the visibilities in the *uv*-plane corresponds to the brightness distribution on the sky convolved with the Point Spread Function of the interferometer, which is the response of the interferometer to an ideal point-like source. In interferometry, the Point Spread Function is rather called the "synthesised beam". An example of the shape of this synthesised beam is given in Fig. 8.2. Because of its imperfections (such as side-lobes and diffraction rings), the synthesised beam is referred to as the "dirty beam", and the convolved image as the "dirty image". An algorithm of image deconvolution is then applied to "clean" the dirty image: the cleaning algorithm.

The cleaning algorithm is designed to give the best *representation* of the sky, by modelling the emission with a series of peaks, overlaid on a noise-dominated background. The algorithm can be described as a two-step process:

- (1) peaks of emission are identified and subtracted from the dirty image, each emission peak represented by a scaled version of the dirty beam, until all emission has thus been removed and only noise is left; this is the residual map. The emission peaks are delta functions and are referred to as "clean components";
- (2) the clean components are convolved with a "clean beam" (or "restoring beam"), which is an elliptical Gaussian fit to the central region of the dirty beam. They are subsequently added to the residual map. After this operation, the final image is obtained: the "clean image".

In addition to the synthesised beam, the interferometer is characterised by another beam: the primary beam. This beam represents the large-scale response of the individual elements making up an interferometer and quantifies the decrease of the sensitivity towards the edge of the field of view. In the case of the JVLA, the width at half-maximum of the primary beam is $\sim 32'$.

## 8.3 Data reduction and calibration

These data were taken during the upgrade of the VLA to the Extended VLA (EVLA). In this paper we refer to the instrument as the VLA, the retrofitted antennae as EVLA antennae, and non-retrofitted antennae as VLA antennae. This emphasises the hybrid nature of the instrument and distinguishes it from the far more powerful JVLA it has become since 2012.

The H I observations were carried out in spectral-line mode and their reduction performed with the AIPS software[1] (Greisen, 2003). The relevant observing parameters are given in Tables 8.1, 8.2 and 8.3 for each system, NGC 7252, Arp 245 and Arp 105, respectively. In most cases, we used three array configurations: the D-array and C-array to probe low surface brightness and extended emission, and the B-array to probe higher surface brightness compact structures. B-array data are especially relevant for the study of small scale structures. Sometimes, hybrid configurations are used, like the compact DnC (arm length of 1.3 km with north arm of 3 km), the CnB (arm length of 3 km with north arm of 10 km) and the extended configuration BnA (arm length of 10 km with north arm of 21 km) to compensate for the foreshortening due to the object's low declination; or the CS configuration to partly substitute D-array observations. The

[5]Note that the $\boldsymbol{u}$ and $\boldsymbol{v}$ components are dimensionless distances, normalised as they are by the wavelength at which the observations were done.

[1]The Astronomical Image Processing System is a software package for calibration, data analysis, image display, plotting, and a variety of ancillary tasks on Astronomical Data. AIPS is copyrighted by Associated Universities, Inc. using the GNU copyright form.

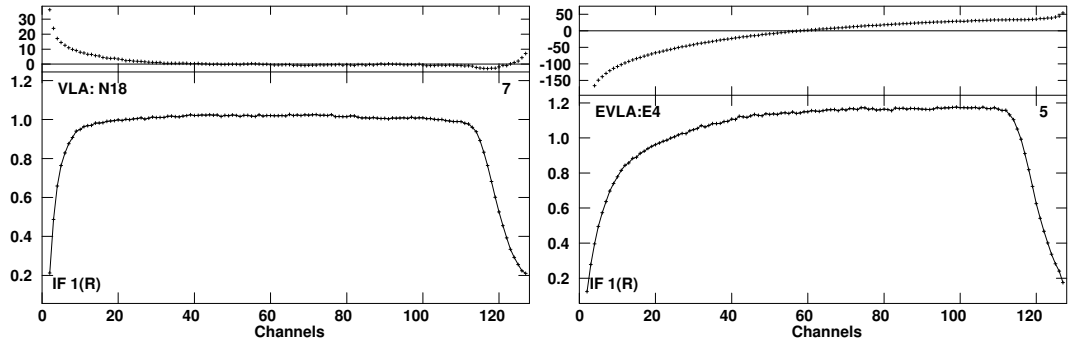


Figure 8.3: Spectral response of a VLA (left) and EVLA (right) antenna in amplitude gain (bottom) and phase (top). The amplitude gain is normalised by the value of the channel 0, the phase is computed relatively to a reference antenna. For the reference antenna (or for a phase-calibrated baseline), the phase is set to zero across the baseband. The channel width and reference velocity are that of IF1 of NGC 7252 observations (see Table 8.1).

exposure times were distributed in such a way as to compensate for the decreasing beam size (and so the decreasing surface brightness sensitivity). As a result, B–array observations require longer observations to approach the same sensitivity level as in the other configurations.

Calibrating the data means determining the amplitude scale (in flux density in units of Jy) and the instrumental phases (expressed as angles, in degrees). We address here only specific concerns inherent in our data set. Especially, one of the specificity of our observations was that they were made during a phase of transition of the VLA: the upgrade of the antenna receivers (EVLA antenna receivers), followed by the upgrade of the correlators. For an extensive description of the standard calibration, we refer the reader to the book Synthesis Imaging in Radio Astronomy II (Taylor et al., 1999) and to the AIPS cookbook.

### 8.3.1 Bandpass and amplitude calibrations

Since we are dealing with spectral line measurements, the passband of the instrument must be calibrated. The typical spectral responses of VLA and EVLA antenna receivers are shown in Fig. 8.3. One immediately notices the drop in sensitivity on the edges of the baseband. Because of this, about 1/8 of the bandwidth has to be cut on each side of the baseband, at the start of the process of data calibration. There is also a systematic difference between the bandpass shape of VLA and EVLA antennas. If uncorrected before doing the complex gain calibration, this would lead to large closure errors. This is why it is important to start the calibration with the bandpass correction.

AIPS generates automatically a single channel data, the so-called channel-0 (**CH0**), by averaging uniformly the 75% central channels. CH0 has a high signal-to-noise ratio (**SNR**), which is taken advantage of for amplitude and phase calibrations[6]. The CH0 provided by AIPS is created before any bandpass correction has been applied, so this is discarded and a new CH0 created (using the task AVSPC) with the bandpass correction applied.

At the time the observations of NGC 7252 were made, the VLA interferometer was being upgraded. The analog VLA-antenna front–ends were being replaced by new, digital EVLA ones, but the old correlator was initially being retained. This required the use of digital-to-analog

[6]The spectrum of the amplitude calibrator being flat across the relatively narrow bandwidth used or 21–cm spectral line observations, a frequency-independent calibration can be performed.

| | | | | | |
|---|---|---|---|---|---|
| Galaxies involved (Type) | NGC 7252 (E) | | | | |
| Phase centre[1] ($\alpha_{2000}$, $\delta_{2000}$) | ($22^h20^m40\overset{s}{.}0$, $-24°39'00''$) | | | | |
| Velocity centre (Heliocentric) | $\sim 4700\,\mathrm{km\,s^{-1}}$ | | | | |
| Primary Beam (FWHM) | $32'$ | | | | |
| Phase calibrator | 2137-207 | | | | |
| Flux calibrator | 3C48 (0137+331) | | | | |
| Array configuration | DnC[2] | CnB[2] | BnA[2] | DCB[3] | |
| Date | Jun 2008 | Feb 2008 | Sep–Oct 2007 (4 nights) | | |
| Bandwidth (MHz) | 1.56 (×2) | 1.56 (×2) | 1.56 (×2) | 2.3[a] | |
| Number of channels | 128 (×2) | 128 (×2) | 128 (×2) | 192[b] | |
| Central velocity of IF1 ($\mathrm{km\,s^{-1}}$) | 4827.63 | 4827.63 | 4827.63 | 4827.63 | |
| Central velocity of IF2 ($\mathrm{km\,s^{-1}}$) | 4572.48 | 4572.48 | 4572.48 | 4572.48 | |
| Channel separation ($\mathrm{km\,s^{-1}}$) | 2.6 | 2.6 | 2.6 | 2.6 | |
| Time on source (hr) | 2.9 | 5.0 | 16.0 | | |
| Weighting Function | | | | Natural | Robust[4] |
| Synthesised beam: | | | | | |
| - FWHM: Major x Minor axis | | | | $20\overset{''}{.}8 \times 15\overset{''}{.}3$ | $15\overset{''}{.}3 \times 13\overset{''}{.}6$ |
| - Position Angle: | | | | $56\overset{°}{.}6$ | $62\overset{°}{.}9$ |
| Velocity resolution ($\mathrm{km\,s^{-1}}$) | | | | 5.2 | 5.2 |
| Noise level per channel ($1\sigma$): | | | | | |
| - Flux density ($\mathrm{mJy\,beam^{-1}}$) | | | | 0.6 | 0.7 |
| - Column density ($10^{19}\,\mathrm{cm^{-2}}$) | | | | 0.54 | 0.83 |
| Conversion factor $T_b(K)/S$ ($\mathrm{mJy\,beam^{-1}}$) | | | | 1.90 | 2.91 |

[1] Corresponds to the location of the base of the NW tail

[2] The hybrid DnC, BnC and BnA configurations have an extended north arm allowing to compensate for the foreshortening of low declination southern sources like NGC 7252

[3] Short for DnC+CnB+BnA, corresponds to the combination of the data sets from the different array configurations

[4] For a value of the ROBUST parameter equals to 0.5

[a] Effective total bandwidth after combining the two IFs (see Sect. 8.3.1 for details)

[b] Effective total number of channels after combining the two IFs

| | | | | | | |
|---|---|---|---|---|---|---|
| Galaxies involved (Type) | North: NGC 2992 (Sa, Seyfert), South: NGC 2993 (Sab) | | | | | |
| Phase centre[1] ($\alpha_{2000}$, $\delta_{2000}$) | ($9^h45^m42\overset{s}{.}0$, $-14°19'35''$) | | | | | |
| Velocity centre (Heliocentric) | 2447.837 km s$^{-1}$ | | | | | |
| Primary Beam (FWHM) | 32′ | | | | | |
| Phase calibrator | 0902-142 | | | | | |
| Flux calibrator | 3C286 (1331+305) | | | | | |
| Array configuration | CS[2] | B | CB[3] | | | |
| Date | Sep. 1997 | Apr. 2001 (2 nights) | | | | |
| | | | High spectral resolution | | Low spectral resolution | |
| Bandwidth (MHz) | 3.125 (×2) | 1.56 (×2) | 2.6[a] (+1.7 only C) | | 2.6[a] (+1.3 only C) | |
| Number of channels | 32 (×2) | 64 (×2) | 175[b] | | 41[b] | |
| Channel separation (km s$^{-1}$) | 21.0 | 5.2 | 5.2 | | 21.0 | |
| Time on source (hr) | ∼ 5.6 | ∼ 9.0 | | | | |
| Weighting Function | | | Natural | Robust[4] | Natural | Robust[4] |
| Synthesised beam: | | | | | | |
| - FWHM: Major x Minor axis | | | $15\overset{''}{.}61 \times 11\overset{''}{.}34$ | $7\overset{''}{.}17 \times 4\overset{''}{.}76$ | $11\overset{''}{.}66 \times 7\overset{''}{.}92$ | $7\overset{''}{.}17 \times 4\overset{''}{.}76$ |
| - Position Angle: | | | $-4\overset{°}{.}0$ | $-0\overset{°}{.}4$ | $-4\overset{°}{.}64$ | $-3\overset{°}{.}38$ |
| Noise level per channel ($1\sigma$): | | | | | | |
| - Flux density (mJy beam$^{-1}$) | | | 0.27 | 0.41 | 0.21 | 0.26 |
| - Column density ($10^{19}$ cm$^{-2}$) | | | 0.88 | 1.32 | 5.28 | 17.68 |
| Conversion factor $T_b(K)/S$ (mJy beam$^{-1}$) | | | 3.42 | 17.76 | 6.56 | 17.76 |

[1] Corresponds to the location of NGC 2992

[2] The CS configuration is close to the C configuration. Some antennae are placed at locations usually employed for the D configuration, which provides a better sampling of short spacings, obviating the need for D-array observations. These observations have been published by Duc et al. (2000). However, the data were affected by strong solar interference, which led us to apply new data reduction techniques (see Sect. 8.3.3).

[3] Short for CS+B, corresponds to the combination of the data sets from the two configurations

[4] For a value of the ROBUST parameter equal to 0

[a] Effective total bandwidth after combining the two IFs (see Sect. 8.3.1 for details)

[b] Effective total number of channels after combining the two IFs

Table 8.3: Arp 105 VLA observations

| | | | | | |
|---|---|---|---|---|---|
| Galaxies involved (Type) | North: NGC 3561A (Sa), South: NGC 3561 (S0) | | | | |
| Phase centre[1] ($\alpha_{2000}$, $\delta_{2000}$) | ($11^h11^m11^s.738$, $28°41'41''.942$) | | | | |
| Velocity centre (Heliocentric) | $\sim 8700\,\mathrm{km\,s^{-1}}$ | | | | |
| Primary Beam (FWHM) | $32'$ | | | | |
| Phase calibrator | 1156+314 | | | | |
| Flux calibrator | 3C286 (1331+305) | | | | |
| Array configuration | D[2] | C[2] | B | DCB[3] | |
| Date | Nov 1993 | Oct 1994 | Apr 2001 (2 nights) | Full sensitivity | Lower sensitivity |
| Bandwidth (MHz) | 3.125 (×2) | 3.125 (×2) | 3.125 (×2) | 1.9[a] | 3.3[a] |
| Number of channels | 64 (×2) | 64 (×2) | 64 (×2) | 39[b] | 67[b] |
| Channel separation ($\mathrm{km\,s^{-1}}$) | 10.9 | 10.9 | 10.9 | 10.9 | 10.9 |
| Time on source (hr) | 4.0 | 13.0 | $\sim 14.0$ | | |
| Weighting Function | | | | Natural | Robust[4] |
| Synthesised beam: | | | | | |
| - FWHM: Major x Minor axis | | | | $10''.19 \times 9''.65$ | $7''.12 \times 7''.03$ |
| - Position Angle: | | | | -17°.52 | -86°.69 |
| Noise level per channel ($1\sigma$): | | | | | |
| - Flux density ($\mathrm{mJy\,beam^{-1}}$) | | | | 0.15 | 0.16 |
| - Column density ($10^{19}\,\mathrm{cm^{-2}}$) | | | | 1.84 | 3.84 |
| Conversion factor $T_b(K)/S$ ($\mathrm{mJy\,beam^{-1}}$) | | | | 6.2 | 12.1 |

[1] Corresponds to the location of the base of the South tail
[2] Improved data reduction; data have been published previously by Duc et al. (1997)
[3] Short for D+C+B, corresponds to the combination of the data sets from the different array configurations
[4] For a value of the ROBUST parameter equal to 1.0
[a] Effective total bandwidth after combining the two receiving bands (see Sect. 8.3.1 for details)
[b] Effective total number of channels after combining the two receiving bands

converters, which unfortunately introduced an aliased signal to enter the low frequency side of the basebands of EVLA × EVLA baselines. The aliased power was especially strong for narrow-band observations and affected mainly low-numbered channels in the L-band, i.e., the bottom 0.5 MHz of the baseband[7]. Fortunately, aliased signal does not correlate on VLA × EVLA baselines. Then, the issue of aliasing was simply solved by flagging all EVLA × EVLA baselines at the start of the data calibration process. Given that, at that time, 15 antennas out of 27 were EVLA antennas, (i.e., 15 × 14 / 2 baselines out of 27 × 26 / 2), this represented a cut of 30% in the initial data.

### 8.3.2 Phase calibrations

The standard way of calibrating the phases of interferometric data is performed by using an unresolved (i.e., point-like source), near the target. The standard calibration sometimes fails in determining the phase solutions accurately enough, which can translate into stripes and/or ripples in the image data cube. High *uv*–frequencies (sampled by the longest baselines) are more sensitive to phase errors than low *uv*–frequencies. Consequently, the longest baselines are harder to calibrate. A possible way to improve the phase (and amplitude gain) calibration is self–calibration, where the emission in he target field is used to improve the phase solutions in the calibration. Here we give a (non-exhaustive) list of some of the more common issues self calibration can deal with:

- the location of the phase calibrator is too far away from the target. The phase gain solutions are computed at the location of the phase calibrator. They are expected to be good approximations of the phase gain solution at the location of the target. But, when moving from the location of the phase calibrator to the location of the target, some drifts can be introduced in the solutions;
- the phase calibrator is not a point-like source, which is an issue more specific to B-array data. This situation can generally be avoided by applying restrictions on the *uv*–range to consider. These restrictions are given in the calibrator manual[8];
- the positions of the antennas might have slight residual errors leading to phase drifts;
- the physical conditions of the atmosphere vary quickly. In this case, the phase gain solutions, generally determined every 30 min, might not track the variations of the atmosphere;
- the phase calibrator is faint and the time-on-source is too short. A phase gain solution is computed per calibrator scan, by averaging the data over the duration of the calibrator scan. The effective duration (or time-on-source) of the calibrator scan depends on the duration of the antenna moves, but this is taken into account during observation scheduling (calibrator scans are always overestimated, so that the most unfavourable antenna positions, producing the longest slews, can still lead to reasonably long time-on-sources);
- Low-level artifacts are present and require a more accurate phase calibration. These artifacts can appear when a bright source is located near the target. In the case of NGC 7252, a 1.16 Jy bright source located in the south of the field, PKS 2217–251, at $(\alpha_{2000}, \delta_{2000}) = (22^h20^m37.65^s, -24°53'58.0'')$ created artifacts.

[7] see http://www.vla.nrao.edu/astro/guides/evlareturn/aliasing.shtml/ for further details.
[8] http://www.aoc.nrao.edu/ gtaylor/csource.html

B-array data are likely to benefit the most from self-calibration. The method consists in iteratively creating a model of the emission in the target field, using clean components (see Sect. 8.2.1 for a definition of the clean components) to represent this emission and to compute the phase solutions. As the source is in the same field as the target, any errors introduced by the antenna moves are avoided.

Initially, only the most significant features of the source structures are selected, low-level emission is ignored. The first set of calibration solutions is generated from this simplified model. In subsequent iterations the model is improved by the addition of further clean components and the process of self-calibration is iterated until no further improvement of the calibration is obtained. The quality of the calibration can be assessed at each iteration: attenuation (or even disappearance) of the stripes and ripples in the image plane, decreasing phase corrections to apply (otherwise, it means that the solution does not converge and the phase solutions can't be improved) and a decrease in the measured noise level, down to the thermal noise.

### 8.3.3 Other specifics

**Bandstitching and frequency matching (CVEL, UVGLU, AVSPC, SPECR)**

Performing high spectral resolution observations sets an important constraint on the setup of the correlator. At the time our observations were made, the VLA correlator capabilities (especially the sampling frequency) were such that achieving a $2.5-5.0\,\mathrm{km\,s^{-1}}$ resolution implied restricting the velocity range covered by each Intermediate Frequency (IF) to $\sim 320\,\mathrm{km\,s^{-1}}$. The sensitivity drop on the edges of the bandpass restricts this velocity range even more, down to about $\sim 250\,\mathrm{km\,s^{-1}}$ (see Sect. 8.3.1).

The systems under study are spread over a spectral window larger than $250\,\mathrm{km\,s^{-1}}$. A simple solution consists in splitting the incoming signal between two carefully centred IFs, so that they partially overlap in frequency and form a single continuous bandwidth covering $\sim 480\,\mathrm{km\,s^{-1}}$. Taking into account the deletion of channels on the edges of each IF, the central frequencies must be shifted by 3/4 of the spectral width. This technique is referred to as bandstitching and was applied specifically to each system. This overlapping the IFs requires that the data in the overlap region are carefully aligned in frequency.

**(1) NGC 7252** – When observing the H I line an adjustment needs to be made to the frequency at which the observation is performed to take into account the Earth's motion around the Sun (and to a lesser extent, its rotation around its axis). This is in addition to the frequency shift due to the recession velocity of the galaxy as a whole, its systemic velocity. Doppler tracking can be used to compensate for this additional frequency or velocity shift which can amount to $\sim 30\,\mathrm{km\,s^{-1}}$. Archival VLA data are taken with Doppler tracking enabled, but EVLA data are not. The correction for the Earth's radial velocity component must therefore be applied manually as part of the calibration of the mixed VLA-EVLA observations of NGC 7252. The task CVEL is used to shift the spectral line data to a given frequency. The task UVCOP extracts the required number of channels and the task UVGLU glues the two IFs into one. Note that Hanning smoothing was applied[9], which results in the spectral resolution being smoothed to $\sim 5\,\mathrm{km\,s^{-1}}$, corresponding to double the original channel width.

**(2) Arp 105** – In general, two polarisations (Right-hand and Left-hand polarised) are observed by each IF, ensuring an increase in sensitivity by $\sqrt{2}$ over a single polarisation observation.

[9] Hanning smoothing is applied to suppress "ringing" around sharp spectral features. After Hanning smoothing, the spectral resolution is twice the channel separation. In archival data, every other channel is discarded and the spectral resolution is equal to the channel separation.

However, at the time the observations of Arp 105 were made, the computational power of the VLA was too low to provide two polarisations at the spectral resolution and frequency coverage we wanted to achieve. So, only a single polarisation was observed which allowed an increase in total bandwidth for each IF, but at the cost of a decrease in nominal sensitivity. We again used bandstitching of overlapping IFs to cover the entire velocity range present in the system.

**(3) Arp 245** – The case of Arp 245 is specific for two reasons. First, the spectral resolutions of the C-array and B-array data were different. Before shifting the frequencies, the data were first brought to the same spectral resolution:

- either by averaging the B-array data in frequency, with AVSPC, resulting in a high sensitivity data cube;
- or by interpolating the C-array data and oversampling them, with SPECR, resulting in a high spectral resolution data cube. This assumes that, at the resolution achieved by C-array configuration, any structure in velocity (frequency) space changes smoothly from channel to channel.

Second, the spectral window covered by the B-array data is too narrow to allow the creation of a model of the continuum emission using the standard method. This point will be dealt with below.

### Continuum subtraction (UVLSF, UVSUB, BLANK, APCLN)

Traditionally,the continuum emission is modelled from emission line free channels. The continuum emission modelling can be performed either in the image plane (by using the task IMLIN) or in the *uv*–plane (by using UVLIN or UVLSF[10]). The continuum fitting often turns out to be more efficient in the *uv*–domain. When bright continuum sources are present in the field, which was the case for NGC 7252, they produce artifacts (ripples, stripes) that UVLSF failed to remove. Then, it is sometimes useful to subtract first the *uv*–components associated with these sources (with the task UVSUB), before fitting and removing the residual continuum with UVLSF.

Occasionally, the number of emission line free channels is too small to permit an accurate continuum emission modelling. This was the case for the B-array data of Arp 245. This can often be overcome by realising that the location of the emission coming from the target changes as a function of frequency/velocity. So, portions of the image data cube, corresponding to regions free from emission lines in some but not necessarily all frequency channels, are selected and averaged to create a model of the continuum. The noise level in the continuum map is no longer uniform across the field, but can be calculated based on the number of channels that contribute to the continuum map at each pixel. Regions of an image can be selected with the task BLANK. In addition, BLANK is used at the end of the data reduction process to select the regions of emission and create "blanked" maps (see Sect. 8.4).

At first sight, this method only allows a continuum subtraction in the image plane. However, this method can be adapted to generate a continuum model based on clean components that can be subtraction in the *uv*–domain. Firstly, a "dirty" image data cube is created containing both continuum and target emission. Target emission is then masked using the task BLANK. Then, averaging the planes of this masked dirty image data cube provides a dirty image of the continuum emission only, that can be cleaned in the image domain with the task APCLN. The

[10] UVLSF offers more options than UVLIN, especially the possibility of producing a *uv*–dataset of the continuum emission.

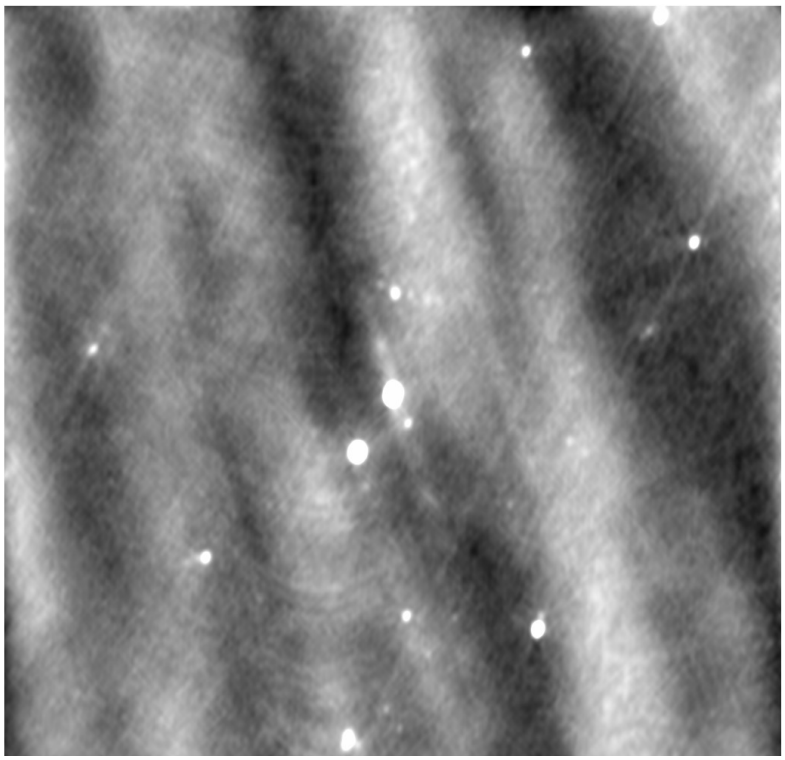

Figure 8.4: Image of data affected by solar interference (Arp 245)

clean components thus found are subtracted from the original data with UVSUB. Finally, low level continuum residuals are removed by iterating the creation of the continuum map once more, and subtracting this residual continuum in the image domain.

**Solar interference removal (UVFIX)**

When observations are made during daylight, solar radio emission can enter through one of the secondary lobes of the antenna pattern ($\boldsymbol{A}$, defined in 8.2.1) and contaminate the observed signal. Fig. 8.4 illustrates the effect this contamination has on a map. As the Sun is an extended source, short baselines of D-array (and sometimes up to C-array) are the most affected. In Fig. 8.5, we present the input power received at various baselines (calibrated in units of Jy) as a function of the distance in the $uv$–domain (expressed in kilo-wavelength). From Eq. 8.8, we derive that the longest baseline in C-array configuration, which is 3.6 km long, corresponds to $\sim 17\,\mathrm{k}\lambda$. The typical distance below which solar interference starts to dominate is $\sim 1.5\,\mathrm{k}\lambda$. This corresponds to baselines shorter than $\sim 320$ m. Using Eq. 8.3, we derive that the angular size of the solar regions producing the interference are larger than $2'.3$.

In the case of Arp 245, the amplitude of the solar interference in our maps was of order $1.0\,\mathrm{mJy\,beam^{-1}}$, more than three times higher than the noise level, $0.3\,\mathrm{mJy\,beam^{-1}}$. We managed to decrease its amplitude down to $\sim 0.5\,\mathrm{mJy\,beam^{-1}}$ (without having to flag a considerable amount of data which would have caused a significant increase in the noise level and the loss of information on extended structures in our target). The method relies on a specific property that

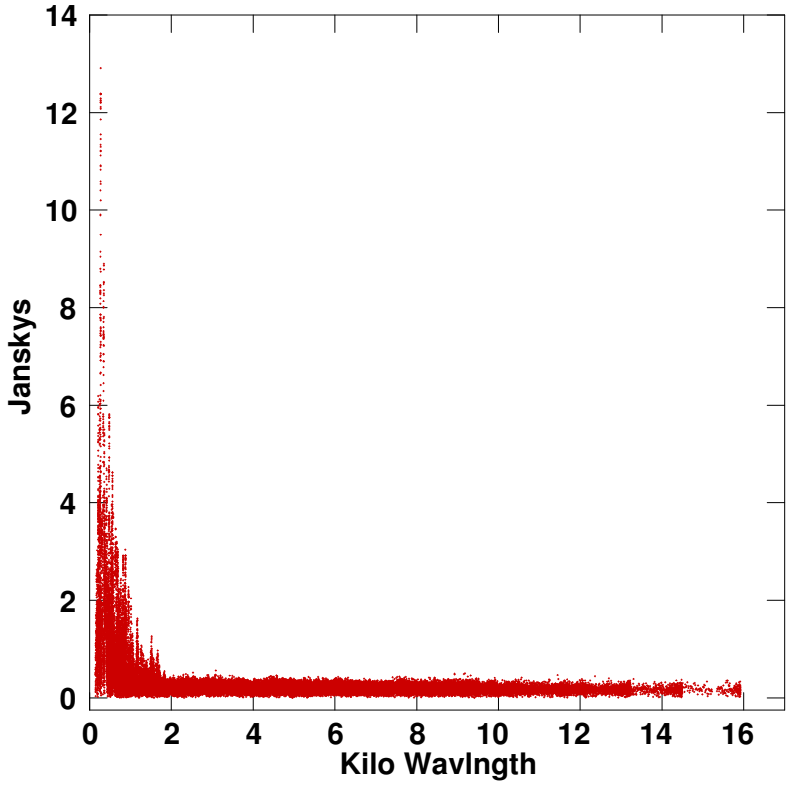


Figure 8.5: Input power (calibrated in units of Jy) received in the various baselines of the interferometer, as a function of the distance in the *uv*–domain (expressed in kilo-wavelength). The input power corresponds to channel 0 data, taken during the 2.5h the solar interference was the strongest.

interferometers have: the possibility to arbitrarily change the phases between antenna pairs, i.e., the direction on the sky where a map is created from the *uv*–data (see Sect. 8.2.1). We proceeded to shift the *uv*–data to the location of the Sun (task UVFIX), and cleaned the dirty image using a process that is called multi-scale cleaning (see below, in Sect. 8.4). The clean components extracted by this cleaning algorithm constitute the model of the Sun. This model was then subtracted from the original, non-shifted *uv*–data, reducing the contamination by the Sun.

#### Multi-scale cleaning

As explained in Sect. 8.2.2, the standard cleaning algorithm models the emission with a series of Dirac $\delta-$functions. This model is not well adapted to cleaning low-level, diffuse emission. Furthermore, if the regions of emission are much larger than the synthesised beam of the interferometer, artifacts can be introduced. The oscillating wings of the dirty beam (see Fig. 8.2), even if at low-level can, after several iterations of the cleaning process create fake peaks of emission and/or modify the emission coming from the object being targeted.

A simple solution to the issue of large scale structure reconstruction, consists in adapting dynamically the size of the dirty beam to that of the emission regions. Instead of creating a model of many tens of thousands of $\delta$–functions, the emission is modelled by a series of gaussian peaks of varying, pre–set widths. The user sets the number of gaussians and their size, the largest one adapted to the size of the largest emission regions, the smallest one is the natural beam (determined by the longest baselines). As a rule of thumb, the width at half-maximum of the successive gaussians is chosen to follow a geometrical sequence with a common ratio of $\sqrt{3}$ (this is inspired by the ratio between the longest baseline length in B–, C–, and D–array (see Sect. 8.2.1). The cleaning algorithm starts with one beam, iterates until a stopping criterion is reached, then moves to another beam, and so on, cycling quasi–randomly among the typically 3 or 4 size scales (this is controlled by the parameter IMAGRPRM(11) of the task IMAGR).

## 8.4 Moment maps and H I mass measurements

The maps we present here are the result of the data reduction we performed and that is described in the previous sections. Masks were created and applied to the data to select only emission above 2.5 $\sigma$ using conditional blanking based on maps that were spatially convolved to lower resolution to bring out low–level, extended emission (see Walter et al. (2008) for details). As a last step, primary beam correction was applied to the final image data cubes and H I surface brightness maps.

#### Moment 0 and H I mass measurements

Once the data have been blanked, the task XMOM can be used to create moment maps where the moment 0 is a map created by simple integration along the frequency axis (or velocity axis) of the data cube. Moments 1 and 2 are the intensity weighted velocity field and velocity dispersion, respectively. In the moment 0 of a data cube, the value of pixel (j,k) is $\sum_{i=1}^{n} S_i(j,k) \times \delta v$, where:

- n is the total number of channels;
- $S_i(j,k)$ is the H I flux measured in the i$^{th}$ channel, in units of mJy beam$^{-1}$ (or Jy beam$^{-1}$). The units are beam dependent, since the beam is the resolution element;
- $\delta v$ is the spectral resolution in units of km s$^{-1}$.

The H I column densities and H I masses are measured from the moment 0 of data cubes. In general, the final data are blanked, so that channels that do not contain emission are set to "blanked" values (i.e. magic values)[11]. For the sake of simplicity, we will express summation over channels that contain emission and will note $i_1$ the first channel to contain emission and $i_2$ the last one to contain emission.

Calculating H I column densities and H I masses first requires expressing the data in units that are telescope beam independent (like brightness temperatures, expressed in Kelvin). Starting with the Rayleigh-Jeans approximation, relating the Brightness Temperature of a Black Body $T_B$, in Kelvin, and the power per unit frequency interval per unit solid angle, $B_{RJ}$:

$$B_{RJ}(\nu, T) = 2\frac{kT_B}{\lambda^2} \tag{8.9}$$

we can derive the power per unit frequency interval received by the interferometer in a small solid angle $d\Omega$, around the direction $\overrightarrow{\Omega}$:

$$B_{RJ}(\nu, T)P(\overrightarrow{\Omega})d\Omega = 2\frac{kT_B}{\lambda^2}P(\overrightarrow{\Omega})d\Omega, \tag{8.10}$$

where $P(\overrightarrow{\Omega})$ is the normalised angular power pattern of the interferometer (i.e., the synthesised beam). This can be integrated and under the assumption that the brightness temperature, $T_B$, does not vary over the size of the beam, we obtain the expression for $S_\nu$, the flux per unit of frequency, within one beam (in units of mJy):

$$S_\nu = 2\frac{kT_B}{\lambda^2}\iint_{mb} P(\overrightarrow{\Omega})d\Omega. \tag{8.11}$$

It is quite straightforward to find $\iint_{mb} P(\overrightarrow{\Omega})d\Omega$: assuming the beam can be well approximated by a 2–D Gaussian function with a FWHM along the major ($\delta\alpha$) and minor axis ($\delta\beta$), the integral equals $1.13 \times \delta\alpha \times \delta\beta$, with $\delta\alpha$ and $\delta\beta$ in units of arcsec..

Then, $T_B$, the brightness temperatures in units of Kelvin, independent of the beam size, are simply obtained by inverting the previous relation:

$$T_B[K] = \frac{606}{\delta\alpha \times \delta\beta} \times S_\nu[\mathrm{mJy\,beam^{-1}}] \tag{8.12}$$

From the brightness temperature, the gas column density can be derived assuming optically thin radiation[12] ($\tau \ll 1$)):

$$N_{HI}(j,k)\,[\mathrm{atom\,cm^{-2}}] = 1.8224 \times 10^{18} \times \sum_{i=i_1}^{i_2} T_{B,i}(j,k) \times \delta v \tag{8.13}$$

or

$$N_{HI}(j,k)\,[\mathrm{M_\odot\,pc^{-2}}] = 1.46026 \times 10^{-2} \times \sum_{i=i_1}^{i_2} T_{B,i}(j,k) \times \delta v \tag{8.14}$$

where channels in the range $[i_1, i_2]$ contains emission, $T_{B,i}(j,k)$ is in [Kelvin per pixel] and $\delta v$ in $\mathrm{km\,s^{-1}}$. From there, one can derive the H I mass, in units of $\mathrm{M_\odot}$, by simply integrating the last

[11] The great advantage of blanking the data is that it reduces to a minimum the noise in the moment maps; blanking also can assist in separating regions of emission that overlap along the line of sight but are at distinct radial velocities.

[12] p. 336 of Wilson et al. (2009)

mentioned relation over the desired area and multiplying by the pixel size, expressed in units of $pc^2$. Alternatively, one can derive the mass of the entire system via:

$$M_{HI}[\mathrm{M}_\odot] = 235.6 \times D^2 \times \sum_{i=i_1}^{i_2} S_i \times \delta v \tag{8.15}$$

where D is the distance of the system in Mpc and the summation refers to emission encompassed by a given region, integrated over velocity, in units of $\mathrm{mJy\,km\,s^{-1}}$.

### Moment maps and spatial distribution of gas properties

We present the moments 0 of our 3 data cubes in Figure 8.6, 8.7 and 8.8, the moments 1 in Figure 8.9a & 8.9b, 8.10a & 8.10b and 8.11a & 8.11b and the moments 2 in Figure 8.12a & Figure 8.12b, 8.13a & 8.13b and 8.14a & 8.14b.

The large field of view of the interferometer allows us to cover the full spatial extent of the systems and reveals the global gas properties across the system:

- the contrast between inner regions, with low gas densities, and outer regions, encompassing most of the H I supply;
- global velocity gradients revealing the dynamics of tidal tail, their expansion in the intergalactic medium;
- differences of gas velocity dispersions between inner regions and outer regions, with higher velocity dispersion near the central regions.

The high spatial resolution allows us to resolve local peaks of H I density within the tidal tails. Coupled with a high spectral resolution, we are also able to resolve the gas kinematics on small scales and disentangle possible projection effects (like tidal tail turnover).

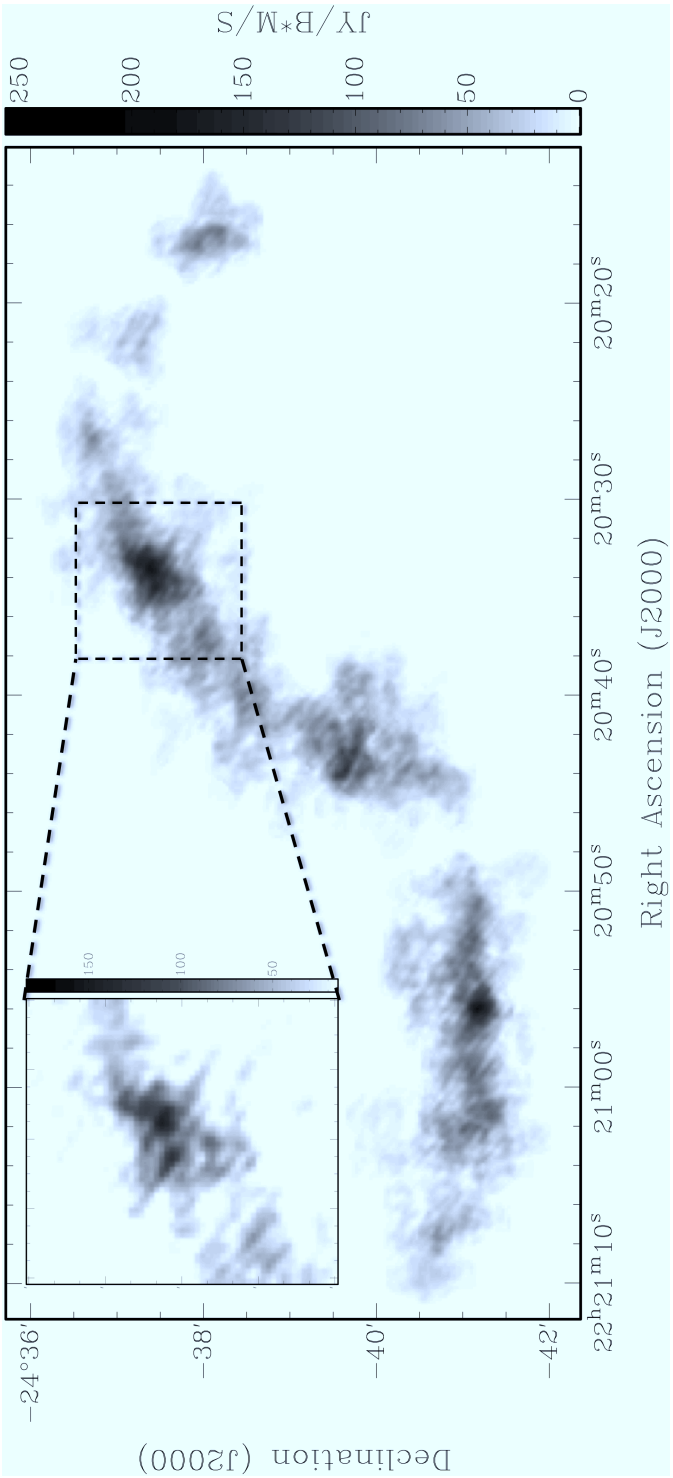


Figure 8.6: Spatial distribution of the integrated H I flux in NGC 7252 (Natural weights, $20\farcs8 \times 15\farcs3$ resolution). A robust-weight map ($15\farcs3 \times 13\farcs6$ resolution) of the spatial distribution of the integrated H I in the TDG NGC 7252NW is also displayed in the top left corner of the figure.

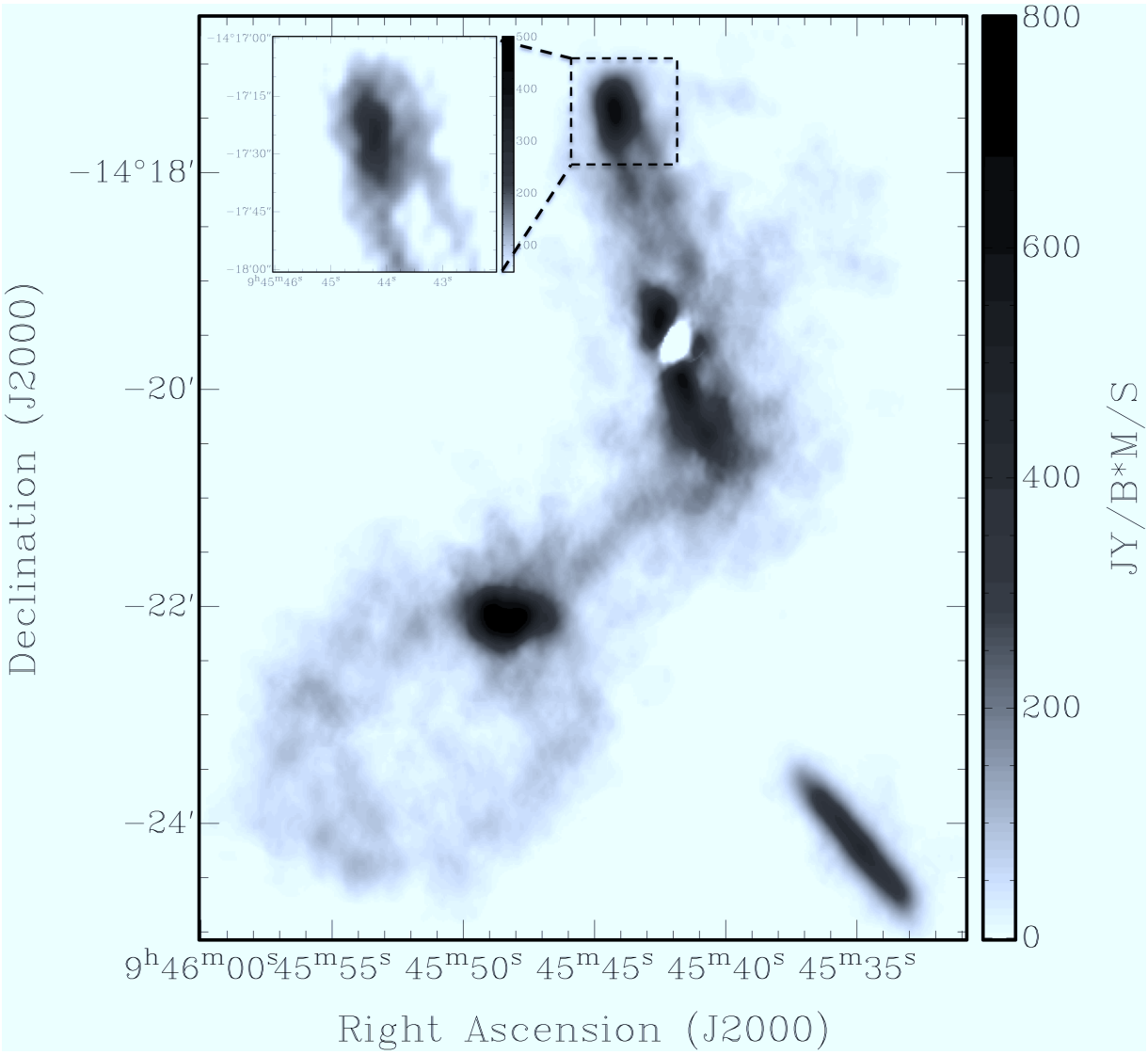


Figure 8.7: Spatial distribution of the integrated H I flux in Arp 245 (Natural weights, 11.″66×7.″92 resolution). A robust-weight map (7.″17 × 4.″76 resolution) of the spatial distribution of the integrated H I in the TDG Arp 245N is also displayed in the top left corner of the figure. Note the two "branches" in the north tail. They correspond to different parts of the tidal tail along the line-of-sight. Thanks to the high spatial resolution of the data, we are able to disentangle them.

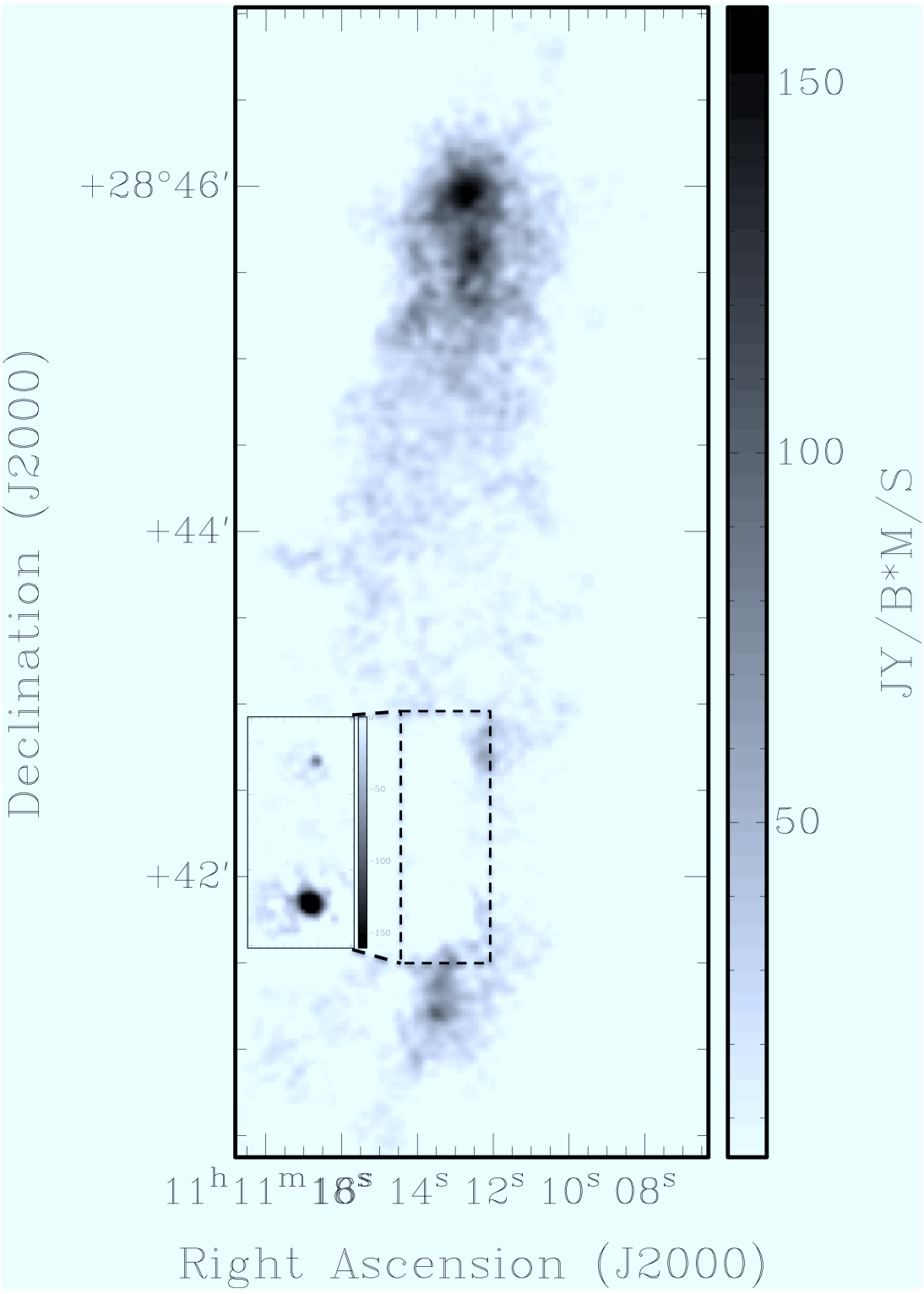


Figure 8.8: Spatial distribution of the integrated H I flux in Arp 105 (Natural weights, 10.″19×9.″65 resolution). A robust-weight map (7.″12 × 7.″03 resolution) of the spatial distribution of the H I seen in absorption is also shown for the central regions.

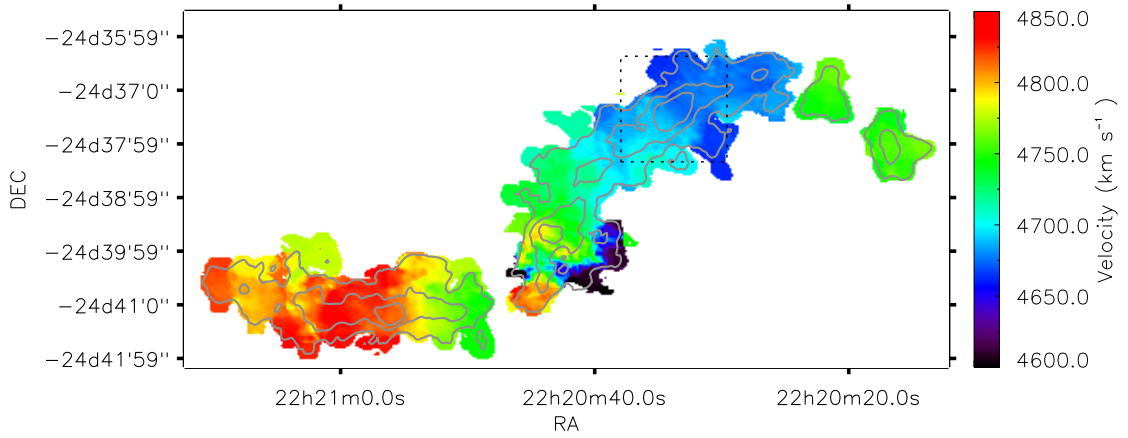


(a) Global distribution

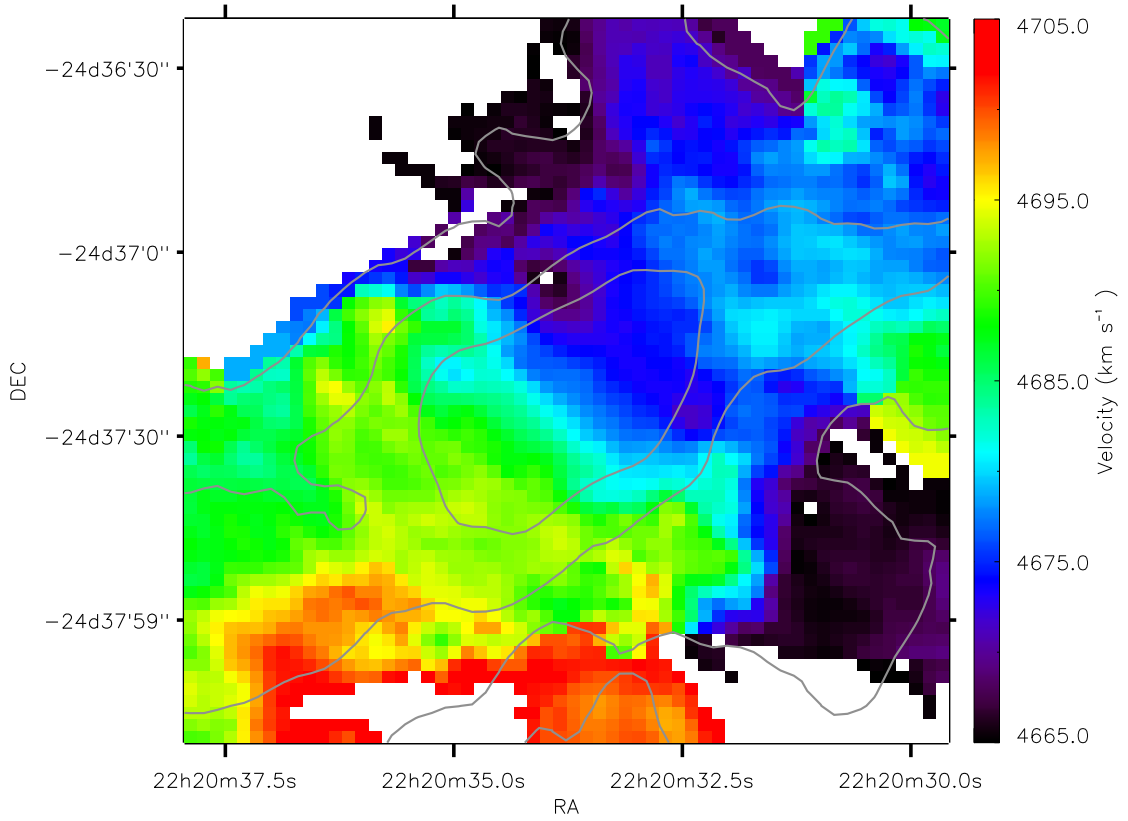


(b) Local distribution, around NGC 7252NW

Figure 8.9: (a) Spatial distribution of the integrated H I velocity in NGC 7252. Note the overall velocity gradient along the tidal tails. (b) Spatial distribution of the H I velocity around the TDG NGC 7252NW (delimited by the dotted square in the top figure). The change in velocity is due to rotation locally, associated with the TDG. In both figures, density contours at $0.2\,M_\odot\,pc^{-2}$, $1.0\,M_\odot\,pc^{-2}$ and $2.0\,M_\odot\,pc^{-2}$ of a 21″ resolution map have been overlaid in grey.

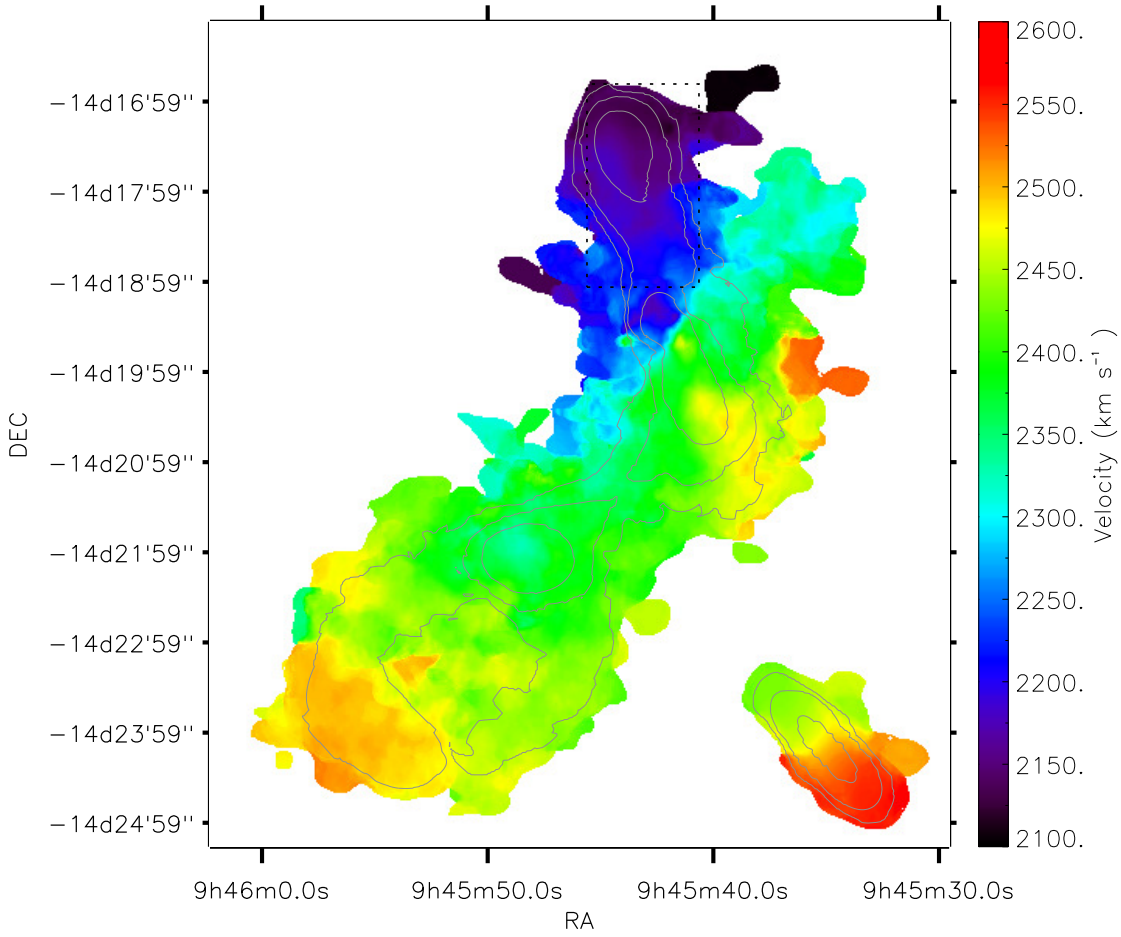


(a) Global distribution

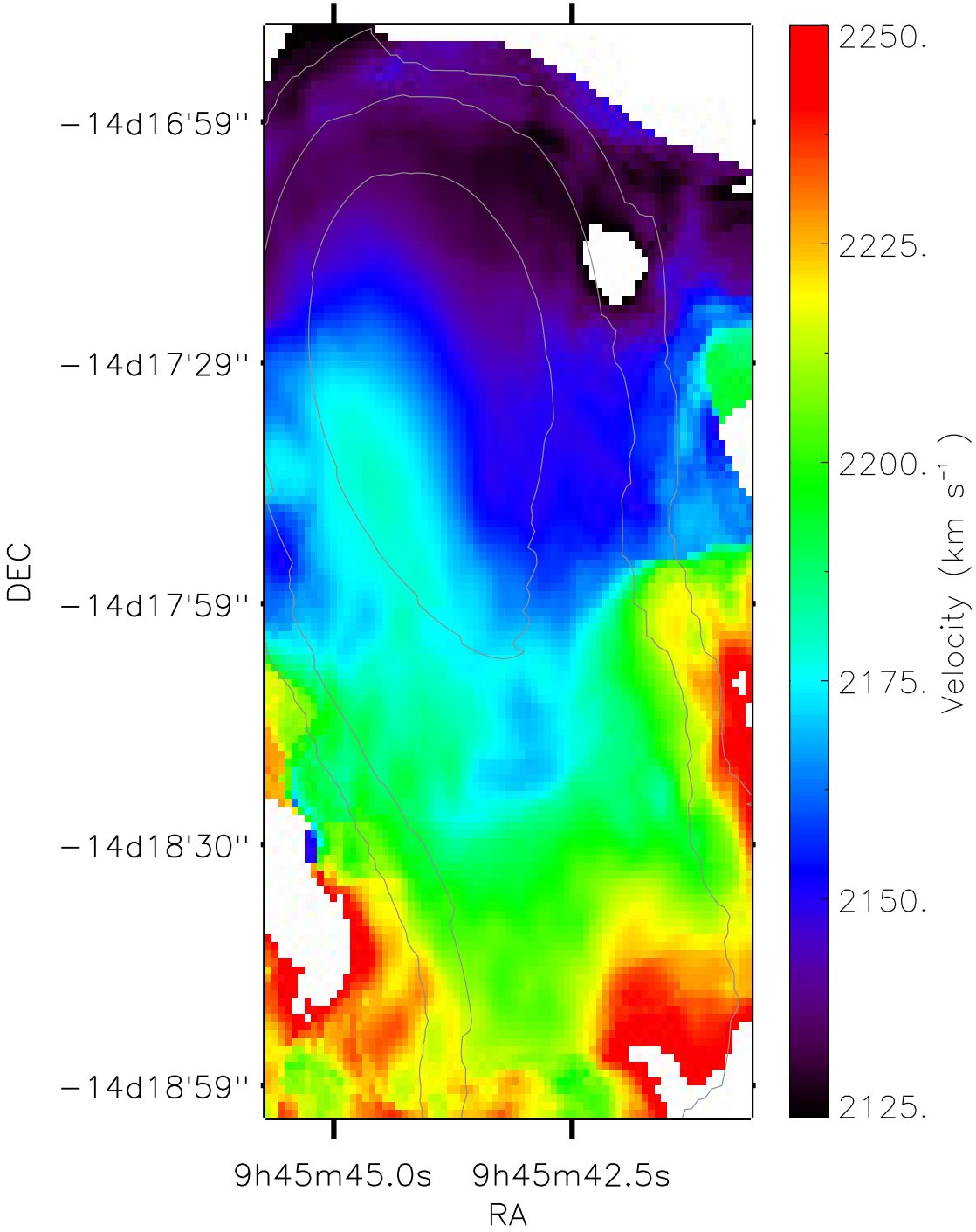


(b) Local distribution, around Arp 245N

Figure 8.10: (a) Spatial distribution of the integrated H I velocity in Arp 245. Note the overall velocity gradient along the tidal tails. The rotation of the South West companion can be clearly seen. (b) Spatial distribution of the H I velocity around the TDG Arp 245N, delimited by the dotted rectangle in panel (a). In both figures, density contours at $1.5\,M_\odot\,pc^{-2}$, $4.0\,M_\odot\,pc^{-2}$ and $9.0\,M_\odot\,pc^{-2}$ of a 30″ resolution map have been overlaid in grey.

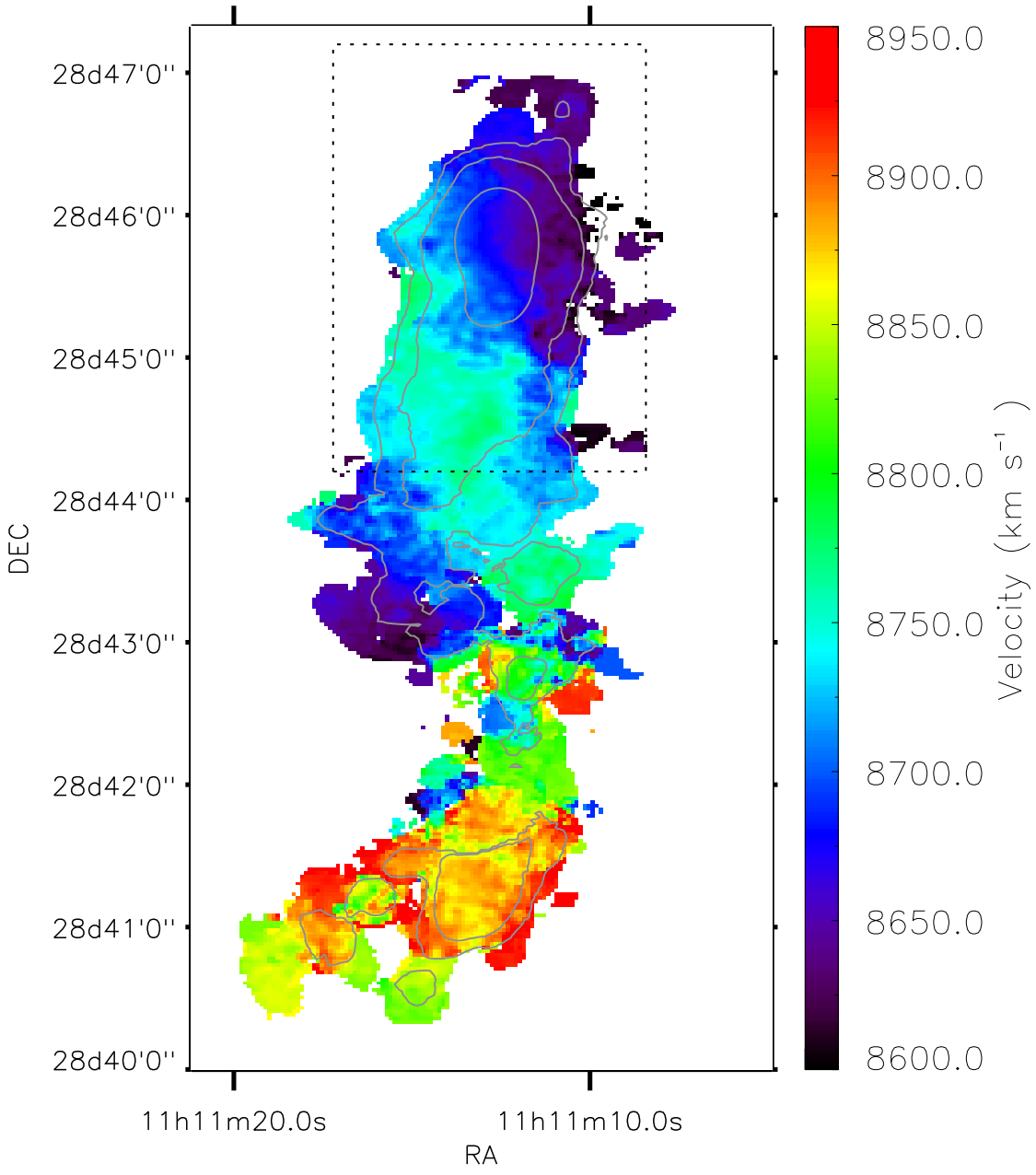


(a) Global distribution

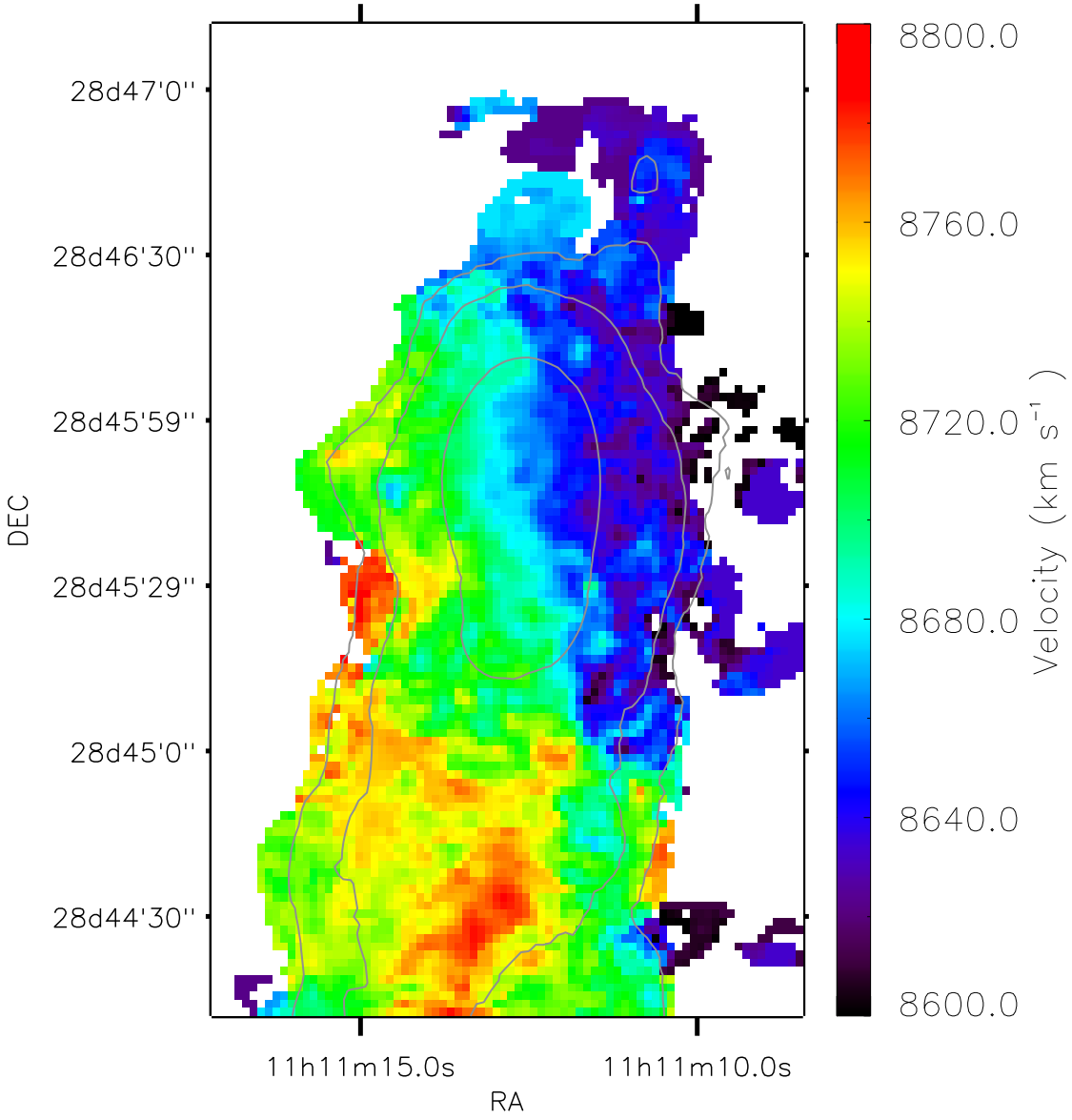


(b) Local distribution, around Arp 105N

Figure 8.11: (a) Spatial distribution of the integrated H I velocity in Arp 105. Note the overall velocity gradient along the tidal tails. (b) Spatial distribution of the H I velocity around the TDG Arp 105N, delimited by the dotted rectangle in panel (a). In both figures, density contours at 0.5 $M_\odot$ pc$^{-2}$, 1.5 $M_\odot$ pc$^{-2}$ and 5.0 $M_\odot$ pc$^{-2}$ of a 21″ resolution map have been overlaid in grey.

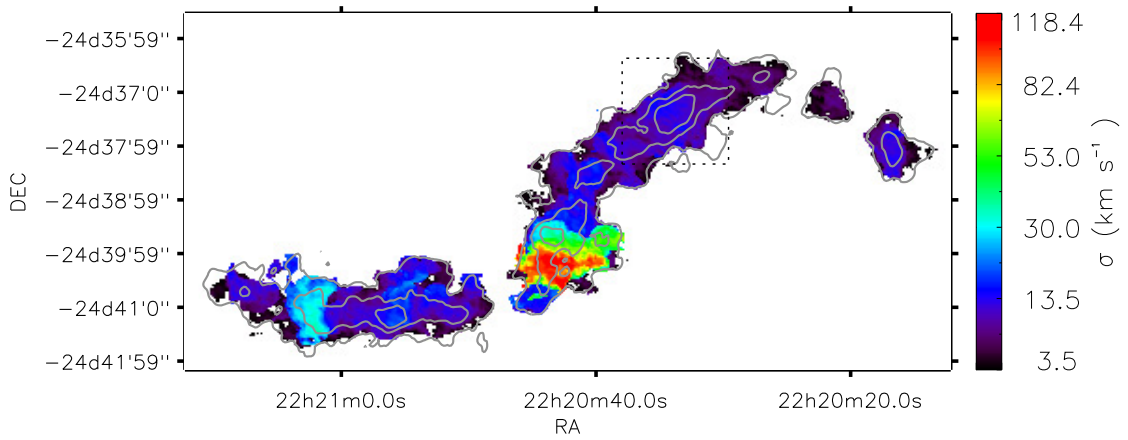


(a) Global distribution

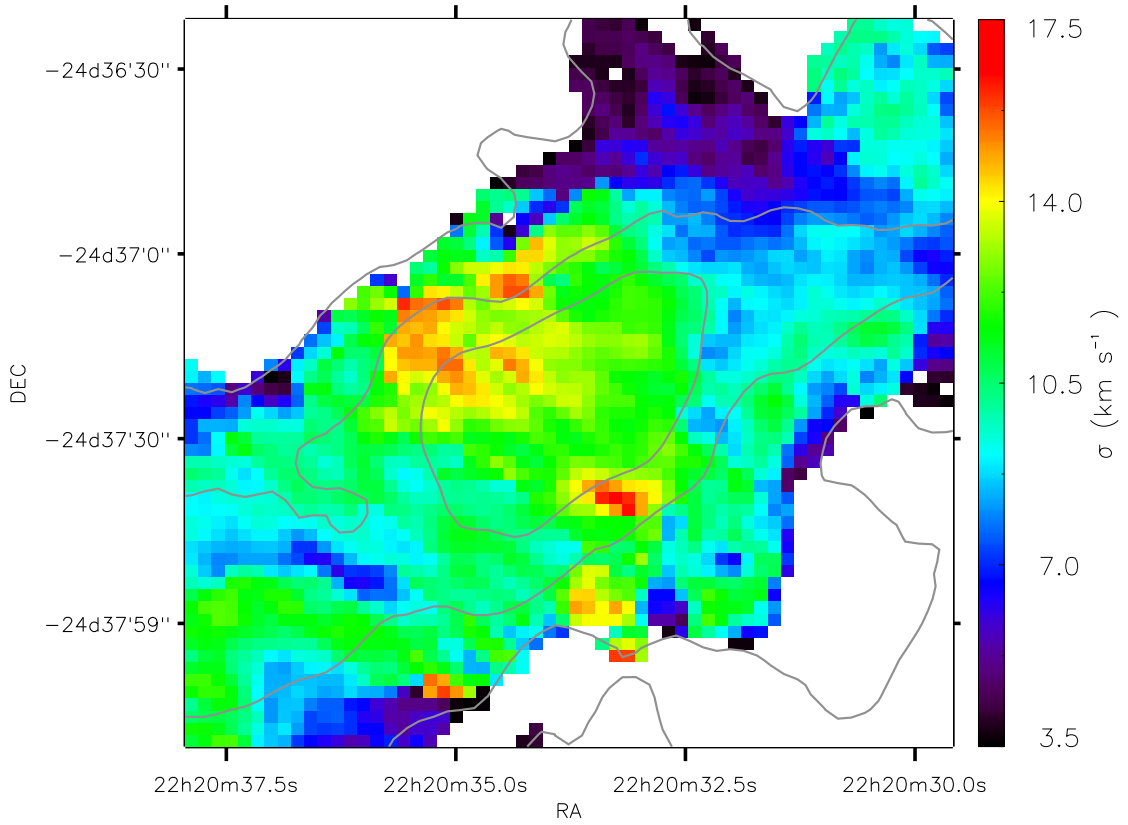


(b) Local distribution, around NGC 7252NW

Figure 8.12: (a) Spatial distribution of the integrated H I velocity dispersion in NGC 7252. Note that the colour scale follows a square root progression. The velocity dispersion appears quite heterogeneous across the system, with extreme values (above 100 km s$^{-1}$) at the base of the North West Tail. (b) Spatial distribution of the velocity dispersion around the TDG NGC 7252NW (delimited by the dotted square on the top figure). In both figures, density contours at 0.2 $M_\odot$ pc$^{-2}$, 1.0 $M_\odot$ pc$^{-2}$ and 2.0 $M_\odot$ pc$^{-2}$ of a 21″ resolution map have been overlaid in grey.

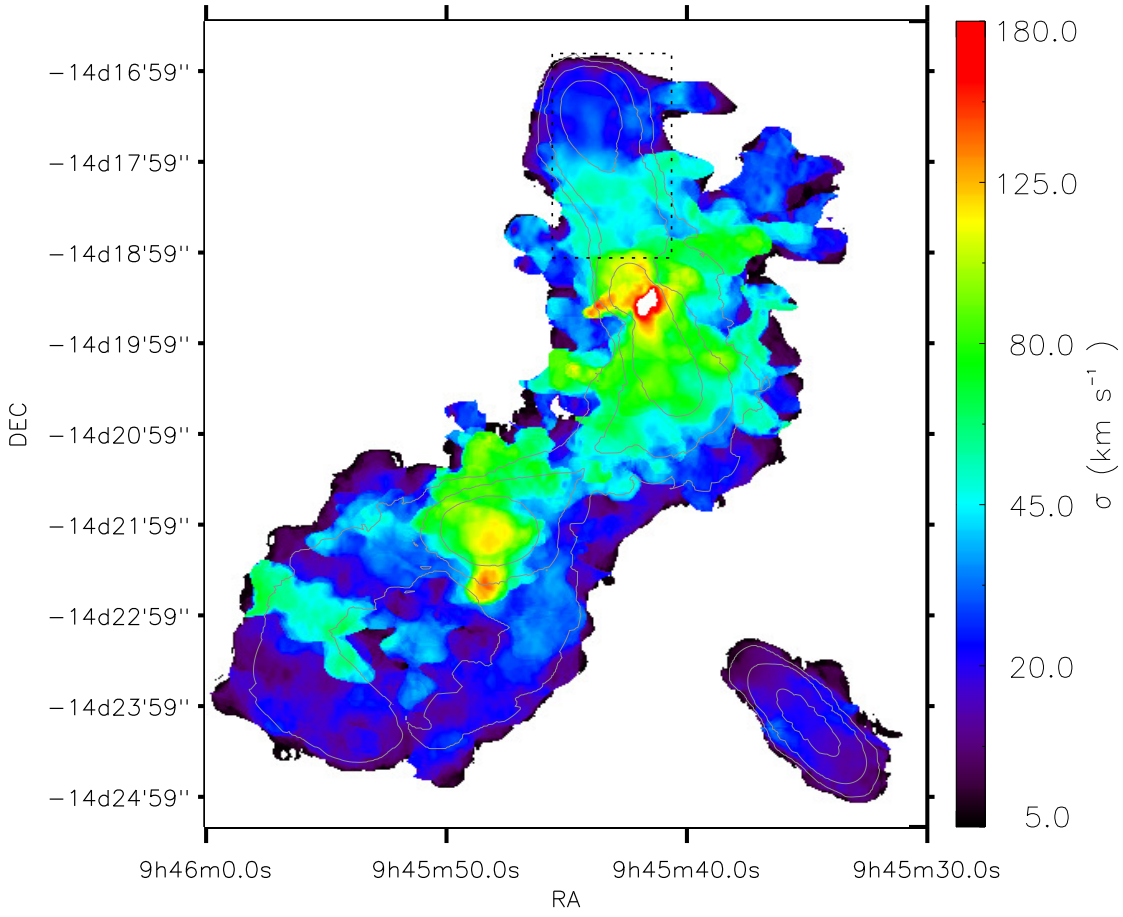


(a) Global distribution

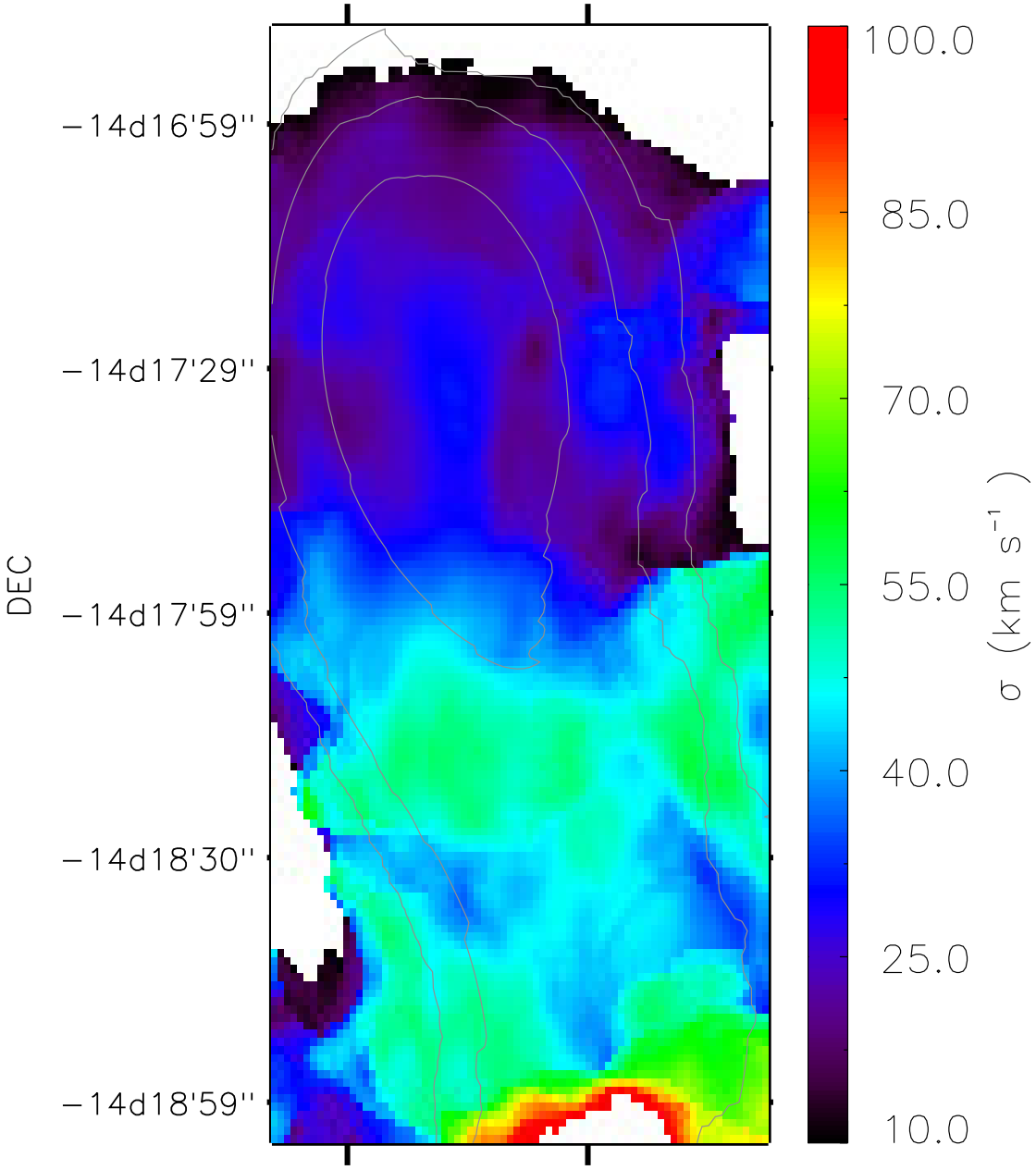


(b) Local distribution, around Arp 245N

Figure 8.13: (a) Spatial distribution of the integrated H I velocity dispersion in Arp 245. Note that the colour scale follows a square root progression. The velocity dispersion appears quite heterogeneous across the system, with extreme values (above 100 km s$^{-1}$) in the vicinity of the central galaxies. (b) Spatial distribution of the velocity dispersion around the TDG Arp 245N, delimited by the dotted rectangle in panel (a). In both figures, density contours at 1.5 $M_\odot$ pc$^{-2}$, 4.0 $M_\odot$ pc$^{-2}$ and 9.0 $M_\odot$ pc$^{-2}$ of a 30″ resolution map have been overlaid in grey.

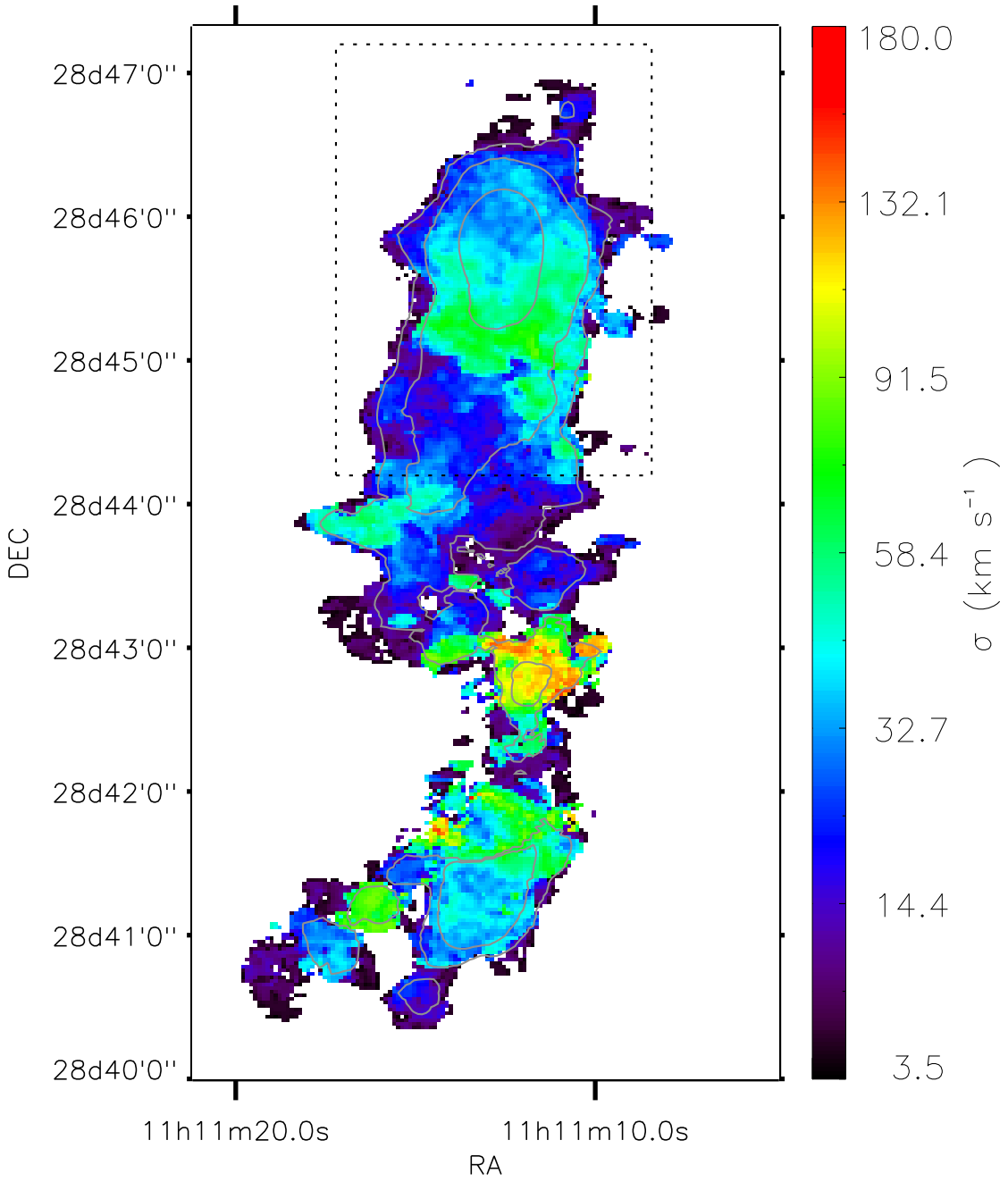


(a) Global distribution

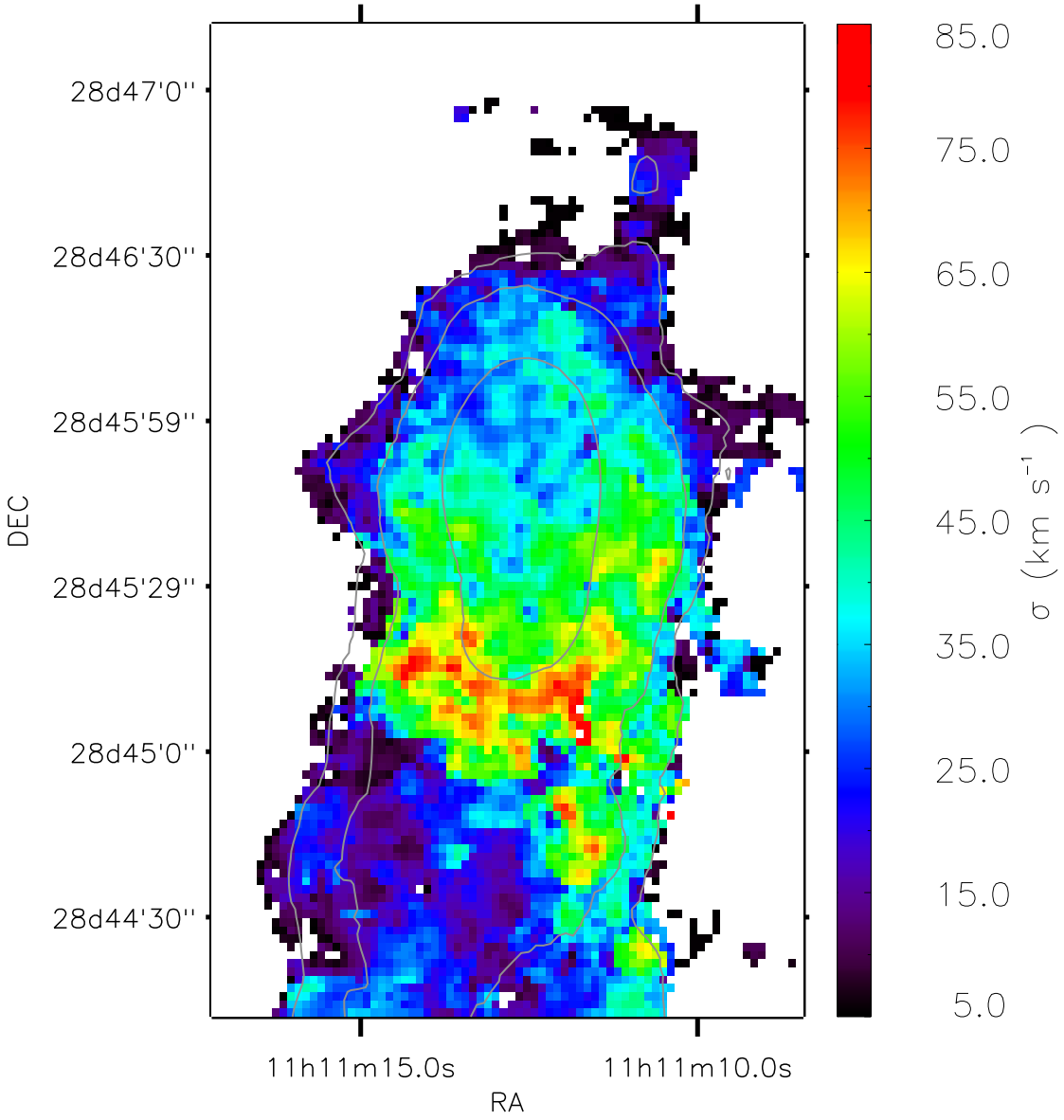


(b) Local distribution, around Arp 105N

Figure 8.14: (a) Spatial distribution of the integrated H I velocity dispersion in Arp 105. Note that the colour scale follows a square root progression. The velocity dispersion appears quite heterogeneous across the system, with extreme values (above $100\,\mathrm{km\,s^{-1}}$) in the vicinity of the central galaxies. (b) Spatial distribution of the velocity dispersion around the TDG Arp 105N, delimited by the dotted rectangle in panel (a). In both figures, density contours at $0.5\,\mathrm{M_\odot\,pc^{-2}}$, $1.5\,\mathrm{M_\odot\,pc^{-2}}$ and $5.0\,\mathrm{M_\odot\,pc^{-2}}$ of a 21″ resolution map have been overlaid in grey.

# Chapter 9

# The SFR–HI relation

## 9.1 The sample of star forming regions

### 9.1.1 Global properties of the selected galaxies

The three interacting systems of our sample were primarily selected for having, at least in the extended tidal tail of one member of the pair, evidence of star-formation. Two are observed at an early stage of the collision, and one is an advanced merger.

• **Arp 245** consists of two interacting spiral galaxies, NGC 2992 (to the North) and NGC 2993 (to the South), that are well separated and connected by a bridge. Fig. 9.1 shows an optical image of the system, combining $B$, $V$ and $I$ bands. This is the closest system of our sample; we will adopt 29 Mpc as the distance of this system. NGC 2992 is a peculiar Sa galaxy, with Seyfert-type nuclear activity; NGC 2993 is spiral galaxy of type Sab. According to the numerical model of the collision by Duc et al. (2000), the system is observed about 100 Myr after the first pericentre passage. The two gaseous tidal tails have an optical counterpart and are relatively short: 33 kpc for NGC 2992 and 55 kpc for NGC 2993 (15.5 kpc and 26.6 kpc in the optical, respectively). The tail North of NGC 2992 is seen close to edge-on and appears shorter than it actually is, because of projection effects. A turn-over may be seen in the H I and UV data.

At the apparent tip of the northern tail, a massive cloud, Arp 245N, was identified as a self-gravitating TDG (Bournaud et al., 2004), with a large reservoir of H I gas, $8.9 \times 10^8 M_\odot$ according to Duc et al. (2000) and a non-negligible fraction of $H_2$ gas at a level of $\sim 17\%$ of the H I mass, i.e., $1.5 \times 10^8 M_\odot$, according to Braine et al. (2001). The main properties of the system, relevant to the present study are summarised in Table 9.1.

• **Arp 105**, also called "The Guitar", consists of two interacting galaxies, NGC 3561A (North) and NGC 3561 (South), that are still distinct. Fig. 9.2 shows an optical image of the system, combining $B$, $V$ and $R$ bands. With an adopted distance of $\sim 120$ Mpc, this is the most distant system of our sample. NGC 3561 is an elliptical galaxy (S0 type), with nuclear activity (Véron-Cetty & Véron, 2006), whereas NGC 3561A is a gas-rich spiral galaxy (Sa type).

According to the 3D reconstruction of the collision by Duc et al. (1997), the system is seen after first pericentre passage. The two gaseous tidal tails, that arise from the spiral galaxy, have optical counterparts and are quite extended: $\sim 100$ kpc for the northern tail and $\sim 50$ kpc for the southern tail, in projection. The plane of propagation of the tails is perpendicular to the observational plane (this is an ideal situation for a study of gas kinematics). The southern tail

Figure 9.1: Optical image of Arp 245 taken with the NTT (Duc et al., 2000), combining $B$, $V$ and $I$ bands.

Table 9.1: Arp 245 properties

| Type | NGC 2992<br>Spiral (Sa), Seyfert | NGC 2993<br>Spiral (Sab) | Arp 245N<br>TDG |
|---|---|---|---|
| Distance (Mpc) [a] | 29 | 29 | 29 |
| $R_{25}$ [b] | 106″ | 41″ | – |
| $L_B$ ($10^9\,L_\odot$) [c] | 16.8 | 13.0 | 1.1 |
| $L_{IR}(8\mu m - 1000\mu m)$ ($10^9\,L_\odot$) [d] | 25.3 | 32.7 | – |
| SFR ($M_\odot\,yr^{-1}$) | 4.4[e] | 5.7[e] | 0.02[f] |
| H I mass ($10^9\,M_\odot$) [g] | 0.4 (+4.8 in tail) | 1.7 (+2.6 in tail) | 0.3 – 0.6 |
| $H_2$ mass ($10^9\,M_\odot$) [h] | 1.2 | 1.2 | 0.13 |
| $\tau_{dep}(H_2)$ (Gyr) [i] | 0.3 | 0.2 | 6.5 |
| $\tau_{dep}$(H I+$H_2$) (Gyr) [i] | 0.4 | 0.6 | 26.6 – 46.7 |

[a] NED

[b] Mean apparent major isophotal radius from the RC3 catalogue (Corwin et al., 1994). The radii are measured at, or reduced to a surface brightness level of $\mu_B = 25.0$ $B-$mag per square arcsecond

[c] Duc et al. (2000)

[d] Sanders et al. (2003), determined using the fluxes in all four IRAS bands

[e] using the SFR–$L[8\mu m - 1000\mu m]$ calibration of Kennicutt (1998a)

[f] Boquien et al. (2010); obtained by SED fitting and assuming a Salpeter IMF, consistent with the value given by Braine et al. (2000), $SFR = 0.03\,M_\odot\,yr^{-1}$

[g] This thesis

[h] Braine et al. (2001) (Braine et al. (2000) for Arp 245N), from CO, using $X_{CO} = 2 \times 10^{20}\,[cm^{-2}\,/\,(K\,km\,s^{-1})]$ and including helium contribution

[i] Estimated from the data presented in this table, taking into account a helium contribution of 1.34 in terms of mass fraction. The IR luminosity of NGC 2992 includes an AGN contribution, which contaminates the SFR and depletion times derived from it. NGC 2993 has a $\tau_{dep}(H_2)$ smaller than the $\sim 2 \times 10^9$ yr time scale of spiral galaxies. Fig. 9.4 shows that NGC 2993 falls between the sequence of spiral galaxies and the sequence of starbursts, as defined by Daddi et al. (2010b).

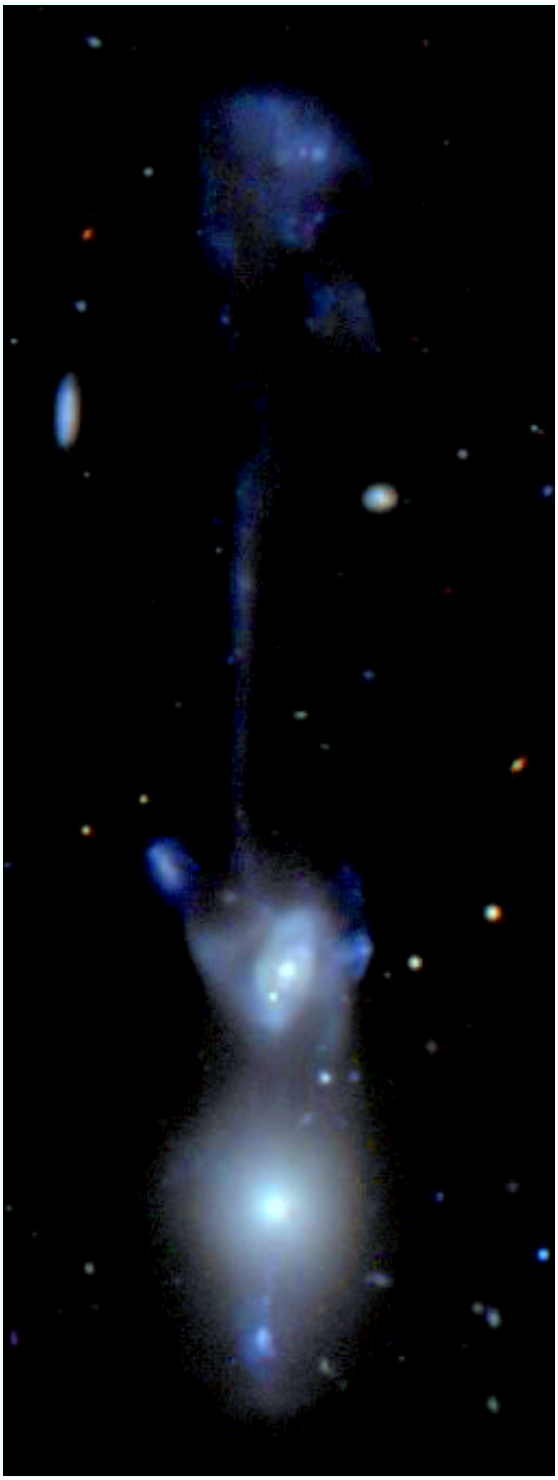

Figure 9.2: Optical image of Arp 105 taken with the MegaCam on CHFT, combining $B$, $V$ and $R$ bands (courtesy Jean-Charles Cuillandre)

Table 9.2: Arp 105 properties

| Type | NGC 3561A Spiral (Sa) | NGC 3561 Elliptical (S0) | Arp 105N TDG | Arp 105S TDG |
|---|---|---|---|---|
| Distance (Mpc) [a] | 120 | 120 | 120 | 120 |
| $R_{25}$ [b] | 26″ | 20″ | – | – |
| $L_B$ ($10^9$ L$_\odot$) [c] | 14 | 22 | 5.1 | 9.8 |
| $L_{IR}(8\mu m - 1000\mu m)(10^9$ L$_\odot$) | 225[d] | – | – | – |
| SFR (M$_\odot$ yr$^{-1}$) | 39.6[e] | – | – | 0.3[f] |
| H I mass ($10^9$ M$_\odot$) [g] | $< 0.36$ | – | $\sim 1.2$ | 0.78 |
| $H_2$ mass ($10^9$ M$_\odot$) | $\sim 7.7$[c] | – | – | 0.24[h] |
| $\tau_{dep}(H_2)$ (Gyr) [i] | $\sim 0.2$ | – | – | 0.8 |
| $\tau_{dep}$(H I+$H_2$) (Gyr) [i] | $0.2 - 0.21$ | – | – | 4.3 |

[a] NED
[b] Mean apparent major isophotal radius from the RC3 catalogue (Corwin et al., 1994). The radius are measured at, or reduced to a surface brightness level of $\mu_B = 25.0$ $B-$mag per square arcsecond.
[c] Duc & Mirabel (1994); the $H_2$ mass is calculated assuming $D = 120$ Mpc and $X_{CO} = 2 \times 10^{20}$ [cm$^{-2}$ / (K km s$^{-1}$)]
[d] From IRAS fluxes at 12 $\mu$m, 25 $\mu$m, 60 $\mu$m and 100 $\mu$m given by Geller et al. (2006), transformed into $L_{IR}(8\mu m - 1000\mu m)$ using the formula given in Table 1 of Sanders & Mirabel (1996)
[e] using the SFR–$L[8\mu m - 1000\mu m]$ calibration of Kennicutt (1998a)
[f] Boquien et al. (2010); obtained by SED fitting and assuming a Salpeter IMF
[g] This thesis
[h] Braine et al. (2000), from CO, using $X_{CO} = 2 \times 10^{20}$ [cm$^{-2}$ / (K km s$^{-1}$)] and including helium contribution
[i] Estimated from the data presented in this table, taking into account a helium contribution of 1.34 in terms of mass fraction NGC 3561A has a $\tau_{dep}(H_2)$ smaller than the $\sim 2 \times 10^9$ yr time scale of spiral galaxies. Fig. 9.4 shows that NGC 3561A falls on the sequence of starbursts, as defined by Daddi et al. (2010b)

crosses in front of the elliptical galaxy, such that H I can be seen in absorption at this location. Interestingly, Duc & Mirabel (1994) observed an extreme segregation between the atomic and molecular gas distributions: most of the H I reservoir ($\sim 90\%$) is located in the tidal tails, whereas the central region gathers most of the molecular gas ($\sim 90\%$).

Additionally, Duc & Mirabel (1994) and Duc et al. (1997) reported the presence of several compact star forming regions along the tidal tails with at their tips massive TDGs. The northern tail hosts Arp105 N, an irregular galaxy of Magellanic type. The southern tail hosts a dwarf galaxy resembling a Blue Compact Dwarf (BCD), Arp 105S. They are self-gravitating structures (Duc et al., 1997). Braine et al. (2001) measured M(H I) $= 5.4 \times 10^8$ M$_\odot$ and estimated M($H_2$) $\geq 2.4 \times 10^8$ M$_\odot$. The main properties of the system, relevant to the present study are summarised in Table 9.2.

• **NGC 7252**, also called "Atoms for Peace", is an advanced-stage merger: the central galaxy shows a light profile similar to an elliptical galaxy (Schweizer, 1982; Whitmore et al., 1993). Fig. 9.3 shows an optical image of the system, combining $B$ and $R$ bands. We will adopt

Figure 9.3: Optical image of NGC 7252, combining $B$ and $R$ bands (Source ESO/MPI 2.2m/WFC). The two tidal tails are clearly visible on optical images: the Eastern Tail (ET) and the Northwestern Tail (NWT).

66.5 Mpc as the distance of this system. A great variety of stellar clusters orbit the remnant galaxy. According to the numerical model of the collision by Hibbard & Mihos (1995), the tidal tails started to form 770 Myr ago. The two gaseous tidal tails are still visible and have optical counterparts. They are $\sim$ 180 kpc (Northwestern Tail) and $\sim$ 100 kpc (East Tail) in projected length. The H I Northwestern tail propagates toward us and crosses in front of the remnant, whereas the East Tail propagates away from us, crosses behind the remnant and swings back toward us. The East tail is affected by projection effects and appears shorter than it actually is.

At two-thirds along the Northwestern tail, NGC 7252NW, a massive TDG was identified as a self-gravitating object with a large reservoir of H I gas, $7.3 \times 10^8 M_\odot$ (taking into account He contribution) and a small fraction of $H_2$ gas, $2.2 \times 10^7 M_\odot$ (Braine et al., 2001) (see Sect. 12.2 for the detailed study of this system). The main properties of the system, relevant to the present study are summarised in Table 9.3.

Figure 9.4 shows the location of the three galaxies on the SK-relation. Integrated values are used here. The gas surface density is computed from the total H I plus $H_2$ mass, including a correction for helium content. The integrated star-formation rates were estimated from the total far-infrared luminosity of the galaxies, as measured by IRAS. As usually done in the literature, a surface of $\pi \times R_{25}^2$ was assumed to compute the gas and SFR surface densities. All relevant data are given in Tables 9.1, 9.2 and 9.3. The galaxies in our sample bar one, lie in Fig. 9.4 on the sequence of starburst galaxies, as defined by Daddi et al. (2010b). The exception is NGC 3561,

Table 9.3: NGC 7252 properties

| Type | NGC 7252<br>Merger remnant (E) | NGC 7252NW<br>TDG |
|---|---|---|
| Distance (Mpc) [a] | 66.5 | 66.5 |
| $R_{25}$ [b] | 58″ | – |
| $L_B$ ($10^9$ $L_\odot$) | 52[c] | – |
| $L_{IR}(8\mu m - 1000\mu m)$ ($10^9$ $L_\odot$) | 46[c] | – |
| SFR ($M_\odot$ yr$^{-1}$) | 8.0[d] | 0.03[e] |
| H I mass ($10^9$ $M_\odot$) [f] | 0 (3.2 in NWT, 2.0 in ET) | 0.54 |
| $H_2$ mass ($10^9$ $M_\odot$) [g] | 3.9 | $2.2 \times 10^{-2}$ |
| $\tau_{dep}(H_2)$ (Gyr) [h] | 0.49 | 0.7 |
| $\tau_{dep}$(H I+$H_2$) (Gyr) [h] | 0.49 | 24.8 |

[a] from NED
[b] Mean apparent major isophotal radius from the RC3 catalogue (Corwin et al., 1994). The radius are measured at, or reduced to a surface brightness level of $\mu_B = 25.0$ $B-$mag per square arcsecond.
[c] Dupraz et al. (1990)
[d] Using the SFR–$L[8\mu m - 1000\mu m]$ calibration of Kennicutt (1998a)
[e] Boquien et al. (2010); obtained by SED fitting and assuming a Salpeter IMF
[f] This thesis; NWT stands for North Western Tail, ET stands for East Tail
[g] Braine et al. (2001)
[h] Estimated from the data presented in this table, taking into account a helium contribution of 1.34 in terms of mass fraction. Since no H I is detected in association with the NGC 7252 remnant (not even in absorption), the total gas depletion time of the remnant equals the molecular gas depletion time.

which is gas-poor Early-Type Galaxy with very low star-formation activity. Also note that the SFR of NGC 2992 is uncertain, because of the contamination of its IR luminosity by the central nuclear activity.

### 9.1.2 Selection of Star Forming regions

In this section we present the method we used to identify the star forming regions located in our interacting systems and to measure their SFRs. We aimed at comparing the properties of star formation in mergers with those in the outer discs of spiral galaxies and dwarf galaxies (Bigiel et al., 2010). We used the UV emission as our main star formation tracer, as was done in that reference study. All UV images were obtained from surveys made with the *GALEX* space telescope. *GALEX* offers two bands of observations, FUV ($\lambda_{eff} = 151$ nm) and NUV ($\lambda_{eff} = 227$ nm), of which basic characteristics are given in Table 9.4 for the three systems under considerations.

The photometry was carried out with the IRAF package. The background emission was first subtracted from the original images. A second order Legendre polynomial was used to model the background emission. Note that the background was fitted globally, and not assessed locally. This makes a comparison possible between central and outer regions in the systems (see Sect. 9.2.1). The data were set to a common resolution of 4.5 kpc, imposed by the H I data. The maps were convolved using the kernels and the convolution algorithm of Aniano Porcile et al. (2012). The pixel sizes were matched with the task WREGISTER, and flux conservation

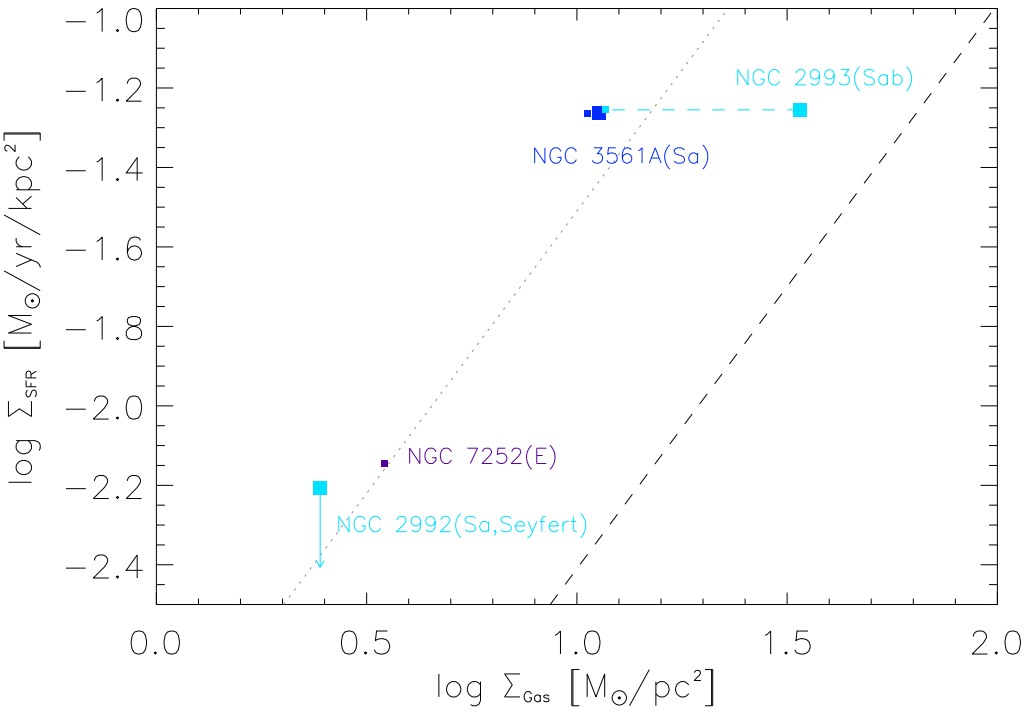


Figure 9.4: Location of the interacting systems on the SK-relation. The integrated values of the total gas, H I+$H_2$ plus helium contribution (large squares), the molecular gas, $H_2$ plus helium contribution (small squares), and SFR within $R_{25}$ are plotted. The dashed line shows the locus of regular star-forming galaxies, whereas the dotted line corresponds to the starburst sequence, as defined by Daddi et al. (2010b).

Table 9.4: *GALEX* observations

| System (band) | Exposure Time (s) | Survey |
|---|---|---|
| Arp 245 (FUV) | 1045 | Nearby Galaxy Survey |
| Arp 245 (NUV) | 5830 | Nearby Galaxy Survey |
| Arp 105 (FUV) | 115 | All-sky Imaging Survey |
| Arp 105 (NUV) | 959 | Nearby Galaxy Survey |
| NGC 7252 (FUV) | 562 | Medium Imaging Survey |
| NGC 7252 (NUV) | 562 | Medium Imaging Survey |

was applied; $2.5\sigma$ clipping was applied. Figs. 9.5, 9.6 and 9.7 show the resulting NUV emission. Note that, at fixed exposure time, setting a common linear resolution for all data results in a better sensitivity for more nearby systems. For this reason, low-level diffuse NUV emission is clearly visible in Arp 245, whereas NUV emission appears more clumpy in the two other systems that are more distant. This effect is further enhanced by the long exposure time of the observations of Arp 245 (5830s), compared to those of the other systems (562s and 959s for NGC 7252 and Arp 105, respectively). As shown in Fig. 9.5, the spatial correlation between NUV emission and H I is striking for Arp 245. Low level, diffuse star formation is present in the tenuous tails, and peaks of NUV emission are associated with H I peaks. This strong correlation suggests that higher sensitivity NUV observations of NGC 7252 and Arp 105 would probably also reveal a diffuse emission in-between the UV peaks (see Figs. 9.6 and 9.7). Conversely, all UV emitting regions are associated with H I gas, apart from the central regions of some galaxies. Note that because of this strong NUV-H I correlation, the PDF of the gas density (see Chapter 7.2) can be probed by a restricted sample of star forming regions, not necessarily covering the full spatial extent of the system.

The NUV maps being often more sensitive than the FUV maps (by up to a factor 2, see next section), the star forming regions were selected in NUV maps. Only star-forming regions above a clip level of $2.5\sigma$ are selected. The regions are chosen to be independent of each other, similar to the pixel-by-pixel approach of Bigiel et al. (2010) in their analysis of spiral discs and dwarf galaxies. By cross-correlation with optical images, we discard emission which is not associated with the system: foreground stars and background galaxies. Note that this is performed before image convolution. We identified 61 star forming regions in our interacting systems, five of them corresponding to the central galaxies:

- 29 star forming regions in Arp 245, of which 2 correspond to the central galaxies NGC 2993 and NGC 2992;
- 22 star forming regions in Arp 105, of which 2 correspond to the central galaxies NGC 3561A and NGC 3561;
- 10 star forming regions in NGC 7252; of which 1 corresponds to the central merger.

These regions are identified with circles in Figs. 9.5, 9.6, and 9.7. The central regions of the galaxies involved are plotted as squares. We observe that the largest star forming regions are preferentially located at the tip of the tidal tails. These regions are associated with both NUV and H I peaks. Many observations of dwarf galaxies, called Tidal Dwarf Galaxies (TDGs), have been reported in the outermost regions of interacting systems (see for instance Mirabel et al. 1992; Duc & Mirabel 1994 and Sect. 12.2 of this thesis).

### 9.1.3 Star Formation Rate measurements

Fluxes were measured with QPHOT[1] and converted to physical units using zero magnitudes, $m0_{UV}$, given by the *GALEX* photometric calibration (Morrissey et al., 2007):

$$m_{UV}^{\mathbf{AB}} = m0_{UV} - 2.5 \times \log f_{UV} \tag{9.1}$$

where $m_{UV}^{\mathbf{AB}}$ is the UV magnitude in the AB system and $f_{UV}$ is the dead-time corrected count rate (normalised by the flat field map). $m0_{NUV}$ ($m0_{FUV}$, respectively) is, the zero magnitude, corresponding to a 1 count $s^{-1}$ NUV detection (FUV detection, respectively) and equals 20.08

[1] Task of the IRAF package

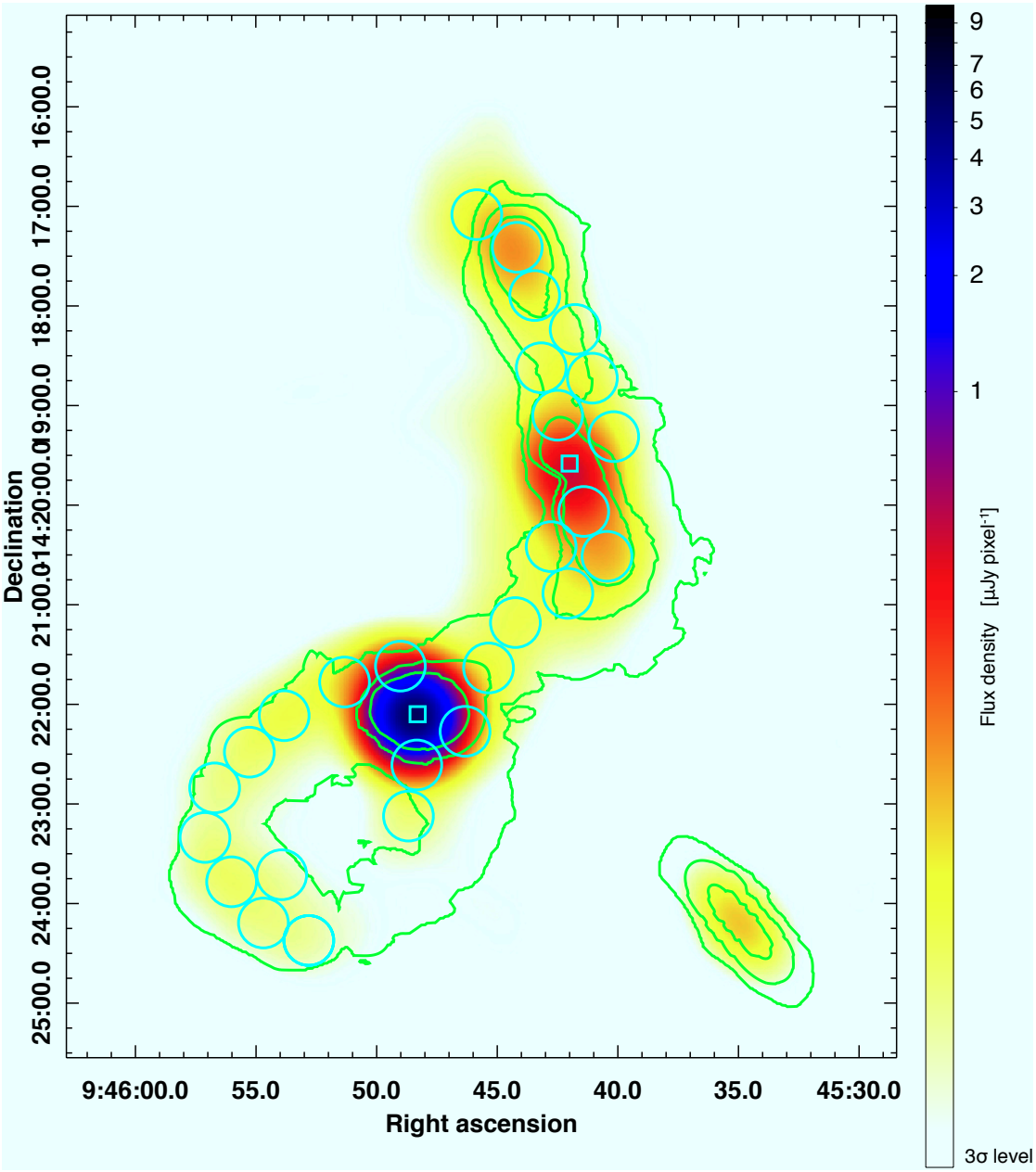


Figure 9.5: NUV emission of Arp 245, ranging from the $3\sigma$-level to 10 [$\mu$Jy per pixel]. The linear resolution of the NUV map is 4.5 kpc. Cyan circles locate the star-forming regions we selected and the apertures we used to measure the NUV fluxes. The diameter of the circles corresponds to 4.5 kpc. Squares locate the central galaxies of the system. H I contours, drawn from a 21″ resolution map, have been overlaid in green at 1 $M_\odot$ pc$^{-2}$, 5 $M_\odot$ pc$^{-2}$ and 9 $M_\odot$ pc$^{-2}$.

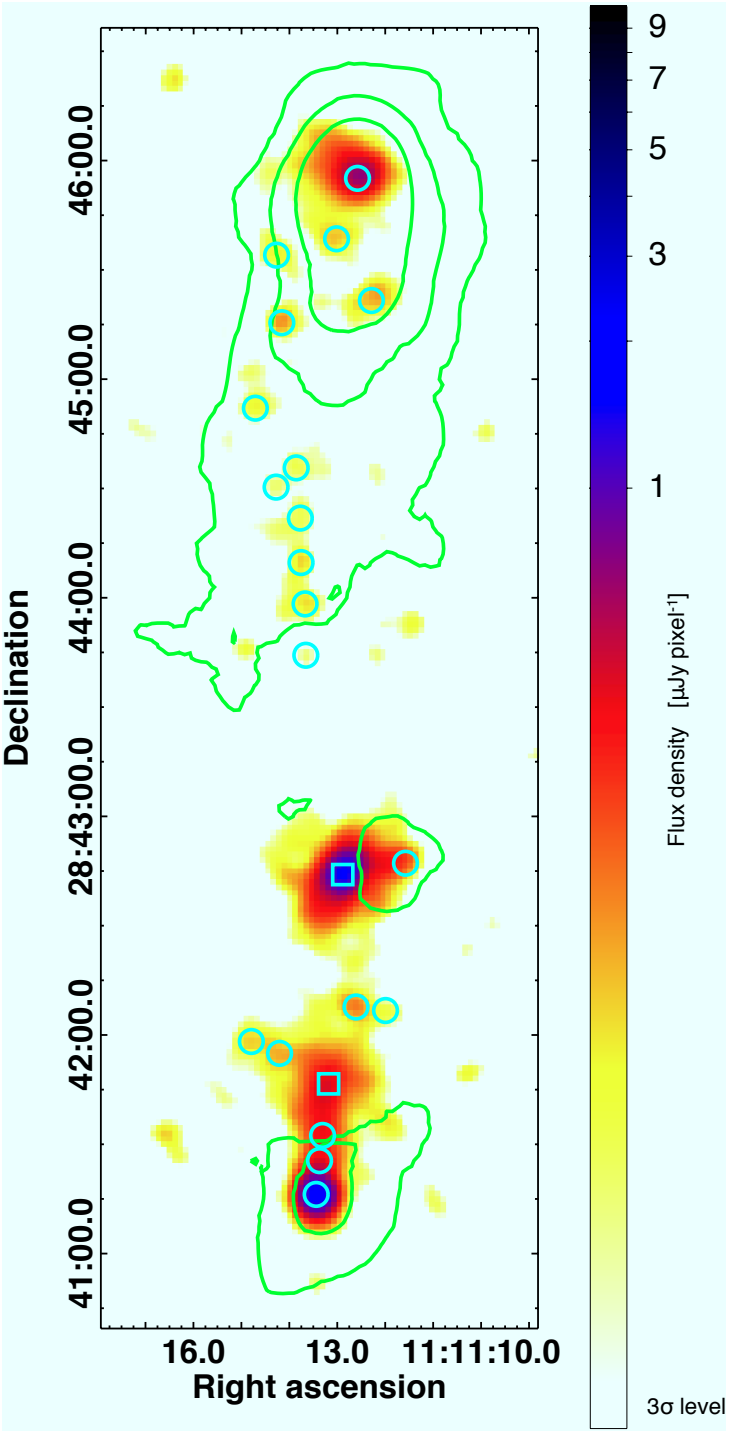


Figure 9.6: NUV emission of Arp 105, ranging from the $3\sigma$-level to 10 [$\mu$Jy per pixel]. The linear resolution of the NUV map is 4.5 kpc. Cyan circles locate the star-forming regions we selected and the apertures we used to measure the NUV fluxes. The diameter of the circles corresponds to 4.5 kpc. Squares locate the central galaxies of the system. H I contours, drawn from a 30″ resolution map, have been overlaid in green at 1 $M_\odot$ pc$^{-2}$, 3 $M_\odot$ pc$^{-2}$ and 5 $M_\odot$ pc$^{-2}$.

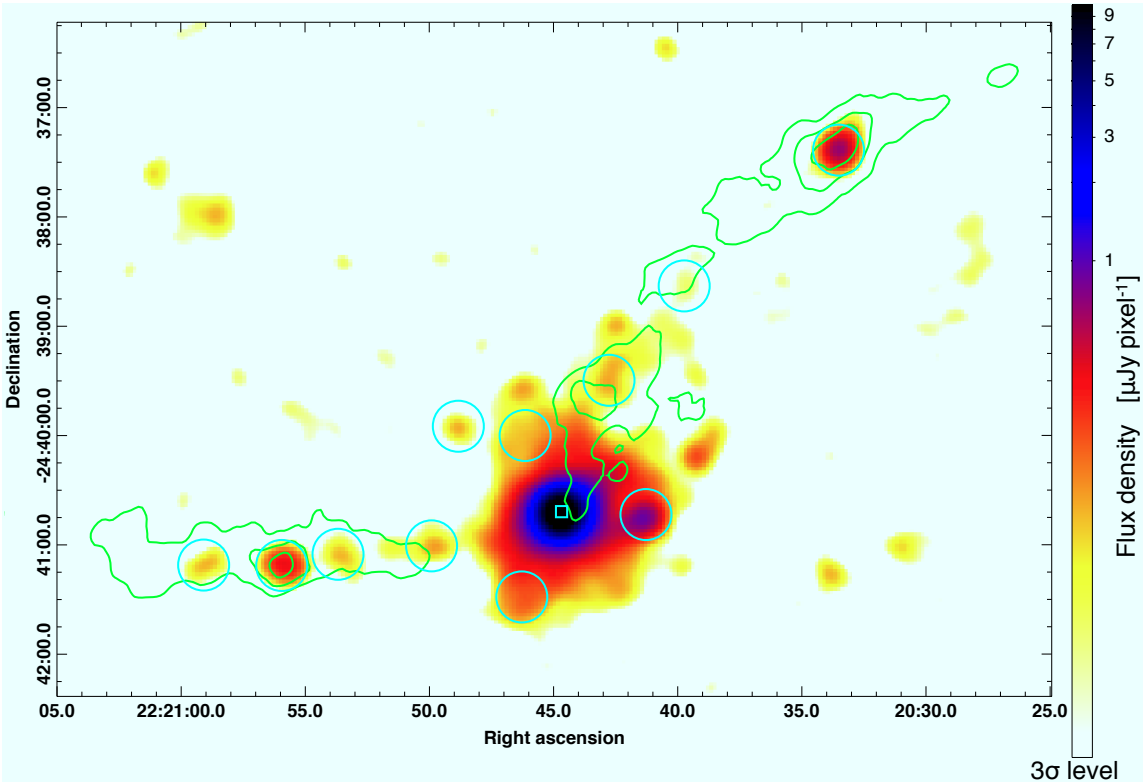


Figure 9.7: NUV emission of NGC 7252, ranging from the $3\sigma$-level to 10 [$\mu$Jy per pixel]. The linear resolution of the NUV map is 4.5 kpc. Cyan circles locate the star-forming regions we selected and the apertures we used to measure the NUV fluxes. The diameter of the circles corresponds to 4.5 kpc. A square locates the merger remnant. H I contours, drawn from a 21″ resolution map, have been overlaid in green at $1\,M_\odot\,pc^{-2}$, $2\,M_\odot\,pc^{-2}$ and $3\,M_\odot\,pc^{-2}$.

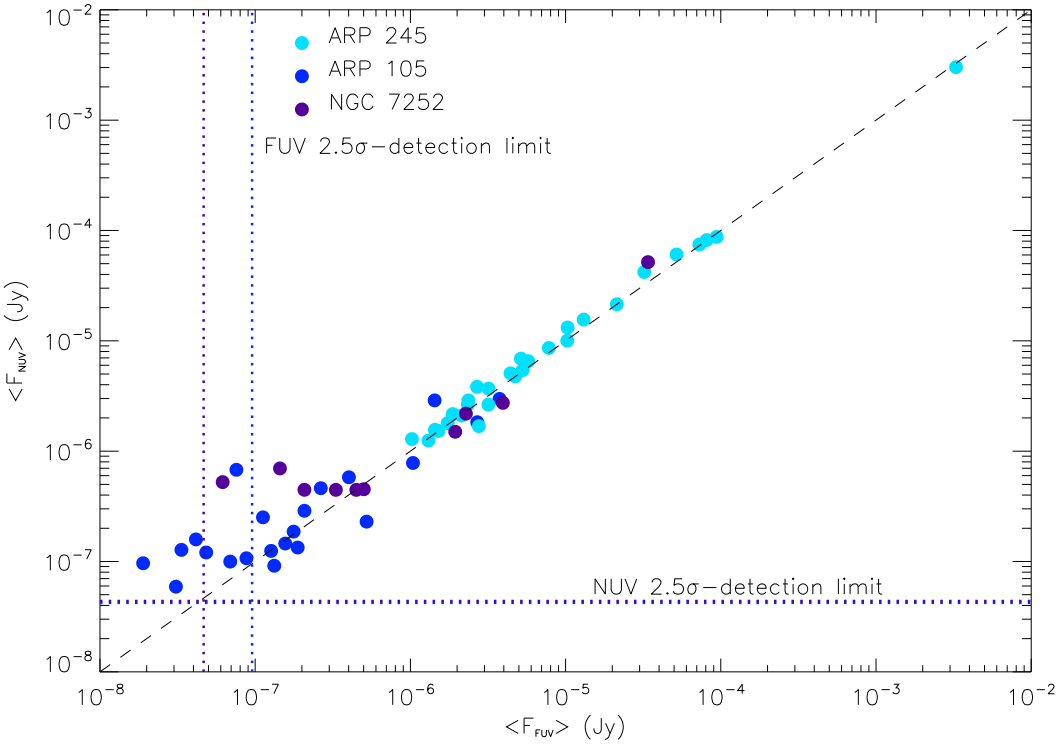


Figure 9.8: Comparison between FUV and NUV fluxes of our sample of star forming regions in interacting systems. The data were all taken at the same linear resolution, 4.5 kpc, and fluxes were averaged over 4.5 kpc apertures and corrected for extinction (internal and foreground Galactic). The 2.5$\sigma$-detection limits of the FUV data (NUV data) are represented by a vertical (horizontal) dotted line, for each system. The 2.5$\sigma$-detection limits for Arp 245 fall below $10^{-8}$ Jy, and hence beyond the plotting range. The NUV flux limits for the other two systems are virtually identical. Clipping at 2.5$\sigma$ was applied to each system and each tracer, apart the FUV emission of Arp 105 for which the statistics of photons was too low to allow a determination of the noise level in the 4.5 kpc resolution map. Instead, the noise of the FUV data of Arp 105 was determined in a 12.5 kpc resolution map then estimated for a 4.5 kpc resolution one.

(18.82, respectively). The relation between AB magnitude and flux density, $F_\nu$ in units of $\mathrm{W\,m^{-2}\,Hz^{-1}}$, is:

$$m_{UV}^{\mathbf{AB}} = -2.5 \times \log F_\nu - 56.10 \tag{9.2}$$

Combining Equations 9.1 and 9.2 gives:

$$F_{\nu,NUV}[\mu\mathrm{Jy}] = 33.73 \times f_{NUV}[\mathrm{count\,s^{-1}}] \tag{9.3}$$

$$F_{\nu,FUV}[\mu\mathrm{Jy}] = 170.65 \times f_{FUV}[\mathrm{count\,s^{-1}}] \tag{9.4}$$

For the sake of consistency, the conversion of UV fluxes (in Janskys) into SFR were done the same way as Bigiel et al. (2010); i.e., using the Salim et al. (2007) calibrations, obtained from SED fits of *GALEX* UV data and SDSS optical multi-band photometric data for a sample of $\sim$ 50000 galaxies, and a Kroupa (2001) IMF. Original calibrations by Salim et al. (2007) give:

$$\mathrm{SFR}[\mathrm{M_\odot\,yr^{-1}}] = 1.08 \times 10^{-28} L^0_{FUV}[\mathrm{erg\,s^{-1}\,Hz^{-1}}] \tag{9.5}$$

We will show below that we have a tight relation between the FUV and NUV fluxes, which ensures that we can use the Salim et al. (2007) calibration for the NUV fluxes as well. Additionally, we converted the calibration to a Kroupa (2001) IMF by dividing by an extra factor 1.59. In the end, we have the following relation[2]:

$$\mathrm{SFR(UV)}[\mathrm{M_\odot\,yr^{-1}}] = 8.2 \times 10^{-8} D[\mathrm{Mpc}]^2 F_{\nu,UV}[\mu\mathrm{Jy}] \tag{9.6}$$

We took into account internal dust extinction and corrected for it by assuming a Galactic extinction law (Cardelli et al., 1989) and using our H I data. Extinction of the FUV emission is simply given by $A_{FUV}/E(B-V) = 8.24$, but, because of the bump at 2175 Å in the Galactic extinction law, $A_{NUV}$ is not proportional to $E(B-V)$; it rather follows a quadratic law (Wyder et al., 2007). If $E(B-V) < 0.1$, this relation can be well approximated by:

$$\frac{A_{NUV}}{E(B-V)} = 8.2 \tag{9.7}$$

In collisional debris, extinction is generally low but can vary a lot, because of the quite heterogeneous distribution of the dust. For instance, Temporin et al. (2005) focused on CG J1720-67.8, a compact group of galaxies, exhibiting tidal tails and TDGs. They found colour excesses $E(B-V)$ varying between 0.0 and 0.2 mag in the vicinity of some star forming regions, whereas, on average, $E(B-V) = 0.5 \pm 0.2$ in the entire tidal tails. We will assume that the previous relation holds in the surrounding of our star forming regions. Then, assuming a constant gas-to-dust ratio, we can derive the $E(B-V)$ associated with our H I gas column densities. Surveys of interstellar H I directly gives (Bohlin et al., 1978):

$$\frac{N(HI)}{E(B-V)} = 5.8 \times 10^{21}\,\mathrm{cm^{-2}\,mag^{-1}} \tag{9.8}$$

Note that we did not take into account extinction due to the molecular gas component nor H I seen in absorption. Consequently, we underestimate UV fluxes in the central regions, where the molecular gas component can dominate (see Tables 9.1, 9.2 and 9.3). We corrected our fluxes for Galactic extinction, which is estimated from the infra-red based map of Schlafly & Finkbeiner (2011).

In Fig. 9.8, we compare the extinction-corrected NUV and FUV fluxes measured for our sample of 61 star forming regions; 2.5$\sigma$-detection limits are represented by dotted lines. We find a tight one–to–one correlation between FUV and NUV over more than 3 orders of magnitude. Because NUV is more sensitive than FUV, we will use the former for the remainder of this study.

[2] from here onwards when referring to UV we mean NUV.

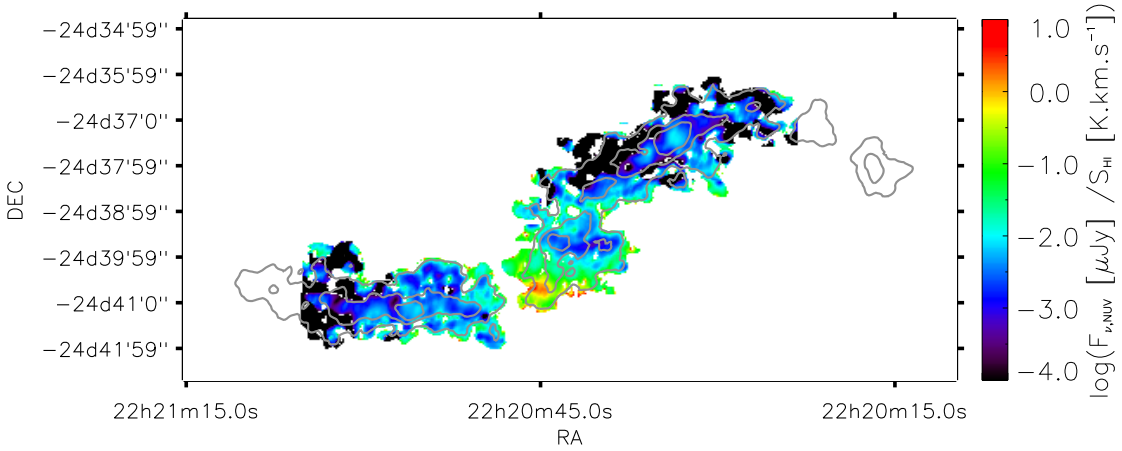


Figure 9.9: Distribution of the NUV/H I ratio across NGC 7252, at 4.5 kpc resolution. A logarithmic scale was used for the colour coding, such that the highest value of the ratio is 5 dex higher than the smallest value. Density contours at 0.2 $M_\odot$ pc$^{-2}$, 1.0 $M_\odot$ pc$^{-2}$ and 2.0 $M_\odot$ pc$^{-2}$ of a 21″ resolution map have been overlaid in grey. Regions of low gas column density can produce high values of the NUV/H I ratio.

## 9.2 The SFR – H I relation

### 9.2.1 Spatial variations of the NUV/H I ratio

In this section, we determine how the UV emission varies with H I line flux across the systems, from their inner to their outermost regions. In Figs. 9.9, 9.10, and 9.11, we present the spatial distributions of the NUV flux – H I line intensity ratio (a proxy of the unobscured SFR/H I ratio) for the 3 interacting systems in our sample: NGC 7252, Arp 245 and Arp 105, respectively. The UV/H I ratio maps highlight a spatial segregation:

- the highest values of the UV/H I ratio are found in the central regions, even before taking into account the high extinction there. As shown on the maps on which the H I contours have been superimposed, this excess cannot be solely due to the higher level of nuclear star-formation. In the case of NGC 7252 or NGC 3561A, it reveals rather a strong H I deficiency in the core of the merging systems. For instance, there is no detectable H I towards the nucleus of NGC 7252 while its star formation is as high as SFR = 8 $M_\odot$ yr$^{-1}$;
- the lowest values of the UV/H I ratio are found in the outer regions i.e., in the gas–rich tidal tails, with some local scatter, however, corresponding to prominent star forming regions. In particular at the tip of the tidal tails, the ratios can reach values similar to those found in the inner regions.

The H I deficiency in the central regions, and accumulation of gas in the outskirts has two origins. First, as a result of the gravitational torques that are exerted on the gas during the collision, large quantities of gas are expelled into the intergalactic medium (see Sect. 5.1). Second, the H I gas reservoir in central regions can be depleted by the (vigorous) star formation that takes place in them. A gas phase transition occurs there: H I is transformed into $H_2$ and is followed by star formation. Variations of the SFR/H I ratios would then originate from variations in the dense gas fraction, with higher fractions in nearby central regions. What precisely the UV/H I ratio tells about the SFE is discussed in the next chapter.

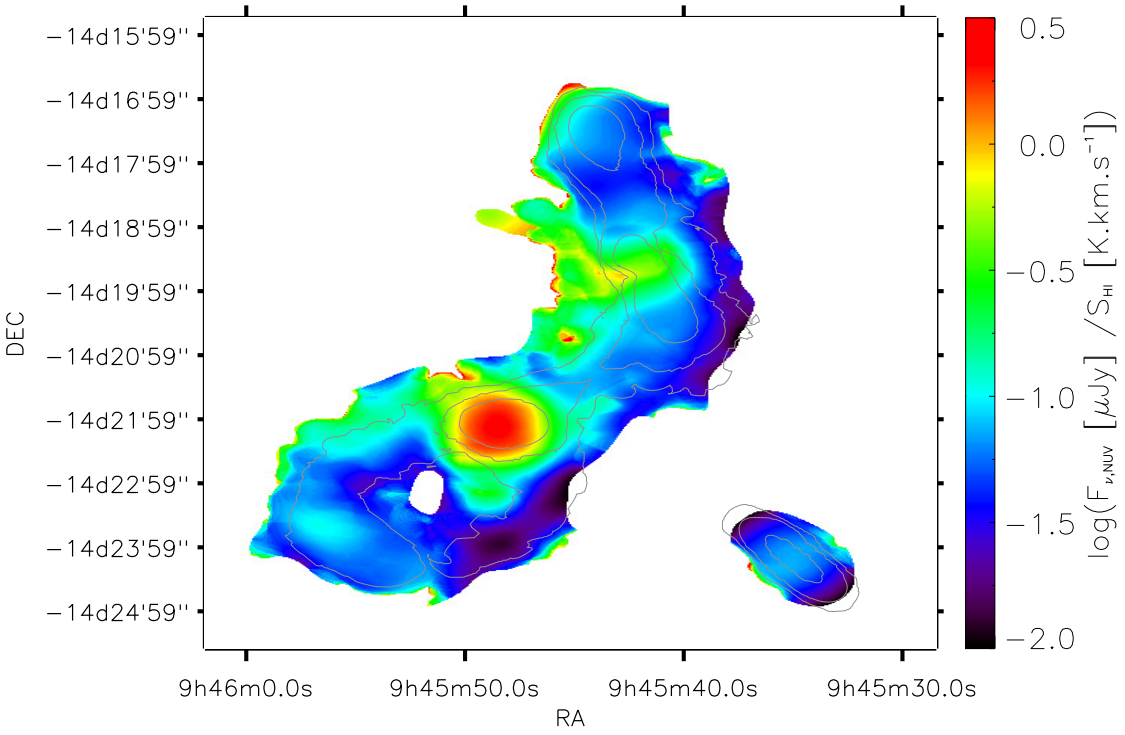


Figure 9.10: Distribution of the NUV/H I ratio across Arp 245, at 4.5 kpc resolution. A logarithmic scale was used for the colour coding, such that the highest value of the ratio is 2.5 dex higher than the smallest value. Density contours at 1.5 $M_\odot$ pc$^{-2}$, 4.0 $M_\odot$ pc$^{-2}$ and 9.0 $M_\odot$ pc$^{-2}$ of a 30″ resolution map have been overlaid in grey. Regions of low gas column density can produce high values of the NUV/H I ratio.

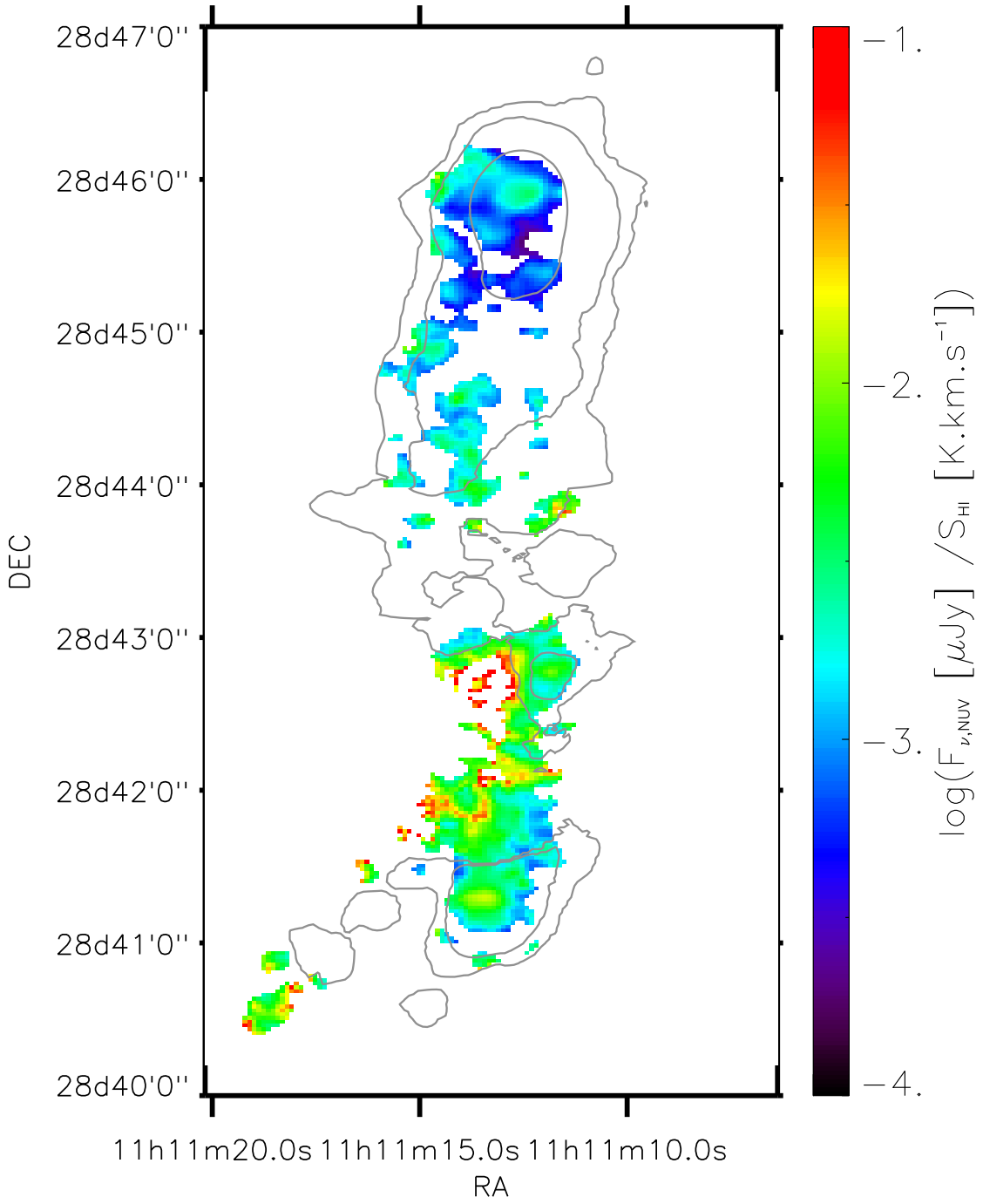


Figure 9.11: Distribution of the NUV/H I ratio across Arp 105, at 4.5 kpc resolution. A logarithmic scale was used for the colour coding, such that the highest value of the ratio is 3 dex higher than the smallest value. Density contours at 0.5 $M_\odot$ pc$^{-2}$, 1.5 $M_\odot$ pc$^{-2}$ and 5.0 $M_\odot$ pc$^{-2}$ of a 21″ resolution map have been overlaid in grey. Regions of low gas column density can produce high values of the NUV/H I ratio, like in the South-East detached region of the map.

### 9.2.2 The SFR – H I surface density relation

In this section we explore further the connection between H I gas and Star Formation by representing our sample of star forming regions in mergers in the $\Sigma_{SFR} - \Sigma_{HI}$ plane – see Fig. 9.12 and 9.13. Motivated by the observation of strong differences in the UV/H I ratios (see Sect. 9.2.1), we isolated the inner most, H I–poor, regions, representing them by squares, and used for the others a circle with size proportional to the projected distance to the centre of the progenitor galaxy.

The conditions that prevail in the outskirts of mergers — an H I-rich environment, with no prominent stellar disk — appear *a priori* similar to the ones found in the external regions of gas-rich spirals, and in star-forming H I–dominated dwarf galaxies. It was thus tempting to compare our investigation of the spatially resolved SFR – H I density relation with that made by Bigiel et al. (2010) in the outer discs of spiral galaxies and in dwarf galaxies, as part of the THINGS survey. Note though at this stage, that the resolution of their pixel to pixel analysis, $\sim 750$ pc, was much higher that the one we could achieve: 4.5 kpc.

We compare our results with those in the literature in Figs. 9.12 and 9.13. To increase the statistics for mergers, we added the star forming regions observed by Boquien et al. (2011) in the collisional debris of Arp 158 (6.4 kpc-resolution, H I-gas surface density measured at peak) and VCC 2062, a TDG candidate observed by Duc et al. (2004) around NGC 4694 (2 kpc-resolution). All these studies were made at different linear resolutions, we will discuss the bias that this introduces on their comparison below.

The figures highlight three domains of H I gas surface densities:

- for low gas surface densities, $\Sigma_{HI} \leq 1\,M_\odot\,pc^{-2}$, the statistics of star forming regions is small. These data show however that stars form even at low H I column densities. We do not observe a clear threshold for the onset of star-formation, a result in agreement with the study of Leroy et al. (2008);
- for intermediate gas surface densities, $1\,M_\odot\,pc^{-2} < \Sigma_{HI} \leq 5\,M_\odot\,pc^{-2}$, a correlation is found between $\Sigma_{SFR}$ and $\Sigma_{HI}$. The data points are located along the line of constant depletion time, $10^{10}$ yr. The H I depletion times for the external regions of mergers are found to be shorter, on average, than those found in the environment of outer discs of spirals and dwarf galaxies (Bigiel et al., 2010);
- for high gas surface densities, $\Sigma_{HI} > 5\,M_\odot\,pc^{-2}$, $\Sigma_{SFR}$ rises rapidly as a function of $\Sigma_{HI}$, until this reaches a saturation level beyond which the ISM becomes $H_2$ dominated. Apart from the central regions, no star forming regions in mergers exceeds an H I gas surface density of $\sim 15\,M_\odot\,pc^{-2}$ and a SFR density of $10^{-2}\,M_\odot\,yr^{-1}\,kpc^{-2}$. In galactic discs, Bigiel et al. (2008) measured the threshold of H I saturation at $9\,M_\odot\,pc^{-2}$. We will come back to the meaning of this threshold in Sect. 11.1.

### 9.2.3 The spatially resolved SFE, as traced by the UV/H I flux ratio

The UV/H I flux ratio is a proxy of the star-formation efficiency, at least in the regions where H I is the dominant gas phase. This is the case in the external regions of mergers, where the molecular fraction does not exceed 30 % (Braine et al., 2001). SFE is defined here as $\Sigma_{SFR}/\Sigma_{HI}$. Fig. 9.14 displays the mean SFE-H I relation for different bins of distances to the central galaxy and compares it to the fits to the data found by Bigiel et al. (2010) for their sample of outer disks and dwarfs. The plot is restricted to star-forming regions with $\Sigma_{HI} > 1\,M_\odot\,pc^{-2}$.

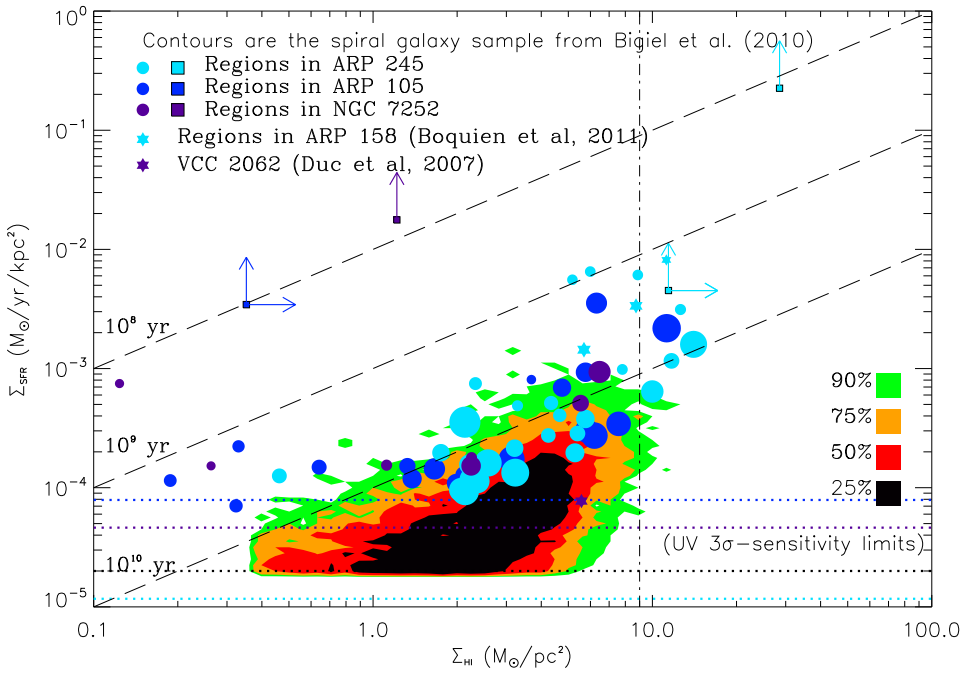


Figure 9.12: $\Sigma_{SFR} - \Sigma_{HI}$ density relation for our sample of star forming regions in mergers. All fluxes were corrected for internal and Galactic extinction. The size of the symbols is directly proportional to the distance of the star forming region to the central galaxy. Squares indicates the nuclei of the galaxies, for which extinction measurements were underestimated. For comparison, the data obtained by the pixel-to-pixel study of the outer discs of spiral galaxies by Bigiel et al. (2010) are plotted, together with additional data on mergers taken from the literature: Arp 158 and VCC 2062. The dashed lines represent lines of constant SFE (or constant depletion time). The vertical dotted line represents the saturation value of H I, as measured by Bigiel et al. (2008) from a sample of spiral galaxies.

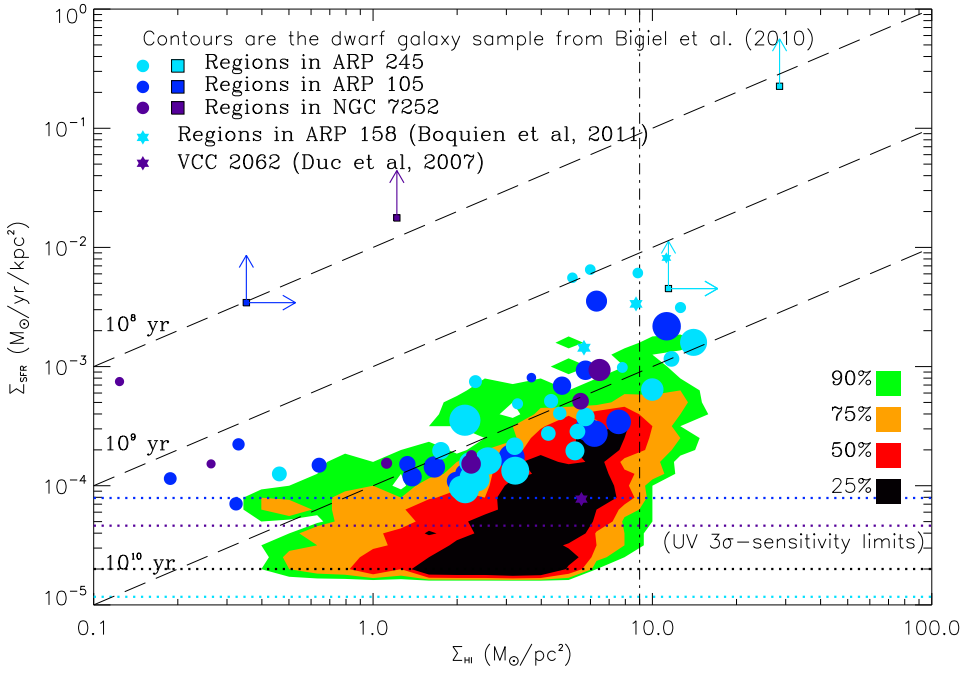


Figure 9.13: Same as 9.12, but showing the sample of dwarf galaxies of Bigiel et al. (2010).

On average, the external regions of mergers exhibit higher values of $\Sigma_{SFR}/\Sigma_{HI}$ than star forming regions located in the outer discs of spirals or dwarf galaxies. This is totally consistent with the predictions of the numerical simulations presented in Sect. 7.2. The innermost regions exhibit the highest $\Sigma_{SFR}/\Sigma_{HI}$ ratios, which will be interpreted in Sect. 11.2.

Despite the sensitivity limits of our data reaching down to $\sim 10^{-5}\,M_\odot\,yr^{-1}\,kpc^{-2}$, we do not observe any star forming region with $\Sigma_{SFR} < 5 \times 10^{-5}\,M_\odot\,yr^{-1}\,kpc^{-2}$. As shown below, the value of this minimum level is likely to depend on the size of the aperture used to measure the surface densities.

The pixel-by-pixel analysis of Bigiel et al. (2010) was made at $\sim 750$ pc resolution, whereas we made our analysis at the 4.5 kpc resolution. What would be the effects of using a smaller spatial sampling on:

(1) our surface densities? Two competing effects can change the distributions of surface densities (both the SFR surface density and the gas surface density) and their minimum (and maximum) values. On the one hand, smaller apertures would increase the scatter of the surface density distributions, by separating star-forming regions (previously averaged into the same single aperture). On the other hand, a higher resolution would come with a higher noise level, causing a clipping of the faintest star-forming regions. Then, depending on the space density of the star-forming regions in the system, and their relative intensity, the minimum surface densities could be lower (if the density of faint star-forming regions is high) or higher (if the system is dominantly populated by massive, vigorous star-forming regions). In our sample of interacting systems, the space density and the relative intensity (or mass) of the star-forming regions can vary a lot: near the tip of the north tail of Arp 245 we find several star-forming regions (some

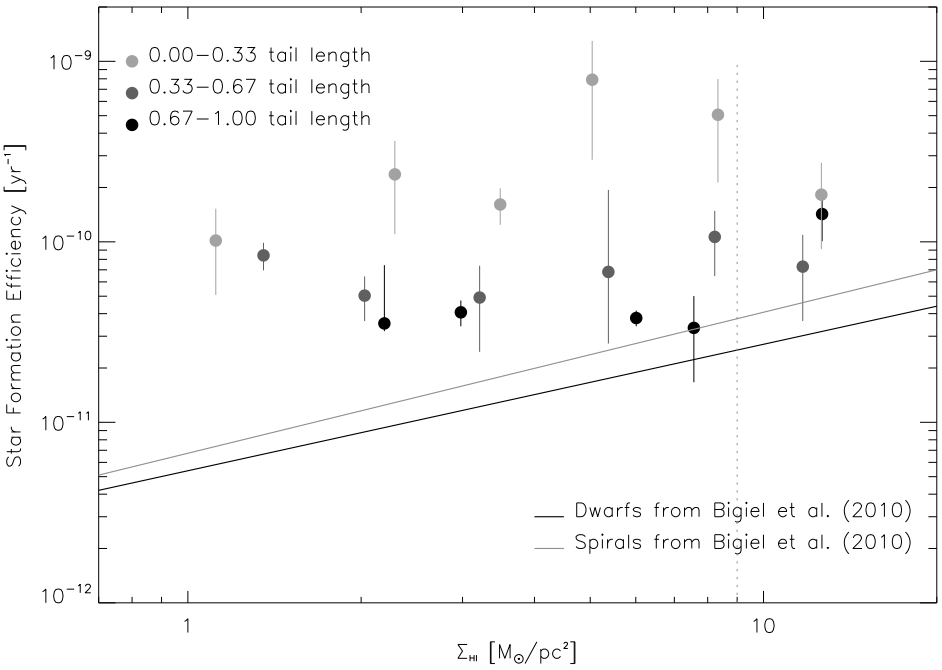


Figure 9.14: SFE-H I relation, per bin of $\Sigma_{HI}$ and distances to the central galaxy. The SFE is defined as $\Sigma_{SFR}/\Sigma_{HI}$. Filled circles correspond to the median SFE (corrected for extinction) and mean $\Sigma_{HI}$ within each bin. The error bars represent the statistical dispersion within each bin. When the statistical dispersion is greater than the median value, the lower error bar corresponds to [median - min value]. When the bins contain only one value, the statistical dispersion is taken to be half of the SFE. The solid lines are power-law fits to the distributions of spirals and dwarfs of Bigiel et al. (2010). In both cases, the slope is $\sim 0.7$. Estimates of the SFE take into account the contribution of helium (factor of 1.34).

are massive and extended, some are smaller and compact), whereas in NGC 7252 star-forming regions appear to be quite massive and well-detached from each other.

(2) their ratio (i.e., the SFEs) or the SFR-Gas relation? Fig. 15 in Bigiel et al. (2008) gathers several measurements of SFR surface densities and Total Gas surface densities, both made on a global scale (like Kennicutt 1998b) and on a small scale (like their own at the 750 pc-resolution). The overlap between the various kind of measurements suggests that the size of the aperture used to measure the surface densities has no (or little) effect on the SFEs or the SFR-Gas relation. Differences may arise at very small scales (see for instance Schruba et al. 2010 which explore the variations of the molecular gas depletion time down to a few tens of pc). Our measurement being made at a spatial resolution in between the 750 pc-resolution of Bigiel et al. (2008) and those of Kennicutt (1998b), we do not expect the SFR-Gas relation to be changed when using smaller apertures.

## 9.3 Effect of gas kinematics on the SFR – H I relation

In this section, we introduce a new parameter in our study of the Star Formation – H I gas connection: the velocity dispersion of the gas. Local measurements of dispersion velocities are made directly on the moment 2 of our data cubes, at the same resolution and within the same apertures as for the H I gas density.

Fig. 9.15 displays the maps of the H I velocity dispersion, organised as a function of merger stage. The ISM in our objects is highly turbulent: we measure averaged velocity dispersions of $26.7\,\mathrm{km\,s^{-1}}$, $32.4\,\mathrm{km\,s^{-1}}$, and $12.9\,\mathrm{km\,s^{-1}}$ in the outer regions of Arp 245, Arp 105 and NGC 7252, respectively. Note that the measurements were made in the tidal tails only, to avoid contamination by rotation or infall of gas in the central regions. As shown in Fig. 9.15, these values are much higher than those found in galaxy discs, in agreement with the predictions of numerical simulations.

Furthermore, we observe a correlation between the H I gas surface density and the velocity dispersion (See Fig. 9.16). Since we used a fixed linear resolution for all systems, gas surface densities are directly proportional to H I masses. The H I masses scale with velocity dispersion, following the Jeans mass relation: $M_J \propto \sigma^4$. The more turbulent the gas, the higher the gravitational potential needed to confine the gas to a bound structure. The scatter in the relation is important, partly because of biases in velocity dispersion measurements due to projection effects and rotation motions at small scales (in the TDGs; see a striking example in Sect. 12.2.3).

The velocity dispersion maps might also help to better understand the connection between the spatial distribution of the H I and star-forming regions. If NUV emission is never observed without being associated with H I (apart in some central regions), the opposite is not true. A few prominent gas clouds seem to have little star formation activity, like for instance at the base of the North West Tail of NGC 7252. In this region, we measure high levels of turbulence, up to 10 times higher than those found in star forming regions. This high turbulence is likely to explain why the SFR is low in these clumps. The process of dissipation of gas turbulence is key, it allows the contraction of the cloud. Therefore part of the scatter in the SFR–H I relation is explained by local variations of the gas turbulence.

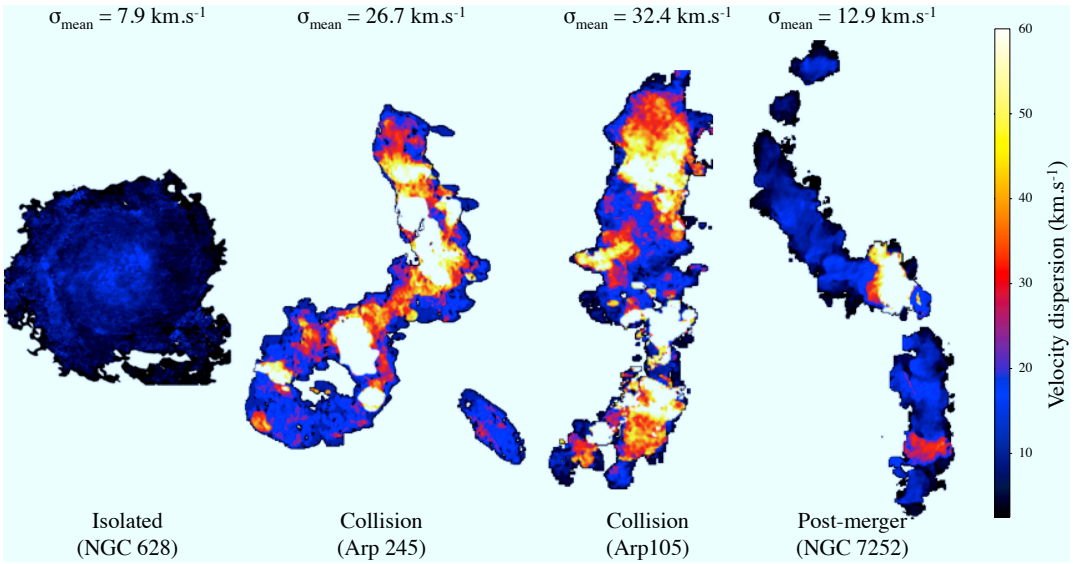


Figure 9.15: Evolution of the velocity dispersion of the H I gas as a function of merger stage. For the isolated case, a galaxy from the THINGS survey was used, NGC 628 (Walter et al., 2008). The moment 2 maps of each galaxy are shown, together with the mean velocity dispersion.

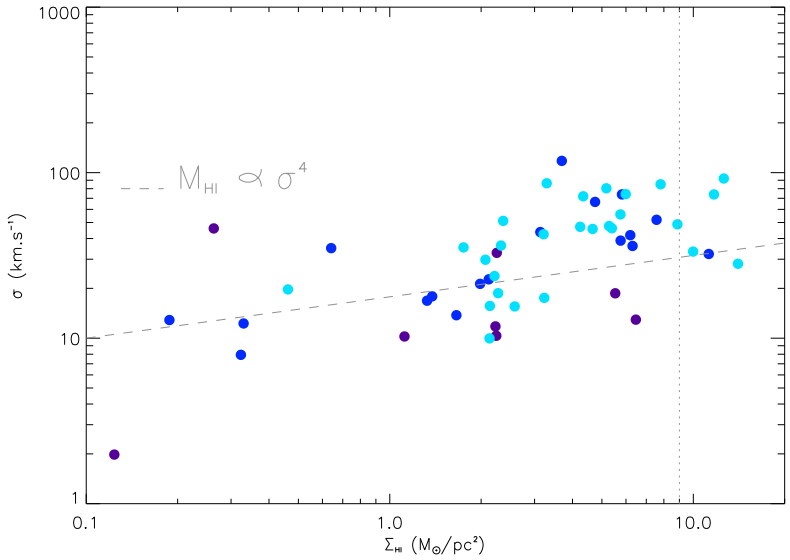


Figure 9.16: Mass – $\sigma$ relation in our sample of star forming regions in tidal tails of interacting systems. A colour is attributed per system. The Jeans relation has been represented by a grey dashed line.

## 9.4 Summary

Comparing, in a sample of interacting/merging starbursting galaxies, the H I and UV spatial distribution, and their flux ratio, we found that:

- On the $\Sigma_{SFR}$ vs $\Sigma_{HI}$ plane, the external, star-forming regions of mergers are located along a line of constant depletion time, $10^{10}$ yr;
- The SFR(UV)/H I ratio, a proxy of the SFE in H I–dominated regions, is higher on average in the external regions of mergers (in particular in the tidal tails) than in the outer discs of spirals or dwarf galaxies, a result consistent with the predictions of the hydrodynamical simulations presented earlier. However, the SFR(UV)/H I ratio is *globally* not enhanced to the level corresponding to the gas depletion time of $10^8$ yr, expected for mergers. Thus the outer regions alone cannot account for the strong deviations of the SK-relation shown by mergers;
- The scatter of the H I–UV relation is large, with highest values in the central regions of mergers, where an H I deficiency is observed, indicating a gas phase transition and/or a high SFE.

# Part IV

# Discussion and Future Prospects

# Chapter 10

# Extending the H I study

The study done as part of this thesis allowed us to obtain interesting trends, in particular the enhanced SFR/H I ratio in the outer most regions of colliding galaxies with respect to isolated disks. However our results relied on the analysis of the H I maps of only three systems. Besides we only used one tracer of the SFR: the UV which can suffer from extinction. An essential follow-up of this work is then its extension to a larger sample of galaxies and to other SFR tracers. We present below our plans in this direction.

## 10.1 The Chaotic THINGs project

Our understanding of the SFR-H I relation will be greatly improved by enlarging the sample of high resolution spectral line radio observations. This extension would first of all offer a broader range of star-forming region environments, including systems at different phases of the merger evolution, and increase the star-forming region statistics at a given stage of evolution. In addition, it will allow us to improve the spatial scale at which the star-forming regions are probed. Presently, the spatial resolution was set at 4.5 kpc, a value imposed by the best resolution achievable for the most distant system: Arp 105. Extending the survey would allow us a to define a statistically significant sample of nearby objects for which a kpc scale resolution is attainable instead. As argued in the first part of the thesis, this is a critical scale to study the star formation relations.

The above considerations have led to the definition of a project entitled "Chaotic THINGS" (PI: P-A. Duc), which has initially been granted 60 hours of JVLA observing time, distributed over 3 new interacting systems (at different stages of interaction): Arp 82, Arp 270, and The Mice (NGC 4676 A & B), to be observed in D, C, and B-array configurations. These new data represent a dramatic improvement over older, low-resolution, VLA data existing in the archives of these objects. The observing time was distributed taking into account the relative distance of the systems, the brightness temperature of their H I emission lines and the clumpiness of their tails (systems that apparently exhibit clumpy tidal tails were allocated more time in B-array relative to the other configurations). Observations in C-array and B-array configuration were done in 2012; observations in D-array configuration will be performed by the end of April 2013.

In parallel, more accurate measurements of the velocity dispersion of the H I gas will be performed. Thus far, the accuracy of these measurements is limited by projection effects, especially in edge-on tails, and small scale rotation at the location of Tidal Dwarf Galaxies (TDGs), which broaden emission lines. As shown by the numerical simulations of Bournaud et al. (2004), the

signature of projection effects can be identified in Position-Velocity diagrams. At a $2.5-5\,\mathrm{km\,s^{-1}}$ spectral resolution, i.e., below the minimum level of turbulence in the ISM, rotation motions and gas turbulence can be disentangled, provided the star-forming regions are resolved by the beam of the interferometer. This will likely lower the dispersion of the Mass - $\sigma$ scaling relation, presented in Fig. 9.16

## 10.2 The IR and $\mathrm{H}_\alpha$ tracers of star formation

Throughout this study, the SFR was estimated via the amount of UV light that is emitted by young stars (typically younger than 100 Myr). However, a fraction of the UV light is absorbed by the dust present in the ISM and re-emitted in the IR domain. The extinction causes the actual amount of UV radiation emitted by young stars to be underestimated. Two main methods can correct for this effect:

- the UV is directly corrected for extinction by measuring the amount of dust obscuration. It was estimated here from the H I column density, and the assumption of a standard dust-to-gas ratio. The method suffers from saturation effects, however, and is hampered by the H I deficiency in the core of some systems. A more straightforward way is to derive it from the mid– or far–infrared emission of the dust.
- the SFR estimated from the UV and the IR emission are combined into a hybrid SFR tracer.

Mid-IR 8.0 $\mu$m data from *Spitzer*/IRAC and 24 $\mu$m data from *Spitzer*/MIPS are already available for all our systems (See Table 10.1). Alternatively, SFRs can be estimated using Spectral Energy Distribution (SED) fitting. This requires the combination of multi-wavelength observations (NUV, FUV, Near-IR, mid-IR, Far-IR) in order to constrain as much as possible the fit (Boquien et al., 2010).

| | Near IR | | Mid IR | | | | Far IR | | | | | |
|---|---|---|---|---|---|---|---|---|---|---|---|---|
| | JHK bands | 2.4 $\mu$m[a] | 3.6 $\mu$m[b] | 4.5 $\mu$m[b] | 8.0 $\mu$m[b] | 24 $\mu$m[b'] | 70 $\mu$m[c] | 100 $\mu$m[c] | 160 $\mu$m[c] | 250 $\mu$m[c'] | 350 $\mu$m[c'] | 500 $\mu$m[c'] |
| ARP 245 | yes | yes | yes | yes | yes | no | no | no | no | yes | yes | yes |
| NGC 7252 | yes | yes | yes | yes | yes | yes | no | no | no | yes | yes | yes |
| ARP 105 | yes | no | yes | yes | yes | no | yes | yes | yes | no | no | no |

[a] N2 filter on Akari
[b] IRAC (*Spitzer*)
[b'] MIPS (*Spitzer*)
[c] PACS (*Herschel*)
[c'] SPIRE (*Herschel*)

Table 10.1: Near-IR, Mid-IR and Far-IR data available for the systems that have been considered so far.

# Chapter 11

# Adding the contribution of $H_2$ gas

We argued earlier that some interesting constraints could be obtained studying the H I density distribution; nevertheless molecular gas remains a key ingredient of star formation and there are regimes of Star Formation for which the $H_2$ gas simply cannot be ignored[1] and should at some point be included in our study of star-formation in mergers. We present below the few CO-based studies of *spatially resolved* SF that have so far been done on these objects and our plans for future molecular gas observations of our own sample.

## 11.1 Gas phase regimes in isolated galaxies

The study of the kpc-scale Star Formation law in the disc of nearby galaxies, in particular done as part of the THINGS survey, revealed several "regimes" of Star formation:

- the H I–dominated regime — for $\Sigma_{Gas} < 9\,M_\odot\,pc^{-2}$ — is characterised by low SFR/H I ratios, and a correlation between the $\Sigma_{SFR}$ and $\Sigma_{HI}$, with a power-law index of 1.7, though with a large dispersion. This regime prevails in particular in the outskirts of late-type galaxies and in dwarf galaxies (Bigiel et al., 2010).
- a transition regime occurs at $\Sigma_{Gas} = 9\,M_\odot\,pc^{-2}$; it is identified by the S-shape of the $\Sigma_{SFR}$ vs $\Sigma_{gas}$ curve, corresponding to H I gas saturation: beyond it, H I transforms into $H_2$ and thus at the kpc-scale, no H I gas is expected to be found above this gas column density threshold.
- in the $H_2$–dominated regime — for $9\,M_\odot\,pc^{-2} < \Sigma_{Gas} < 900\,M_\odot\,pc^{-2}$ — , the molecular gas is usually traced by the CO molecule; $\Sigma_{SFR}$ is tightly correlated with $\Sigma_{H2}$, scaling with a the power-law index of unity (Bigiel et al., 2008).
- above $900\,M_\odot\,pc^{-2} < \Sigma_{Gas}$, the molecular gas is dense enough to be traced by the HCN (see Gao & Solomon 2004a and references therein) or CS molecules; $\Sigma_{SFR}$ scales **linearly** with $\Sigma_{HCN}$ (Gao & Solomon, 2004b)[2].This might correspond to the so–called starburst

[1] Note though that a recent study by Krumholz (2012) shows that the formation of molecules in the ISM is not a necessary condition to star formation. Under some conditions, especially in a low metallicity environment (i.e., a strong deficiency in C, O, and N elements), gas can cool down rapidly enough so that it forms stars before the bulk of the phase converts into $H_2$ gas (i.e., before the gas phase becomes $H_2$–dominated). This relies on the difference of times scales between thermal equilibrium and chemical equilibrium of the gas.

[2] Note that $900\,M_\odot\,pc^{-2}$ corresponds to the typical gas density at which HCN is observed. Yet, based on extinction considerations in molecular clouds, Lada et al. (2010) argue that the threshold beyond which the relation between SFR and cloud mass is linear would be $\Sigma_{H2} = 116\,M_\odot\,pc^{-2}$

regime of mergers, characterised by a high dense gas fraction, although observations are still lacking at the kpc-scale to confirm this.

## 11.2 Gas phase regimes in mergers

Information on the molecular gas distribution of mergers is so far mostly available for the inner regions, even for nearby systems. In Sect. 9.1.1, we presented the masses of molecular and atomic gas found in the central regions of the interacting systems in our sample (see Tables 9.1, 9.2 and 9.3). In most cases, the $H_2$ far dominates the gas budget, which indicates that the central regions belong to the $H_2$–dominated or starburst regime described here-above.

The literature is rather poor on the molecular content of the outer regions of mergers. The vast majority of the data come from pointed observations of TDGs located in the collisional debris, and the spatial resolution is much higher than the kpc-scale achieved on nearby isolated spirals.

Braine et al. (2001) presents pointed CO(1-0) and CO(2-1) observations (at 115 and 230 MHz) with the 30-metre antenna on Pico Veleta (IRAM) of a sample of TDGs, some belonging to the systems studied here: Arp 245 (TDG Arp 245N), Arp 105 (TDG Arp 105S) and NGC 7252 (NGC 7252NW). On average, Braine et al. (2001) determined a molecular-to-atomic gas fraction of about 30% in collisional debris, with fluctuations from one system to the other, as shown in Fig. 11.1. Lisenfeld et al. (2009) found a molecular gas fraction smaller than 40% for a sample of 4 TDGs (VCC 2062, Arp 245N, J1023+1952, SQB), while Knierman et al. (2012) measured a fraction smaller than 10% in 3 star-forming regions located in the tidal tails of NGC 2782.

Therefore, in the external regions of mergers, at least those hosting TDGs, the atomic phase seems to dominate in mass. The SFR/H I ratio is for these regions a good approximation of the Star Formation Efficiency (SFE), as defined by the ratio of the SFR to the total gas mass. We could check this for three star-forming regions of our sample with available CO measurements from (Braine et al., 2001) (see Fig. 11.2). This corresponds to the H I–dominated regime that, as shown by Bigiel et al. (2010), also prevails in the outer discs of spirals. However, we observed that the SFE is higher, on average, in the external regions of mergers. As shown in Fig. 11.2, its value rather corresponds to the level observed at the optical radius of isolated galactic discs (Bigiel et al., 2008). Furthermore, in the case of mergers, $\Sigma_{SFR}$ is proportional to $\Sigma_{HI}$ (with a large scatter though); i.e. contrary to the external regions of spirals, the SFE or the gas depletion time, does not depend on the gas density, just like in the inner regions of spiral disks. In other words,*although the external regions of mergers are H I–dominated in mass, the SF law observed there seems to rather correspond to that of the $H_2$–dominated regime* described above. This is consistent with the numerical simulations presented in Chapter 7, which show how the increased gas turbulence in mergers contributes to triggering of the formation of dense pockets of molecular gas and thus increase the SFE.

We also observed in the mergers studied here a weak trend towards higher SFEs for star-forming regions closer to the central regions. However, as mentioned above, in the inner kpc regions, the molecular gas fraction rapidly increases, and the H I is no longer a good tracer of the total gas density. Without having high spatial resolution maps of the total (H I + CO) gas content in the central regions, we cannot yet determine how much the global enhancement of the SFE measured in our mergers (from values integrated over the whole galaxy) correspond to the increased SFE observed in the external H I–dominated regions or to a putative jump of the SFE in the nuclear starburst.

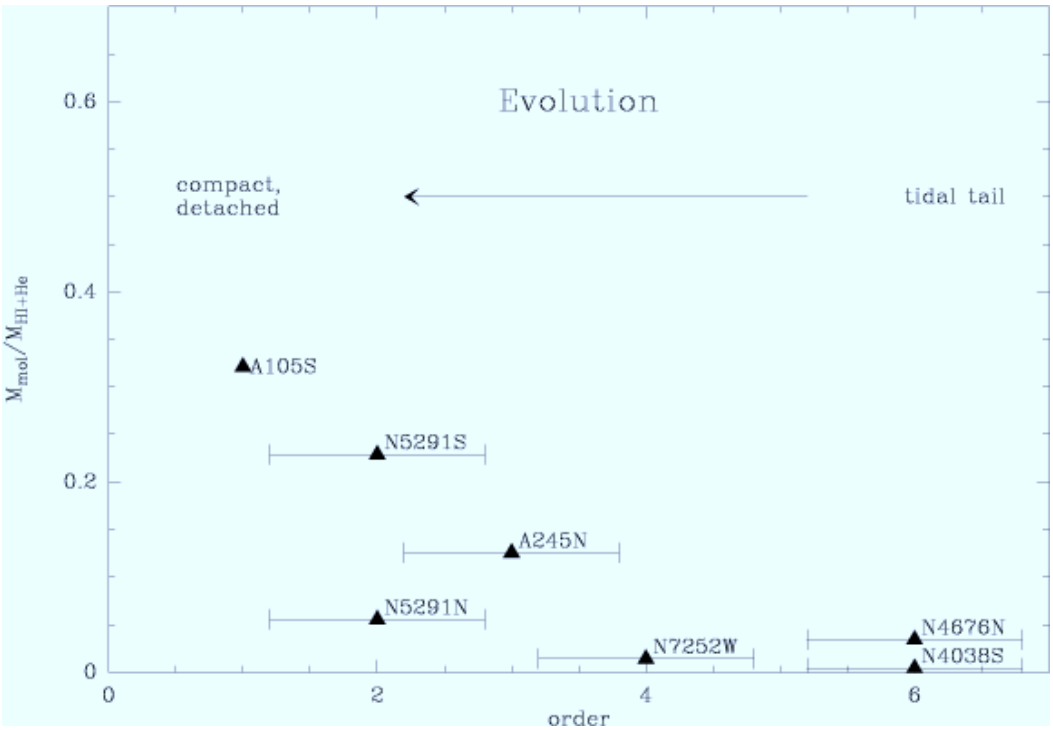


Figure 11.1: [From Braine et al. (2001)] Comparison of the $H_2$/H I mass ratios in different TDGs. The TDGs are sorted according to a possible age sequence.

The study by Boquien et al. (2011) of the interacting system Arp 158 is one of the first attempt to investigate the spatially resolved KS relation over an entire system. The distribution of molecular (CO), H I gas and star formation regions were compared. They found within that galaxy the two sequences of Star Formation highlighted by Daddi et al. (2010b), with the central regions corresponding to the starburst regime, and the tidal tails to the normal regime of isolated disks. Unfortunately, this study did not reach the kpc-scale resolution required to really probe the local environment.

Clearly, observations with millimetre–wave antennas (at IRAM, the PdBI, or eventually with ALMA) would be a natural follow-up of our H I-survey. As a first step in this direction, we (P.I.: N. Brassington) proposed CO observations with the IRAM/30m HERA receiver. Mapping the molecular gas at high resolution is however very costly. An alternative way to indirectly determine the total gas mass is through far-infrared observations of the dust component as explained in Chapter 12.

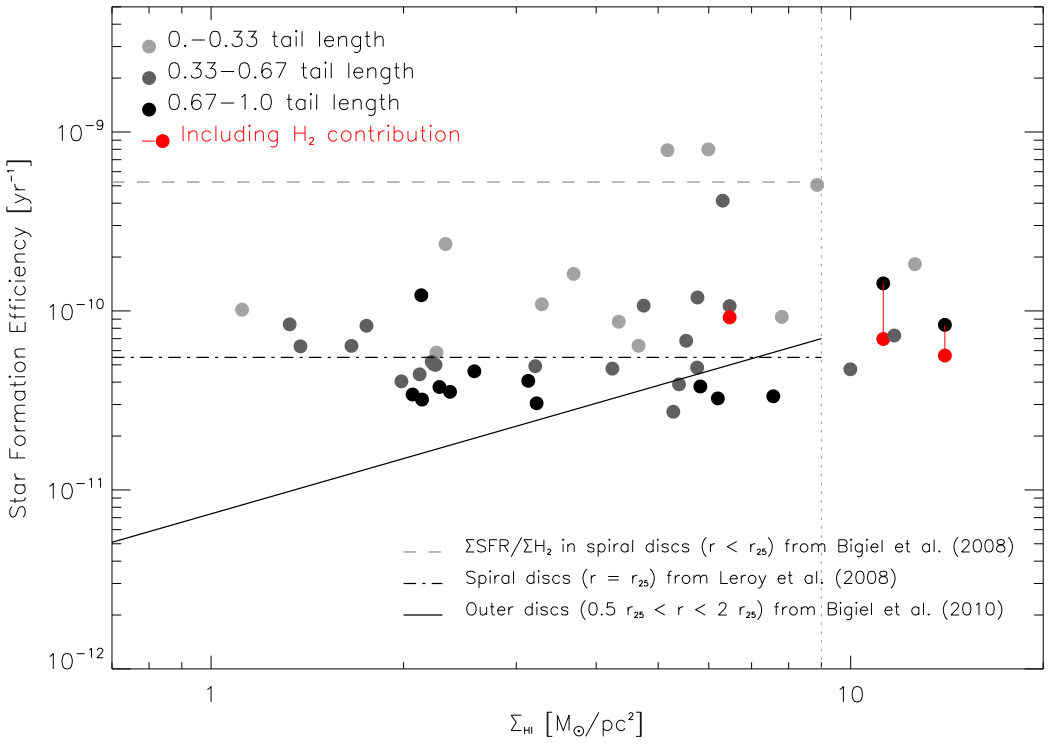


Figure 11.2: Star Formation Efficiency versus H I surface density in our merger sample, grouped into three bins of increasing distance to the central galaxy. Black and grey filled circles represent SFEs computed using the atomic gas component only, instead of the total gas mass. We checked the validity of this approximation for the outer regions of mergers for three star-forming regions with available CO data and thus for which we could determine the H I+$H_2$ mass (red points). The solid line corresponds to a power-law fit to the SFE versus $\Sigma_{HI}$ relation for the H I–dominated regime that prevails in the outer discs of spirals (Bigiel et al., 2010). The slope is about $\sim 0.7$. The dashed horizontal lines represent various estimates of the SFE at several galactocentric radii in isolated spirals computed using the total gas (H I+$H_2$) (Leroy et al., 2008) or $H_2$ only (Bigiel et al., 2008). All SFEs plotted in the figure take into account the contribution of Helium (a factor of 1.34 like in Bigiel et al. (2010)).

## 11.3 Uncertainties in the determination of the H I and $H_2$ mass and consequences for the KS–relation

### 11.3.1 Optically thick H I

Generally, the H I emission lines are assumed to be optically thin. This hypothesis is motivated by the usual physical conditions for optically thin H I emission lines as given by Kulkarni & Heiles (1988):

- H I column densities lower than $9 \times 10^{20}\,\mathrm{atom\,cm^{-2}}$;
- velocity dispersion within the $7 - 10\,\mathrm{km\,s^{-1}}$ range;
- brightness temperatures typically higher than 60 K, implying kinetic temperatures ($T_K$) greater than 50 K.

Unfortunately, this does not guarantee that all the H I is optically thin. Small regions with $T_K = 50\,\mathrm{K}$ and $\sigma \lesssim 1\,\mathrm{km\,s^{-1}}$ may exist in the ISM and hide some gaseous content. If thick, the brightness temperature of these lines emitted by these regions would be $\sim 50\,\mathrm{K}$. The issue of H I self–absorption was addressed by Zwaan et al. (1997) in order to assess the fraction of gas missed in their Arecibo H I extragalactic survey of the 21–cm line. Based on an empirical law by Haynes & Giovanelli (1984), they assessed the average fraction of missing H I mass to be $\sim 10\%$ (all galaxy morphologies gathered), and at most 20% (for Sb galaxies).

As a consequence, the SFE in outer regions of mergers, which we found to be approximately equal to the $\Sigma_{SFR}/\Sigma_{HI}$ ratio, could be overestimated by 10-20%. However, star-forming regions in outer discs of spirals and dwarf galaxies would be affected by this bias the same way which means that they can be compared nonetheless.

### 11.3.2 The infamous $X_{CO}$ factor

Until now, we assumed that the two sequences of the KS relation (starburst/disk) had been well established. However recent papers (Narayanan et al., 2011) raise doubts about it, claiming that it could be artificial and due to the way the molecular gas mass is determined. The $H_2$ mass is derived from the CO line fluxes, assuming a $X_{CO}$ conversion factor. Some studies of the properties of Giant Molecular Clouds in various environments tend to indicate that $X_{CO}$ is different in starbursts and in isolated disks (see e.g., Downes & Solomon 1998; Tacconi et al. 2008; Carilli et al. 2010), hence the choice of Daddi et al. (2010b) to choose two different factors for normal and starbursting galaxies. Had a single $X_{CO}$ factor been used, or a factor linearly varying with the local properties of the gas, as proposed by Narayanan et al. (2011), the difference between the SFEs of each class of galaxies would decrease.

The $X_{CO}$ factor has also been claimed to vary with metallicity. This may create an additional complication for studies of the KS relation in spiral disks which usually have a strong metallicity gradient. The apparent low molecular fraction in the H I dominated regime (in the outer H I disk) could partly be explained by the difficulty to detect CO in this very metal poor environment. In interacting systems however, due to the strong radial mixing that occurs during the merger (See Section 6.4.3), metallicity gradients are somehow erased. Thus, at least the Z-dependence of the $X_{CO}$ factor may be ignored.

The difficulties to measure the $H_2$ mass from CO lines is another reason to look for other tracers of molecular gas. The other methods we have explored are presented in the next chapter.

# Chapter 12

# Taking into account all the gas phases

A study of the SFE requires in principle taking into account the gas in all its phases: atomic hydrogen (and Helium), $H_2$ molecular hydrogen, as traced by CO, and the dense molecular gas traced for instance by the molecule HCN. Each of the tracers of the different phases of the gas has its own biases (see the uncertainties on the H I and $H_2$ mass estimates in Sect. 11.3.1 and 11.3.2) that could lead to an underestimate of the total gas mass. The difference between the mass determined from the usual tracers and the total gas mass is known as the "dark gas". Methods to estimate the quantity of dark gas fraction are described here. The nature of the dark gas is also discussed.

## 12.1 Dark gas in galaxies

### 12.1.1 Discovery and nature of the dark gas

There is increasing evidence for the existence of a phase of molecular gas that is not traced by CO, but which could be involved in the Star Formation process. Perhaps the most convincing case for the presence of dark gas in galactic disks comes from observations with the Planck telescope in the FIR-submm domain (350 and 500 $\mu$m) of our Milky Way. They showed an excess of thermal dust emission in an intermediate range of total gas (H I+CO) column density: $8.0-50\times10^{20}$ atom cm$^{-2}$ (Planck Collaboration et al., 2011c), consistent with earlier observations with COBE-DIRBE (Hauser et al., 1998). This FIR excess with respect to the emission expected from a standard dust-to-gas ratio likely reveals the presence of additional gas, not traced by molecular surveys.

Other observations and theoretical studies have led to the hypothesis of there being "dark gas":

- molecular gas not traced by CO was found by comparing *IRAS* 100 $\mu$m surface brightness maps to H I and CO emission lines surveys (Heiles et al., 1988; Blitz et al., 1990; Reach et al., 1994);
- $\gamma$-rays (with energy above 100 MeV) are produced by collisions of cosmic-rays with interstellar nucleons. They provide a global tracer of the total nucleon density, independent of that derived from H I and CO surveys. Using two different cold dust tracers, the emission

at 94 GHz and the reddening E(B-V), Grenier et al. (2005) unveiled vast clouds of cold dust not seen in radio nor submm, but detected in $\gamma$-rays. The excess emission is systematically located in the surroundings of CO clouds, bridging the molecular phase to the atomic phase of the cloud. Thus the hypothesis that the dark gas phase would be a photo-dissociated molecular gas region was raised. In the Milky Way, the minimum dark gas fraction was assessed to be 30% of the H I mass. More recently, Abdo et al. 2010 estimated the dark gas layer to represent about 50% of the mass traced in the CO-bright molecular cores;

- High Velocity Clouds (HVCs) are known to break the linear dust-to-gas relation (Lockman & Condon, 2005): the ratio E(B-V)/N(H I) is higher for HVCs, probably the consequence of the gaseous content they hide. IR observations of Complex C suggested that the amount of hidden H I could be high (Miville-Deschênes et al., 2005), even though no $H_2$ absorption line (Murphy et al., 2000) nor CO(1-0) emission (Dessauges-Zavadsky et al., 2007) has been detected so far in this system. The inter-clump gas or the physical conditions inside the HVCs may explain these non detections. For example, a fractal organisation of HVCs has been invoked to explain the potentially large amount of matter they could hide (Vogelaar & Wakker, 1994). Reddening excess is also observed in correlation with higher H I brightness temperatures in the galactic disc (typically $T_{\rm B}({\rm H\,I}) > 12\,{\rm K}$), suggesting that self-shielding of a dense atomic phase might be responsible for such an excess as well (Lockman & Condon, 2005). Parallel to this, UV–absorption lines were observed with FUSE in the galactic disc and the halo (low-velocity, intermediate velocity and high velocity clouds) and detected in some extragalactic targets (Wakker, 2006);

- from a theoretical point of view, Wolfire et al. (2010) and Glover et al. (2010) predict that an $H_2$ layer exists outside the CO region of a clump, in a photo-dissociated gas phase of C and C+. The fraction of dark gas is, again, about 30% of the molecular mass.

As an alternative to the dark gas hypothesis, another form of cold $H_2$, distributed in a rotationally supported disc but not involved in star formation, has been suggested by Pfenniger et al. (1994) as an alternative to the conventional dark matter[1]. They propose a phase of high-density[2] and cold[3] gas. The gravitational stability of the disc (i.e., preventing the formation of stars in the outer disc) would be ensured by a clumpy (fractal) structure (Pfenniger & Combes, 1994), resulting from the fragmentation of the clumps into small "clumpuscules" (Pfenniger et al., 1994) with typical densities of $10^9\,{\rm cm}^{-3}$, typical sizes of 30 AU and typical masses of $10^{-3}\,{\rm M}_\odot$. The gas would be sufficiently diluted to avoid (at least delay) the formation of stars. The hypothesis of dark matter in a disc is supported by a series of dynamical arguments: large spiral patterns in discs of galaxies (Bureau et al., 1999; Masset & Bureau, 2003), the presence of instabilities in the H I discs (Revaz et al., 2009) and especially vertical instabilities which may be at the origin of warps (Revaz & Pfenniger, 2004).

### 12.1.2 The detection of dark gas in our systems

We try to determine the dark gas fraction in our merging systems using two methods: from the dust distribution and from the kinematic analysis of collisional debris.

[1] "Conventional dark matter" refers to the massive component that dominates the rotation curve of galaxies at large radii

[2] hence encompassed in a small volume

[3] in practise the gas in the outer disc baths in a 3 K environment

We gained time on the *Herschel* space telescope to map the cold dust emission over the entire spatial extent of the interacting systems observed as part of the Chaotic THINGS survey. The total gas mass will be derived from the dust mass, assuming a constant gas-to-dust mass ratio. In starburst environments, this method has the great advantage of avoiding the use of an uncertain $X_{CO}$ factor and to provide additional tracers of star formation (like at 70 and 100 $\mu$m).

Bournaud et al. (2007) proposed an alternative method, based on the kinematics of TDGs. TDGs are self-gravitating structures born in collisional debris, with evidence of being rotationally supported (Bournaud et al. 2007; Duc et al. 2004). Because TDGs are made of "recycled" material, they share the "genetic signature" of their parent galaxy disk. In particular they should have inherited their dark gas but be devoid of dark matter. The kinematic information gleaned from these recycled, dark–matter poor and gas–rich, galaxies can be used to determine their total baryonic mass. From a detailed study of gravitationally bound objects in the $H_2$ collisional ring around NGC 5291, multi-wavelength observations of the system, coupled with dedicated numerical simulations, Bournaud et al. (2007) unveiled the presence of a missing mass, probably of baryonic origin. The dark component appeared to be rather important, about twice the total visible mass (dominated by the H I mass). The inferred dark gas fraction appeared to be much higher than what Planck had disclosed in the MW: about 30 %. Alternative explanations were proposed to account for the missing mass, such as modified gravity (Gentile et al., 2007). All this argues in favour of studying other interacting systems.

The following sections present our investigation of dark gas in the collisional debris of the "prototypical" advanced merger, NGC 7252.

## 12.2 Case study of dark gas detection: NGC 7252NW

### 12.2.1 Description of the system

With its single-nucleus remnant and prominent tidal tails, NGC 7252 is the prototype of an advanced stage merger; it is part of the famous Toomre sequence of galaxy mergers (Toomre, 1977). The global star-forming properties of NGC 7252 were presented in Sect. 9.1.1 and given in Table 9.3. The shape of the two tidal tails could be reproduced accurately by numerical simulations (Mihos et al., 1993; Hibbard & Mihos, 1995; Chien & Barnes, 2010).

Its northwest tail hosts, near its tip, a prominent H I condensation associated with a star forming region where $H_\alpha$ (Hibbard et al., 1994) and CO emission (Braine et al., 2001) had been detected. Its size, luminosity, and mass are typical of dwarf galaxies. Observations by Hibbard et al. (1994) suggest that this H I condensation could be self–gravitating and thus the object qualifies as a TDG, according to the definition proposed by Duc et al. (2004). We will refer to it as NGC 7252NW. Age estimates of the objects range between less than 100 Myr (from a Colour–Magnitude diagram; Knierman et al. 2003) to 300 Myr (from a fit of the Spectral Energy Distribution from the UV to the mid-IR; Boquien et al. 2010). In any case, NGC 7252NW is found to be younger than the host tail, dated at 770 Myr according to dynamical models by Hibbard & Mihos (1995). Interestingly, WFPC2 observations revealed a clumpy structure (Knierman et al., 2003) spread over about 1 kpc and embedded in high surface brightness material: NGC 7252NW is surrounded by seven star clusters that potentially formed before or simultaneously.

### 12.2.2 H I and $H_\alpha$ observations

The analysis of the gas composition and gas kinematics of NGC 7252NW is based on two components: atomic gas and ionised gas.

The JVLA observations that we presented in Sect. 8.3 provide the atomic gas component. These data have a considerably higher spatial and velocity resolution than those published by Hibbard et al. (1994). After combination of the different arrays (D+C+B) and continuum subtraction in the *uv*–domain, two sets of maps were produced using two different weighting functions:

- a "natural" weighting function, emphasising extended emission, resulting in a beam size of $20\farcs8 \times 15\farcs3$ and a sensitivity level of 0.6 mJy beam$^{-1}$ ;
- a "robust" weighting function (with the ROBUST parameter equal to 0.5), optimising resolution, resulting in a beam size of $15\farcs3 \times 13\farcs6$ and a sensitivity level of 0.7 mJy beam$^{-1}$.

At the distance of NGC 7252, the angular resolution achieved by our data set corresponds to a linear resolution of 4.5 kpc (at best), and, after Hanning smoothing, the spectral resolution is 5.2 km s$^{-1}$, about one fourth of the typical rotation velocity of TDGs.

Table 12.1 lists the properties of NGC 7252, component by component. Adopting the total H I mass based on our data we find $M(H\,I)/L_B = 0.1 M_\odot/L_\odot$ and $M(H_2)/M(H\,I) = 0.7$, (using $X_{CO} = 2 \times 10^{20}$ cm$^{-2}$ / (K km s$^{-1}$)), values that are similar to those found in NGC 3921, another prototype of a late-stage merger (Hibbard & van Gorkom, 1996).

In addition to the H I data, we obtained optical IFU data of NGC 7252NW of the $H_\alpha$ emission associated with the ionised gas in the central region. The optical angular resolution reaches down to angular sizes below $1''$. The optical data are complementary to the H I in the sense that they allow us to access the kinematics at much smaller scales (such as the innermost velocity gradient of the central region) and to confirm the velocity information at lower spatial resolution given by the H I data.

The data were taken with the GIRAFFE spectrograph mounted on UT2 of the VLT. They were reduced using the standard ESO FLAMES–GIRAFFE pipeline. The observing parameters are given in Table 12.2.

### 12.2.3 Kinematics of the H I gas

We carried out a detailed study of the gas kinematics of the region around NGC 7252NW. Fig. 12.1 shows the H I emission (green contours) associated with the stellar component of NGC 7252NW. $H_\alpha$ emission, represented as red contours, is associated with prominent optical emission.

We produced a Position–Velocity (PV) diagram using a crosscut along which H I spectra are extracted adapted to the geometry of the tidal tail: it follows the linear trend of the middle part of the tail then has a break at the top of the tail to track the upper part. We used a width of 4 pixels for the crosscut. Fig. 12.2 represents the crosscut we used (top) and the PV–diagram obtained (bottom). We identify two structures with different kinematic behaviour:

- a global velocity gradient, following roughly a linear trend and extending over several arcminutes ;
- a structure with a different kinematic signature, breaking the linear trend of the global gradient and associated with NGC 7252NW.

The fact that NGC 7252NW appears to be kinetically independent from the tidal tail implies it is likely a TDG. The global velocity gradient along the tidal tail is 0.5 km s$^{-1}$ kpc$^{-1}$, similar

Table 12.1: Global properties of NGC 7252 and its tidal tails

| | | |
|---|---|---|
| **Merger Remnant** | | |
| Centre position | $(\alpha_{2000}, \delta_{2000}) = (22^h20^m44^s, -24°40'41'')$ | Rothberg & Joseph (2006) |
| $V_{hel}$(optical spectroscopy) | $4792 \pm 1\,km\,s^{-1}$ | Rothberg & Joseph (2006) |
| Distance | $66.5 \pm 4.7\,Mpc$ | Assumed using $H_0 = 73\,km\,s^{-1}\,Mpc^{-1}$ |
| CO velocity | $4740 \pm 14.4\,km\,s^{-1}$ | Dupraz et al. (1990) |
| $M(H_2)$[1] | $3.5 \times 10^9\,M_\odot$ | Dupraz et al. (1990) |
| $L_B$ | $5.2 \times 10^{10} L_\odot$ | Dupraz et al. (1990) |
| $L_{IR}$ | $4.6 \times 10^{10} L_\odot$ | Dupraz et al. (1990) |
| $M_K$ | -24.84 | Rothberg & Joseph (2006) |
| $\sigma_0$ (central stellar velocity dispersion) | $166 \pm 5\,km\,s^{-1}$ | Rothberg & Joseph (2006) |
| **Northwestern Tail** | | |
| Velocity range ($km\,s^{-1}$) | $4660 - 4830$ | This study |
| $M_{HI}$ | $3.2 \times 10^9\,M_\odot$ | This study |
| B-R | $1.0 - 1.34$ | Hibbard et al. (1994) |
| $L_B$ | $0.30 \times 10^{10}\,L_\odot$ | Hibbard et al. (1994) |
| **Eastern Tail** | | |
| Velocity range ($km\,s^{-1}$) | $4745 - 4835$ | This study |
| $M_{HI}$ | $2.0 \times 10^9\,M_\odot$ | This study |
| B-R | $0.88 - 1.3$ | Hibbard et al. (1994) |
| $L_B$ | $0.09 \times 10^{10}\,L_\odot$ | Hibbard et al. (1994) |
| **Total** | | |
| Velocity range ($km\,s^{-1}$) | $4596 - 4837$ | This study |
| $M_{HI}$ | $5.45 \times 10^9\,M_\odot$ | This study |
| $L_B$ | $5.7 \times 10^{10}\,L_\odot$ | Hibbard et al. (1994) |
| $L_{IR}$ | $4.6 \times 10^{10}\,L_\odot$ | Dupraz et al. (1990) and references therein[2] |
| $M(H_2)$/ $L_B$ [1] | $0.06\,M_\odot/L_\odot$ | Dupraz et al. (1990); Hibbard et al. (1994) |
| $L_{IR}$ / $L_B$ | 0.9 | Hibbard et al. (1994) |
| $L_{IR}$ / $M(H_2)$ [1] | $13.2 \times\ L_\odot/M_\odot$ | Hibbard et al. (1994) |
| 21-cm line flux | $4.58\,Jy\,km\,s^{-1}$ | Richter et al. (1994) |
| 21-cm line flux | $5.0\,Jy\,km\,s^{-1}$ | This study |

[1] where we assumed $X_{CO} = 2.0 \times 10^{20}\,cm^{-2}\,/\,(K\,km\,s^{-1})$

[2] Lonsdale & Helou (1985) and Thronson et al. (1989)

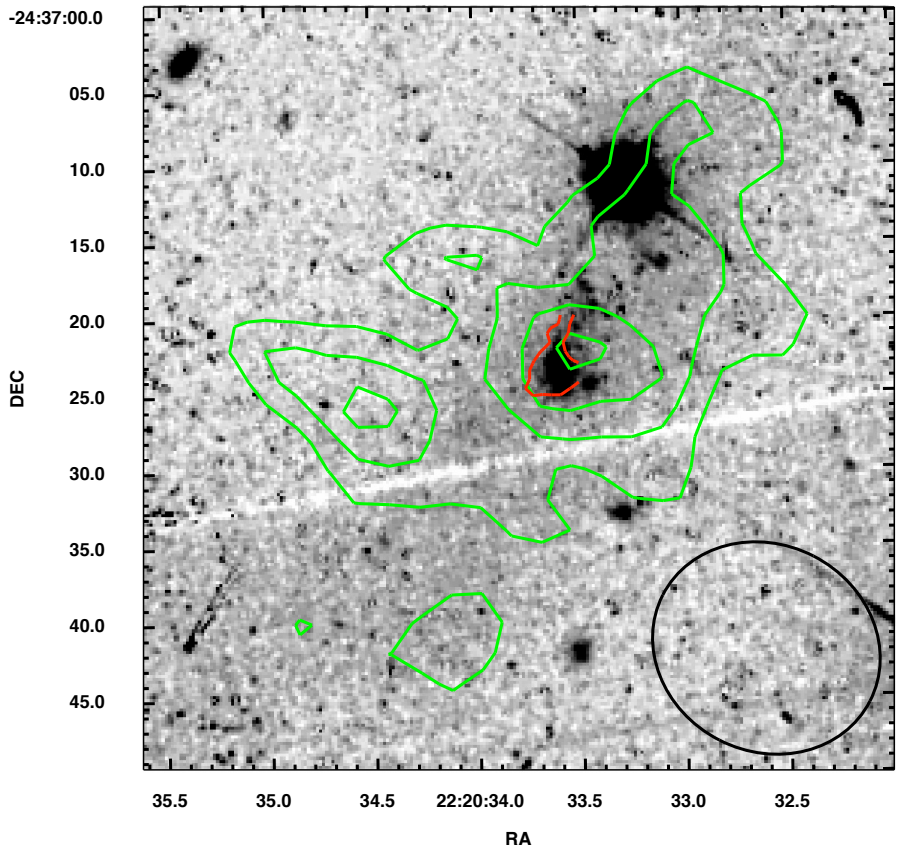


Figure 12.1: HST image (with F555 filter on WFPC2) of the TDG with H I (green) and $H_\alpha$ (red) contours overlaid. The H I contours span the range $3.0 - 6.0\,M_\odot\,pc^{-2}$ in steps of $1.0\,M_\odot\,pc^{-2}$. The $H_\alpha$ contour corresponds to the $7\sigma$ detection level. The spatial resolution of the H I data is that of the Robust–weight data (the beam is shown in the bottom right corner).

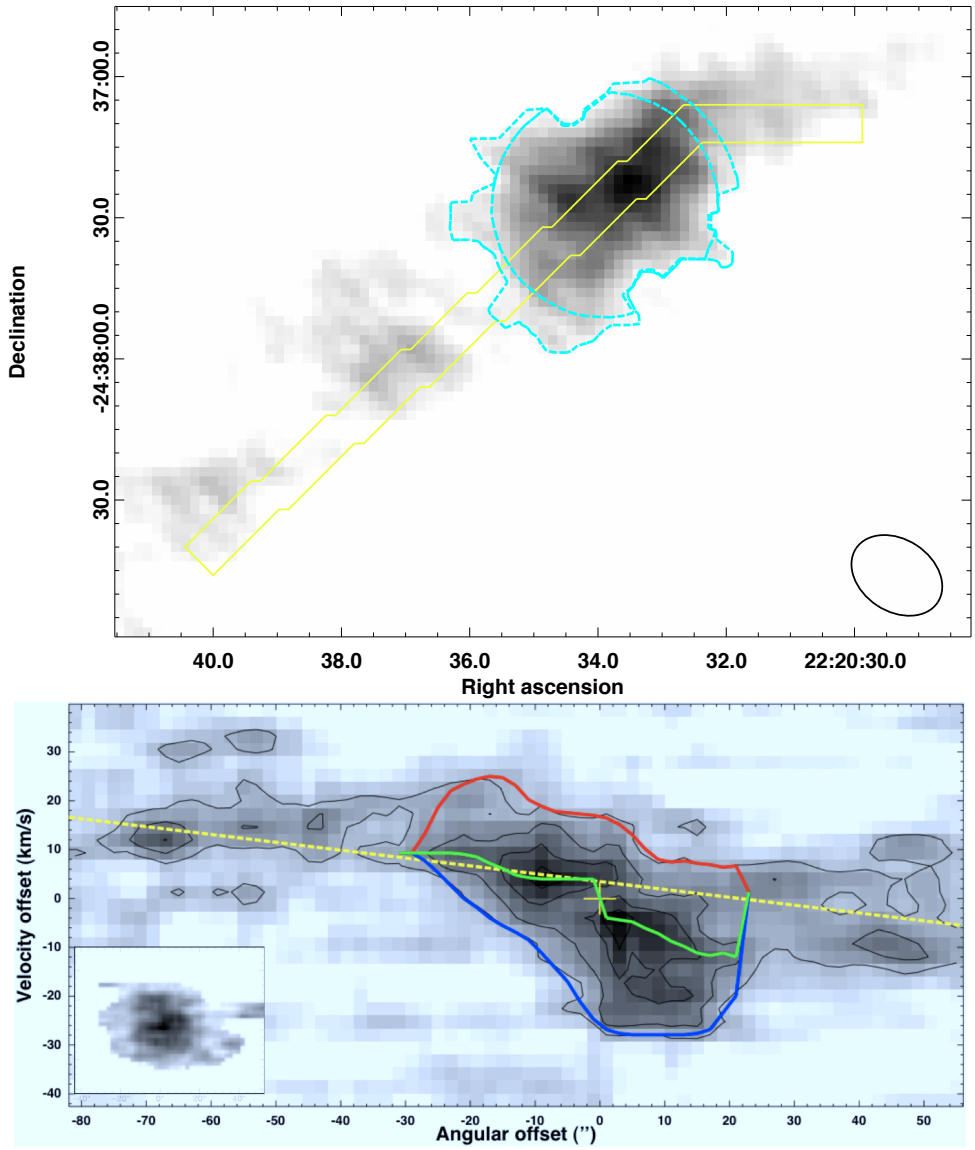


Figure 12.2: **Top panel:** Crosscut (yellow outline) used to extract the emission lines of the NWT. The width and the length of the crosscut indicate the pixels that were included. The outline follows approximately the shape of the tidal tail. We sampled and binned the data at 2″ interval. We show surface densities above a level of $1\,M_{\odot}\,pc^{-2}$. The cyan dashed regions represent the minimum and maximum spatial extents of the kinematic structure. **Bottom panel:** Position–Velocity diagram along the crosscut (grey scale) with black signal–to–noise ratio (S/N) contours overlaid at values of: $3\sigma$, $5\sigma$, $7\sigma$ and $9\sigma$. The green line shows the ridge line following the emission maximum along each line of sight. The red and blue lines show the width of the line measured at $2.5\sigma$ (see text for further details). The yellow dashed line represent the large scale velocity gradient of the tidal tail. The yellow cross locates the centre of the kinematic structure associated with the TDG. The PV–diagram along an orthogonal crosscut through the centre of the TDG is presented in the bottom left corner.

Table 12.2: Giraffe observing parameters

| | |
|---|---|
| Date | 20 Jul 2009 |
| Telescope | ESO–VLT–UT2 |
| Pointing ($\alpha_{2000}$, $\delta_{2000}$) | ($22^h20^m33.4^s$, $-24°37'24.2''$) |
| Instrument | Giraffe |
| Instrument mode | Argus |
| Grating Name | HR |
| Filter name | HR15 |
| Grating $\lambda_{central}$ (nm) | 665 |
| Grating $\Delta\lambda$ (nm) | 0.005 |
| Velocity resolution ($\mathrm{km\,s^{-1}}$) | 2.3 |
| Number of pixels | $14 \times 22$ |
| Pixel size | $0\farcs3 \times 0\farcs3$ |
| Field of view | $6\farcs6 \times 4\farcs2$ |
| Observatory (corrected) seeing | $0\farcs7$ |
| Integration time (s) | 1365 |

to the edge–on tidal tail seen in IC 1182 (Bournaud et al., 2004).

We extract the projected angular size and the gas motions (rotation and velocity dispersion) from the PV–diagram shown in Fig. 12.2. This diagram is based on Natural-weight data in order to obtain the highest sensitivity. The pixel size is $\delta P \times \delta V = 2'' \times 2.6\,\mathrm{km\,s^{-1}}$. The angular resolution along the position axis is $\sim 16''$.

The extent of the TDG corresponds to the outline delineated by the $5\sigma$ contour. The TDG blends with the NWT at the $3\sigma$ level. The TDG appears as a single kinematic structure with a velocity gradient that is distinct from that of the rest of the tidal tail, resulting in a Z–shape in the PV–diagram. The extent of the TDG falls within the range $3-5\sigma$. More precisely, the limits of the TDG are:

- on the SE side (with negative angular offsets) between -28″($5\sigma$ level) and -38″(where the emission becomes brighter in the tail than in the TDG);
- on the NW side (with positive angular offsets) between 20″($5\sigma$ level) and 24″.

Averaging these values gives an angular size of $55'' \pm 7''$. At a distance of 66.5 Mpc, this corresponds to a linear radius R = $8.9 \pm 1.1$ kpc. Fig. 12.2 (top) shows the minimum and maximum spatial extent of the TDG (cyan dashed lines) and shows the location chosen as the origin of the PV–diagram (yellow cross). This centre is slightly offset with respect to the H I peak density and the optical counterpart of the TDG, and is located at ($22^h20^m33\fs7$ ; $-24°37'24\farcs0$).

The two bright regions located symmetrically on either side of the adopted centre of the TDG (at $7\sigma$ and above), have velocity offsets relative to the TDG centre of ($\pm 4-5\,\mathrm{km\,s^{-1}}$) with respect to the centre of the kinematic structure (see yellow cross). Combined with the characteristic Z–shape, we take this as a strong indication that the H I gas associated with the TDG is rotating. If correct, this implies that the SE side of the TDG (associated with the left lobe) is red–shifted whereas the NW side is blue–shifted.

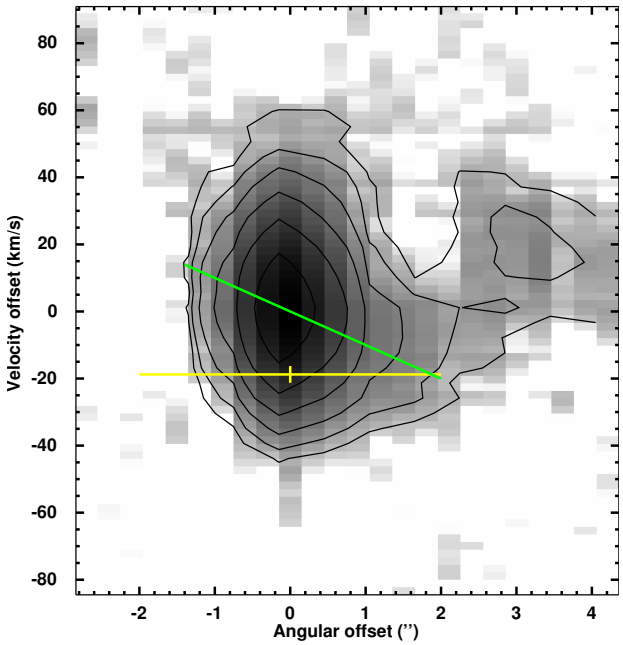


Figure 12.3: PV–diagram of $H_\alpha$ along the same crosscut as that used for the H I component. The yellow cross locates the centre of the kinematic structure associated with the TDG (see Fig. 12.2. The green line represents the velocity gradient, as expected from the H I kinematics (see Fig. 12.2).

### 12.2.4 Kinematics of the ionised gas

Fig. 12.3 shows a PV–diagram of the GIRAFFE data cube. This diagram is the analog of Fig. 12.2 for the $H_\alpha$ component and was obtained by using the same crosscut as for the H I component. The pixel size is $\delta P \times \delta V = 0.3'' \times 2.3\,\mathrm{km\,s^{-1}}$.

We do not see a velocity gradient in the GIRAFFE data. Any sign of rotation, if it exists, is hidden by the high velocity dispersion of the gas. The $H_\alpha$ emission line is broad: the FWHM is approximately $35\,\mathrm{km\,s^{-1}}$ and the line-width down to zero intensity is more than $90\,\mathrm{km\,s^{-1}}$ (which represents more than twice the value expected from the H I). A secondary peak, $3''$ to the East from the main peak, marks the location of a non-identified structure, possibly connected to the main one. All this suggests a highly turbulent structure, asymmetric and possibly in expansion.

The heliocentric central velocity of the $H_\alpha$ emitting gas is $4666 \pm 2.3\,\mathrm{km\,s^{-1}}$. The velocity of the H I emitting gas obtained from radio observations, $4681 \pm 2.6\,\mathrm{km\,s^{-1}}$, is somewhat offset with respect to this value but the data do not allow us to draw any inferences, e.g., the $H_\alpha$ showing a modest blue-shift with respect to the systemic velocity that could indicate outflow or an expanding ionised gas shell.

### 12.2.5 Mass budget

#### Dynamical mass

The velocity field of the TDG is not sufficiently resolved to apply a deprojection algorithm (such as a tilted–ring model). We therefore estimated the dynamical mass via:

$$M_{dyn} = \varepsilon \times \frac{R(V_{rot}^2 + \sigma^2)}{G} \tag{12.1}$$

In this equation

- $V_{rot}$ is the intrinsic rotation of the gas. The observed rotation velocity is $V_{rot}^{obs} = V_{rot}\sin(i)$. As $i$ is unknown, we will assume the TDG is seen edge–on ($i = 90°$) leading to a lower limit of the dynamical mass;
- $\sigma$ is the 3D–velocity dispersion of the gas. We will assume $\sigma = \sigma_r$ ($\sigma_r$ being the radial velocity dispersion), a conservative assumption discussed in Sect. 12.2.5;
- R is the linear radius of the gaseous structure associated with the TDG, as derived from the PV–diagram;
- $\varepsilon$ is a parameter introduced to take into account the non spherical mass distribution of a rotating disc. As mentioned by Bournaud et al. (2007), its value for TDGs hovers mostly around $0.95 \pm 0.05$.

For a relatively flat rotation curve, the rotation velocity is then given by the maximum (respectively minimum) velocity of a red–shifted (resp. blue–shifted) emission line. Simulations (see Fig. S4 by Bournaud et al. 2007) confirmed that the rotation velocity was best retrieved in a barely resolved case as we are dealing with here, by using velocities at 50% of the peak of emission ($w_{50}$). This is a more robust measure (Donley et al., 2006) than $w_{20}$ (width at 20% of the peak), which is more susceptible to noise (Koribalski et al., 2004). Authors like (Sancisi & Allen, 1979; Swaters et al., 2009) have shown, though, that in edge–on galaxies, the velocity is best retrieved based on the outer edges of the line profile, i.e., closer to using $w_{20}$. We will use $w_{20}$ throughout this analysis, and will compare with $w_{50}$, to see how either choice affects our results (see Sect. 12.2.5).

We indicate in Fig. 12.2 how we proceeded. The green line shows the ridge line defined by the peak intensity. The peak–to–peak velocity difference between the SE and NW sides of the TDG is $10\,\mathrm{km\,s^{-1}}$ with an unresolved transition near the centre of the TDG. The red and blue curves in Fig. 12.2 indicate the outer edges of the line profile (located by using $w_{20}$); they closely follow the $3\sigma$ contour.

The projected peak–to–peak rotation velocity, measured between the red curve in the SE and blue curve on the NW is $54\,\mathrm{km\,s^{-1}}$ which, assuming we see the TDG edge–on, gives a $V_{rot} = 26.8 \pm 5.0\,\mathrm{km\,s^{-1}}$.

The velocity dispersion of the gas around NGC 7252NW is shown in Fig. 8.12.b. We find a mean velocity dispersion of $\sim 7\,\mathrm{km\,s^{-1}}$ in the upper part of the NWT, and of $\sim 10\,\mathrm{km\,s^{-1}}$ in the lower part (just below the TDG). We conservatively adopt $7\,\mathrm{km\,s^{-1}}$ as the velocity dispersion of the H I gas.

Using the full spatial extent of the kinematic structure $\mathrm{R} = 8.9 \pm 1.1\,\mathrm{kpc}$ and $\varepsilon = 0.95$ results in:

$$\mathrm{M_{dyn}} \geq 15.0 \pm 7.1 \times 10^8\,\mathrm{M_\odot}.$$

**Total visible mass**

The visible mass of galaxies is dominated by three components: atomic gas, molecular gas, and stars.

The H I gas mass was measured from the H I data cube, by averaging the fluxes found in the two apertures represented in cyan in Fig. 12.2. We took into account the fact that a fraction of the gas within the apertures might not be bound to the TDG but belong to the tidal tail. Around the TDG, the gas surface density is about $1.1\,\mathrm{M_\odot\,pc^{-2}}$, we restricted the apertures[4] to regions where the gas surface density was above this threshold and obtained:

$$\mathrm{M(H\,I)} = 5.4 \pm 0.4 \times 10^8\,\mathrm{M_\odot}.$$

Corrected for the contribution of He (taken as 1.34 in mass fraction), we find:

$$\mathrm{M_{gas}} = 7.3 \pm 0.6 \times 10^8\,\mathrm{M_\odot}.$$

Because the metallicity of TDGs mimics that of the parent galaxies, CO is readily detected in these dwarf systems, contrary to low mass, low metallicity dwarf irregulars. Braine et al. (2001) derived a molecular mass of $0.2 \times 10^8\,\mathrm{M_\odot}$ (Table 2) for a distance of 64 Mpc. For a distance of 66.5 Mpc, this changes to:

$$\mathrm{M(H_2)} = (0.22 \pm 0.04) \times 10^8\,\mathrm{M_\odot}\ .$$

The emission from the underlying stellar population was measured from a Near–Infrared (NIR) image of NGC 7252 taken with the N2 filter (centred at $2.4\,\mu$m) of the *Akari* space telescope and published by Boquien et al. (2010). Their Table 1 gives a flux of $132.4 \pm 11.9\,\mu$Jy associated with the TDG in the NWT. Stellar masses are obtained by fitting the Spectral Energy Distribution (SED) from the Ultraviolet to the NIR (see Boquien et al. 2009, 2010, for details). The stellar mass of the TDG was found to be $94 \times 10^6\,\mathrm{M_\odot}$ . The uncertainty on this value may be quite high because of the strong contribution of two foreground stars. We modelled and subtracted the emission of these foreground stars and of the stellar background (from the tidal tail), and subsequently measured a value for the flux 2.7× lower than that given by Boquien et al. (2010). Erring on the conservative side, we decided, though, to retain the value published by these authors:

[4]Note that the mass inferred from the entire TDG area is obtained by averaging the values obtained within each of the two cyan apertures.

Table 12.3: Mass budget of NGC 7252NW, compared with the TDGs in NGC 5291 and VCC 2062

| Component | NGC 7252NW ($10^8$ M$_\odot$) | NGC 5291N ($10^8$ M$_\odot$) | NGC 5291S ($10^8$ M$_\odot$) | NGC 5291SW ($10^8$ M$_\odot$) | VCC 2062 ($10^8$ M$_\odot$) |
|---|---|---|---|---|---|
| Atomic (H I+He[1]) | $7.3 \pm 0.6$ | $5.7^{+0.8}_{-0.5}$ | $6.2^{+0.9}_{-0.6}$ | $3.3 \pm 0.1$ | 0.84 |
| $H_2$[2] | $0.22 \pm 0.04$ | $2.0 \pm 0.5$ | $2.3 \pm 0.6$ | no observation | 0.17 |
| Stars | $0.94^{a} \pm 0.08$ | $1.1^{b} \pm 0.3$ | $0.75^{b} \pm 0.3$ | $0.3 \pm 0.2$ | $0.3 - 0.7^{c}$ |
| Baryonic Mass | $8.5 \pm 0.7$ | $9.0^{+1.0}_{-0.7}$ | $9.3^{+1.1}_{-0.9}$ | $\sim 5.0 \pm 1.5$ | $\sim 1.6$ |
| Dynamical mass | $\geq 15.0 \pm 7.1$ | $30.0 \pm 8.6$ | $27.0 \pm 8.5$ | $12.0 \pm 4.5$ | $3 - 4 \pm 1$ |
| $M_{dyn}/M_{vis}$ | $\geq 1.8 \pm 1.0$ | $3.3^{+1.3}_{-1.2}$ | $2.9^{+1.3}_{-1.2}$ | $2.4 \pm 1.6$ | $\geq 2.2$ |

[1] using a ratio N(He)/N(H) = 0.085 (Asplund et al., 2009)
[2] using $X_{CO} = 2 \times 10^{20}$ [cm$^{-2}$ / (K km s$^{-1}$)] (Braine et al., 2001)
[a] Boquien et al. 2010
[b] from $K$–band and assuming $M/L_K = 0.3$
[c] Boquien 2007

$$M(\text{stars}) = (0.94 \pm 0.08) \times 10^8\, M_\odot\ .$$

The sum of all the components leads to a total detectable baryonic mass of:

$$M_{vis} = 8.5 \pm 0.7 \times 10^8\, M_\odot.$$

A summary of the mass budget of NGC 7252NW is given in Table 12.3. The contribution of the warm molecular gas and of the ionised gas are negligible in the total visible budget in systems such as TDGs; PAH emission lines were detected in two TDGs of NGC 5291 (Higdon et al., 2006) revealing that, in this system, the mass of the warm, ionised gas phase was less than 0.1% of the cold gas mass inferred from CO measurements. Ionised gas, as shown in Fig. 12.1 is confined to the innermost regions and represents a low fraction of the total gas. As is clear from Table 12.3 the dynamical mass appears to be higher, by at least a factor 2, than the visible mass.

### Missing mass

Thus, we derived a total visible mass and a lower limit of the dynamical mass for the TDG of:

- $M_{vis} = 8.5 \pm 0.7 \times 10^8\, M_\odot$;
- $M_{dyn} \geq 15.0 \pm 7.1 \times 10^8\, M_\odot$ .

The lower limit of the ratio suggests a discrepancy between dynamical budget and baryonic budget, with a 79% probability: $M_{dyn}/M_{vis} \geq 1.8 \pm 1.0$. $M_{dyn}/M_{vis}$. This depends on distance according to $D^{-1}$. It is clear that an uncertainty in the distance of NGC 7252 can hardly explain the observed discrepancy: to reconcile the two masses, the distance would have to be 1.8 times greater than the assumed distance of $66.5 \pm 4.7$ Mpc, which is not compatible with its error bars.

In what follows we will revisit the individual mass determinations, their uncertainties, and the implicit and explicit assumptions made.

| | $\alpha = 1$ | | | |
|---|---|---|---|---|
| $\sigma$ ($\mathrm{km\,s^{-1}}$) | 7 | 8 | 9 | 10 |
| Increasing rate (%) | 0.0 | 2.0 | 4.2 | 6.7 |
| | $\alpha = 2$ | | | |
| $\sigma$ ($\mathrm{km\,s^{-1}}$) | 7 | 8 | 9 | 10 |
| Increasing rate (%) | 6.4 | 10.3 | 14.8 | 19.7 |
| | $\alpha = 3$ | | | |
| $\sigma$ ($\mathrm{km\,s^{-1}}$) | 7 | 8 | 9 | 10 |
| Increasing rate (%) | 12.8 | 18.7 | 25.4 | 32.8 |

Table 12.4: Influence of the parameters involved in the rotation model ($\alpha$, $\sigma$) on the dynamical mass. The values of the dynamical mass are expressed in percent, relatively to the value obtained with the couple ($\alpha$, $\sigma$) = ($1, 7\,\mathrm{km\,s^{-1}}$).

### Uncertainties

**A conservative value of $\mathrm{M_{dyn}}$:** First of all, we highlight the existence of a preferential orientation of the crosscut used to extract the emission lines around the peak of H I density. Adopting a non-optimised orientation and location would result in a lower value of the dynamical mass. Although our tests did not reveal a better configuration, we underline the intrinsic limitation of this method: it is biased toward lower limits.

Then, from the PV–diagram, the dynamical mass is measured assuming a model for rotation. In Eq. 12.1, we introduced $\sigma$, the 3D–dispersion velocity of the gas, corresponding to the turbulent component of the kinetic energy of the system. However, observations only gives access to the radial component of this velocity, $\sigma_r$, such that $\sigma = \alpha \times \sigma_r$. The value of $\alpha$ is related to the dynamical properties of the medium:

- a collisional gaseous medium has an isotropic dispersion velocity: $\sigma_r = \sigma_t = \sigma_z$, which gives $\sigma^2 = 3 \times \sigma_r^2$;
- a purely non collisional medium gives $\alpha = 2$ (Ceverino et al., 2012).

Despite these theoretical considerations suggesting that for a real ISM one should adopt a value of $\alpha$ between 2 and 3, we choose a conservative approach and set $\alpha = 1$. In addition to this, we adopt $\sigma = 7\,\mathrm{km\,s^{-1}}$, a conservative value in comparison with $10\,\mathrm{km\,s^{-1}}$, the largely adopted value for ISM turbulence. A more realistic set of parameters ($\alpha$, $\sigma$) would give a dynamical mass between 6% and 30% higher than the conservative value we adopted (see Table 12.4). If the lower limit of the dynamical mass was 20% higher ($\alpha = 2$, $\sigma = 10\,\mathrm{km\,s^{-1}}$), we would obtain: $\mathrm{M_{dyn}/M_{vis}} \geq 2.2 \pm 1.2$ ($\mathrm{P(M_{dyn}/M_{vis} \geq 1)} = 0.84$).

Finally, the strongest assumption we made applies to the inclination angle of the spin axis of the TDG. We assumed the TDG is seen edge-on, which restricted our measurements to a lower limit of the dynamical mass. Based on the numerical model by Chien & Barnes (2010) and a 3D-visualisation of the system, we could estimate that the spin axis of the galaxy at the origin of the NWT was inclined by an angle of $\sim 60°$ with respect to the observer line-of-sight. Then, under the assumption that the spin axis of the TDG is perpendicular to the plane of propagation of the NWT, we can adopt 60° as an estimate of the inclination angle. Such an hypothesis is justified by the origin of TDGs: coming from the galactic disc, their spin axis is likely to have been aligned with the global kinetic moment of the system. The alignment and the stabilisation of the spin axis of structures is often a consequence of long–term effects of tidal forces. Using 60° as the inclination angle, we obtain the most likely estimate of the dynamical mass:

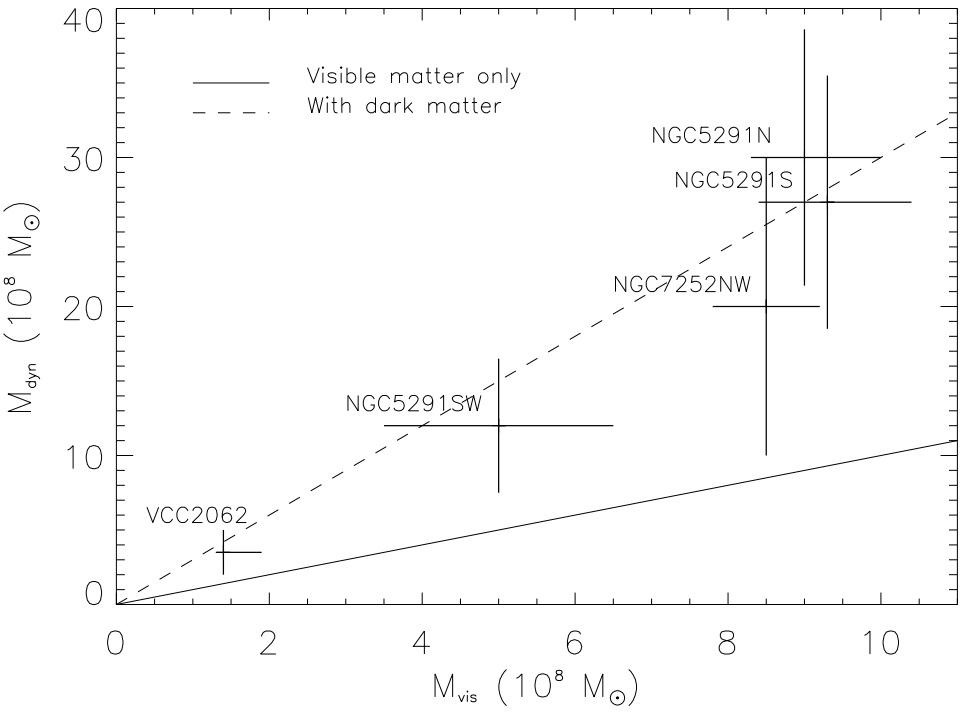


Figure 12.4: Visible and dynamical masses of five recycled galaxies. Dark matter-free objects would lie on the black plain line. The error bars of NGC 5291's objects were taken from Bournaud et al. (2007). The error bars of NGC 7252NW are associated to the most likely estimate of the dynamical mass (see text). The error bars of VCC 2062 are from Duc et al. (2000). The five galaxies define a trend for which the dark mass is about twice the visible mass (dashed line).

$$\mathrm{M_{dyn}} = 19.8 \pm 9.6 \times 10^8\,\mathrm{M_\odot}.$$

Fig 12.4 compares the most likely dynamical–to–visible mass ratio of NGC 7252NW, $2.3 \pm 1.3$, with those of TDGs in a similar system, NGC 5291 (Bournaud et al., 2007), and a dwarf irregular galaxy, VCC 2062 (a TDG candidate presented by Duc et al. 2007). The five objects show consistent values of the dynamical–to–visible mass ratio and makes the overall confidence level of dark matter detection greater than 99%.

**Factors that could lead to an over-estimating $\mathrm{M_{dyn}}$:** In the hypothesis where the TDG would not be completely detached from the tidal tail, a fraction of the unbound H I emitting gas could provide an additional contribution to the velocities measured in the PV–diagram and lead to overestimating $\mathrm{M_{dyn}}$. Using an extended crosscut through the NWT, we estimated the projected velocity gradient of the tidal tail to be approximately $0.5\,\mathrm{km\,s^{-1}\,kpc^{-1}}$ (see yellow curve on Fig. 12.2). For a 8.9 kpc (resp. 5.8 kpc) structure, the contribution can potentially be $4.5\,\mathrm{km\,s^{-1}}$ (resp. $2.9\,\mathrm{km\,s^{-1}}$). In practise, tests reveals that the shape of the rotation curve is modified only at large radii, with no effect on the determination of the rotation velocity itself. This behaviour is consistent with the small ratio of the kinetic widths of the tidal tail and the

TDG (see Fig. 12.2).

The most important factor that could lead to over-estimating $M_{dyn}$ is the choice of the line-width proxy. Based on the dynamical properties of the TDG and simple geometrical considerations, we adopted $w_{20}$ as best proxy of the line-width. Using half-peak velocities would provide a projected rotation velocity of $20 \pm 5.0\,km\,s^{-1}$, $23.1 \pm 5.8\,km\,s^{-1}$ if corrected by the inclination angle. This would lower the dynamical–to–visible mass ratio down to $1.3 \pm 0.7$, still implying a ratio greater than 1 with a 67% probability.

**Error bars and systematic biases on $M_{dyn}$:** The error bars that have been presented so far only reflect the precision of the measurements, we investigate here the accuracy of the method and adopt a conservative approach.

The main systematic bias of the method comes from the dynamical properties of the H I gas: its dispersion velocity produces a systematic scatter of $3.5\,km\,s^{-1}$ on the velocity measurements. This effect dominates the $2.6\,km\,s^{-1}$ instrumental error. In addition to this, the $\varepsilon$ parameter adds an extra 5% error on the dynamical mass measurement. We consider an inclination angle of 60° (with no error) and we take into account the error on the distance of the system.

Eventually, combining these biases gives: $M_{dyn} = 19.8 \pm 13.0 \times 10^8\,M_\odot$ (value corrected for projection effects). $M_{dyn}/M_{vis}$, which would equal $2.3 \pm 1.7$, would be greater than 1 with a 78% probability.

**Error bars on M(H I) and systematic biases:** We discuss here the contribution of systematic biases on the H I mass measurements. Three main biases can be accounted for.

First, the TDG–tail coupling, described in 12.2.5, biases our measurements toward higher H I masses. Since it has no effect on $M_{dyn}$, its effect translates to an underestimate of the actual dynamical–to–visible mass ratio. In the most unfavourable case, the contribution of the tidal tail is uniform across the whole TDG area and accounts for 41.5% of the measured H I mass. Then, once again, the value adopted for the H I mass of the TDG, which assumes no contribution from the tail, is conservative.

All the measures of H I masses are based on the assumption that the H I emission lines are optically thin (see Sect. 11.3.1). The brightness temperature of the lines we observe are $\sim 50\,K$, a value similar to that found for optically thick emission lines. This suggests that a fraction of the H I mass may be missed. Eventually, taking the TDG-tail coupling and a 20% mass fraction of optically thick H I, we obtain a total visible mass:

$$M_{vis} = 10.2^{+0.8}_{-5.0} \times 10^8\,M_\odot.$$

The errors bars on the total visible mass of the TDG implies a dynamical-to-visible mass ratio of $1.9^{+1.9}_{-1.1}$, higher than 1 with a 84% probability. From this likelihood and those found in previous sections, we conclude that, despite various uncertainties and systematic biases that affect the value of the ratio $M_{dyn}/M_{vis}$, the confidence in the presence of a dark component is never less than 67%, generally within the range 75-85% and up to 99% if measurements in other TDGs are taken into account.

**Stellar mass:** One may first think that the stellar content could be dominated by low–luminosity stars and would be largely underestimated. It was claimed that the Initial Mass Function could be top-heavy in the central regions of mergers, due to the extreme physical conditions of the gas. But stars represent only 11% of the total baryonic budget (see Table 12.3). Reconciling baryonic and dynamical budgets would imply that the stellar mass would have been underestimated by more than a factor 7. In other words, the mass-to-light ratio would be 7 times higher. This value is unrealistic, especially in the quiescent regions that are the tips of tidal tails.

**Molecular mass: an unusual CO–to–$H_2$ conversion factor?** The baryonic budget of the TDG involves the molecular component. To derive $M(H_2)$, Braine et al. (2001) used the CO(2-1) emission as a tracer of the molecular gas and a standard CO–to–$H_2$ conversion factor [$X_{CO} = 2 \times 10^{20}\,cm^{-2}\,/\,(K\,km\,s^{-1})$]. However, as discussed in Sect. 11.3.2, it is well known that this factor largely depends on the metallicity. Here, the metallicity of [12+log(O/H) = 8.6 ± 0.1] (Braine et al., 2001) is is close to the solar value, which is not surprising given the nature of the present system, a recycled galaxy made of material from the outer regions of a spiral galaxy (Duc, 1995). According to the $\alpha_{CO(1-0)}$ — 12+log(O/H) relation given by Genzel et al. (2012), the conversion factor $\alpha_{CO(2-1)}$ would give $M(H_2) = 3.3 \pm 0.6 \times 10^8\,M_\odot$ and $M_{vis} = 11.6 \pm 1.4 \times 10^8\,M_\odot$ in the most excessive case. This hypothesis would give a ratio of $1.7 \pm 1.0$, i.e. a 75% probability of having a ratio greater than 1.

Finally, an additional contribution to the molecular content can be provided by $H_2$ molecules not traced by CO, in a dense non star–forming form of gas. This hypothesis requires the presence of a different gaseous component, baryonic but unseen, it will be discussed in the next section.

### 12.2.6 Evidence for the presence of dark gas

In the following section, we consider the most likely value of the dynamical–to–visible mass ratio, about 2.3, and explore the implications of a discrepancy between dynamical and visible budgets.

If we adopt the standard Λ–CDM paradigm (Spergel et al., 2003), which successfully explains the formation of large scale structures, non–baryonic dark matter (NBDM) is distributed in extended isothermal halos supported by random motions (Navarro et al., 1996; Zemp, 2009). The typical velocity of the particles is expected to be a few $100\,km\,s^{-1}$, an order of magnitude higher than those found in TDGs. Baryonic matter falls into the centre of the potential well created by the massive halo and settles in a disc. The decomposition of galactic rotation curves reveals that baryonic matter dominates the mass budget in the first kpc around the galactic centre. This distribution has a direct effect on the composition of TDGs: they are mostly made of gas and should contain only a few percent of bound NBDM (Bournaud, 2010). Then, while travelling through the halo, TDGs should not be able to enrich significantly in NBDM (Barnes & Hernquist, 1992; Bournaud et al., 2004; Bournaud & Duc, 2006). Given the abundance of unseen matter we observe in the TDG material, we conclude that this component is mostly baryonic.

Dark, cold, molecular gas is a robust candidate. At the location of the TDG, we measure an H I column density of $7.9 \times 10^{20}\,cm^{-2}$. Braine et al. (2001) gives $I_{CO} = 0.27\,K\,km\,s^{-1}$ (CO(2-1) measurement) corresponding to $N(H_2) = 0.54 \times 10^{20}\,cm^{-2}$. Then, the total gas column density marginally fits within the range $8.0 - 50 \times 10^{20}\,cm^{-2}$, i.e., where recent observations by the Planck satellite suggested the presence of phase of dark gas. Nevertheless, estimating the abundance of dark gas in NGC 7252NW is difficult. In the Milky Way, the dark gas column density can represent up to 60% of the total hydrogen column density (Planck Collaboration et al., 2011a). But, in the case of a TDG, the contribution of the dark gas should be much less than this value, probably between 10% and 30%. The Planck collaboration (Planck Collaboration et al., 2011c,b) could map the spatial distribution of the dark gas and confirm its average abundance: 28% of the atomic gas mass and 118% of the CO emitting gas. The dark gas especially dominates over the $H_2$ traced by CO at high galactic longitude, outside the molecular ring and represents between 40% and 60% of the H I content (Planck Collaboration et al., 2011a). Taking the mass fractions inferred in the solar neighbourhood, 28% of M(H I+He) and 118% of $M(H_2)$, gives a total mass of $\sim 2.3 \times 10^8\,M_\odot$, that is, between 20% and 35% of the total missing mass in the TDG.

The abundance of dark gas appears to be insufficient to reconcile baryonic and dynamical budgets. An additional candidate could represent an important (dominant?) contribution in

the missing baryons budget of the TDG material. Several constraints must be satisfied by such a candidate. If in the form of cold gas, it escaped detection in the Planck surveys and is then not associated with dust. This implies that this putative cold gas does not participate in star formation and/or is too diluted to be observable. The hypothesis of Pfenniger et al. (1994), which we presented earlier, fits these conditions: a clumpy structure of small, cold and dense clumpuscules of molecular gas, not dense enough to trigger star formation and dispersed into the ISM would not been detectable and could represent a huge fraction of gas. If the candidate is not in a cold phase, the Warm Hot Intergalactic Medium[5] would be a plausible alternative hypothesis since it can represent a significant fraction of the baryons at low $z$, between 40 and 50% of the baryons according to numerical simulations (Cen & Ostriker, 2006). However, the hypothesis of missing baryons hidden in the WHIM has two main downsides in the case of TDGs. First, the WHIM is distributed in diffuse halos or filaments, and not in discs. As a result its contribution to the material of TDGs, which originates from galactic discs, is probably weak. Second, the WHIM is mostly found in clusters of galaxies implying that its relative contribution in isolated galaxies or pairs of interacting galaxies is likely to be much smaller.

### 12.2.7 Conclusions and perspectives

We have presented JVLA observations of the advanced stage merger NGC 7252. Thanks to the high spatial and spectral resolution achieved, we can probe the kinematic properties of the H I gas associated with what is now confirmed to be a TDG located in the North West tidal Tail of the system. Our study revealed that:

- the TDG is associated with a large halo of atomic gas with a projected radius of $8.9 \pm 1.1$ kpc and an H I mass of $5.4 \pm 0.4 \times 10^8\,M_\odot$;
- the TDG is supported by rotation (conform to the definition of a TDG as proposed by Duc et al. 2004), the projected rotation velocity being $26.8 \pm 5.0\,km\,s^{-1}$ ;
- a lower limit of the dynamical mass of the TDG is $15.0 \pm 7.1 \times 10^8\,M_\odot$.

The measurements have large uncertainties and suffer from the lack of knowledge of the inclination angle under which the TDG is observed. Despite these constraints, the dynamical-to-visible mass ratio shows a probability of being greater than 1 with a 79% probability, suggesting the presence of an unseen component. From numerical modelling, the most likely value of the inclination angle is estimated to be $\sim 60°$, resulting in a dynamical mass of $M_{dyn} = 19.8 \pm 9.6 \times 10^8\,M_\odot$ . This places NGC 7252's TDG on the $M_{dyn} - M_{vis}$ relation defined by 4 other TDGs, 3 in NGC 5291 (Bournaud et al., 2007) and VCC 2062 (Duc et al., 2007). This relation reveals, at more than a 99% confidence level, that a dark mass, hidden in the material of TDGs, corresponds to about twice the visible mass. In the specific case of NGC 7252's TDG, accounting for various systematic biases does not lower the confidence level below 67%.

According to the scenario of formation of TDGs, their material originates from the disc of the progenitor galaxy. Given the abundance of the dark component that is observed, it cannot be exclusively made of conventional non–baryonic dark matter. The mass of TDGs is dominated by gas, a significant contribution could then be provided by a phase of dark gas, i.e. a form of cold molecular gas associated with dust but with no H I nor CO counterpart. However, the recent results obtained with the Planck satellite (Planck Collaboration et al., 2011c) on the fraction

[5] At $z \geq 2$, observations of Ly$\alpha$ absorption lines revealed the presence of photo-ionised diffuse gas in the intergalactic medium (Rauch, 1998; Kirkman et al., 2003; Nicastro et al., 2005). This showed evidence that large amounts of baryons could reside in a tenuous Warm–Hot Intergalactic Medium (WHIM), distributed in halos or along filaments.

of dark gas in the Milky Way disc, do not allow us to explain the total missing baryon budget in NGC 7252's TDG. Future observations will reveal if alternative candidates such as hot gas in the WHIM or small clumpuscules of cold molecular hydrogen (Pfenniger et al., 1994), could represent a significant fraction of the missing baryons in the Local Universe, or, alternatively, if the fraction of dark gas was underestimated.

# Part V

# Conclusion and summary

The global objective of this thesis was to study the Star formation - Gas interplay in the extreme environment of colliding galaxies. The major merger of two spiral discs is expected to produce important modifications of the Inter-Stellar Medium (ISM) properties, resulting in particular in:

- an enhancement of the formation of massive star clusters, i.e., a higher fraction of young massive clusters in comparison with the fractions found in isolated discs;
- an increase in the efficiency of the star formation process, i.e., a higher Star Formation Rate (SFR) per unit of gas mass in comparison with isolated spiral galaxies.

To study these effects, I had at my disposal the output of a high-resolution numerical simulation of a wet major merger and a set of observational data on a sample of three colliding galaxies (Arp 245, Arp 105, and NGC 7252), including in particular high-resolution radio-interferometric Jansky Very Large Array observations of H I. For the modelling part of the thesis, I wrote a pipeline that allowed me to identify, track and thus determine the origin and fate of the star clusters that formed in the simulation. This is the first time such a detailed analysis could be done on a simulated merging system. For the observational part, I performed the data reduction and calibration of the radio-interferometric data and combined the H I maps I produced with tracers of star formation from archival data. The originality of our approach was to perform a *region-by-region* measurement of the SFR to H I mass ratio and compare it to that of isolated disks.

The analysis of the simulation revealed the formation of 15 massive clusters with masses above $10^{7.5}\,M_{\odot}$. Most of these Super Star Clusters formed early-on during the interaction, in the outer disc of the galaxies, suggesting that their formation is triggered by the increase of the gas turbulence in the system, in agreement with theoretical predictions. The compactness of the most massive clusters varied between those of Local Group dwarfs and Ultra-Compact Dwarfs; a few of them exhibit signs of rotation, like the Tidal Dwarf Galaxies (TDG) found in the tidal tails of interacting systems. Furthermore, the analysis of the shape of the Cluster Mass Function (CMF) seems to indicate that the population of (ultra-)massive clusters is in excess with respect to that expected given standard mass cluster distributions. Such a bi-modal distribution, or top–heavy CMF should be confirmed by even higher resolution numerical simulations that would furthermore help to determine the long-term evolution of the clusters and check whether some of them could be the progenitors of Globular Clusters. A Cluster Luminosity Function was computed, with basic assumptions on the stellar populations of the clusters, and compared to that measured on a sample of (Ultra)-Luminous Infrared mergers observed with the HST. Global agreements were found, indicating that our simulation, although idealised, was sufficiently realistic.

Hydrodynamical simulations of mergers developed by the Saclay team provided us with predictions on the effect of the collision on the structure and distribution of the ISM, in particular an increase of the turbulence triggering a change of shape of the Probability Density Function (PDF) of the ISM towards higher densities. I could check this in my sample of interacting galaxies. Their H I maps, tracing the low density gas, indicate that the external regions, in particular the tidal tails, are gas-rich, with the H I dominating by far the baryonic budget, while, for at least 2 galaxies, the inner regions are H I-poor. The SFR (determined from UV emission) and H I mass per unit area were compared at the 4.5 kpc-scale. The SFR/H I mass ratio in the external regions, a proxy of the Star-Formation Efficiency in that environment, was found to be higher than that found in H I–dominated regions of isolated systems, like the outer discs of spiral galaxies.

Besides, in the outer regions of mergers, the Star Formation Efficiency (SFE) or the gas depletion time, appears to be independent of the H I gas density, just as observed for the internal disks of isolated spiral galaxies, characterised by a high molecular gas fraction. In other words, the outskirts of mergers, though they are formally H I–dominated, show a regime of Star-Formation more characteristic of the one that prevails in the $H_2$–dominated regions of isolated spirals. Our H I and UV data does not allow us to derive the SFE in the inner starbursting regions and to investigate whether the global enhanced SFE found in nearby and distant starbursts, including in our systems — which translates in the widely used Kennicutt-Schmidt diagram with a double sequence —, is mostly due to the physical conditions of the gas there, or whether the enhanced SFE also found in the outer regions contribute to the excess.

Having a full census of the gas component is key for studies of the Star Formation process, in particular the SFE. Recent studies of the ISM of our Milky Way indicate that part of the gas might have been missed by traditional H I, or molecular line surveys. I exploited an original method, based on a kinematic analysis of the H I gas in gravitationally bound collisional debris, to probe the presence of this dark gas component. Indeed, missing mass was tentatively found in a TDG hosted by the advanced merger NGC 7252.

In summary, mergers contribute to enhance the dense gas fraction of the ISM over all the systems. This translates to a higher local Star-Formation-Rate to H I mass ratios, a triggered formation of massive clusters (possibly generating a top-heavy CMF), and likely, but not discussed in this thesis, in enhanced formation of massive stars, i.e., a top–heavy Initial Mass Function.

Future prospects of this work are multiple, especially on the observational side. Additional observations would be required to:

- decrease the spatial scale at which gas properties are probed, down to the 1–kpc scale, and improve the statistics on the number of sampled regions, so that a proper pixel-to-pixel analysis can be done on systems sampling the whole merger sequence and compared to that done on normal galaxies, in particular as part of the THINGS project. This is the goal of the on-going Chaotic THINGs project which started to acquire new H I observations with the upgraded Karl G. Jansky Very Large Array (JVLA).
- complement our H I data with other tracers of the gas, such as CO, tracing the intermediate density molecular component, or HCN tracing the densest phases, or even the far infrared emission of cold dust, which indirectly tells about the total gas content, including the so-called dark gas.

Herschel time has been approved for some of our targets whereas ALMA proposals have been written to probe the molecular component. Having the complete census of the gas, at the highest possible resolution, will allow us to probe the full shape of the PDF and at last be in a position to test, check or challenge the predictions of recent state of the art hydrodynamical simulations.

# Bibliography


Abdo, A. A., Ackermann, M., Ajello, M., et al. 2010, ApJ, 710, 133

Allen, L., Megeath, S. T., Gutermuth, R., et al. 2007, Protostars and Planets V, 361

Aniano Porcile, G. J., Draine, B. T., Gordon, K. D., & Sandstrom, K. 2012, in American Astronomical Society Meeting Abstracts, Vol. 219, American Astronomical Society Meeting Abstracts 219, 446.05

Asplund, M., Grevesse, N., Sauval, A. J., & Scott, P. 2009, ARA&A, 47, 481

Ballesteros-Paredes, J., Klessen, R. S., Mac Low, M.-M., & Vazquez-Semadeni, E. 2007, Protostars and Planets V, 63

Barnes, J. & Hut, P. 1986, Nature, 324, 446

Barnes, J. E. 1988, ApJ, 331, 699

Barnes, J. E. & Hernquist, L. 1992, Nature, 360, 715

Barnes, J. E. & Hernquist, L. 1996, ApJ, 471, 115

Bastian, N. 2008, MNRAS, 390, 759

Bastian, N., Adamo, A., Gieles, M., et al. 2012, MNRAS, 419, 2606

Bigiel, F., Leroy, A., Walter, F., et al. 2010, AJ, 140, 1194

Bigiel, F., Leroy, A., Walter, F., et al. 2008, AJ, 136, 2846

Blitz, L., Bazell, D., & Desert, F. X. 1990, ApJ, 352, L13

Bohlin, R. C., Savage, B. D., & Drake, J. F. 1978, ApJ, 224, 132

Bonnell, I. A., Smith, R. J., Clark, P. C., & Bate, M. R. 2011, MNRAS, 410, 2339

Boquien, M. 2007, PhD thesis, Université Paris Diderot

Boquien, M., Duc, P.-A., Galliano, F., et al. 2010, AJ, 140, 2124

Boquien, M., Duc, P.-A., Wu, Y., et al. 2009, AJ, 137, 4561

Boquien, M., Lisenfeld, U., Duc, P.-A., et al. 2011, A&A, 533, A19

Bouché, N., Cresci, G., Davies, R., et al. 2007, ApJ, 671, 303

Bournaud, F. 2010, Advances in Astronomy, 2010

Bournaud, F., Chapon, D., Teyssier, R., et al. 2011, ApJ, 730, 4

Bournaud, F., Duc, P., & Emsellem, E. 2008, MNRAS, 389, L8

Bournaud, F. & Duc, P.-A. 2006, A&A, 456, 481

Bournaud, F., Duc, P.-A., Amram, P., Combes, F., & Gach, J.-L. 2004, A&A, 425, 813

Bournaud, F., Duc, P.-A., Brinks, E., et al. 2007, Science, 316, 1186

Bournaud, F., Elmegreen, B. G., Teyssier, R., Block, D. L., & Puerari, I. 2010, MNRAS, 409, 1088

Braine, J., Duc, P.-A., Lisenfeld, U., et al. 2001, A&A, 378, 51

Braine, J., Lisenfeld, U., Duc, P.-A., & Leon, S. 2000, Nature, 404, 904

Bureau, M., Freeman, K. C., Pfitzner, D. W., & Meurer, G. R. 1999, AJ, 118, 2158

Caputi, K. I., Lagache, G., Yan, L., et al. 2007, ApJ, 660, 97

Cardelli, J. A., Clayton, G. C., & Mathis, J. S. 1989, ApJ, 345, 245

Carilli, C. L., Daddi, E., Riechers, D., et al. 2010, ApJ, 714, 1407
Cen, R. & Ostriker, J. P. 2006, ApJ, 650, 560
Ceverino, D., Dekel, A., Mandelker, N., et al. 2012, MNRAS, 420, 3490
Chapman, S. C., Blain, A. W., Smail, I., & Ivison, R. J. 2005, ApJ, 622, 772
Chary, R. & Elbaz, D. 2001, ApJ, 556, 562
Chien, L.-H. & Barnes, J. E. 2010, MNRAS, 407, 43
Corwin, Jr., H. G., Buta, R. J., & de Vaucouleurs, G. 1994, AJ, 108, 2128
Cowie, L. L., Songaila, A., Hu, E. M., & Cohen, J. G. 1996, AJ, 112, 839
Cox, T. J., Jonsson, P., Primack, J. R., & Somerville, R. S. 2006, MNRAS, 373, 1013
Daddi, E., Bournaud, F., Walter, F., et al. 2010a, ApJ, 713, 686
Daddi, E., Dickinson, M., Morrison, G., et al. 2007, ApJ, 670, 156
Daddi, E., Elbaz, D., Walter, F., et al. 2010b, ApJ, 714, L118
Dalcanton, J. J. 2007, ApJ, 658, 941
Dasyra, K. M., Tacconi, L. J., Davies, R. I., et al. 2006, ApJ, 638, 745
de Grijs, R., Anders, P., Bastian, N., et al. 2003, MNRAS, 343, 1285
Dessauges-Zavadsky, M., Combes, F., & Pfenniger, D. 2007, A&A, 473, 863
Di Matteo, P., Bournaud, F., Martig, M., et al. 2008, A&A, 492, 31
Di Matteo, P., Combes, F., Melchior, A.-L., & Semelin, B. 2007, A&A, 468, 61
Di Matteo, P., Montuori, M., Lehnert, M. D., Combes, F., & Semelin, B. 2011, in IAU Symposium, Vol. 277, IAU Symposium, ed. C. Carignan, F. Combes, & K. C. Freeman, 246–249
Donley, J. L., Koribalski, B. S., Staveley-Smith, L., et al. 2006, MNRAS, 369, 1741
Downes, D. & Solomon, P. M. 1998, ApJ, 507, 615
Duc, P. A. 1995, PhD thesis, PhD thesis. Univ. Paris , (1995)
Duc, P.-A., Bournaud, F., & Masset, F. 2004, A&A, 427, 803
Duc, P.-A., Braine, J., Lisenfeld, U., Brinks, E., & Boquien, M. 2007, A&A, 475, 187
Duc, P.-A., Brinks, E., Springel, V., et al. 2000, AJ, 120, 1238
Duc, P.-A., Brinks, E., Wink, J. E., & Mirabel, I. F. 1997, A&A, 326, 537
Duc, P.-A., Cuillandre, J.-C., Serra, P., et al. 2011, MNRAS, 417, 863
Duc, P.-A. & Mirabel, I. F. 1994, A&A, 289, 83
Duc, P.-A. & Mirabel, I. F. 1998, A&A, 333, 813
Duc, P.-A. & Renaud, F. 2012, Lectures Notes in Physics, in press (arXiv 1112.1922)
Dupraz, C., Casoli, F., Combes, F., & Kazes, I. 1990, A&A, 228, L5
Elbaz, D., Daddi, E., Le Borgne, D., et al. 2007, A&A, 468, 33
Elbaz, D., Dickinson, M., Hwang, H. S., et al. 2011, A&A, 533, A119
Ellison, S. L., Patton, D. R., Simard, L., & McConnachie, A. W. 2008, AJ, 135, 1877
Elmegreen, B. G. 2005, in Astrophysics and Space Science Library, Vol. 329, Starbursts: From 30 Doradus to Lyman Break Galaxies, ed. R. de Grijs & R. M. González Delgado, 57
Elmegreen, B. G., Kaufman, M., & Thomasson, M. 1993, ApJ, 412, 90
Elmegreen, B. G. & Scalo, J. 2004, ARA&A, 42, 211
Fall, S. M., Chandar, R., & Whitmore, B. C. 2009, ApJ, 704, 453
Fellhauer, M. & Kroupa, P. 2005, MNRAS, 359, 223
Fleck, J.-J. & Kuhn, J. R. 2003, ApJ, 592, 147
Fujii, M. S., Saitoh, T. R., & Portegies Zwart, S. F. 2012, ApJ, 753, 85
Gao, L., Springel, V., & White, S. D. M. 2005, MNRAS, 363, L66
Gao, Y. & Solomon, P. M. 2004a, ApJS, 152, 63
Gao, Y. & Solomon, P. M. 2004b, ApJ, 606, 271
Geller, M. J., Kenyon, S. J., Barton, E. J., Jarrett, T. H., & Kewley, L. J. 2006, AJ, 132, 2243

Gentile, G., Famaey, B., Combes, F., et al. 2007, A&A, 472, L25
Genzel, R., Tacconi, L. J., Combes, F., et al. 2012, ApJ, 746, 69
Gerhard, O. E. 1981, MNRAS, 197, 179
Gieles, M., Heggie, D. C., & Zhao, H. 2011, MNRAS, 413, 2509
Gingold, R. A. & Monaghan, J. J. 1977, MNRAS, 181, 375
Glover, S. C. O., Federrath, C., Mac Low, M.-M., & Klessen, R. S. 2010, MNRAS, 404, 2
Goerdt, T., Moore, B., Kazantzidis, S., et al. 2008, MNRAS, 385, 2136
González, V., Labbé, I., Bouwens, R. J., et al. 2011, ApJ, 735, L34
Gramann, M. 1988, MNRAS, 234, 569
Greisen, E. W. 2003, Information Handling in Astronomy - Historical Vistas, 285, 109
Grenier, I. A., Casandjian, J.-M., & Terrier, R. 2005, Science, 307, 1292
Hancock, M., Smith, B. J., Struck, C., Giroux, M. L., & Hurlock, S. 2009, AJ, 137, 4643
Harris, W. E. 1996, AJ, 112, 1487
Hauser, M. G., Arendt, R. G., Kelsall, T., et al. 1998, ApJ, 508, 25
Haynes, M. P. & Giovanelli, R. 1984, AJ, 89, 758
Heiles, C., Reach, W. T., & Koo, B.-C. 1988, ApJ, 332, 313
Hernquist, L. 1987, ApJS, 64, 715
Hernquist, L. & Katz, N. 1989, ApJS, 70, 419
Hibbard, J. E., Guhathakurta, P., van Gorkom, J. H., & Schweizer, F. 1994, AJ, 107, 67
Hibbard, J. E. & Mihos, J. C. 1995, AJ, 110, 140
Hibbard, J. E., Van der Hulst, J. M., Barnes, J. E., & Rich, R. M. 2001a, AJ, 122, 2969
Hibbard, J. E. & van Gorkom, J. H. 1996, AJ, 111, 655
Hibbard, J. E., van Gorkom, J. H., Rupen, M. P., & Schiminovich, D. 2001b, in Astronomical Society of the Pacific Conference Series, Vol. 240, Gas and Galaxy Evolution, ed. J. E. Hibbard, M. Rupen, & J. H. van Gorkom, 657
Higdon, S. J., Higdon, J. L., & Marshall, J. 2006, ApJ, 640, 768
Hopkins, P. F., Bundy, K., Croton, D., et al. 2010a, ApJ, 715, 202
Hopkins, P. F., Croton, D., Bundy, K., et al. 2010b, ApJ, 724, 915
Hubble, E. 1926, Contributions from the Mount Wilson Observatory / Carnegie Institution of Washington, 324, 1
Hunter, D. A., Ficut-Vicas, D., Ashley, T., et al. 2012, AJ, 144, 134
Iglesias-Páramo, J. & Vílchez, J. M. 2001, ApJ, 550, 204
Jordán, A., McLaughlin, D. E., Côté, P., et al. 2006, ApJ, 651, L25
Jordán, A., McLaughlin, D. E., Côté, P., et al. 2007, ApJS, 171, 101
Juneau, S., Narayanan, D. T., Moustakas, J., et al. 2009, ApJ, 707, 1217
Karl, S. J., Naab, T., Johansson, P. H., et al. 2010, ApJ, 715, L88
Kartaltepe, J. S., Dickinson, M., Alexander, D. M., et al. 2012, ApJ, 757, 23
Kaufman, M., Elmegreen, B. G., & Thomasson, M. 1994, in Mass-Transfer Induced Activity in Galaxies, ed. I. Shlosman, Cambridge: Cambridge University Press, 404
Kaviraj, S., Darg, D., Lintott, C., Schawinski, K., & Silk, J. 2012, MNRAS, 419, 70
Kaviraj, S., Ellis, R., Yi, S., et al. 2010, in IAU Symposium, Vol. 262, IAU Symposium, ed. G. Bruzual & S. Charlot, 168–171
Kaviraj, S., Peirani, S., Khochfar, S., Silk, J., & Kay, S. 2009, MNRAS, 394, 1713
Kennicutt, Jr., R. C. 1998a, ARA&A, 36, 189
Kennicutt, Jr., R. C. 1998b, ApJ, 498, 541
Kennicutt, Jr., R. C., Roettiger, K. A., Keel, W. C., van der Hulst, J. M., & Hummel, E. 1987, AJ, 93, 1011

Kim, J.-H., Wise, J., & Abel, T. 2009, in APS April Meeting Abstracts, G8009
Kirkman, D., Tytler, D., Suzuki, N., O'Meara, J. M., & Lubin, D. 2003, ApJS, 149, 1
Klypin, A., Kravtsov, A. V., Valenzuela, O., & Prada, F. 1999, ApJ, 522, 82
Knierman, K., Knezek, P. M., Scowen, P., Jansen, R. A., & Wehner, E. 2012, ApJ, 749, L1
Knierman, K. A., Gallagher, S. C., Charlton, J. C., et al. 2003, AJ, 126, 1227
Koribalski, B. S., Staveley-Smith, L., Kilborn, V. A., et al. 2004, AJ, 128, 16
Kroupa, P. 1997, New Astronomy, 2, 139
Kroupa, P. 1998, MNRAS
Kroupa, P. 2001, MNRAS, 322, 231
Kroupa, P. & Weidner, C. 2003, ApJ, 598, 1076
Krumholz, M. R. 2012, ArXiv e-prints
Krumholz, M. R., McKee, C. F., & Tumlinson, J. 2009, ApJ, 699, 850
Kulkarni, S. R. & Heiles, C. 1988, Neutral hydrogen and the diffuse interstellar medium (Kellermann, K. I. and Verschuur, G. L.), 95–153
Lada, C. J., Forbrich, J., Lombardi, M., & Alves, J. F. 2012, ApJ, 745, 190
Lada, C. J. & Lada, E. A. 2003, ARA&A, 41, 57
Lada, C. J., Lombardi, M., & Alves, J. F. 2010, ApJ, 724, 687
Lamers, H. J. G. L. M., Gieles, M., Bastian, N., et al. 2005, A&A, 441, 117
Larsen, S. S. 2002, AJ, 124, 1393
Larsen, S. S. 2009, A&A, 503, 467
Le Floc'h, E., Papovich, C., Dole, H., et al. 2005, ApJ, 632, 169
Lequeux, J., Peimbert, M., Rayo, J. F., Serrano, A., & Torres-Peimbert, S. 1979, A&A, 80, 155
Leroy, A. K., Walter, F., Bigiel, F., et al. 2009, AJ, 137, 4670
Leroy, A. K., Walter, F., Brinks, E., et al. 2008, AJ, 136, 2782
Lisenfeld, U., Bournaud, F., Brinks, E., & Duc, P.-A. 2009, ArXiv e-prints
Lockman, F. J. & Condon, J. J. 2005, AJ, 129, 1968
Lonsdale, C. J. & Helou, G. 1985, Cataloged galaxies and quasars observed in the IRAS survey (ESO)
López-Sanjuan, C., Balcells, M., Pérez-González, P. G., et al. 2010, ApJ, 710, 1170
López-Sanjuan, C., Le Fèvre, O., de Ravel, L., et al. 2011, A&A, 530, A20
Lotz, J. M., Jonsson, P., Cox, T. J., et al. 2011, ApJ, 742, 103
Lucy, L. B. 1977, AJ, 82, 1013
Mac Low, M.-M. & Klessen, R. S. 2004, Reviews of Modern Physics, 76, 125
Magnelli, B., Elbaz, D., Chary, R. R., et al. 2009, A&A, 496, 57
Maraston, C., Bastian, N., Saglia, R. P., et al. 2004, A&A, 416, 467
Maraston, C., Kissler-Patig, M., Brodie, J. P., Barmby, P., & Huchra, J. P. 2001, A&A, 370, 176
Marchesini, D., van Dokkum, P. G., Förster Schreiber, N. M., et al. 2009, ApJ, 701, 1765
Masset, F. S. & Bureau, M. 2003, ApJ, 586, 152
McCrady, N. & Graham, J. R. 2007, ApJ, 663, 844
McLure, R. J., Pearce, H. J., Dunlop, J. S., et al. 2012, ArXiv e-prints
Melott, A. L., Einasto, J., Saar, E., et al. 1983, Physical Review Letters, 51, 935
Mendes de Oliveira, C., Plana, H., Amram, P., Balkowski, C., & Bolte, M. 2001, AJ, 121, 2524
Metz, M. & Kroupa, P. 2007, MNRAS, 376, 387
Mieske, S., Hilker, M., & Misgeld, I. 2012, A&A, 537, A3
Mihos, J. C., Bothun, G. D., & Richstone, D. O. 1993, ApJ, 418, 82
Mihos, J. C. & Hernquist, L. 1996, ApJ, 464, 641
Mihos, J. C., Richstone, D. O., & Bothun, G. D. 1991, ApJ, 377, 72

Mihos, J. C., Richstone, D. O., & Bothun, G. D. 1992, ApJ, 400, 153
Mirabel, I. F., Dottori, H., & Lutz, D. 1992, A&A, 256, L19
Miralles, D., Belles, P.-E., Duc, P., Bournaud, F., & Colina, L. 2012, MNRAS, submitted
Miralles-Caballero, D., Colina, L., Arribas, S., & Duc, P.-A. 2011, AJ, 142, 79
Misgeld, I. & Hilker, M. 2011, MNRAS, 414, 3699
Miville-Deschênes, M.-A., Boulanger, F., Reach, W. T., & Noriega-Crespo, A. 2005, ApJ, 631, L57
Moore, B., Ghigna, S., Governato, F., et al. 1999, ApJ, 524, L19
Morrissey, P., Conrow, T., Barlow, T. A., et al. 2007, ApJS, 173, 682
Mullan, B., Konstantopoulos, I. S., Kepley, A. A., et al. 2011, ApJ, 731, 93
Murphy, E. M., Sembach, K. R., Gibson, B. K., et al. 2000, ApJ, 538, L35
Naab, T., Johansson, P. H., & Ostriker, J. P. 2009, ApJ, 699, L178
Narayanan, D., Krumholz, M., Ostriker, E. C., & Hernquist, L. 2011, MNRAS, 418, 664
Navarro, J. F., Frenk, C. S., & White, S. D. M. 1996, ApJ, 462, 563
Negroponte, J. & White, S. D. M. 1983, MNRAS, 205, 1009
Newman, A. B., Ellis, R. S., Bundy, K., & Treu, T. 2012, ApJ, 746, 162
Nicastro, F., Elvis, M., Fiore, F., & Mathur, S. 2005, Advances in Space Research, 36, 721
Noeske, K. G., Weiner, B. J., Faber, S. M., et al. 2007, ApJ, 660, L43
Noguchi, M. & Ishibashi, S. 1986, MNRAS, 219, 305
Pannella, M., Carilli, C. L., Daddi, E., et al. 2009, ApJ, 698, L116
Passot, T. & Vázquez-Semadeni, E. 1998, Phys. Rev. E, 58, 4501
Peebles, P. J. E. 1971, Physical cosmology
Peeples, M. S., Pogge, R. W., & Stanek, K. Z. 2009, ApJ, 695, 259
Perez, J., Michel-Dansac, L., & Tissera, P. B. 2011, MNRAS, 417, 580
Pfenniger, D. & Combes, F. 1994, A&A, 285, 94
Pfenniger, D., Combes, F., & Martinet, L. 1994, A&A, 285, 79
Planck Collaboration, Abergel, A., Ade, P. A. R., et al. 2011a, A&A, 536, A21
Planck Collaboration, Ade, P. A. R., Aghanim, N., et al. 2011b, A&A, 536, A16
Planck Collaboration, Ade, P. A. R., Aghanim, N., et al. 2011c, A&A, 536, A19
Rauch, M. 1998, ARA&A, 36, 267
Reach, W. T., Koo, B.-C., & Heiles, C. 1994, ApJ, 429, 672
Renaud, F., Boily, C. M., Fleck, J.-J., Naab, T., & Theis, C. 2008, MNRAS, 391, L98
Renaud, F., Boily, C. M., Naab, T., & Theis, C. 2009, ApJ, 706, 67
Revaz, Y. & Pfenniger, D. 2004, A&A, 425, 67
Revaz, Y., Pfenniger, D., Combes, F., & Bournaud, F. 2009, A&A, 501, 171
Richter, O.-G., Sackett, P. D., & Sparke, L. S. 1994, AJ, 107, 99
Rothberg, B. & Joseph, R. D. 2006, AJ, 131, 185
Rupke, D., Kewley, L., & Barnes, J. 2010a, in Astronomical Society of the Pacific Conference Series, Vol. 423, Galaxy Wars: Stellar Populations and Star Formation in Interacting Galaxies, ed. B. Smith, J. Higdon, S. Higdon, & N. Bastian, 355
Rupke, D. S. N., Kewley, L. J., & Barnes, J. E. 2010b, ApJ, 710, L156
Saitoh, T. R., Daisaka, H., Kokubo, E., et al. 2010, in Astronomical Society of the Pacific Conference Series, Vol. 423, Galaxy Wars: Stellar Populations and Star Formation in Interacting Galaxies, ed. B. Smith, J. Higdon, S. Higdon, & N. Bastian, 185
Saitoh, T. R., Daisaka, H., Kokubo, E., et al. 2011, in IAU Symposium, Vol. 270, Computational Star Formation, ed. J. Alves, B. G. Elmegreen, J. M. Girart, & V. Trimble, 483–486
Salim, S., Rich, R. M., Charlot, S., et al. 2007, ApJS, 173, 267

Sancisi, R. & Allen, R. J. 1979, A&A, 74, 73
Sanders, D. B., Mazzarella, J. M., Kim, D.-C., Surace, J. A., & Soifer, B. T. 2003, AJ, 126, 1607
Sanders, D. B. & Mirabel, I. F. 1996, ARA&A, 34, 749
Sargent, M. T., Béthermin, M., Daddi, E., & Elbaz, D. 2012, ApJ, 747, L31
Scannapieco, C., Tissera, P. B., White, S. D. M., & Springel, V. 2008, MNRAS, 389, 1137
Schlafly, E. F. & Finkbeiner, D. P. 2011, ApJ, 737, 103
Schmidt, M. 1959, ApJ, 129, 243
Schruba, A., Leroy, A. K., Walter, F., Sandstrom, K., & Rosolowsky, E. 2010, ApJ, 722, 1699
Schweizer, F. 1982, AJ, 252, 455
Schweizer, F. 1996, Observational Evidence for Interactions and Mergers, ed. R. C. Kennicutt, Jr., F. Schweizer, & J. E. Barnes, 105–274
Schweizer, F. & Seitzer, P. 1998, AJ, 116, 2206
Sheen, Y., Jeong, H., Yi, S. K., et al. 2009, AJ, 138, 1911
Spergel, D. N., Verde, L., Peiris, H. V., et al. 2003, ApJS, 148, 175
Springel, V., Frenk, C. S., & White, S. D. M. 2006, Nature, 440, 1137
Springel, V., White, S. D. M., Jenkins, A., et al. 2005, Nature, 435, 629
Swaters, R. A., Sancisi, R., van Albada, T. S., & van der Hulst, J. M. 2009, A&A, 493, 871
Tacconi, L. J., Genzel, R., Neri, R., et al. 2010, Nature, 463, 781
Tacconi, L. J., Genzel, R., Smail, I., et al. 2008, ApJ, 680, 246
Taylor, G. B., Carilli, C. L., & Perley, R. A., eds. 1999, Astronomical Society of the Pacific Conference Series, Vol. 180, Synthesis Imaging in Radio Astronomy II
Temporin, S., Staveley-Smith, L., & Kerber, F. 2005, MNRAS, 356, 343
Temporin, S., Weinberger, R., Galaz, G., & Kerber, F. 2003, ApJ, 587, 660
Teyssier, R., Chapon, D., & Bournaud, F. 2010, ApJ, 720, L149
Thronson, Jr., H. A., Bally, J., & Hacking, P. 1989, AJ, 97, 363
Toomre, A. 1977, in Evolution of Galaxies and Stellar Populations, ed. B. M. Tinsley & R. B. G. Larson, D. Campbell, 401
Toomre, A. & Toomre, J. 1972, ApJ, 178, 623
Vazquez-Semadeni, E. 1994, ApJ, 423, 681
Véron-Cetty, M.-P. & Véron, P. 2006, A&A, 455, 773
Villegas, D., Jordán, A., Peng, E. W., et al. 2010, ApJ, 717, 603
Vogelaar, M. G. R. & Wakker, B. P. 1994, A&A, 291, 557
Wakker, B. P. 2006, ApJS, 163, 282
Walter, F., Brinks, E., de Blok, W. J. G., et al. 2008, AJ, 136, 2563
Waters, C. Z., Zepf, S. E., Lauer, T. R., Baltz, E. A., & Silk, J. 2006, ApJ, 650, 885
Wei, L. H., Keto, E., & Ho, L. C. 2012, ApJ, 750, 136
Weidner, C. & Kroupa, P. 2005, ApJ, 625, 754
Weidner, C., Kroupa, P., & Larsen, S. S. 2004, MNRAS, 350, 1503
White, S. D. M. 1978, MNRAS, 184, 185
White, S. D. M., Frenk, C. S., Davis, M., & Efstathiou, G. 1987, ApJ, 313, 505
Whitmore, B. C., Chandar, R., & Fall, S. M. 2007, AJ, 133, 1067
Whitmore, B. C., Schweizer, F., Leitherer, C., Borne, K., & Robert, C. 1993, AJ, 106, 1354
Whitmore, B. C., Zhang, Q., Leitherer, C., et al. 1999, AJ, 118, 1551
Wilson, T. L., Rohlfs, K., & Hüttemeister, S. 2009, Tools of Radio Astronomy (Springer-Verlag)
Wolfire, M. G., Hollenbach, D., & McKee, C. F. 2010, ApJ, 716, 1191
Wong, T. & Blitz, L. 2002, ApJ, 569, 157
Wyder, T. K., Martin, D. C., Schiminovich, D., et al. 2007, ApJS, 173, 293

Xu, C. & Sulentic, J. W. 1991, ApJ, 374, 407
Yang, X., Mo, H. J., Jing, Y. P., & van den Bosch, F. C. 2005, MNRAS, 358, 217
Zaritsky, D., Kennicutt, Jr., R. C., & Huchra, J. P. 1994, ApJ, 420, 87
Zemp, M. 2009, mpla, 24, 2291
Zhang, Q. & Fall, S. M. 1999, ApJ, 527, L81
Zwaan, M. A., Briggs, F. H., Sprayberry, D., & Sorar, E. 1997, ApJ, 490, 173

# Appendices

# Appendix A

# Paper submitted to MNRAS: comparative study between simulations and observations

Mon. Not. R. Astron. Soc. **000**, 1–10 (??) Printed 3 June 2012 (MN LATEX style file v2.2)

# The evolution of the cluster mass function in galaxy-galaxy collisions.

D. Miralles-Caballero[1⋆], P.-E. Belles[2], P.-A. Duc[2], F. Bournaud[2] and L. Colina[1]
[1]*Departamento de Astrofísica, Centro de Astrobiología, CSIC-INTA, Ctra. de Torrejón Ajalvir km 4, Torrejón de Ardoz, 28850 Madrid, Spain*
[2]*Laboratoire AIM, CEA, CNRS Université Paris Diderot, Irfu/Service dAstrophysique CEA-Saclay, 91191 Gif sur Yvette Cedex, France*

Accepted ??. Received ??; in original form ??

**ABSTRACT**

**Numerical simulations of galaxy collisions allow us to follow the details of the interaction and, in particular, the formation of stellar sub-structures within the galaxies. In this paper, we investigate the output of a high resolution simulation of a major merger, and determine how the mass function of the star clusters born in the merger evolves as a function of time and merger stage. A cluster luminosity function (CLF) is inferred (using stellar population synthesis techniques) and compared with observations at three characteristics phases: pre-merger, merger and post-merger. The observational data consist of a sample of young stellar knots observed in nearby colliding (Ultra-)Luminous Infrared Galaxies, (U)LIRGs.**

**The mass function of the cluster population is best described by a power-law relation with slope $\alpha \sim 1.8$, with no clear dependence on the merger stage. We have, in contrast, found a weak evidence of a steepening of the slope of the inferred cluster luminosity function as the interaction proceeds.** The evolution of the slope is found to be correlated with the evolution of the relative fraction of very young ($\leqslant$ 20 Myr) clusters to older ones as a function of time; most of the clusters are formed in the early stages of the interaction. A similar steepening of the slope of the luminosity function of young clusters is found in our reference sample of (U)LIRGs observed at different merger stages. We do not find clear evidence that the shape of the CLF change with the instantaneous star-formation rate.

**Key words:** galaxies: evolution, galaxies: interactions, galaxies: star formation, methods: numerical, stars: luminosity function, mass function

## 1 INTRODUCTION

**Among the diverse consequences of the violent processes that galaxy encounters undergo, the enhancement of the star formation in some stages of the interaction leads to the formation of many bound stellar objects. Such young objects have been observed during the last two decades in interacting galaxies (Whitmore et al. 1993, 1999, 2007; Duc et al. 1997, 2000; Bik et al. 2003; Maraston et al. 2004; Weilbacher et al. 2000; Hancock et al. 2009; Peterson et al. 2009). Their masses range from that of star clusters (i.e., $10^4$-$10^7$ $M_\odot$) up to that of dwarf galaxies (i.e., $10^7$-$10^9$ $M_\odot$). Those with a mass up to about $10^7$ $M_\odot$ are thought to be progenitors to the globular clusters observed in ellipticals, and the most massive ones to Tidal Dwarf Galaxies (TDGs; Duc 2011).**

**The properties (i.e., luminosities, sizes, ages) of the most massive stellar objects born in mergers have now been extensively characterized, although the physical processes that lead to their formation and evolution are still not well understood (see Belles et al. 2012, MNRAS submitted; hereafter BE12). The general population of young clusters, in particular the shape of the overall cluster mass (CMF) and luminosity function (CLF) and possible evolution with time, has also been the subject of a large number of studies and debates. The slope of the CLF is found to be universal for clusters born in recent mergers: a power-law with an index of about -2 (e.g., Schweizer et al. 1996; Miller et al. 1997; Whitmore et al. 1999; Zhang & Fall 1999; Bastian et al. 2005; Gieles et al. 2006; Haas et al. 2008; Goddard et al. 2010; Santiago-Cortés et al. 2010).** On the other hand, the luminosity and inferred mass functions of the evolved globular clusters around massive galaxies are generally characterized by a Gaussian distribution with a mean value of $M_V \sim$ -7.4 (see compilation in Ashman & Zepf 1998). **If at least part of these GCs were born during the**

⋆ Current address: Departamento de Física Teórica, Facultad de Ciencias, Universidad Autónoma de Madrid, Cantoblanco, 28049 Madrid, Spain. E-mail: daniel.miralles@uam.es

**merger episodes that build up their host galaxies, the observed difference between the shapes of the CLF around young and older mergers implies that the CLF and thus the MLF evolve with time. Among the processes that might account for the evolution, cluster disruption mechanisms, such as the infant mortality, continued stellar mass loss, gravitational shocks, have been suggested (see the theoretical works of Fall & Zhang 2001; Fall et al. 2005; Mengel et al. 2005; Bastian et al. 2005; Whitmore et al. 2007; Fall et al. 2009).**

**The measure of the CLF requires a precise identification of the individual clusters, which is limited to a few nearby systems. The sampling of the interaction stages is limited, and thus the study of the evolution of the cluster population very difficult. Observational biases and/or selection effects can arise, making impossible to determine whether the CLF and CMF evolve due to external, environmental or internal processes. Therefore, only simulations are able to follow evolutionary processes during the interaction extent.** The role played by interactions and mergers in enhancing star formation has been widely studied in the last decades by means of numerical simulations (e.g., Barnes & Hernquist 1992; Mihos & Hernquist 1994, 1996; Springel 2000; Barnes 2004; Springel et al. 2005; Bournaud & Duc 2006; Cox et al. 2006; Di Matteo et al. 2007, 2008; Teyssier et al. 2010). According to the models, star formation is triggered by gas infall (Mihos & Hernquist 1996), local shocks (Barnes 2004; Di Matteo et al. 2008; Saitoh et al. 2010) and enhanced turbulence (Bournaud et al. 2008; Teyssier et al. 2010). **In contrast, a few numerical works have been carried out on the formation of star clusters in mergers, as the identification of the individual bound stellar objects with the typical size of massive clusters, and the determination of a realistic CMF requires the costly implementation of large number of particles.**

Bournaud et al. (2008) presented a simulation of a wet galaxy merger with the highest resolution in mass and spatial sampling reached until then. Using a total of about 36 million particles and a fixed grid cell size of 32 pc, they were able to directly identify dense structures with typical masses of $10^6$-$10^8$ $M_\odot$, similar to young massive superclusters (SSCs) and progenitors to dwarf-like objects. They argued that these dense structures are tightly bound and dense enough to potentially survive gas expulsion, hence being likely progenitors of long-lived globular clusters and tidal dwarf galaxies. **With this simulation, telescope-expensive or inaccessible properties (e.g., current mass, mass gain/loss, aging) for observations of the same cluster population can be tracked throughout the whole interaction process. This paper makes use of this simulation to study the evolution of the MF and LF of the cluster population formed during the encounter, so as to investigate if (and how) the environment (i.e., interaction stage) and global star formation rate affects the cluster mass function. BE12 details how the clusters were identified and tracked during the merger, then focusses on the physical characterization of the most massive and stable clusters and discusses their future evolution. The work presented in this paper extends the study to all mass ranges, down to about $10^6$ $M_\odot$, and mainly addresses the evolution of the cluster mass and luminosity functions.**

**Our simulation results provide predictions on the CMF and indirectly on the CLF which might be compared with observations. As mentioned earlier, reference observations studies are so far very limited. One sample which nevertheless has a similar spatial resolution as in our numerical model, and contains enough systems to study the possible evolution of the CLF** is that studied by Miralles-Caballero et al. (2011) (thereafter MC11), which consists of 32 (Ultra)Luminous Infrared Galaxies, (U)LIRGS, all evolved in an on-going merger. These systems, with infrared luminosity $10^{11} L_\odot \leqslant L_{\rm bol} \sim L_{\rm IR}[8-1000\ \mu{\rm m}] \leqslant 10^{12}$ $L_\odot$ (LIRGs) and $10^{12} L_\odot \leqslant L_{\rm IR}[8-1000\ \mu{\rm m}] \leqslant 10^{13}$ $L_\odot$ (ULIRGs), represent the most extreme cases of starbursts and interactions in the local Universe. A few thousands of young star-cluster or star cluster complexes could be identified on HST images.

**The numerical model by Bournaud et al. (2008) was tuned to ensure the formation of many clusters with a large range of masses. In fact, the observed sample of (U)LIRGS is also biased towards systems with high rate of star and cluster formation, making the comparison of both sets of data relevant.** An intriguing result on that observational study is the (slight) evolution of the slope of the LF of the knots with the interaction phase. **Which physical process can induce this variation? What do the models indicate on this matter?** We also know that the luminosity function and the mass function are somehow related. Thus, the variation may also be reflected in the shape of the mass function.

This paper investigates in detail the evolution of the MF and LF of the cluster population formed during the simulated wet merger of Bournaud et al. (2008) during the whole interaction process. We compare our results with those obtained in observations of compact stellar knots in a representative sample of (U)LIRGs. The layout of the paper is as follows: section 2 provides a description of the data considered in this study and how we characterize the merger state (i.e., interaction phases) of the interaction. We then present the results of the study of the evolution of the mass and luminosity function of the cluster population as a function of merger state in section 3, and compare with that of the observed knots in (U)LIRGs. The luminosities of the clusters in the simulations are obtained by means of stellar population synthesis techniques. We discuss in section 4 the drawbacks of the comparison and biases in the techniques used that can affect our results and/or interpretations. Finally, in section 5 we summarize the main conclusions of this work.

## 2 DATA AND DEFINITIONS

### 2.1 Numerical simulation

We have analyzed the wet galaxy merger simulation of Bournaud et al. (2008) at different times. The simulation was performed with a particle-mesh code based on a FFT Poisson solver for the gravity. The gas dynamics was modeled with a sticky-particle scheme, and a Schmidt law was used for star formation. Supernovae feedback is taken into account in the simulation. The initial setup was chosen so as to be representative of an equal-mass wet merger of two spirals at z < 1 with an initial gas fraction of 17%. The encounter corresponds to a prograde orbit for one galaxy and a retrograde orbit for the other one, with an inclination angle of the encounter of 30° and 70°, respectively. A total number of 36 million particles were used in the simulation, corresponding to 6 million particles per galaxy per component (gas, stars and dark matter). Each stellar disk has an initial mass of $2x10^{11}$ $M_\odot$.

The dataset corresponds to 81 datacubes with the spatial distribution of young particles of equal mass (8333 $M_\odot$) regularly spaced in time, 13 Myr between two time-steps, covering the temporal evolution of the galaxy encounter up to 1053 Myr. All the components of the simulation (gas, young stars, old stars and dark

matter) were simulated but the study was carried out only on young stars. We extracted a total of 78 snapshots, since the star formation is triggered at t=39 Myr, when our analysis starts. Examples of snapshots are shown in Bournaud et al. (2008) and in BE12. In order to identify the bound stellar clusters, the datacube with the 3D position of the particles was projected on three 2D-planes. Clusters were then identified using an algorithm based on particle counts and extracted above a S/N with respect to the local background. Finally, they were cross-correlated between the planes to recover their 3D positions. Thus, the simulated clusters represent a group of bound sticky particles. A thorough description of the analysis and the methodology applied to the detection, measurement of the mass and tracking of a cluster is explained BE12. The spatial resolution achieved (the softening length of the gravitational potential) in this model corresponds to 32 pc. With a stellar mass resolution of about $10^5$ $M_\odot$, the identified clusters are typically more massive than $10^6$ $M_\odot$ and up to $10^9$ $M_\odot$.

### 2.2 The observational data

High angular resolution archival *HST* images were retrieved for a representative sample of 32 local (U)LIRGs in the *F814W* ($\sim I$) and *F435W* ($\sim B$) photometric bands. Thirty were taken with the Advanced Camera for Surveys (ACS) and two with the Wide Field Planetary Camera 2 (WFPC2), giving a pixel size of $\sim 0.05''$. The sample spans a significant fraction of the infrared luminosity range of (U)LIRGs ($L_{IR}$ =[2.5,34.7]x$10^{11}$ $L_\odot$), covers the redshift range $0.016 \leqslant z \leqslant 0.124$ and includes all types of nuclear activity as well as all different morphologies, i.e., snapshots of the different evolutionary phases of the galaxy interactions. A thorough description of the sample selection and the main properties of the systems can be found in MC11.

Photometric measurements were performed for close to 3000 compact regions, defined as knots, detected simultaneously in both filters, and with high surface brightness usually bluer than the underlying galaxy (see MC11 for full details and analysis). The knots, most of them likely to consist of cluster complexes, cover a wide range of luminosity (-20 $\lesssim$ $M_{F814W}$ $\lesssim$ -9 and -19.5 $\lesssim$ $M_{F435W}$ $\lesssim$ -7.5) and color (-1 $\lesssim$ $M_{F435W}$-$M_{F814W}$ $\lesssim$ 5). Most of them are compact with $r_{eff}$ smaller than 100 pc, the median value being 32 pc.

To avoid the distance dependence of the photometric properties, which was discussed in MC11, we included in this study the observational data of only those systems at similar distance (about 2200 knots in 22 (U)LIRGs). The galaxies are located at a median distance of 125 Mpc, with a dispersion of 40 Mpc. At this distance and with the instrumentation used, the spatial resolution averages around 30 pc per pixel.

### 2.3 Interaction Phases in the Simulation

**In all our analysis, the cluster mass and luminosity functions have been determined at each snapshot. Additionally, to better make comparisons with observations, three interaction phases have been defined: pre-merger, merger and post-merger.**

MC11 classified the (U)LIRG sample in four interaction phases according to the optical morphology of the systems. A similar classification scheme to that in Veilleux et al. (2002) was followed there, though with a few simplifications. Based on the morphological similarties both in the observations and in the simulation, we identified each morphological class defined in MC11 and assigned in the simulation a typical age to characterize the merger state. Given the uncertainties involved when performing morphological classifications and in order to make a more realistic comparison, we considered a window of about 150 Myr to characterize the properties of each class. We then identified in the simulation typical ages (central ages in the window) for the pre-merger, merger and post-merger interaction phases to be 299, 585 and 988 Myr. We then considered snapshots covering ± 75 Myr to define the interaction phase.

Due to computing time issues, the simulation in this study extends only up to 1 Gyr. However, the duration of a merger can be more extended in time until the system completely relaxes (e.g., simulations by Di Matteo et al. 2008 extend to longer than 2 Gyr). The comparison of this simulation with very relaxed galaxies (i.e., a very old elliptical galaxy) is therefore not appropriate. But a comparison with a (U)LIRG remnant, with past signs of interaction (e.g., outer asymmetries), no fully relaxed, is not worrysome.

In MC11 a few galaxies were identified to be in a first-contact phase (before the first pericenter passage). This phase, corresponding to the first snapshots in the simulation, is not considered for this study because only a few clusters are detected (e.g., only 34 clusters in the snapshot number 8, at t=104 Myr). This unrealistic early scenario is the consequence of how the star formation was implemented in the code, in such a way that no star formation existed before the encounter.

## 3 RESULTS

### 3.1 Evolution of The Cluster Mass Function

**Our cluster identification technique allowed us to determine the number of particles associated to each cluster formed in the simulation, and thus to determine its stellar mass and overall the Cluster Mass Function.**

**In general, the shape of the MF may be fitted with a Schechter (Schechter 1976) function:**

$$\frac{dN}{dM} \propto \left(\frac{M}{M_c}\right)^{-\alpha} exp\left(-\frac{M}{M_c}\right) \quad (1)$$

**This function defines a truncation mass, which is typically between $10^5$ $M_\odot$ to $10^6$ $M_\odot$ (Jordán et al. 2007; Larsen 2009; Gieles 2009) for spirals. Though it may vary from systems to systems, the truncation mass is likely to be well below our completeness value of the MF, above $10^6$ $M_\odot$ at all interaction phases (see Fig. 1). Therefore, the CMF of the young massive clusters formed in the simulation is best described by a simple power-law distribution of the form $dN \propto M^{-\alpha_{MF}}$ dM (MF) with no truncation mass.**

To perform the fit of the MF we applied the methodology explained in MC11, based on fitting equal-sized bin distributions. **Although in MC11 it was applied to the CLF, other studies have applied this methodology to the mass function as well (e.g., Goddard et al. 2010)**. The lower mass for which the cluster sample is complete was thus determined assuming a simple power-law form for the cluster mass distribution.

The slope of the simulated CMF ($\alpha_{MF}$) is typically 1.8 (see Fig. 2, top). Although, a visual trend may be observed towards steeper slopes from the pre-merger to the merger phase, given the uncertainties involved, there is no clear evidence of an evolution of the slope with the phase of the merger.

The slope of the mass function of young star cluster populations in other interacting and galaxy mergers are: $\alpha_{MF}$=1.95±0.03

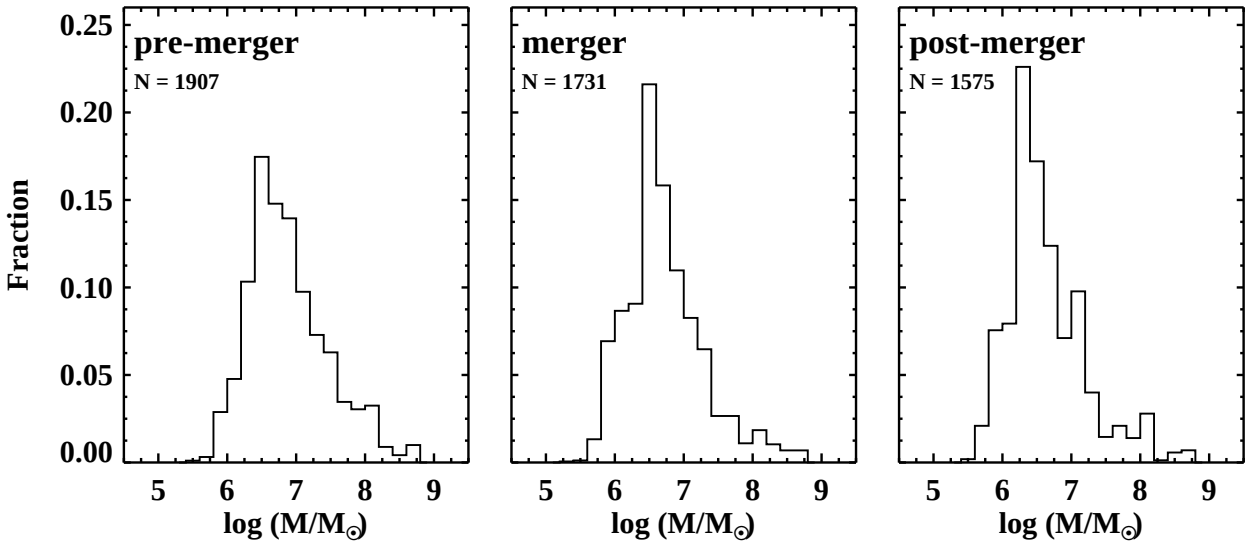


**Figure 1. Mass distributions of the clusters in the simulation, adding up the clusters identified in each of the 11 snapshots in which an interaction phase was defined. N gives de number of detected clusters.**

in the Antennae (Zhang & Fall 1999); $\alpha_{MF}$=1.5±0.4 in Arp 284 (Peterson et al. 2009); $\alpha_{MF}$=1.85±0.11 in NGC 6872 (Bastian et al. 2005); and $\alpha_{MF}$=1.85±0.12 in NGC 3256 (Goddard et al. 2010). Goddard et al. (2010) used the same methodology as in this study, whereas the others fitted equal bin distributions of the MF. The slopes obtained here are consistent with the listed values.

### 3.2 Determination of the Cluster Luminosity Function

**Measuring the mass of clusters from their luminosity is not straightforward and requires costly multi-band photometric data and stellar synthesis models. Thus, only a few observational studies provide information on the mass function (see above). This contrasts with the many papers in the literature studying instead the luminosity function. Thus, in order to check on real systems the predictions of our model, we have computed the cluster luminosity function, after having converted the individual cluster stellar masses in luminosities. This requires the knowledge of the age of the cluster, its star formation history (which is provided by our simulation and our cluster tracking technique) and the use of stellar population synthesis techniques.**

**Doing so, we were specifically motivated by the comparison with the properties of the observed knots in our sample of (U)LIRGs, for which only photometric data in the *F435W* and *F814W* bands exist, and thus for which the derivation of accurate masses would be impossible. Our method to convert masses into luminosities is detailed below.**

#### *3.2.1 Initial mass and growth phase of the clusters*

**The simulated clusters undergo a rapid growth phase in which their mass increases by up to a factor of about 100 during their first 100 Myr or so of existence (see BE12). That is, the cluster star formation history is rather complex during the first 100 Myr or so, consequence of continuous or multiple-phase in-situ star formation rather than accretion from external structures.** This suggests a scenario in which clumps of gas form first and then collapse to form stars. However, the model does not have enough resolution for us to know if the clump fragments and form little clusters which then merge together, or if the collapse is monolithic. **To make reliable estimates of the luminosities of these clusters, the knowledge of their mass and age is essential, and thus this phase had to be characterized.**

Once this phase ends, the mass of the clusters stabilizes to what it is defined as the initial mass ($M_{ini}$). Later on, they lose mass (due to dynamical friction, two-body relaxation, etc.) generally in a much moderate way (see BE12). We thus defined the value of the initial, reference, mass of each cluster to that measured at the end of the growth phase, typically 80-100 Myr (i.e., 6-8 snapshots) after it was detected for the first time.

**One should note however that the apparent duration of the growth phase depends on the mass of the cluster. For the most massive ones (with an initial mass higher than $M_{ini} = 10^8$ $M_\odot$), the rapid growth phase can be completely tracked during the simulation.** Instead, this phase is missed partially or completely for a cluster with lower initial mass, since if we assume that the rapid growth phase is similar, its mass at the beginning of the phase would be too low to be detected against the local background. In the extreme case where the initial mass of a cluster is lower than $M > 10^{6.5}$ $M_\odot$ we identify it for the first time when it has already reached the initial mass. This mass ($10^{6.5}$ $M_\odot$) represents the *global mass detection threshold.*

We decomposed the growth phase in successive bursts of star formation. Since this phase lasts approximately 6 snapshots, the clusters are assumed to be formed by a combination of 6 different stellar populations, with different masses and ages. For each population, we derived the mass fraction and dragged it throughout the whole evolution of the interaction process. Thus, for instance, when a cluster with initial mass higher than $10^8$ $M_\odot$ is detected for the first time, it has only one population. One additional population is created per snapshot until the cluster reaches its initial mass. Then, the mass fraction of each population

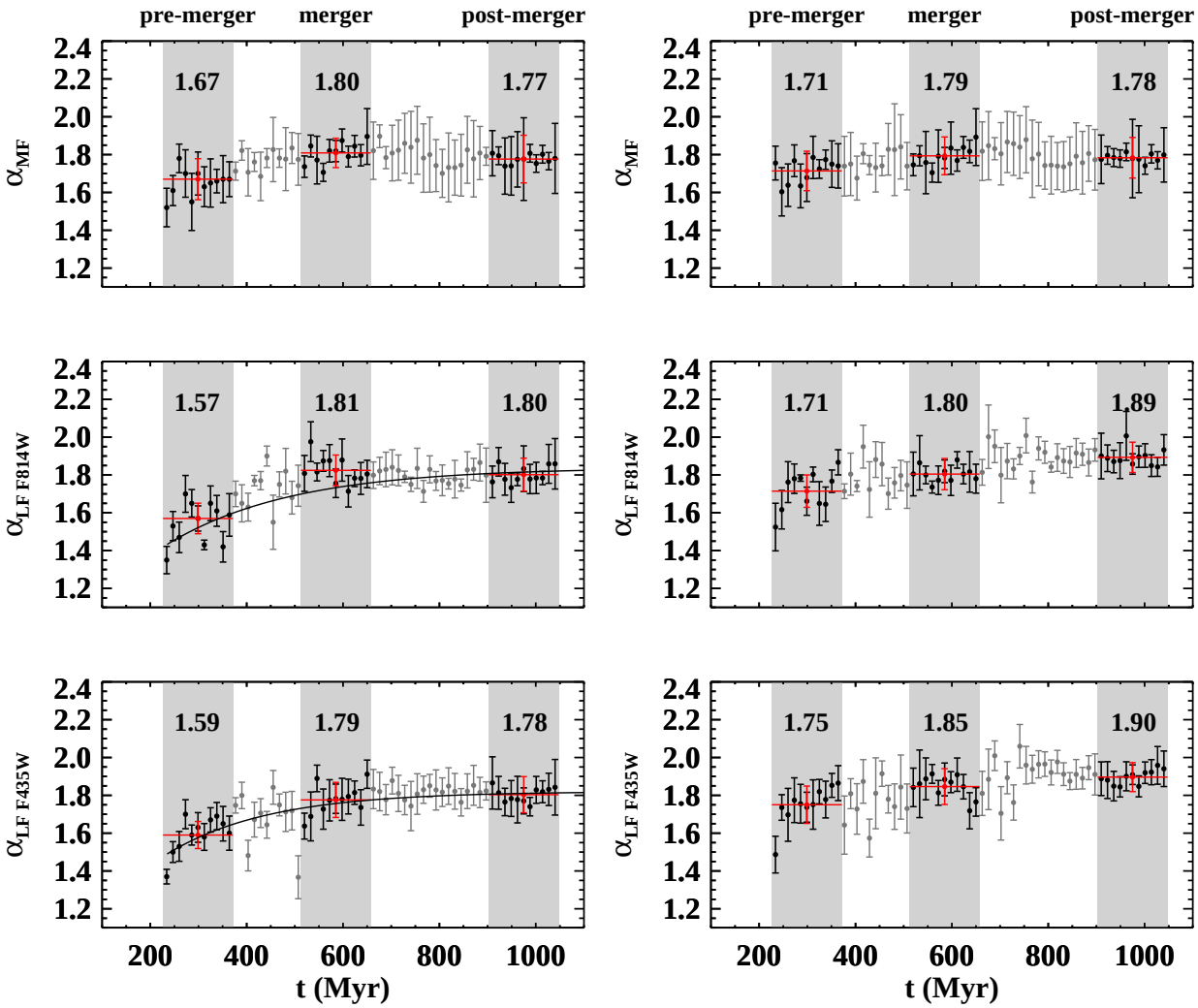


**Figure 2.** Derived slope of the MF (top) and the LF for filter *F814W* (middle) and *F435W* (bottom) of the clusters as the interaction evolves. The red crosses and associated values correspond to median values over periods (i.e., interaction phases) indicated by the shaded areas. **Left:** For all the clusters at any given snapshot. The plain line corresponds to the best fit of the LF, as parametrized by the function $\alpha_{LF}$=-$10^{\beta t/t_0}$+c (see text). **Right:** Excluding the youngest clusters (i.e., those that appeared between the previous and the current snapshot).

is frozen and used as such until the end of the simulation or its dissolution.

### *3.2.2 Modeling the stellar populations*

Knowing the stellar populations involved in the growth phase, and using stellar population synthesis models we were able to derive observables, such as the luminosities in various bands.

Instantaneous burst models were considered, with a Kroupa Initial Mass Function (Kroupa 2002) over the range 0.1-120 $M_\odot$ and solar metallicity. We considered this rather high metallicity even at large radii because global mixing of the ISM in mergers, due to gas inflows and outflows, flattens any metallicity gradient of the parent galaxies (Rupke et al. 2010; Di Matteo et al. 2011; Perez et al. 2011). A solar or slightly subsolar metallicity is consistent with metallicity measurements in tidal tails (Duc & Renaud 2011). The tracks of the starburst99 (SB99, Leitherer et al. 1999; Vázquez & Leitherer 2005) models, optimized for young ages, were used up to t=100 Myr. At older ages, the tracks by Maraston (Maraston05, Maraston 2005) were considered, where a rigorous treatment of the thermally pulsing asymptotic giant branch (TP-AGB) phase is applied (relevant within the interval 0.1-1 Gyr).

**As mentioned before, we were able to characterize the rapid growth phase of clusters more massive than $10^8$ $M_\odot$. A cluster like this is formed between the previous snapshot and the snapshot of its first detection. Since the time elapsed between snapshots (i.e., the time resolution of the simulation) is 13 Myr, we assumed the age of that cluster when it was detected for the first time corresponds to half the time between two consecutive snapshots, i.e., 6.5 Myr old. On the next snapshot we considered the age of the new population to be 6.5 Myr old and the previous one 13+6.5 (19.5) Myr. During the subsequent snapshots we assumed again any new population to be 6.5 Myr, and the previous populations 13 Myr older than the age they were in the previous snapshot.**

For clusters less massive than $10^8$ $M_\odot$ we could not study the rapid growth phase in its whole extent and we assumed that have the same characteristics as for the massive ones. When computing the mass fraction of the 6 stellar populations, we applied a gradual correction:

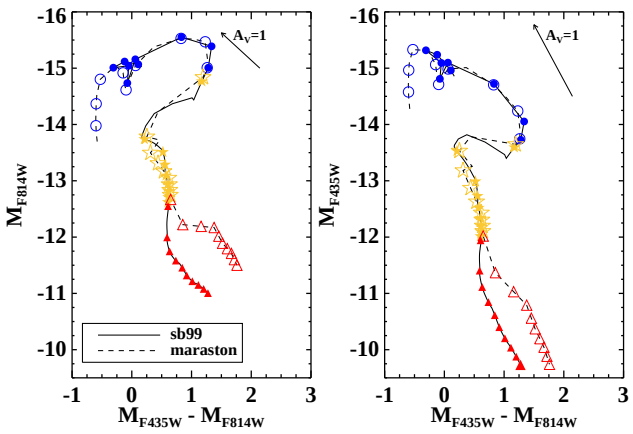


**Figure 3.** Magnitude tracks as a function of color according to the SB99 and to the Maraston05 single stellar population (SSP) models. The curves are normalized to $10^6$ $M_\odot$. Filled blue circles, yellow stars and red triangles indicate the age in the SB99 track in steps of 1 Myr (from 1 to 9 Myr), 10 Myr (from 10 to 90 Myr) and 100 Myr (from 100 to 1000 Myr), respectively. Open symbols show the same for the Maraston tracks. The de-reddening vector ($A_V$ = 1 mag), derived using the curve of Calzetti et al. (2000), is shown in both plots.

(i) For clusters in the interval $10^7$ < $M_{ini}$ ($M_\odot$) < $10^8$ (*first interval*) we assumed to miss the growth phase during 2 snapshots.
(ii) For clusters in the interval $10^{6.5}$ < $M_{ini}$ ($M_\odot$) ⩽ $10^7$ (*second interval*), we assumed to miss it during 4 snapshots.
(iii) Finally, for clusters less massive than the detection threshold (*third interval*, i.e., $M_{ini}$ < $10^{6.5}$ $M_\odot$), we assumed to miss it during 6 snapshots (i.e., the whole phase).

Thus, when a cluster in the first interval is detected for the first time we assume it is already formed by 3 stellar populations, with ages 6.5 Myr (detected), 6.5+13 (19.5) Myr (missed) and 6.5+13+13 (32.5) Myr (missed), respectively. Then, in order to estimate the luminosity we use the averaged mass fractions computed for all the massive clusters when they are formed by 3 populations. At the following snapshot the cluster is assumed to be formed by 4 stellar populations (the older two we missed and the younger two in which the knot was detected). The new mass fractions of the non-detected with respect to the detected populations are computed using the average mass fractions derived for all the massive clusters. Once the cluster reaches the 6 stellar populations (at the fourth snapshot in this case), the final mass fraction values are frozen and dragged until the cluster disappears or until the end of the simulation. A similar analysis process was followed for the clusters in the second interval. The clusters in the third interval are assumed to have already reached their initial mass when they are first detected (i.e., they are already formed by the 6 stellar populations). Hence, we dragged all the populations from the beginning and the mass fractions applied correspond to the average values derived for the most massive clusters.

This process introduces a typical uncertainty of 5-25 % in the knowledge of the mass for each of the 6 populations for the least massive clusters. Another major source of uncertainty comes from the age of the young population. When a cluster is identified for the first time in the simulation we assumed that the youngest out of the 6 populations is 6.5 Myr old, since the age elapsed between two consecutive snapshots is 13 Myr. In order to know how this translates into an uncertainty in luminosity we assumed that the ages distribute following a Gaussian function in the interval 0-13 Myr, with a mean value of 6.5 Myr and a one-sigma ($1\sigma$) deviation of 6.5/3 (i.e., 2.17) Myr. According to the SB99 models (see Fig. 3), this can introduce a $1\sigma$ uncertainty of up to 0.5 mag in the *F814W* band and up to 0.3 mag in the *F435W* band. These uncertainties decrease considerably due to the aging of the clusters while they evolve in the interaction. After about 50 Myr they become negligible (less than 0.1 mag) compared to the uncertainties related to the mass fraction for each of the 6 populations.

Taking into consideration both major sources of uncertainties, the error in the estimated luminosities for the new clusters (at the snapshot when they appear for the first time) can be as high as 0.75 mag. About 3 snapshots later this error drops below 0.2-0.3 mag, since at that time the new population with an age of 6.5 Myr represents a very small fraction in mass. About 7 snapshots later the main source of uncertainty comes from the mass fraction for each of the 6 populations, and the luminosities computed are reliable within less than 0.2 mag. **Although the uncertainty in luminosity can be rather high for the first snapshots (up to a factor of 2) this is by far much better than obtaining masses from luminosities, using only one color (see Fig. 3), where typical uncertainties larger than a factor of 10 are encountered.**

### 3.3 Evolution of the Luminosity Function

#### *3.3.1 Predictions from the simulation*

**Once the individual luminosities of the clusters were derived, we could determine their luminosity functions. They are shown on Fig. 2 for two bands. We measured the slope of the LF ($\alpha_{LF}$), which is described by a power-law distribution:** $dN \propto L_\lambda^{-\alpha} dL_\lambda$**, or the equivalent form using magnitudes,** $dN \propto 10^{\beta M_\lambda} dM_\lambda$**. The slopes in both equations are related as** $\alpha = 2.5\beta + 1$. As discussed in MC11 the uncertainties associated to the fit of the LF do not include other sources of systematic error (e.g., dropping the most luminous bins, adopting another method of binning, moving the magnitude limit). Therefore, like in MC11, we consider a systematic uncertainty of 0.1 dex.

We observe a trend towards steeper slopes $\alpha_{LF}$ as the merger evolves up to about 500 Myr (see Fig. 2, middle- and bottom-left). This trend is less significant for the filter *F435W* (see table 1). We tried to fit empirically the values of $\alpha_{LF}$ at each snapshot with a function of the form $\alpha_{LF}$=-$10^{\gamma t/t_0}$+c, a kind of an exponential decay (with index $\gamma$). However, as shown in Fig. 2 (left) the fit is not very well constrained because the dispersion is very high. Hence, even though the trend can be real within the uncertainties we cannot constrain its shape, given the large dispersions in the different slopes.

We suspect that the youngest population (i.e., clusters during their first snapshots of existance) is responsible for the variation of the slope of the LF, since it can be up to a factor of 10-100 more luminous than the old population (i.e., 1 Gyr) for equivalent total masses (see Fig. 3). If there is a significant fraction of young population, it can overpopulate the bright end of the LF, making it flat. **Additionally, BE12 shows that the most massive clusters are formed early-on in the simulation. They could also contribute in overpopulating the bright end of the LF. However, such change should also be visible on the slope of the MF. Our uncertainties are too large for us to see that difference (should it exist).**

To check whether indeed the main contributor to overpopulat-

**Table 1.** Slopes of the mass and luminosity distributions of the clusters identified in the simulation and observed knots in (U)LIRGs at different interaction phases

| Interaction phase | $N_Y$ (%) | $\alpha_{MF}$ sim | $\alpha_{LF\ F814W}$ sim | $\alpha_{LF\ F814W}$ obs | $\alpha_{LF\ F435W}$ sim | $\alpha_{LF\ F435W}$ obs |
|---|---|---|---|---|---|---|
| pre-merger | 12±7 | 1.67 ± 0.11 | 1.57 ± 0.08 | 1.84 ± 0.03 | 1.59 ± 0.07 | 1.86 ± 0.05 |
| merger | 2±1 | 1.80 ± 0.08 | 1.81 ± 0.07 | 2.00 ± 0.04 | 1.79 ± 0.08 | 1.86 ± 0.02 |
| post-merger | 1±1 | 1.77 ± 0.15 | 1.80 ± 0.10 | 1.76 ± 0.12 | 1.78 ± 0.07 | 1.58 ± 0.17 |

**Notes.** For the simulated data the value represents the average of the median values of the slopes computed for the 11 distributions per interaction phase. $N_Y$ gives the number of *young clusters* (see text) with respect to the total number of clusters per snapshot. The slopes for the observed data for the first contact phase are 1.70 and 1.69 for the red and blue filter respectively.

ing the bright end of the LF is the presence of young population, we explored the same plot ($\alpha_{LF}$ vs. time) but excluding for each snapshot those clusters that appear for the first time in the simulation between the current snapshot and in the previous one. We refer to them as the *young clusters*. When these young clusters are excluded from the fit, the trend tends to disappear in both filters (Fig. 2, right). **It turns out that during the pre-merger phase the number of young clusters with respect to older population represents up to about 20% of the total cluster population. Since in the simulation the cluster formation rate is very low during the merger and the post-merger phases, the number of young clusters is negligible (compatible with 0-1% of the total cluster population) compared to the pre-merger phase.** Therefore, these youngest clusters can be the responsible for overpopulating the bright end of the LF, thus for inducing the flattening of the slope.

### *3.3.2 Comparisons with observations*

**Although a single 1:1 simulation was carried out, it is rather typical and characteristic of many observed real systems. For instance, NGC 7252, the Mice and The Antennae can be modeled by roughly equal-mass mergers with high gas fractions, from 12.5 to 20% (Hibbard & Mihos 1995; Barnes 2004). Three out of the four double system ULIRGs in Colina et al. (2005) also have a mass ratio of 1:1 and most ULIRGs in García-Marín (2007) are compatible with a mass ratio of 1:1 and 1:2. Additionally, the numerical simulation was tuned to ensure the formation of many clusters with a large range of masses, and the observed sample of (U)LIRGS is also biased towards systems with high rate of star and cluster formation.**

**On the other hand, other parameters like the orbit inclination differs significantly from system to system. And the observational data come from a sample of dozens of systems, surely with galaxies having different initial configurations. This should be kept in mind when comparing the observed and simulated data.**

**The derived slope of the CLF for interacting systems in the nearby Universe is typically close to 2, with no perceptible change from system to system (e.g. Schweizer et al. 1996; Miller et al. 1997; Whitmore et al. 1999; Gieles et al. 2006; Haas et al. 2008; Peterson et al. 2009; Santiago-Cortés et al. 2010). However, checking the trend for a slight steepening of the CLF during the interaction predicted by our model requires to have a large sample of real systems observed at different interaction stages. The sample of 22 star-forming interacting systems studied by MC11 is well suited for such a comparison study. Indeed the high IR luminosity of this (U)LIRGs sample implies high star formation rates and thus presumably high cluster formation rates. Their LF could thus be well sampled.**

**Table 1 summarizes the values of slope of the LF for the simulations and the observations. Overall, the values of the simulated and observed $\alpha_{LF}$ are quite similar (within 0.15 dex) and compare well with earlier studies. The marginally significant steepening of the slope of the red band LF during the first phases of the merger, predicted by the numerical model, is observed for the (U)LIRGs sample. For the blue filter the slope does not change perceptibly in the observed sample, though a steepening is predicted by the model. Stellar internal extinction affecting young population may play a role, since in (U)LIRGs it can be moderate and high (see Alonso-Herrero et al. 2006; García-Marín et al. 2009), and the measured light from the blue filter is more affected than that from the red one.**

**This variation of the slope could have the same origin in observations and simulations. Then, even if there is substantial active star formation (i.e., young population) in all interacting phases in (U)LIRGs, it would imply that in the early phases the young population represents a more important percentage ($N_Y \sim$ 5-20%; see table 1) in the optical luminosity with respect to the total population than in the most evolved phases ($N_Y \sim$ 1-2%). The contribution of this overpopulation of young knots observed in (U)LIRGs would flatten the slope of the LF in the early interaction phases.**

## 4 DISCUSSION

**Our numerical model allowed us to compute for the first time in a self-consistent way the mass function of clusters born in mergers and predict its (lack of) evolution during the merger stage, at least up to 1 Gyr. Given the lack of observational data related to the CMF, we have computed the corresponding luminosity mass functions and tried to compare it with real interacting systems. In this comparison, one should however keep in mind the limitations of the data, in particular the lack of spatial resolution and the uncertainties in the star formation history of the clusters. They are discussed here.**

### 4.1 The Limited Spatial Resolution

**Despite the very high number of particles used, the spatial resolution of the simulation remains much lower than the**

**typical size of a star cluster. Nevertheless, the limited spatial resolution only weakly affects the shape of the MF of the gravitationally bound clusters born in the merger (see BE12), even on its low mass end. Indeed, Bournaud et al. (2008) argue, based on energetics arguments that, were the resolution to be larger, the clusters would be even more compact, while their mass would not change. The effective radius measured in the simulated clusters are upper limits. So, whereas the cluster sizes are highly unreliable, their mass and thus the CMF should remain realistic.**

**On the other hand, the consequences of the lack of resolution in the observational data may have more serious effects on the cluster mass and luminosity distributions. The clusters are not directly detected, even on HST images. Rather stellar "knots" are observed. They may correspond to complexes of star clusters. Using simulations, MC11 investigated how the slope of the LF change with the spatial resolution and concluded that the lack of resolution could induce a systematic flattening of the LF by about 0.15 dex. If this is the case, the observed CLF might in reality be steeper than the predicted ones.**

### 4.2 The Limited Knowledge of the Stellar Content of the Clusters

**As shown in section 3.2, the star formation history of the clusters identified in the simulation is rather complex during the rapid phase of cluster growth. Given the time resolution of the simulation, we decided to characterize their population with a grid of six stellar populations. This may result in relatively large uncertainties in the mass-luminosity conversion. They are, though, much smaller than the uncertainties in the mass determination of the observed knots if they are derived from a single photometric color. For instance, according to the stellar population models used in this work, a cluster with a color around $M_{F435W}$-$M_{F814W} \sim 1$ can be as young as 7 Myr or as old as several hundreds of Myr (see Fig. 3). The difference in luminosity for both populations can be as high as a factor of 100. That is, the implied mass can be different by a factor as high as 100.**

**All along the pre-merger phase, clusters are actively formed in the simulation. That is, a lot of young population (in the sense of newly formed clusters) is present. In section 3.2.2 we saw that the uncertainty in luminosity for the newly formed clusters can be as high as 0.75 mag (or a factor of 2 in flux) during the very first few snapshots. Although the uncertainty is rather high, it is taken into account in the fit of the CLF.**

### 4.3 Effect of the global Star-Formation Rate of the System

**We have so far investigated how the CMF/CLF vary as a function of the merger stage. One should however keep in mind that the integrated Star Formation Rate also varies during the interaction, and in our model quickly drops after 250 Myr (see Fig. 4). Determining how the SFR affects the CLF is particularly important, as we compare a single simulation of a merger with real systems selected to be in various interacting stages but all chosen to have rather high SFRs: i.e. they are all (U)LIRGs.**

**The shape of the cluster formation rate (CFR) and the instantaneous SFR, though similar in general, is different on short time-scales (i.e., a few snapshots). First, the CFR peaks for a shorter period than the peak of the SFR, as shown in Fig. 4. Second, the distribution of the CFR is wider than the SFR curve. For instance, at t = 300 Myr the global SFR is already very low (less than 10 $M_\odot$ $yr^{-1}$) compared to the peak ($\sim$ 50$M_\odot$ $yr^{-1}$), and the CFR is only about half the peak value(i.e., it still remains relatively high). At the same time, the slope of the LF can still be quite flat ($\alpha_{LF}$=1.5-1.6). Therefore, the variation of the slope of the LF is likely to be related more to the CFR than to the global SFR.**

**As mentioned before, (U)LIRGs are known to have high SFRs (independently of the interaction phase). If the flat slopes of the LF were directly related to high global SFRs, we would derive flat slopes also in the advanced phases of interaction, which is not the case. If the flat slopes were instead directly related to the CFR, the derivation of steep slopes would imply that only a few clusters are formed there. Assuming this last statement is true, this implies that if a system has a high SFR (i.e., it is a LIRG or a ULIRG), but the current star formation is concentrated on a very few or mainly obscured (i.e., not observable in the optical) clusters/knots, they can barely affect the slope of the LF, which remains steep. Should this be the case, we can interpret that the cluster formation rate is high in (U)LIRGs undergoing early phases of interaction, whereas in those systems undergoing late phases of interaction the cluster formation rate is significantly lower (or, if high, they suffer from such high extinction than cannot be detected in the optical).**

### 4.4 Effects of the system geometry and dust extinction

**The main detection criterion of a simulated cluster is its mass. Provided it contains enough particles, it is detected by our algorithm. Projection effects are minimized since we make the analysis in 3D projecting the data cubes in different planes.**

**Furthermore, no dust model is implemented in our simulation: all clusters are "visible". In reality, the comparison sample consists of systems observed in only one plane, that of the sky, and obscuration with dust might hide some clusters. This is especially the case for our U(LIRG) sample, as discussed in MC11. The total number of detected clusters might thus have been underestimated, especially in the central regions where dust is concentrated. The possible lack of detection of young knots might be the reason why the LF of the observed knots in advanced phases of the interaction is not as flat as in the early stages.**

## 5 SUMMARY AND CONCLUSIONS

**We have analyzed the evolution of the mass and luminosity functions of the cluster population identified in a high spatial resolution major merger simulation, and compared our predictions with observations of a sample of star-forming interacting systems having similar mass ratio, morphologies, gas content and star-formation rates**. Three different interaction phases have been studied: pre-merger, merger and post-merger, occurring in the simulation at about t=200-400 Myr, 500-700 Myr and 1 Gyr, respectively. The high resolution model reproduces and/or explains some observed properties of the star clusters in major mergers. We draw the following conclusions:

(i) The shape of the mass function (MF) of the cluster population

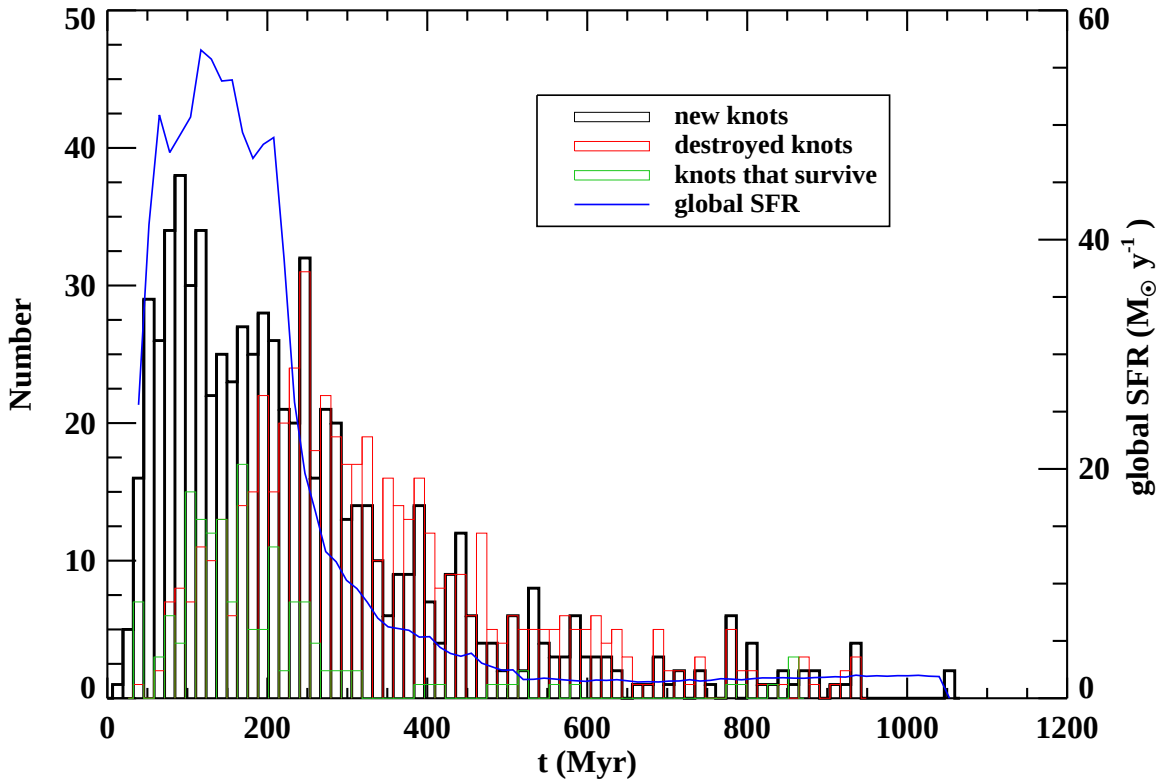


**Figure 4.** Number of clusters newly formed (black) and destroyed (dashed red) per snapshot. The green dashed histogram shows which of the clusters formed at a given snapshot survive until the end of the simulation. The blue line shows the global SFR, which refers to the total mass of new particles formed into stars divided by the time extent of the snapshot. The peak of the global SFR, at about t = 150 Myr, occurs during the first pericenter passage. The detection delay of the clusters less massive than $M_{ini} = 10^8$ $M_\odot$ has been corrected in the plot.

is practically constant along the interaction process. The derived slope, typically $\alpha_{MF} \sim 1.8$, is similar to that obtained for young star cluster populations in observed nearby galaxy mergers.

(ii) **We have also been able to characterize the evolution of the cluster luminosity function (CLF) of the simulated merger with the use of stellar population synthesis techniques.** In this case, the slope may evolve throughout the interaction process. A weak trend towards steeper slopes is observed during the pre-merger phase up to the merger phase, when it stabilizes around $\alpha_{LF} = 1.8$-$1.9$. According to the simulation, this slight variation is likely to be due to high cluster formation rates at early phases of the interaction, which can induce the flatteing of the slope.

(iii) There is no clear evidence that the slope correlates with the global star formation rate of the system. **It better correlates with the cluster star formation rate. This could imply that the slopes in systems with high star formation rates but lower cluster formation rates, the flattening of the slope of the LF is not perteptibly induced by the present young population.**

(iv) **The marginally significant steepening of the slope of the LF during the first phases of the merger, predicted by the numerical mode, is observed for the (U)LIRGs sample. We understand the steepening in advanced phases if the global star formation is concentrated on only a few (and/or extremely obscured) knots of star formation, which are not able to perteptibly induce any flattening of the LF.**.

## ACKNOWLEDGEMENTS

This work has been supported by the Spanish Ministry of Education and Science, under grant BES-2007-16198, projects ESP2005-01480, ESP2007-65475-C02-01 and AYA2010-21161-C02-01. We have made use of observations made with the NASA/ESA Hubble Space Telescope, obtained from the data archive at the Space Telescope Science Institute (STScI ), which is operated by the Association of Universities for Research in Astronomy, Inc., under NASA contract NAS 5-26555.

## REFERENCES

Alonso-Herrero A., Rieke G. H., Rieke M. J., Colina L., Pérez-González P. G., Ryder S. D., 2006, ApJ, 650, 835
Ashman K. M., Zepf S. E., 1998, Globular Cluster Systems
Barnes J. E., 2004, MNRAS, 350, 798
Barnes J. E., Hernquist L., 1992, ARA&A, 30, 705
Bastian N., Gieles M., Efremov Y. N., Lamers H. J. G. L. M., 2005, A&A, 443, 79
Bastian N., Gieles M., Lamers H. J. G. L. M., Scheepmaker R. A., de Grijs R., 2005, A&A, 431, 905
Bastian N., Hempel M., Kissler-Patig M., Homeier N. L., Trancho G., 2005, A&A, 435, 65
Bik A., Lamers H. J. G. L. M., Bastian N., Panagia N., Romaniello M., 2003, A&A, 397, 473
Bournaud F., Duc P., Emsellem E., 2008, MNRAS, 389, L8
Bournaud F., Duc P.-A., 2006, A&A, 456, 481

Calzetti D., Armus L., Bohlin R. C., Kinney A. L., Koornneef J., Storchi-Bergmann T., 2000, ApJ, 533, 682
Colina L., Arribas S., Monreal-Ibero A., 2005, ApJ, 621, 725
Cox T. J., Jonsson P., Primack J. R., Somerville R. S., 2006, MNRAS, 373, 1013
Di Matteo P., Bournaud F., Martig M., Combes F., Melchior A., Semelin B., 2008, A&A, 492, 31
Di Matteo P., Combes F., Melchior A., Semelin B., 2007, A&A, 468, 61
Di Matteo P., Montuori M., Lehnert M. D., Combes F., Semelin B., 2011, ArXiv e-prints
Duc P., Brinks E., Springel V., Pichardo B., Weilbacher P., Mirabel I. F., 2000, AJ, 120, 1238
Duc P.-A., 2011, ArXiv e-prints
Duc P.-A., Brinks E., Wink J. E., Mirabel I. F., 1997, A&A, 326, 537
Duc P.-A., Renaud F., 2011, ArXiv e-prints
Fall S. M., Chandar R., Whitmore B. C., 2005, ApJ, 631, L133
Fall S. M., Chandar R., Whitmore B. C., 2009, ApJ, 704, 453
Fall S. M., Zhang Q., 2001, ApJ, 561, 751
García-Marín M., 2007, 2D structure and kinematics of a representative sample of low-z ultra-luminous infrared galaxies
García-Marín M., Colina L., Arribas S., 2009, A&A, 505, 1017
Gieles M., 2009, MNRAS, 394, 2113
Gieles M., Larsen S. S., Bastian N., Stein I. T., 2006, A&A, 450, 129
Goddard Q. E., Bastian N., Kennicutt R. C., 2010, MNRAS, pp 491–+
Haas M. R., Gieles M., Scheepmaker R. A., Larsen S. S., Lamers H. J. G. L. M., 2008, A&A, 487, 937
Hancock M., Smith B. J., Struck C., Giroux M. L., Hurlock S., 2009, AJ, 137, 4643
Hibbard J. E., Mihos J. C., 1995, AJ, 110, 140
Jordán A., McLaughlin D. E., Côté P., Ferrarese L., Peng E. W., Mei S., Villegas D., Merritt D., Tonry J. L., West M. J., 2007, ApJS, 171, 101
Kroupa P., 2002, Science, 295, 82
Larsen S. S., 2009, A&A, 494, 539
Leitherer C., Schaerer D., Goldader J. D., González Delgado R. M., Robert C., Kune D. F., de Mello D. F., Devost D., Heckman T. M., 1999, ApJS, 123, 3
Maraston C., 2005, MNRAS, 362, 799
Maraston C., Bastian N., Saglia R. P., Kissler-Patig M., Schweizer F., Goudfrooij P., 2004, A&A, 416, 467
Mengel S., Lehnert M. D., Thatte N., Genzel R., 2005, A&A, 443, 41
Mihos J. C., Hernquist L., 1994, ApJ, 431, L9
Mihos J. C., Hernquist L., 1996, ApJ, 464, 641
Miller B. W., Whitmore B. C., Schweizer F., Fall S. M., 1997, AJ, 114, 2381
Miralles-Caballero D., Colina L., Arribas S., Duc P.-A., 2011, AJ, 142, 79
Perez J., Michel-Dansac L., Tissera P., 2011, ArXiv e-prints
Peterson B. W., Struck C., Smith B. J., Hancock M., 2009, MNRAS, 400, 1208
Rupke D. S. N., Kewley L. J., Barnes J. E., 2010, ApJ, 710, L156
Saitoh T. R., Daisaka H., Kokubo E., Makino J., Oakmoto T., Tomisaka K., Wada K., Yoshida N., 2010, in B. Smith, J. Higdon, S. Higdon, & N. Bastian ed., Galaxy Wars: Stellar Populations and Star Formation in Interacting Galaxies Vol. 423 of Astronomical Society of the Pacific Conference Series, Shock-Induced Starburst and Star Cluster Formation in Colliding Galaxies. pp 185–+
Santiago-Cortés M., Mayya Y. D., Rosa-González D., 2010, MNRAS, pp 496–+
Schechter P., 1976, ApJ, 203, 297
Schweizer F., Miller B. W., Whitmore B. C., Fall S. M., 1996, AJ, 112, 1839
Springel V., 2000, MNRAS, 312, 859
Springel V., Di Matteo T., Hernquist L., 2005, MNRAS, 361, 776
Teyssier R., Chapon D., Bournaud F., 2010, ApJ, 720, L149
Vázquez G. A., Leitherer C., 2005, ApJ, 621, 695
Veilleux S., Kim D.-C., Sanders D. B., 2002, ApJS, 143, 315
Weilbacher P. M., Duc P.-A., Fritze v. Alvensleben U., Martin P., Fricke K. J., 2000, A&A, 358, 819
Whitmore B. C., Chandar R., Fall S. M., 2007, AJ, 133, 1067
Whitmore B. C., Schweizer F., Leitherer C., Borne K., Robert C., 1993, AJ, 106, 1354
Whitmore B. C., Zhang Q., Leitherer C., Fall S. M., Schweizer F., Miller B. W., 1999, AJ, 118, 1551
Zhang Q., Fall S. M., 1999, ApJ, 527, L81